UNIVERSITY OF OKLAHOMA

GRADUATE COLLEGE

QUANTITATIVE GEOPHYSICAL INVESTIGATIONS AT THE DIAMOND M FIELD, SCURRY COUNTY, TEXAS.

A DISSERTATION

SUBMITTED TO THE GRADUATE FACULTY

in partial fulfillment of the requirements for the

Degree of

DOCTOR OF PHILOSOPHY

By

OSWALDO ERNESTO DAVOGUSTTO CATALDO
Norman, Oklahoma
2013

QUANTITATIVE GEOPHYSICAL INVESTIGATIONS AT THE DIAMOND M FIELD, SCURRY COUNTY, TEXAS.

A DISSERTATION APPROVED FOR THE
CONOCOPHILLIPS SCHOOL OF GEOLOGY AND GEOPHYSICS

BY

_____
Dr. Kurt J. Marfurt, Chair

_____
Dr. Carl Sondergeld

_____
Dr. John Pigott

_____
Dr. G. Randy Keller

_____
Dr. Steve Roche

_____
Mr. J. W. Thomas

Ad maiorem Dei gloriam

To Alessandro and Andrea

Acknowledgements

First of all I thank God for all. My life has been a rocky road mixed with flat paths. I know it is all has been God's plan for me.

This work has been influenced by several individuals in many ways. When I write this work it is not only restricted to the results contained in this thesis but all the learning in all the different aspects of my life that have been somewhat touched or modeled those individuals. Unfortunately it is impossible for me to list all that learning but what I can do is dedicate a few words in this section to each one of those individuals. Just a few because if not this would be an infinite chapter.

I will begin with my parents Maria Teresa Cataldo and Oswaldo Davogustto. Now that I am a father myself I understand just a little everything that you did and what that sacrifice meant for me. Not in vain there is a saying that you will learn to be a son once you become a parent. Well I thank you both, I owe you all that I have and all that I am. I thank Andrea Miceli, my wife and companion. With you I have become that which I would not have dreamed of being. It is because of you I push myself more and more to become a better man and a better husband. I thank Giovanni Davogustto, my brother.

I thank Dr. Roger A. Young; my life at OU started because you believed in me when I did not even had an idea of what I wanted to be or what I wanted to do. I miss you a lot. I thank Dr. Kurt J. Marfurt, I always felt that life made me your student by chance and I could not have a better example of good luck for me. With your guidance I have learned seismic interpretation, processing, scientific writing, common sense. If I know geophysics it is because of you. I thank Dr. Carl Sondergeld, you have taught me

critical and analytical thinking. I learned the importance of understanding the rocks and their behavior at any scale. More important I have learned from you to be aware and look for the limitations and assumptions on any technique thus improving my understanding and providing better interpretations. I thank Dr. John Pigott, you started the curiosity on my about the carbonates. I have become passionate about their complexity and what they represent for both, the academy and the industry. I thank Dr. G. Randy Keller; your help through these years at OU has been invaluable to me. I admire your dedication to your students and your ability to cheerfully give advice. I thank Dr. Steve Roche; we share that passion for shear-wave data that only a few understand. I have had much fun working with you doing the detective work to understand the shear-wave phenomena and putting all the pieces of this puzzle together. I thank J. W. Thomas; you have taught me about processing and have been a friend to me. I thank Dr. J. Tim Kwiatkowski; we have had fun times together. I have learned from you the importance of all that math and physics that seemed not important when I was an undergrad. I thank Mike Burnett; you have always encouraged me to become a better geophysicist and have taught me the practical aspects of the business.

I would also like to thank Alison Small, Dr. Roger Slatt, Dr. Lynn Soreghan, Teresa Hackney, Nancy Leonard, Donna Mullins, Jocelyn Cooke, Adrianne Fox, Jody Foote and Alison Richardson.

I would like to thank my brothers in arms on this journey Bradley Wallet, Richard Brito, Alfredo Fernandez and Benjamin Dowdell. It has been fun times and there are more to come. There is a long list of people that I would like to thank that I have not mentioned. This is a thank you for y'all.

Table of Contents

List of Tables

List of Figures

1. Abstract

The Diamond M field over the Horseshoe Atoll reservoir of west Texas has produced oil since 1942. Even with some 210 well penetrations, complex reservoir compartmentalization has justified an ongoing drilling program with three wells drilled within the last three years. Accurate reservoir characterization requires accurate description of the geometry, geological facies, and petrophysical property distribution ranging from core, through log to the seismic scale.

The operator has conducted a careful logging and coring process including dipole sonic logs in addition to acquiring a modern 3D vertical phone – vertical vibrator "P-wave" seismic data volume and an equivalent size 2-component by 2-componet "S-wave" seismic data volume. I analyze these data at different scales, integrating them into a whole. I begin with core analysis of the petrophysical properties of the Horseshoe Atoll reservoir. Measuring porosity, permeability, NMR T_2 relaxation and velocities (V_p and V_s) as a function of pressure and find that porosity measurements are consistent when measured with different techniques. When upscaled, these measurements are in excellent agreement with properties measured at the log scale. Together, these measurements provide a lithology-porosity template against which I correlate my seismic P- and S-impedance measurements.

Careful examination of P- and S-impedances as well as density from prestack inversion of the P-wave survey of the original time migrated gathers showed lower vertical resolution for S-impedance and density. These latter two parameters are controlled by the far-offset data, which suffers from migration stretch. I address this shortcoming by applying a recently developed non-stretch NMO technique which not

only improved the bandwidth of the data but also resulted in inversions that better match the S-impedance and density well log data.

The operator hypothesized that 2C by 2C S-wave data would better delineate lithology than conventional P-wave seismic data. Although introduced in the mid-1980s, 2C by 2C data are rarely acquired, with most surveys showing less vertical resolution than conventional (and prior to slip-sweep technology more economically acquired) P-wave data. Initial processing by the service company showed a comparable, but lower frequency, image for the "transverse" component, and poor images for the "radial" component. Although the dipole sonic logs did not indicate the presence of significant anisotropy, shear wave splitting is readily observed on the surface seismic stacks. I therefore developed a prestack Alford rotation algorithm that minimizes the cross-talk between components, resulting vertical resolution comparable to the P-wave data, and independent measure of lithology, and also a direct measure of the direction of the principal axes of anisotropy.

The direction of azimuthal anisotropy is aligned N45E consistent with the regional maximum horizontal stress axis obtained from the world stress map database. On average, the Cisco Formation appears 10% thicker on the slow shear (S_2) volume than on the fast shear (S_1) volume and between 70% and 100% thicker on the P-wave volume. Cross-plotting cumulative production against the various seismic attributes, I find a strong negative correlation to S-impedance and P-impedance. Zones of low S-impedance and low P-impedance correlate to better producing wells. More quantitative correlation will require the analysis of the role fractures versus porosity contribute to production..

2. Introduction

The Permian basin had produced 18 percent of the total U.S. oil production in 1999, and it contains about 23 percent of the proved reserves of the United States excluding unconventional reservoirs (Dutton et al., 2003). The Pennsylvanian and Lower Permian Horse Shoe Atoll carbonate reservoir in the Permian basin has been producing since the late 1940's. Dutton et al. (2003) ranked this reservoir as one of the top four Permian Basin producers with a cumulative production of 2.7 Bbbl. with the Kelly-Snyder and part of the Diamond M field as the largest contributors. In 2000, the Diamond M field produced 1 Mbbl and had a cumulative production of 248 Mbbl since 1940.

The Horseshoe Atoll is an aggregate of carbonate buildups deposited over flat lying lower Pennsylvanian carbonates of the Strawn formation (Sur, 2010). The lithofacies that compose the Horseshoe Atoll are sponge-algal-bryozoan and phylloid-algal-mound wackestones and packestones (Dutton et al., 2003). According to Dutton et al. (2003) subsidence of the Midland Basin led to a repeated back stepping of the platform from Strawn trough Cisco and Canyon time. During Early to Middle Canyon time, high variability of the sea level produced tight to porous layers that caused strong reservoir heterogeneity. Sea level fluctuation also allowed the percolation of fresh water into the sub-aerially exposed carbonates resulting in the development of, caves, karst and fractures as well as fabric selective moldic porosity (Dutton et al., 2003). Porosities in this formation range from 4 to 20 % with an average of 9.8%. Permeabilities range from 1 to 1760 mD and averages 19 mD (Dutton et al., 2003).

My goal in this study is to characterize the Horseshoe Atoll reservoir in the Diamond M field by integrating core, log and, P- and S-wave seismic data. Specifically I want to identify sweet-spots using the pre-stack attributes in order to enhance production. I have built tools and I have applied tools from my peers at the AASPI and IC^3 consortiums to help me achieve this goal.

I present this work in the form of scientific papers in order to document and transfer the technology I have applied or developed.

In Chapter 3, I study the rock properties at core scale from two wells and at log scale from seven wells in the Diamond M field.

In Chapter 4, I apply a non-stretching NMO technique developed at the AASPI consortium by Bo Zhang to enhance simultaneous inversion results on the P-wave data.

In Chapter 5, I develop a shear data pre-stack processing workflow that includes a pre-stack Alford rotation technique to estimate anisotropy direction at each trace in the Diamond M field.

In Chapter 6, I integrate some of the results in Chapters 3, 4 and 5 to understand the relationship between the pre-stack P- and S-wave data attributes and their impact on production.

Chapters 3 to 6 will be submitted to *Interpretation* for review and publication.

In Chapter 7 I have included other work. This paper is an investigation on the applicability of CWT spectral decomposition for reservoir architecture delineation and has been published in *Interpretation*.

Finally, Chapter 8 and Chapter 9 include my conclusions and recommendations.

The Appendix includes the processing workflow I used for the P-wave data as well as the documentation for running the phase-residues algorithm, prestack 2C by 2C rotation, and fracture strike derived from Alford rotation using my software.

3. Motivation and Objectives

Historically shear wave propagation has been relegated to research studies. This is because prior to slip sweep technology shear waves require more effort, time, and money in order to obtain similar results to those compared with compressional wave data. Shear waves have two polarizations. Since they are less sensitive to fluids and hence the water table, their effective weathering zone is thicker and often more irregular than P-waves, giving rise to more difficult statics solutions. Finally, shear waves split when encountering anisotropic media at angles other than along the axes of symmetry.

Although these differences with compressional data sound discouraging, these very facts are why shear wave data are interesting and contribute to understanding rocks and fractures. Crampin (1985) demonstrated that shear waves carry unique information about the internal structure of the rocks through which they propagate using synthetic examples and relating the splitting to the strike of vertical cracks. Alford (1986) showed how after the rotation from survey coordinates to the principal axis of anisotropy coordinates, shear wave data quality is improved and can be easily interpreted. Lynn and Thomsen (1990) built on Alford's hypothesis and demonstrated that the time differences between two crossing shear-wave lines approximately parallel to the principal axis of anisotropy can be used to estimate fracture intensity. Sondergeld and Rai (1992) studied the shear-wave splitting phenomena and confirmed Alford's (1986) assumptions that shear data will split into two orthogonal components for laboratory measurements. Rüger (1996) described how the shear-wave AVO gradients, if they can be reliably extracted from the data, are sensitive to the shear-wave splitting parameter and can be related to the fracture density in the rocks. Roche et al. (1997) integrated

multicomponent data with a time lapse surveying at Vacuum field, New Mexico to detect bulk property variations in the reservoir rock and combined 4D, multicomponent data with well control to provide a general interpretation of the permeability trends in Vacuum Field. Finally, DeVault et al. (2002) implemented a least-squares shear wave AVO analysis to map changes in density, shear wave velocity and fracture density in Vacuum Field, New Mexico.

Recent innovations in encoded sweep technology as well as the widespread availability and use of 3-component digital phones have reduced the cost of "2D by 2C' data to about 20% more than the conventional vertical vibrator "P-wave" data. (J.W. Thomas, personal communication).

In this research, I use detailed analyses of laboratory measurements of rock properties to estimate the limitations of predicting reservoir properties like porosity from log and seismic data. I use the techniques proposed by Alford (1986) to estimate an average fracture direction from the pre-stack shear seismic data. I apply a non-stretch NMO tool to compensate for background drift (Swan, 2007) and avoid crossing events interference in AVO intercept and gradient estimation. Finally I integrate the core, log and inversion data to understand production from this reservoir.

The objective of my research is to provide a workflow that integrates core, log, P- and S-wave seismic data to predict the reservoir rock properties of the Horse Shoe Atoll in the Diamond M Field as well as in other mature fields.

REFERENCES

Alford, R. M., 1986, Shear data in the presence of azimuthal anisotropy: 56th Annual International Meeting, Society of Exploration Geophysicists, Expanded Abstracts, 476-479

Crampin, S., 1985, Evaluation of anisotropy by shear-wave splitting. Geophysics, 50, no 1, 142-152

DeVault, B., T. L. Davis, I. Tsvankin, R. Verm and F. Hilterman, 2002, Multicomponent AVO analysis, Vacuum field, New Mexico. Geophysics, 67, 701-710

Lynn, H. B. and L. Thomsen, 1990, Reflection shear-wave data collected near the principal axes of azimuthal anisotropy. Geophysics, 55, 147-156

Roche, S. L., 1997, Time-lapse, multicomponent, three-dimensional seismic characterization of a San Andres shallow shelf carbonate reservoir, Vacuum field, Lea County, New Mexico: Ph.D. thesis, Colorado School of Mines.

Rüger, A., 2001, Reflection Coefficients and Azimuthal AVO Analysis in Anisotropic Media, Geophysical Monograph Series No. 10, Society of Exploration Geophysicists

Swan, H. W., 2007, Automatic compensation of AVO background drift: The Leading Edge, 26, 1528-1536.

Sondergeld, C. and C. S. Rai, 1992, Laboratory observations of shear-wave propagation in anisotropic media: The Leading Edge, 11, 38-44.

Thomsen, L., I. Tsvankin and M. C. Mueller, Coarse-layer stripping of vertically variable azimuthal anisotropy from shear-wave data. Geophysics, 64, no. 4, 1126-1138

4. Poreshape estimation for the Horseshoe Atoll carbonate reservoir, Midland Basin, Texas: An integrated approach

Oswaldo Davogustto[1] and Carl Sondergeld[1]

[1] University of Oklahoma, School of Geology and Geophysics

ABSTRACT

We measured the petrophysical properties of 34 core plugs from two wells in the Horseshoe atoll, Scurry County, Texas. We measured porosity, permeability, NMR T_2 relaxation and velocities (V_p and V_s) as a function of pressure. Porosity measurements are consistent when measured with different techniques; however, permeabilities vary considerably between direct measurements and NMR estimations. Predicted permeabilities using NMR methods differ by one order of magnitude from measured Klinkenberg corrected permeabilities. Compressional and shear velocities show a strong dependency on porosity. We find that Biot-Gassmann equations are valid if porosities are greater than 8 %. Using Biot-Gassmann's theory and the Kuster and Toksöz scattering model we are able to predict pore shapes using the measured bulk and shear moduli. Using compressional and shear sonic, density, and porosity logs we extend our laboratory observations and deduce that crack like pores are important in the acoustic log seismic response.

INTRODUCTION

Sixty percent of world oil reserves are found on carbonate reservoirs. Petrophysical evaluation of reservoir rocks is a key to understand reservoir performance. The ultimate goal for petrophysical analysis is to identify pay zones in the reservoir and predict properties like porosity or permeability and ultimately fluid type

and saturation. However, achieving this goal is not easy since many factors contribute to the estimation of physical properties of reservoirs and to pay identification. Most evaluation approaches begin with a calibration of logs through core measurements and the use of logs to calibrate seismic data.

Several authors have found empirical or theoretical relationships between measured petrophysical and seismic properties of rock samples and rock behavior. Gassmann (1951) introduced a model for understanding the propagation of elastic waves through a porous media based on the assumptions that pressure variations introduced by the elastic waves are sufficiently slow to allow pore equilibrium, pores must be connected and the medium has to be homogeneous and isotropic. Biot (1956, 1962) developed the theory for the propagation of stress waves in a porous media with pores filled by a compressible fluid. Biot (1956) and Gassman (1951) theories gave rise to the Biot-Gassmann equations widely used in modeling fluid effects on rock properties. Biot-Gassmann equations are given by:

$$K_e = K^* + \frac{K_f n^2}{\left[\Phi + \frac{K_f}{K_0}(n - \Phi)\right]}; n = \left(1 - \frac{K^*}{K_0}\right)$$

$$G_e = G^*$$

where K is the bulk modulus and the subscripts and superscripts refer to the property of e undrained rock; f the fluid; * the dry porous frame, and 0 matrix, respectively. Φ is the effective porosity, n is the Biot coefficient, G_e is the effective saturated shear modulus and G^* is the dry porous frame shear modulus. Kuster and Toksöz (1974) proposed a scattering based model for estimating bulk and shear moduli in two phase media. Kuster and Toksöz (1974) derive the scattered wave field resulting from incidence plane wave

son a rock volume containing a dilute inclusions and find that the concentration and the aspect ratio affect both bulk and shear moduli.

Castagna et al. (1985) provide empirical relationships between compressional and shear waves for a wide set of clastic rocks. They find a linear relationship between shear and compressional wave velocities for their core samples. Castagna et al. (1985) also find good agreement between measured dry bulk modulus and predicted bulk modulus using Gassmann's equations.

In the Permian Basin, carbonates constitute up to 77% of the reservoir rocks for oil plays (Dutton et al. 2004). To our knowledge little has been published on the petrophysical properties of the Horseshoe atoll carbonate reservoir in the Midland Basin, TX. Rafavich et al. (1984) found porosity to be the dominant parameter affecting compressional and shear velocities in carbonate rocks from the Mission Canyon formation, Williston basin, North Dakota; lithology and secondary mineralogy have only a small influence on the velocities. They find that combining compressional and shear velocities can be used to discriminate lithologies. Assefa et al. (2002) acquired laboratory measurements of compressional and shear velocities from Great Oolite Formation of southern England for different saturating fluids. They developed a method to account for the aspect ratios of the porosities and remove its effects from the measured velocities hence achieving a better correlation between porosities and velocities. They find that Biot-Gassmann theory over estimates the predicted velocities due to rock-fluid interaction for these samples. Baechle et al. (2005) found similar results to those of Assefa et al. (2002).

Adam et al. (2006) evaluate the applicability of Gassmann's theory to limestone and dolomite samples. They find that at high pressures and in the seismic frequency range, Gassmann's assumptions are valid for high aspect ratio porosity. For lower aspect ratios, they propose a rock-fluid interaction mechanism that explains why Gassmann's assumptions are not honored.

Bhagat et al. (2012) measured compressional and shear velocities for carbonate rocks from Rus, Dammam and Asmari formations from the United Arab Emirates. Their measurements were made on saturated samples using air, dodecane and a brine of a specific composition to avoid matrix dissolution. They find a good correlation between measured and predicted bulk modulus using Gassmann's theory and furthermore they do not observe any shear modulus change due to rock-fluid interactions. In this work we demonstrate the validity of Biot-Gassmann's theory for the Horseshoe atoll carbonates and compare Biot-Gassmann's results with results from the Kuster and Toksöz (1974) scattering model in an attempt to predict pore shape influence in core samples and well log data.

GEOLGICAL BACKGROUND

Our study is focused on Cisco and Canyon formations of the Horseshoe atoll in Midland Basin, Scurry County, TX (Figure 4.1). The carbonates of the Horseshoe atoll formed during late Pennsylvanian to early Permian time when shallow water carbonate deposits dominated most of the deposition in the Permian basin. The reservoir is classified as a carbonate buildup and is composed mostly of rich biomicritic rocks with some packstone and grainstone occurrences (Fisher, 2005).

METHODOLOGY

Laboratory measurements

We used a set of 34 cylindrical horizontal plugs from two wells in the Diamond M Filed, Texas to obtain porosity, permeability, NMR T_2 relaxation and velocity measurements. We acquired porosity measurements using a helium pycnometer (HPP) and found dry and saturated weights. We acquired pressure dependent porosity and permeability measurements over a confining pressure range between 1000 and 5000 psi. We also acquired nuclear magnetic resonance (NMR) measurements for the dodecane saturated samples and computed porosity and permeability based on these measurements using the Coates et al. (1999) and SDR (1995) correlations. NMR measurements were made using a 2MHz Oxford-Maran ultra spectrometer. The samples were pressure saturated at 2000psi after subjecting the samples to a vacuum. We cleaned the plugs using a Soxhlet extractor and dried them in an oven at 100° C for twelve hours before acquiring dry measurements. We acquired velocity measurements using a pulse transmission technique over a confining pressure range from 250 to 5000 psi with pore pressure equal to atmospheric pressure for both dry and dodecane saturated samples. The nominal frequency of the P and S-waves transducers are 1MHz and 500 kHz, respectively.

Well logs evaluation

We developed a workflow for moduli estimation using well logs from 8 different wells in the Diamond M field, Scurry County, Texas. First, we calculate the dry frame bulk modulus from the well logs using Zhu and McMechan (1990) formula:

$$K^* = \frac{K_e\left[\frac{\Phi K_0}{K_f} + 1 - \Phi\right] - K_0}{\left[\Phi\frac{K_e}{K_f} + \frac{K_e}{K_0} - 1 - \Phi\right]};$$

where K_e is the effective bulk modulus for the fluid saturated rock, K^* is the dry porous rock frame bulk modulus, K_f is the pore fluid bulk modulus, K_0 is the matrix bulk modulus and Φ is the effective porosity. We then proceed to calculate the value of the normalized dry bulk modulus (K^*/K_0) and compared it to the theoretical predictions of Kuster and Toksöz (1974). We assume the matrix bulk modulus to be 74 GPa equal to that of calcite. We calculated fluid bulk modulus the following relationship:

$$\frac{1}{K_f} = \frac{S_w}{K_w} + \frac{S_o}{K_o} + \frac{S_g}{K_g}$$

where K_w is the bulk modulus of water assumed to be 2.417 GPa, K_o is the bulk modulus of the oil in the reservoir, assumed to be 1.352 GPa and K_g is the bulk modulus of the gas in the reservoir, assumed to be 0.08 GPa. Oil and gas saturations were 25% in average according to core reports supplied by Parallel Petroleum LLC.

RESULTS AND DISCUSSION

Porosity and Permeability

Figure 4.2 shows helium porosities versus confining pressure for wells E and J. Porosity values range from 0.5 to 20 % for well E and 0.5 to 15 % for well J. We observe an average near linear decrease in porosity of 16% (3.4%/1000psi) with increase of pressure to 5000 psi. We observed a linear trend in porosity-pressure behavior suggesting volumetric crack contributions are small. Figure 4.3 shows Klinkenberg corrected permeabilities as a function of confining pressure. We observe a decreasing trend in permeability for all the samples with an increase of confining

pressure. Based on these results, we infer the pressence of microcracks in the core plugs since the greater rate of change in permeabilities occurs at lower confining pressures. Hellium porosity measurements at 1000 psi and HPP show a good agreement; porosity values range from 0 to 20 % posoristy (Figure 4.4a). NMR and helium porosity values also show good agreement for all the samples (Figure 4.4b). We also compared the measured permeabilities with calculated Coates (1999) and SDR (1995) estimate permeabilities from NMR measurements and found a poor correlation (Figure 4.5). It appears NMR predicted permeabilities are on average consistently greater than measured permeabilities by about one order of magnitude. This result indicates then that NMR logs in this formation will produce reliable porosity but not permeability values.

Compressional and Shear velocities

Figure 4.6 and Figure 4.7 show the measured wet compressional (V_p^{wet}) and dry shear (V_s^{dry}) velocity as a function of confining pressure for wells E and J, respectively. Both compressional and shear exhibit rapid changes with increase of confining pressure between 250 and 2000 psi. We interpret these changes to be an effect of crack closure with the increase of confining pressure. This observation is in agreement with the observation we made previously for porosities and permeabilities. In both wells we observe an increase in velocity with an increase in pressure for values greater than 2000 psi, this indicates that the velocity change is strongly dependent on crack porosity. This results is in agreement with the observations made by Rafavich et al. (1983), Adam et al. (2006) and Baghat et al. (2012) among others. The fact that velocity measurements do not reach an asymptote at greater confining pressures suggests the presence of high aspect ratio (sphere-like) pores in the samples (Figure 4.6 and Figure 4.7).

Biot-Gassmann modeling

We performed Biot-Gassmann modeling on the data from the core plug measurements. From the measured velocities and densities we computed the dry and saturated bulk and shear moduli for well E and J samples. Figure 4.8 shows the dry shear modulus (G^*) versus the dodecane saturated shear modulus ($G_{dodecane}$) at 5000 psi. We observe a good correlation between G^* and $G_{dodecane}$ implying that there is no fluid-rock interaction between the dodecane and the rock matrix. Figure 4.9 shows the measured dodecane saturated bulk modulus (K_{meas}) versus the effective bulk modulus (K_{pred}) computed using the dry bulk and shear modulus measured for the core plugs at 5000 psi and substituting the bulk modulus of dodecane for air. We also observe a good agreement between the measured and the predicted data. There is a deviation in trend for samples with K_{meas} greater than 42 GPa where the predicted values are either over or under estimated. Bhagat et al. (2012) found the same behavior in carbonates from the United Arab Emirates and correlated it with a porosity threshold of 8%. We interpret the value of 8 % porosity to be the threshold for porosity interaction for some of the samples.

Pore type characterization using Kuster and Toksöz scattering model on core samples

To corroborate the results observed in Figure 4.6 and Figure 4.7 we calculated the normalized dry bulk modulus (K^*/K_0) and the normalized shear modulus (G^*/G_0) for all our samples. Figure 4.10 and Figure 4.11 show the calculated K^*/K_0 and G^*/G_0 versus porosity for the dry core plugs at each confining pressure. We have also plotted the theoretical solution for pore shape stiffness given by Kuster and Toksöz (1974). Using this approach we determine that most of the pore shapes in our samples have a

low aspect ratio. We also observed that with increasing confining pressure the values for K^*/K_0 and G^*/G_0 approach the value of 1 due to closure of low aspect ratio porosity. Previous observations combined with the modeled values using Kuster and Toksöz (1974) theory, and thin section photographs from core samples confirm our predicted pore aspect ratios in the samples (Figure 4.12).

Pore type characterization using Kuster and Toksöz scattering model on well logs

We begin by calculating compressional and shear velocities and total porosity from the well logs and calibrate these derived logs with the measurements made from core samples (Figure 4.13, Figure 4.14, and Figure 4.15). We calculate the normalized dry bulk modulus (K^*/K_0) from our velocity and porosity logs. This approach is slightly different than Xu and White's (1995) approach in which a soft inclusion aspect ratio is selected to best match the log data. We are asking which range of aspect ratios is suggested by the data. This is possible by comparing our derived dry normalized bulk modulus to the theoretical results obtained by Kuster and Toksöz (1974). Using the normalized dry bulk modulus allows us to avoid the attenuation effects for high and low frequency range measurements due to the presence of fluids. Figure 4.16 shows the results for the K^*/K_0 modeling using seven wells in the Diamond M field, unfortunately logs from well E were affected by washout and this well was not included in the modeling. We observe two distinctive pore shapes distributed between 0.1 and 0.01 aspect ratios with a predominance of those that have α=0.1 values. Results also show values of K^*/K_0 that plot above α=1 line. This is an inconsistency; by using a photoelectric factor versus bulk density cross-plot (Figure 4.17) we identify the values with anomalous aspect ratio to fall in one of two classes: either our assumption for the

matrix is wrong or the porosity value is less than 8%. In Figure 4.18, we have color-coded K^*/K_0 using porosity values. We observe that K^*/K_0 values below the 8% porosity threshold display a large scatter suggesting a wide range of pore shapes. K^*/K_0 values for porosity greater than 8% cluster at α=0.1 aspect ratios. As discussed before 8% porosity represents a connectivity threshold in our samples. Although Biot-Gassmann theory does not specifically treat crack or fracture porosity as this is implicitly captured in the value of K*, the lower aspect ratio of this type of porosity in sufficient concentrations is more compliant and will to allow the pore fluid relaxation. Batzle et al. (2001) also observed similar results in their samples.

CONCLUSIONS

We approach the petrophysical characterization of the Horseshoe Atoll using four basic parameters porosity, permeability and compressional and shear acoustic velocities. We found that porosity measurements using different techniques are in good agreement. Measured permeability on the other hand differs by an order of magnitude from NMR based estimates. This means that the borehole NMR tool will predict the true porosity in brine saturated sections but will be unable to predict permeability within an order of magnitude.

Porosity, permeability and acoustic velocity measurements indicate the presence of cracks and microcracks in our samples. This result was inferred by the pore type characterization using the Kuster and Toksöz (1974) models. Although cracks are not considered explicitly in Biot (1956, 1962) or Gassmann (1951) theoretical formulations, but they are implicitly in the measured value of K^*, we observe a good agreement between measured and predicted bulk modulus values suggesting a good pore scale

connectivity. Saturated and dry shear modulus are equivalent in our samples indicating the matrix has neither been weakened nor strengthened by our saturating fluid. From these observations and the agreement between measured and predicted bulk modulus we confirmed that the Biot-Gassmann theory is valid for this reservoir. Core to log calibration allowed us to reproduce log properties. Using these results we are able to model pore shapes based on the well logs. We find that for both, core and log data, that there is a porosity connectivity threshold of about 8%, although it seems to have a greater influence in the low aspect ratio porosity based on our results.

ACKNOWLEDGEMENTS

The authors would like to thank Alison Small and Parallel Petroleum LLC for donating the core samples that made this work possible. AASPI and IC^3 consortia sponsors for their financial support. We also would like to extend special thanks to Gary Stowe, Bruce R. Spears, Aravinda Buddhala, Ali Ousseini Tinni, Andrea Miceli, Bradley Wallet and Dr. J. Tim Kwiatkowski for their invaluable help.

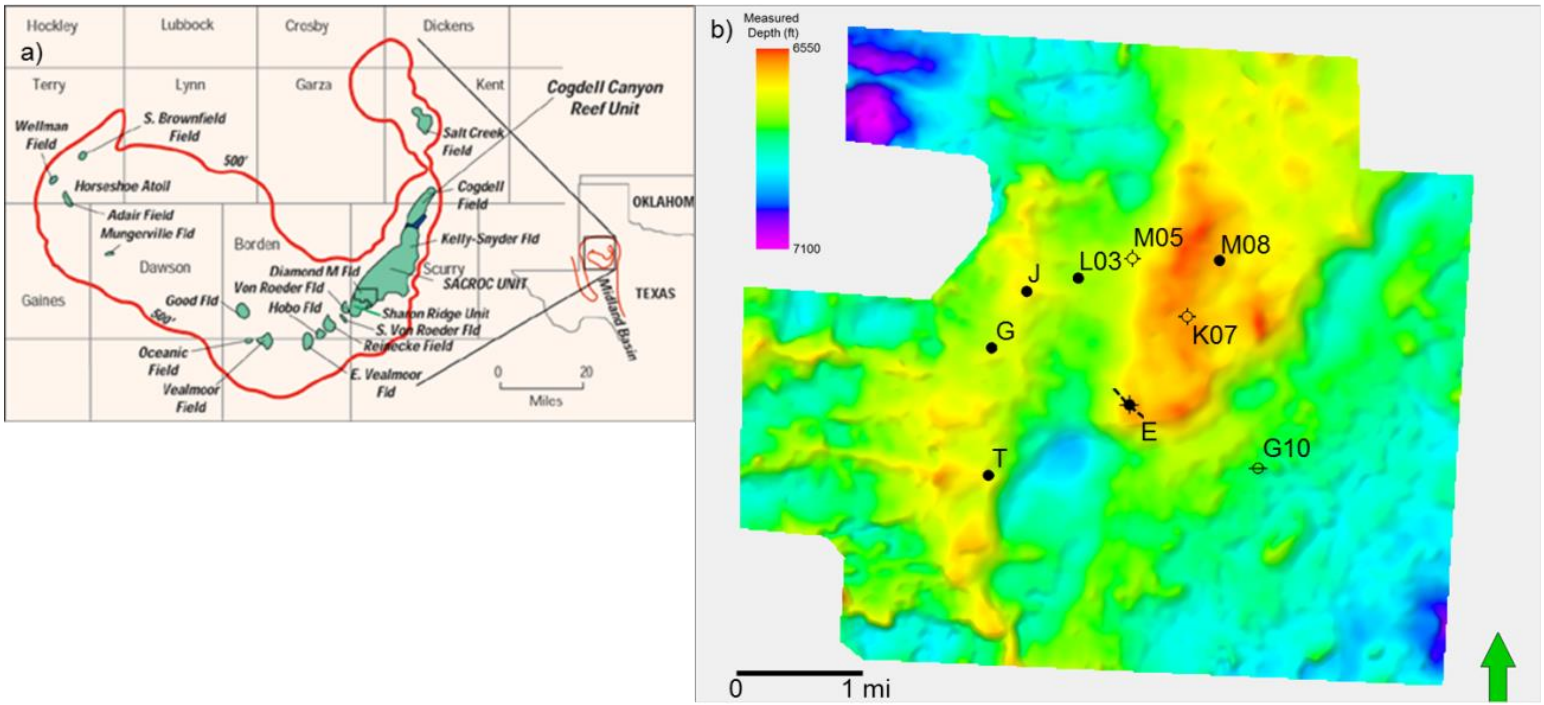

Figure 4.1: (a) Location of the Diamond M Field, Scurry County, TX. (b) Time structure map indicating the location of wells used in this study. The largest carbonate buildup is defined by the red and yellow colors in (b)

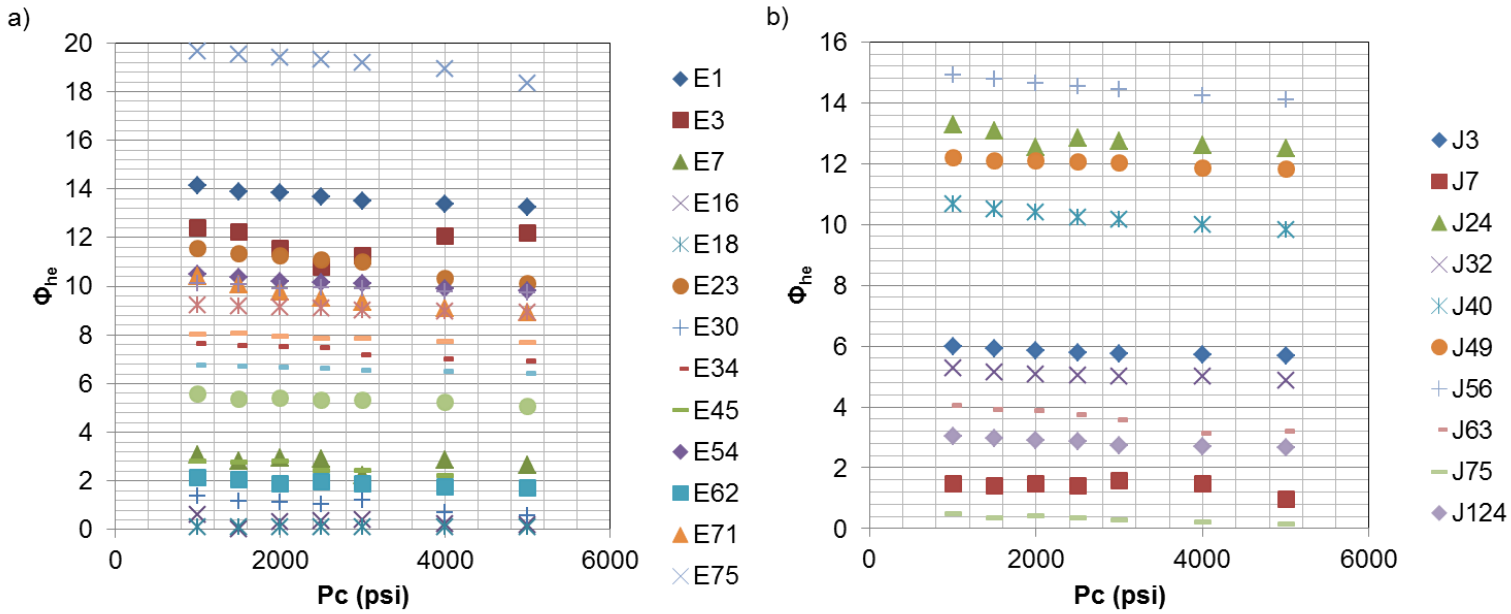

Figure 4.2: Helium porosities as a function of confining pressure for (a) well E and (b) well J. The decrease in porosity with increasing confining pressure suggests that a fraction of the porosity has a low aspect ratio. The relative linear behavior of the porosity curves with pressure suggests that cracks do not possess a significant volume. The average change in porosity for both datasets is about 16% or 3.4%/1000psi.

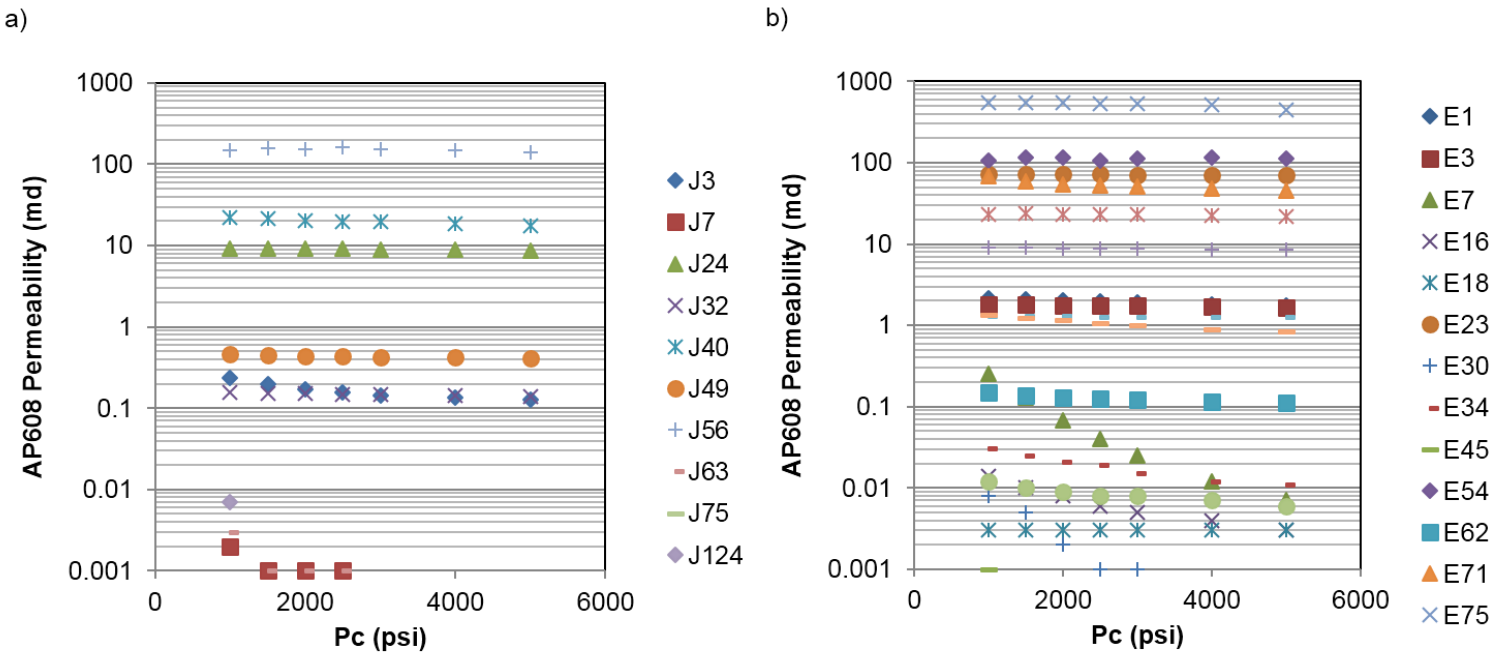

Figure 4.3: Klinkenberg corrected permeabilities as a function of confining pressure for (a) well E and (b) well J. Permeability shows no strong dependency on pressure this implies that permeability is not crack dependent.. The average change in permeability for both datasets is 5%

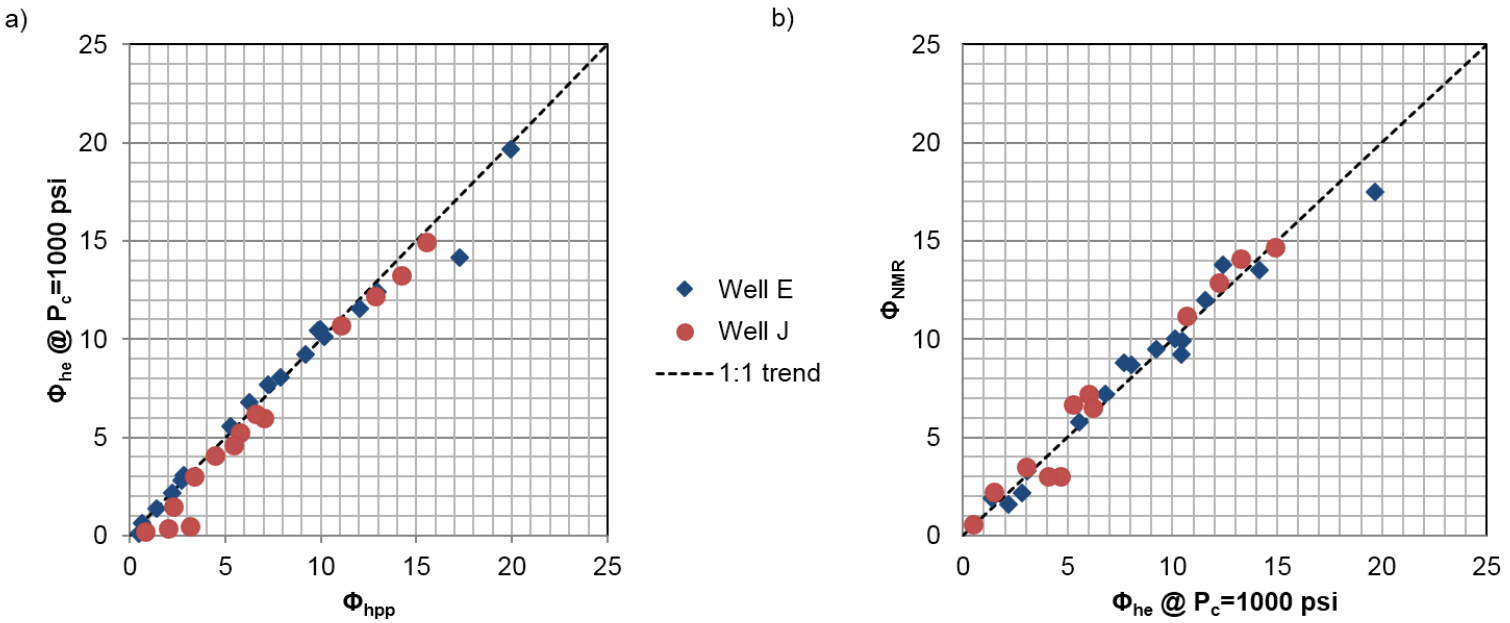

Figure 4.4: Comparison between (a) helium pycnometer-porosimeter (HPP) porosity versus Φ_{he} and (b) Φ_{he} versus Φ_{NMR} for wells E and J. There is a good agreement between all measurements. This is an important result because implies that we will have a very good estimate of true porosity from NMR borehole tools.

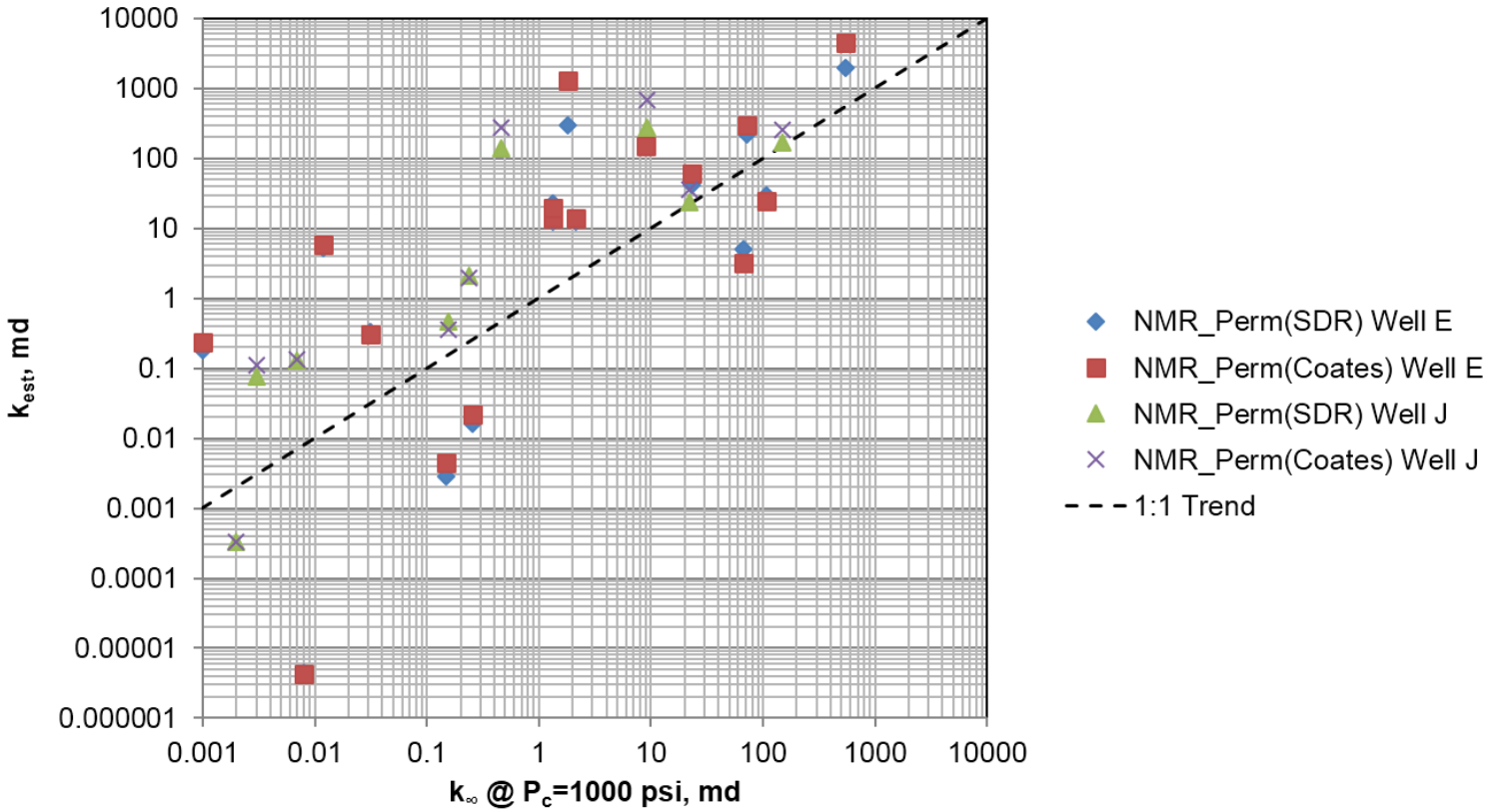

Figure 4.5: Klinkenberg permeability versus NMR for wells E and J. There is a positive correlation between methods but the difference between the measured and predicted permeabilities is on average about one order of magnitude.

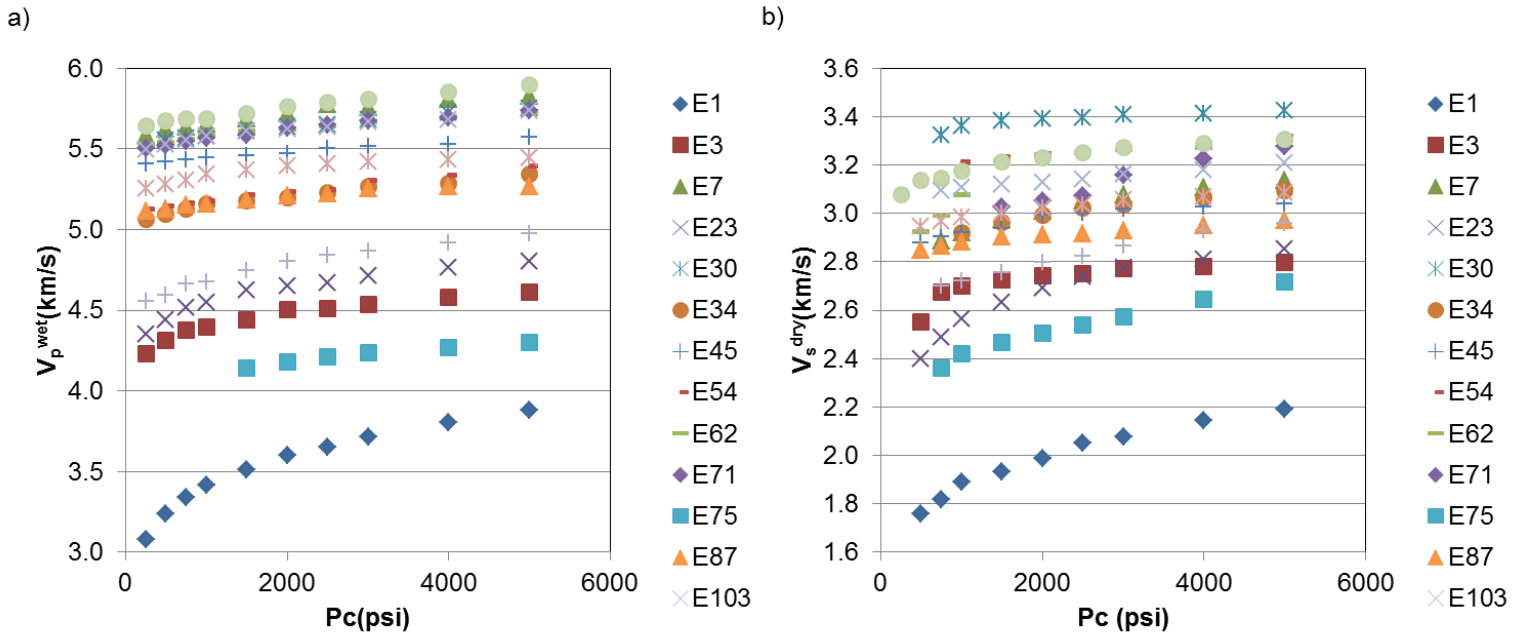

Figure 4.6: (a) Compressional and (b) shear velocities versus confining pressure for well E. Both datasets show a nonlinear increase with the increase of confining pressure. At low pressures we observe a rapid increase of velocities due to reduction of crack porosity. The more gradual changes observed at high pressures are possibly due to high aspect ratio porosity. The average change in compressional and shear velocities with pressure for this well is 5% in both cases.

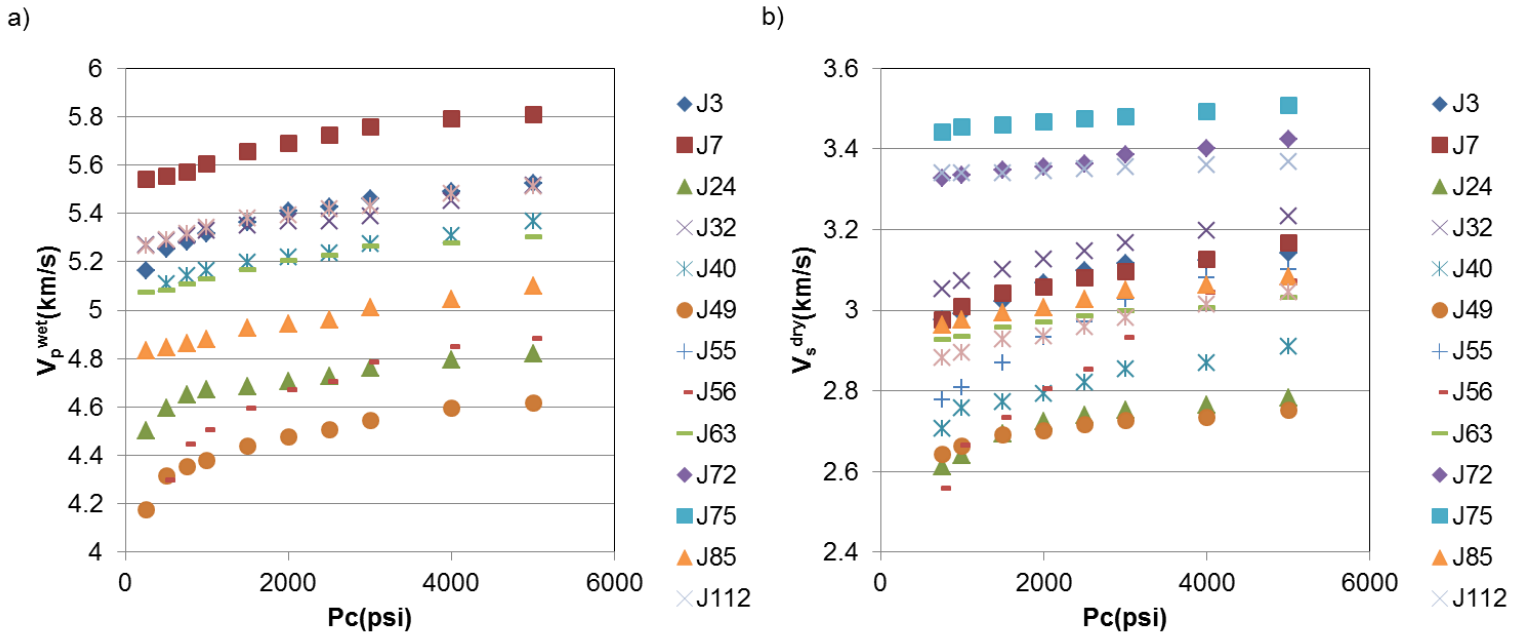

Figure 4.7: (a) Compressional and (b) shear velocities versus confining pressure for well J. Both datasets show a nonlinear increase with the increase of confining pressure. At low pressures we observe a rapid increase of velocities due to reduction of crack porosity. The changes more gradual observed at high pressures are possibly due to high aspect ratio porosity. The average change in compressional and shear velocities with pressure for this well is 5% in both cases.

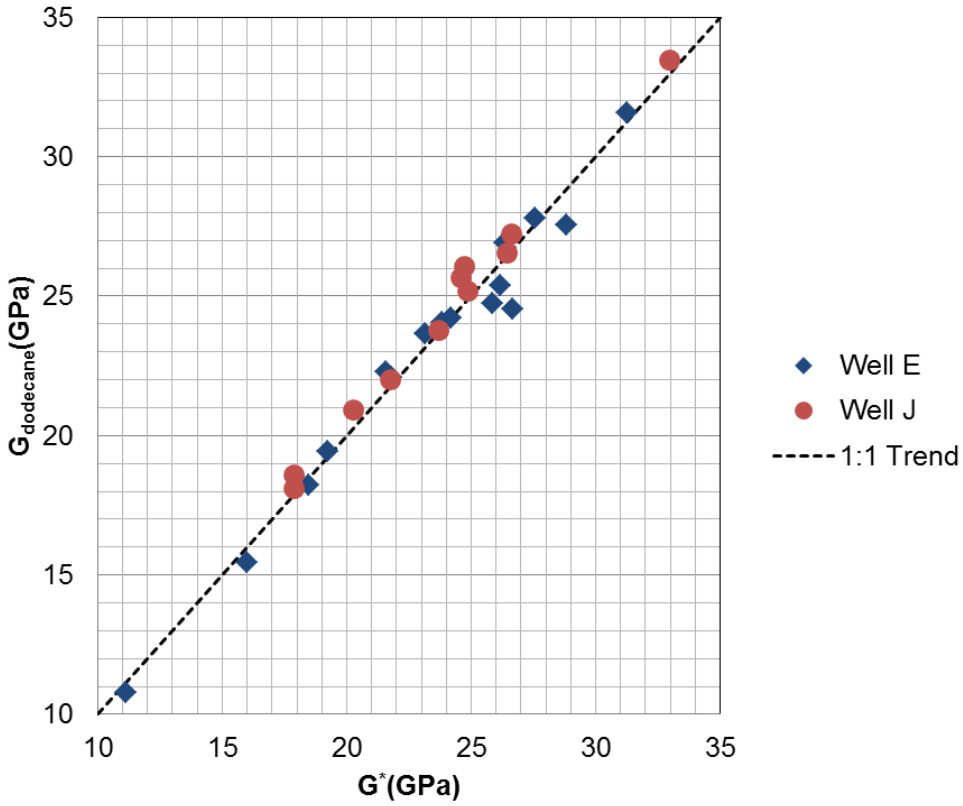

Figure 4.8: Dry versus wet shear modulus computed from the shear velocities and densities for wells E and J. Values align on a 1:1 trend line as inferred from Biot-Gassmann equations and indicating no fluid induced framework changes.

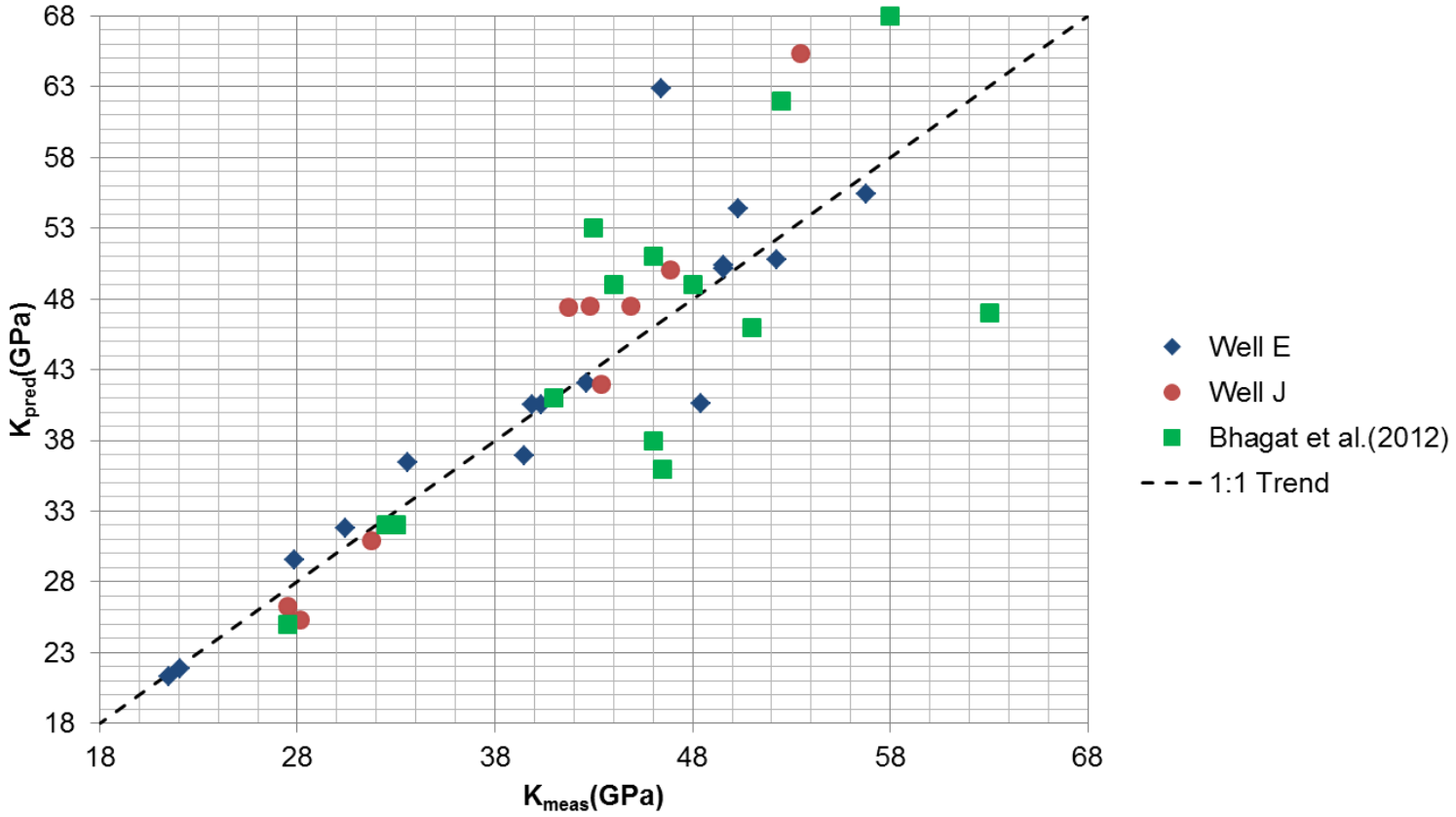

Figure 4.9: Measured (K_{meas}) versus predicted bulk modulus computed from compressional and shear velocities for wells E and J. We observe a good correlation in general between the measured and the predicted bulk saturated modulus. This also confirms that Biot-Gassmann theory works for this reservoir. We observe a change in behavior for samples with a K_{meas} greater than 42 GPa that correspond to a porosities lower than 8%. This result is in agreement with the findings by Bhagat et al. (2012). Bhagat et al. (2012) results are plotted in green for reference.

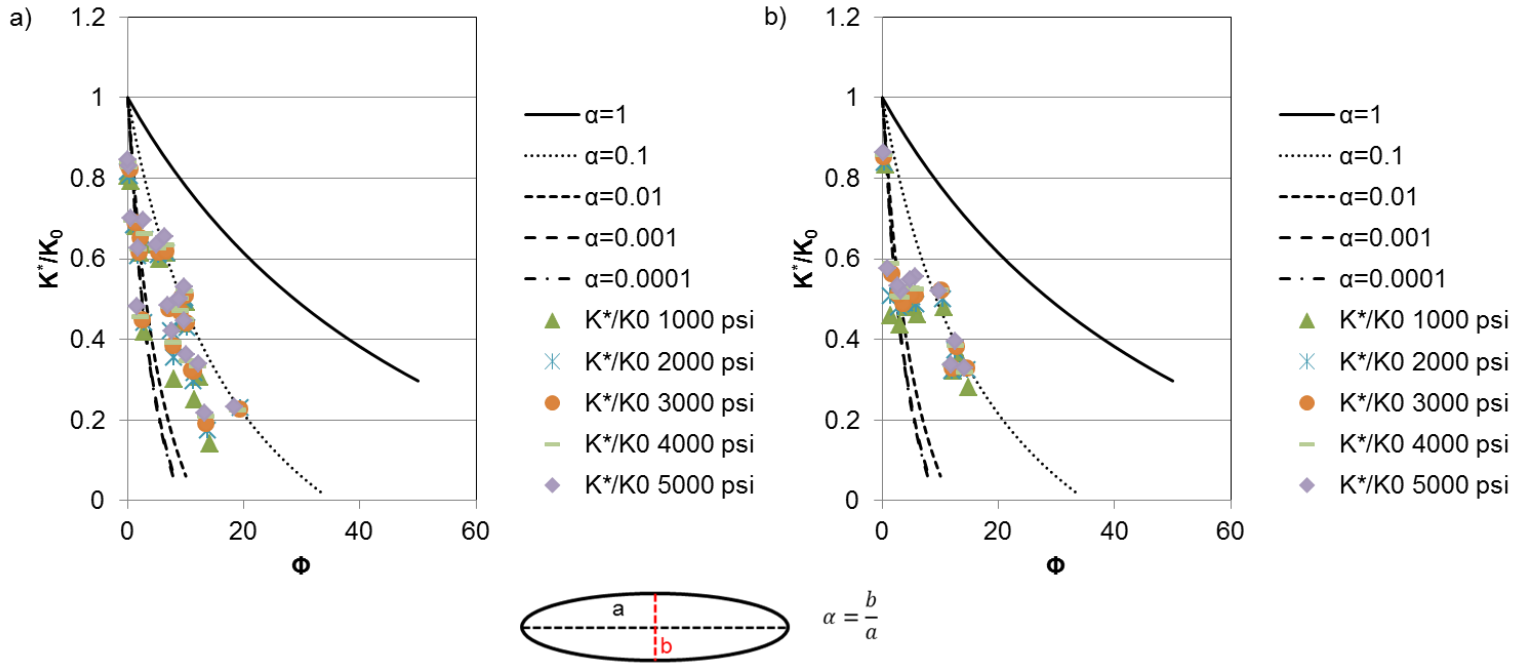

Figure 4.10: Normalized dry bulk modulus versus porosity for (a) well E and (b) well J. Black lines indicate the theoretical solution for the effect of crack aspect ratio on the bulk modulus. Note that for both wells porosity has an aspect ratio lower than 1 indicating crack like porosity.

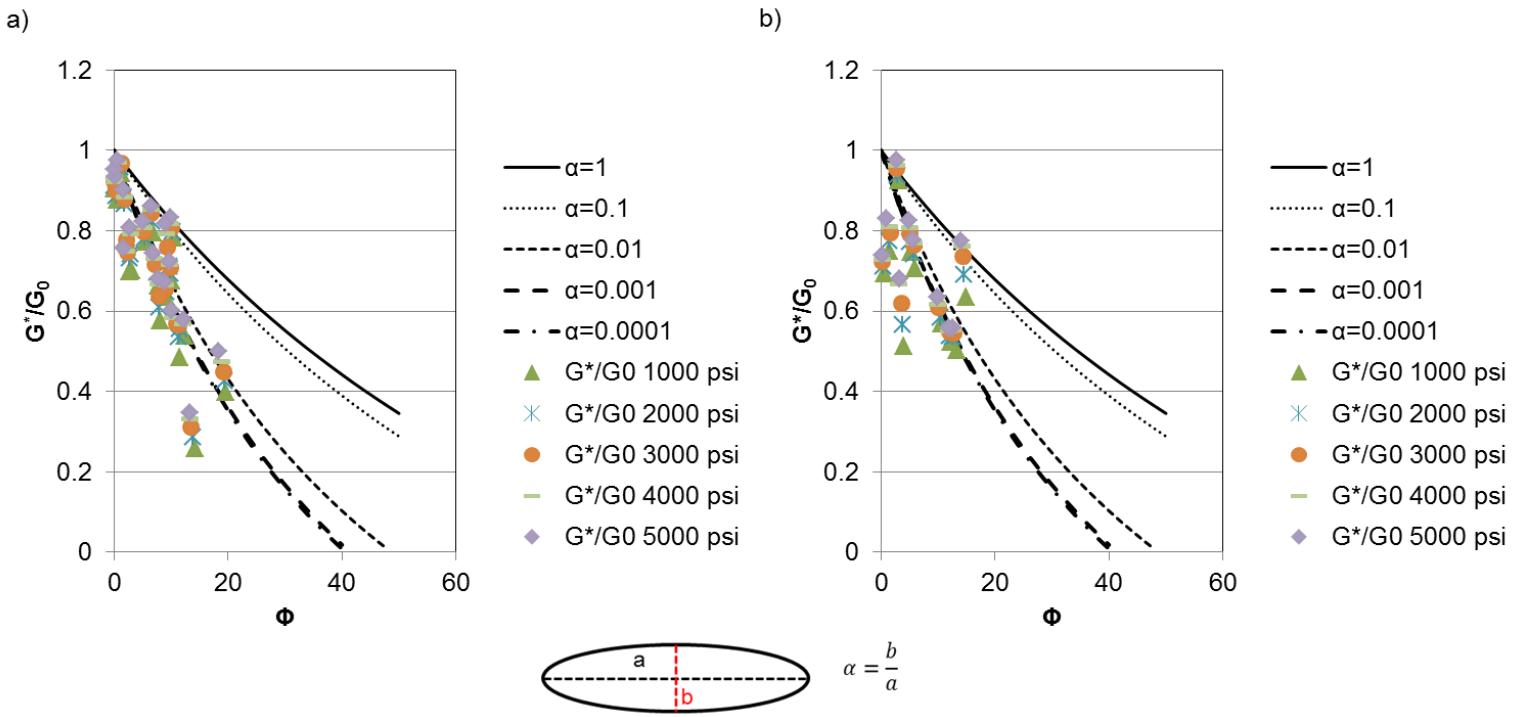

Figure 4.11: Normalized dry shear modulus versus porosity for (a) well E and (b) well J. Black lines indicate the theoretical solution for the effect of crack aspect ratio on the bulk modulus. Note that for both wells most porosity has an aspect ratio lower than 1 indicating crack like porosity.

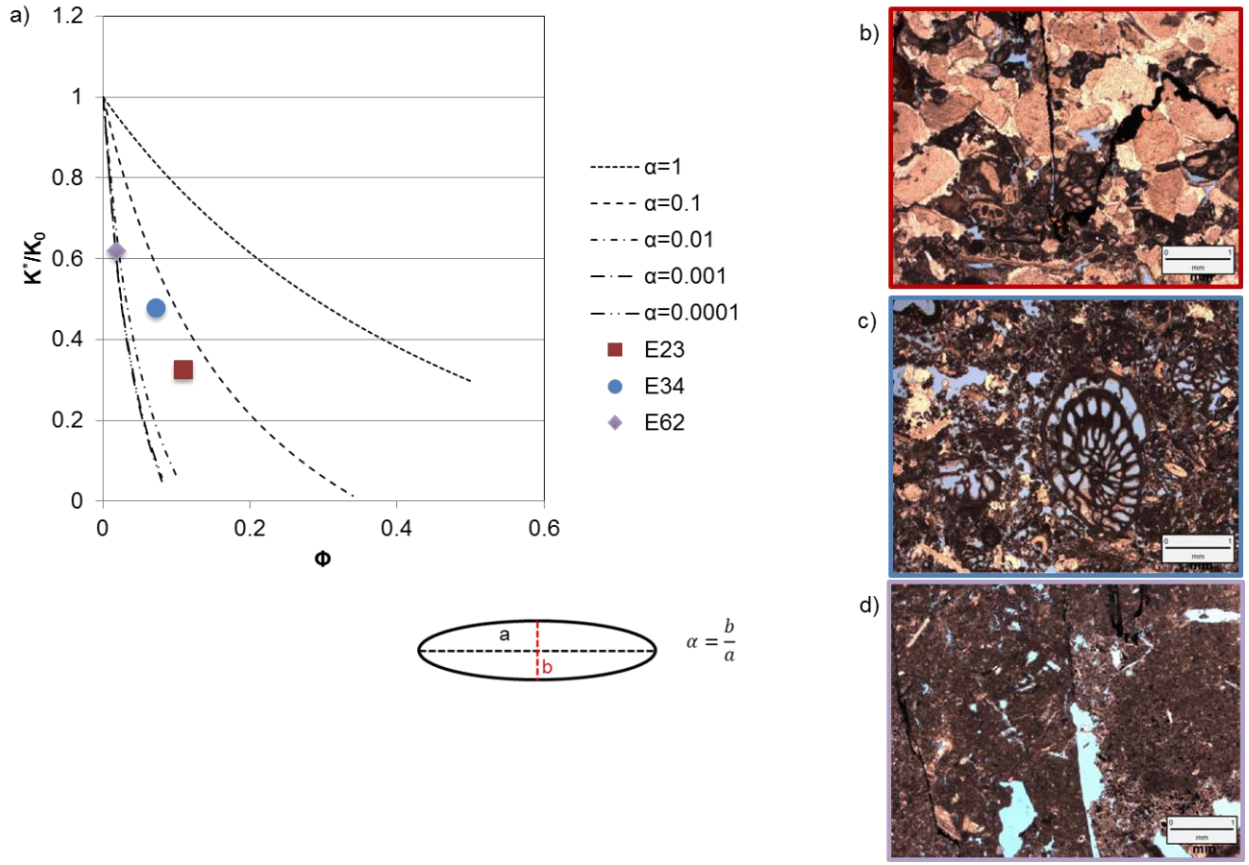

Figure 4.12: (a) Normalized dry bulk modulus versus porosity for samples E23, E34 and E62 of well E. (b), (c) and (d) are the respective thin section photographs for the corresponding samples. There is a good agreement between the predicted aspect ratio for the samples and the observed aspect ratio in the thin section photographs. (a) Black lines indicate the theoretical solution for the effect of crack aspect ratio on the bulk modulus.

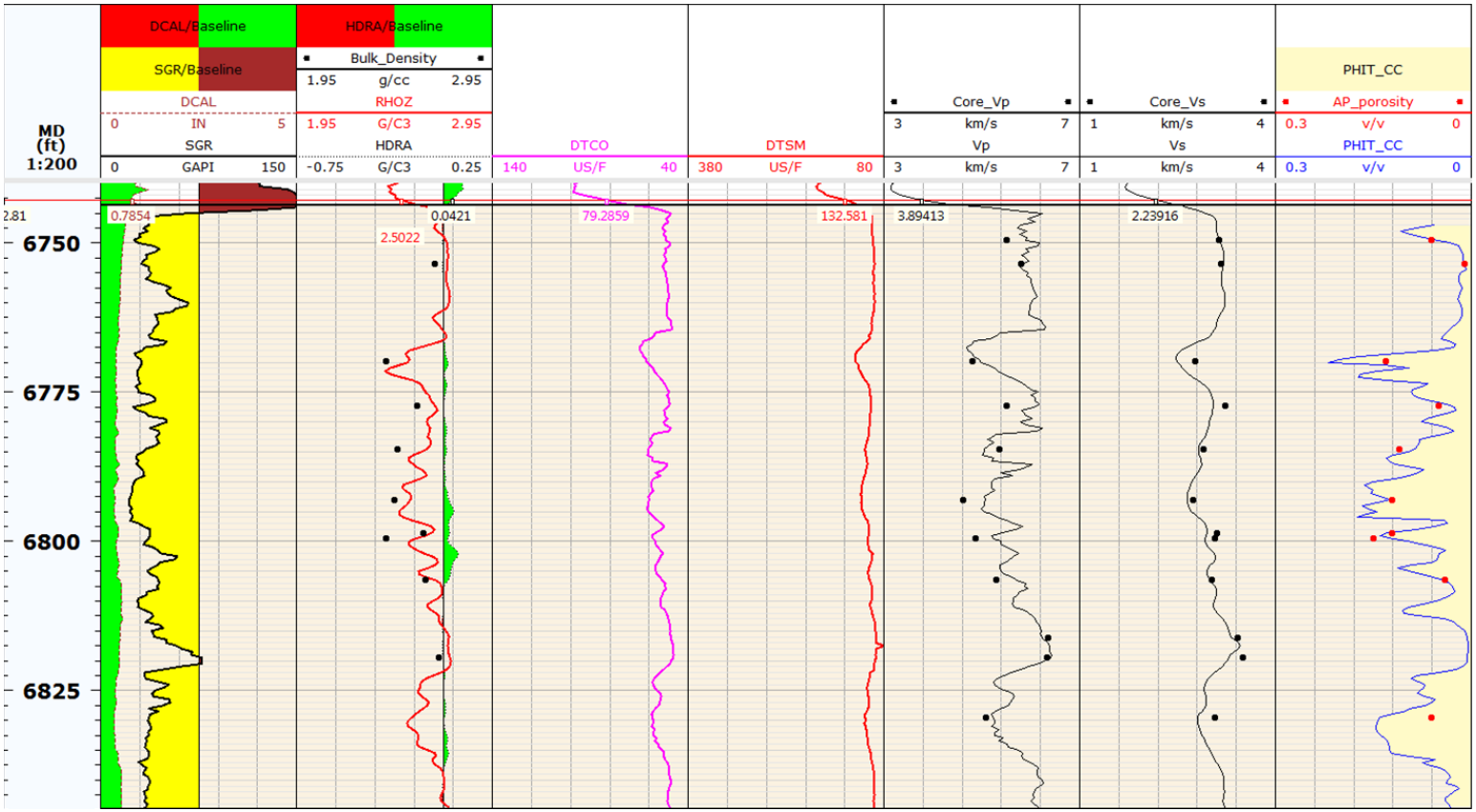

Figure 4.13: Type log from the Horseshoe atoll reservoir interval. Suite of logs displayed is from well J. Continuous curves indicate original or derived logs. Dots indicate measured property values from core. Overall we have a good agreement between log and sample data. We attribute some of the scatter to borehole effects observed in the differential caliper (DCAL) and in the density correction (HDRA) logs.

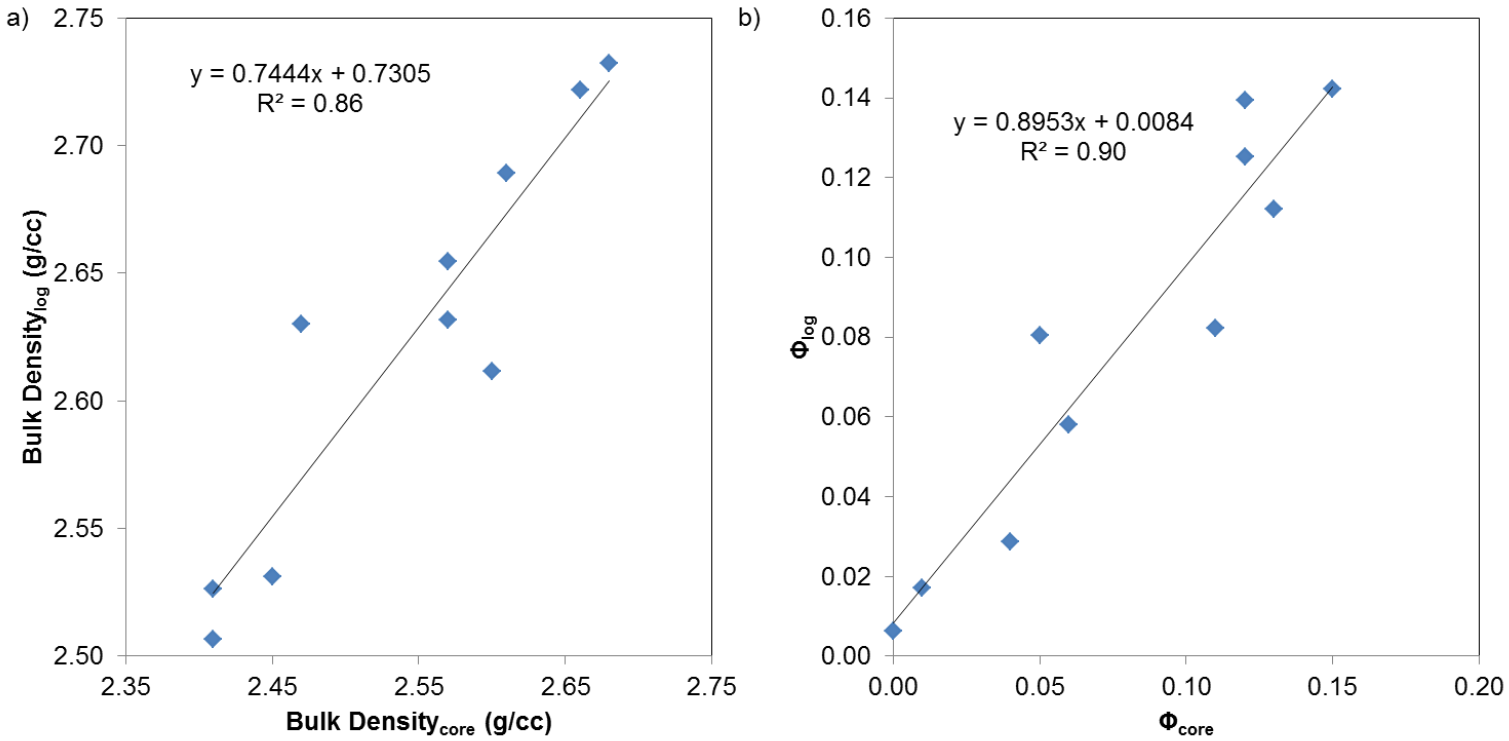

Figure 4.14: Saturated core versus log (a) bulk density and (b) total porosity measurements. Both cross-plots indicate a good agreement between core and log measurements. We attribute the scatter to borehole conditions.

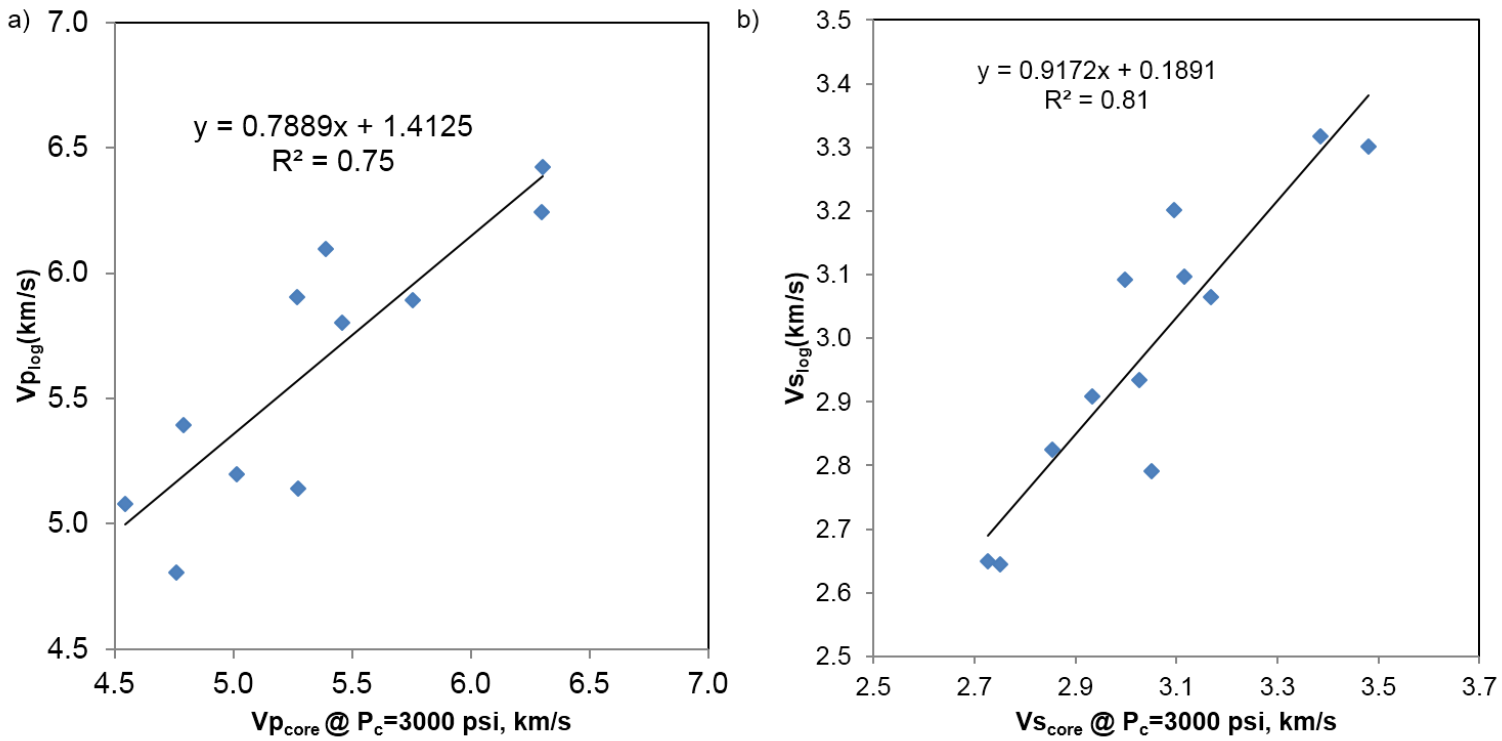

Figure 4.15: Saturated core versus log (a) compressional and (b) shear velocity measurements. Both cross-plots indicate a good agreement between core and log measurements and of statistical significance. We attribute the scatter to borehole conditions.

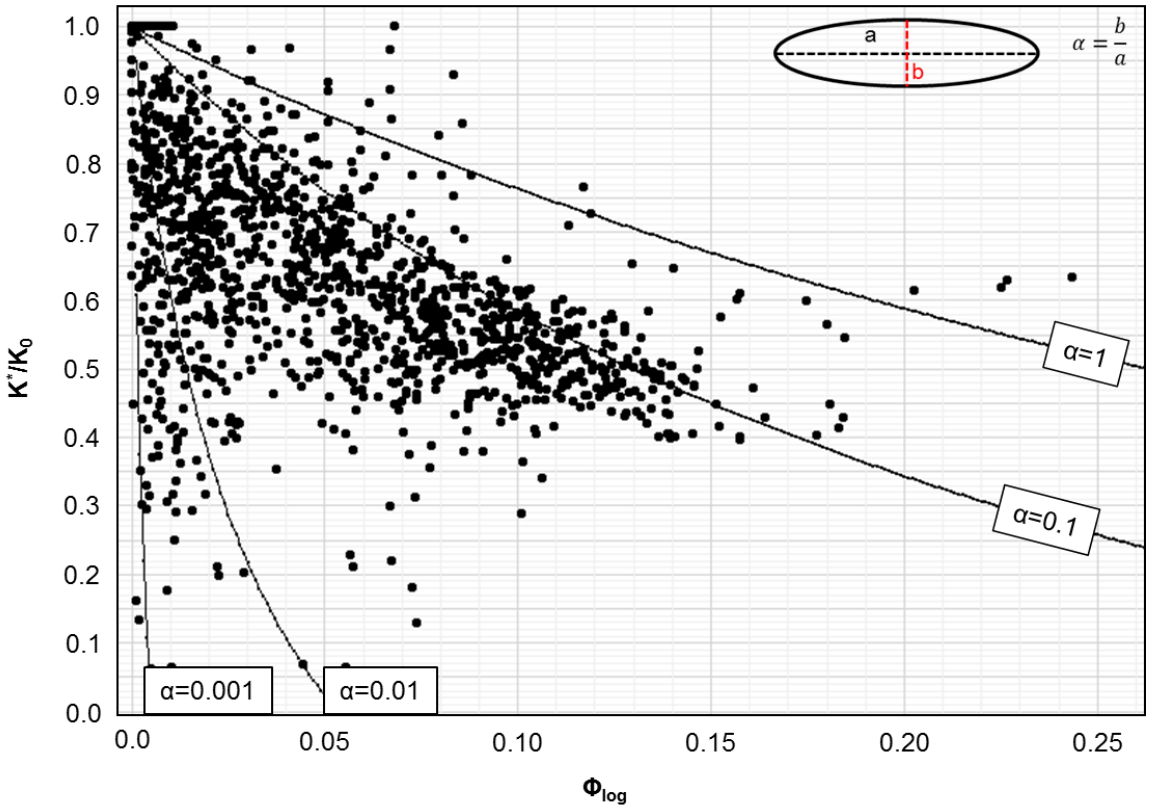

Figure 4.16: Normalized bulk modulus vs. porosity for wells J, T, G10, K07, G, L03, M08 and M05. Most of the pore aspect ratio is distributed between 0.1 and 0.01. These results agree with observations shown in Figure 11

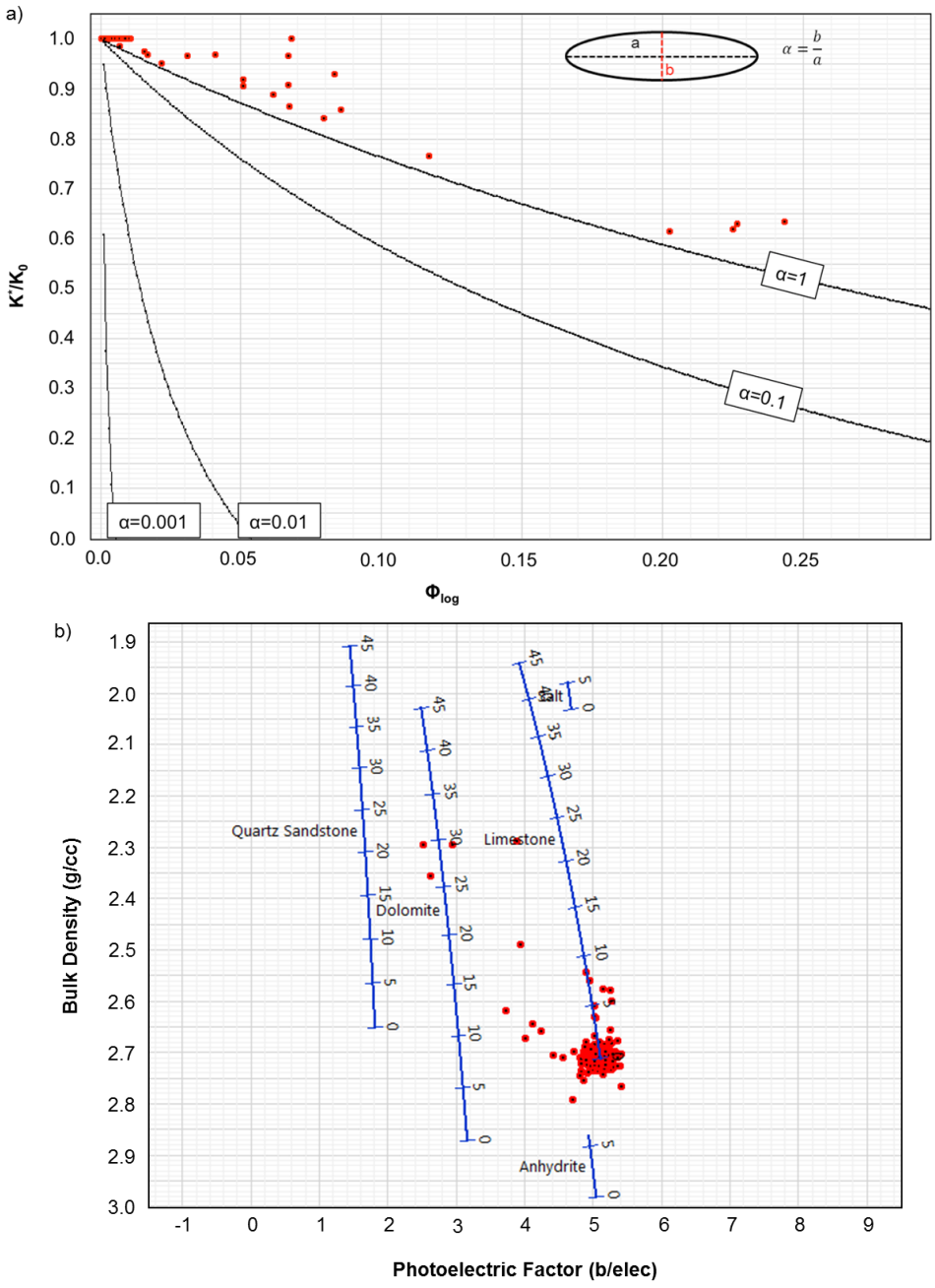

Figure 4.17: (a) Normalized bulk modulus vs. porosity cross-plot for wells J, T, G10, K07, G, L03, M08 and M05. (a) Values above α=1 are interpreted as anomalies that violate our model assumptions. (b) Photoelectric factor vs. bulk density cross-plot for the samples shown in (a). Cross-plotting photoelectric factor vs. bulk density for the anomalous samples show that our assumption of limestone matrix is not honoring the true matrix properties for some samples. The samples with the correct matrix assumption are showing a porosity value less than 8%.

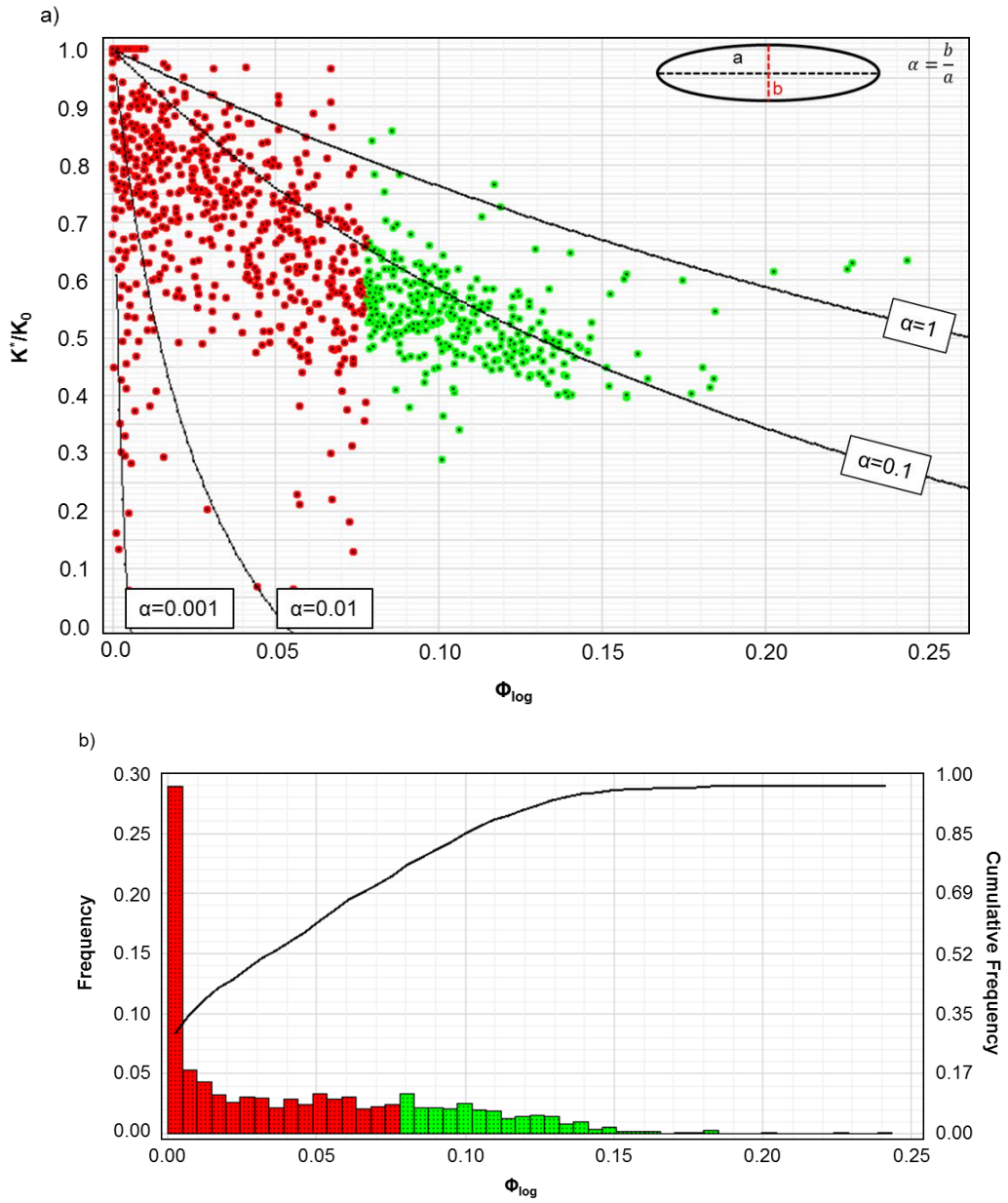

Figure 4.18: (a) Normalized bulk modulus vs. porosity for wells J, T, G10, K07, G, L03, M08 and M05. (b) Porosity histogram for the data shown in (a). We have color coded the porosity values from the log data and separated it in two groups. Porosities lower than 8% are colored in red. Porosities greater than 8% are colored in green. Normalized bulk modulus for samples with less than 8% porosity plot in color red and have a distribution of aspect ratios between 0.1 and 0.001. Normalized bulk modulus for samples with more than 8% porosity plot in color green and cluster towards 0.1 aspect ratio**.**

REFERENCES

Adam, L., M. Batzle and I. Brevik, 2006, Gassmann's fluid substitution and shear modulus variability in carbonates at laboratory seismic and ultrasonic frequencies: Geophysics, 71, F173-F183.

Assefa, S., C. McCann, and J. Sothcott, 2003, Velocities of compressional and shear waves in limestones: Geophysical Prospecting, 51, 1-13.

Baghat A., C. H. Sondergeld, and C. S. Rai, The petrophysical study on UAE carbonates: 82nd Annual International Meeting of the SEG.

Baechle, G. T., R. J. Weger, G. Eberli, J. L. Masaferro and Y. Sun, 2005, Changes of shear moduli in carbonate rocks: Implications for Gassmann applicability: The Leading Edge, 24, 507-510.

Batzle, M, R. Hofmann, D.H. Han, and J. Castagna, 2001, Fluids and frequency dependent seismic velocity of rocks: The Leading Edge, 20, 168-171.

Biot, M. A., 1956, Theory of propagation of elastic waves in a fluid saturated porous solid. I. Low frequency range and II. Higher-frequency range: Acoustical Society of America, 28, 168–191.

Biot, M. A., 1962, Mechanics of deformation and acoustic propagation in porous media: Journal of Applied Physics, 33, 1482-1498.

Dutton, S. P., E. M. Kim, R. F. Broadhead, W. D. Raatz, and C. L. Breton, 2004, Play analysis and digital portfolio of major oil reservoirs in the Permian Basin: Application and transfer of advanced geological and engineering technologies for incremental production opportunities: Annual report, Bureau of Economic Geology, University of Texas.

Fisher, A. J., Predicting spatial distribution of critical pore types and their influence on reservoir quality, Canyon (Pennsylvanian) reef reservoir, Diamond M Field, Texas: Master's thesis, Texas A&M University.

Gassmann, F., 1951, Uber die Elastizität poroser Median: Vierteljarhsschrift der Naturforschenden in Zürich, 96, 1–23.

Kuster, G.T. and M.N. Toksöz, 1974, Velocity and attenuation of seismic waves in two phase media: Geophysics, 39,587-618.

Kenyon, B., R. Kleinberg, C. Straley, G. Gubelin and C. Morriss, 1995, Nuclear Magnetic Resonance Imaging - Technology for the 21st century: Oilfield Review, SDR,19-32.

Xu, S. and R. White, 1995, Poro-elasticity of clastic rocks – a unified model: 36th Ann. Logging Symposium. 1-12.

Zhu, X. and G. A. McMechan, 1990, Direct estimation of the bulk modulus of the frame in a fluid-saturated elastic medium by Biot theory: 60th Ann. Internat. Mtg., Soc. Expl. Geophys., Expanded Abstracts. 787-790.

5. Improving the bandwidth of shear impedance and density estimates using non-stretch nmo

Oswaldo Davogustto[1], Bo Zhang[1], Kurt J. Marfurt[1], Mike Burnett[2] and Alison Small[3]

[1] University of Oklahoma, School of Geology and Geophysics

2TameCAT LLC

3Parallel Petroleum LLC

ABSTRACT

The most accurate result of simultaneous inversion of conventional P-wave seismic data is P-impedance. Neither S-impedance nor density can be obtained from 0^0 data impinging on a flat reflector. In theory, S-impedance estimates become reliable with incident angles approaching 30^0, while density estimates become reliable with incident angles approaching 45^0. In practice, successful inversion requires considerable care be taken in amplitude preservation, velocity analysis, and statics to fit the model assumption. Less well recognized is the impact of NMO and migration stretch on the bandwidth of S-impedance and density inversion results. NMO-stretch decreases the frequency content thus decreasing the ability of mid-, and far offsets to resolve subtle changes when inverting for S-impedance and density. In this work, we apply a recently introduced non stretch NMO correction based on Matching Pursuit NMO (MPNMO) to prestack time-migrated data that maintains the frequency content through the near-, mid-, and far-offsets. Using data from a West Texas carbonate environment, we show how MPNMO corrected gathers improve well tie correlation and produce P-, S-impedance, and density results that match the log data better than conventional (stretched) time-migrated gathers.

INTRODUCTION

Well ties and pre-stack simultaneous inversion are the principal techniques for reservoir characterization in Midcontinent and west Texas conventional and unconventional plays. The quality of the inversion algorithm depends on how well we are able to tie the seismic data to the well data to the near-, mid-, and far-offsets. Also, the wavelet stability and frequency content at near-, mid-, and far-offsets will impact the result of the pre-stack simultaneous inversion. Hampson et al. (2005) proposed a method for pre-stack P-wave simultaneous inversion algorithm representative of most commercial implementations. They assume that the P-wave reflectivity at any angle can be predicted using Fatti et al's. (1994) approximation. They also assume that the logarithms of P- and S-impedances and P-impedance and density hold a linear relationship for an assumed background trend (Figure 5.1). Given these conditions they are able to predict reliably P- and S- impedances as well as density from pre-stack P-wave seismic data.

The quality of the simultaneous pre-stack inversion attributes depends on the quality of the log data, the design of the seismic acquisition program, and the preservation of amplitudes and alignment of seismic events during subsequent seismic data processing. Swan (1991) describes how the reflectivity can be affected by spherical divergence, source-receiver azimuth coverage, differential tuning and NMO stretch. Swan (1997) proposed a method to correct for NMO-stretch which is based on a minimum mean-squared error method. This method relies on an a priori estimate of the non-stretched intercept and gradient that will be used as a guide for building a set of filters to correct for the NMO-stretch in the far offsets.

Singleton (2009) gives a detailed overview of the effects of seismic data preconditioning on pre-stack simultaneous inversion and proposes quality control checkpoints throughout the data conditioning workflow. Specifically, Singleton (2009) demonstrates how the use of structure-oriented filters, NMO-stretch correction and residual velocity analysis can avoid large errors in simultaneous inversion. Singleton's (2009) approach to NMO-stretch correction is based on frequency loss compensation at the far offsets. His algorithm is based on joint time-frequency analysis (Singleton et al. 2006) and relies on a linear estimation of the stretch at any time-offset pair compared to the zero-offset trace. Singleton's (2009) method estimates the bandwidth from the zero-offset trace and a total energy for each reflector is calculated and held constant through the process in order to avoid AVO character alteration.

Zhang et al. (2013) introduced a different approach to avoiding NMO stretch based on concepts used in matching pursuit spectral decomposition. We therefore begin our paper with a methodology review of the matching pursuit non stretch NMO technique. We then apply this algorithm to a pre-stack time-migrated data volume acquired over the Diamond-M field of West Texas and show how this technique improves both the bandwidth of shear impedance inversion and density and the quality of the inverted P- and S-impedance and density. We conclude with a discussion of assumptions and limitations of this technique.

MATCHING PURSUIT NON-STRETCH NMO (MPNMO)

The normal moveout (NMO) correction accounts for the time delay (moveout) of an event measured at source-receiver offset x, when compared to the same event at

offset x=0. This travel time difference, or NMO correction, Δt_{NMO}, is strictly valid for moderate offset data acquired over a stack of flat reflectors:

$$t(x) = t_0 + \Delta t_{NMO} = t_0 + \sqrt{t_0^2 + \frac{x^2}{V^2(t_0)}} \quad (1)$$

where t_0 is the time of the event at offset x=0, V is the RMS velocity of the event, and x is the source-receiver offset. Equation 1 is applied sample by sample to the uncorrected data and such that the samples within a single wavelet will have different amounts of NMO correction resulting in wavelet distortion (Zhang et al., 2013).

Zhang et al. (2013) proposed a method for NMO correction using a matching pursuit technique similar to the one developed by Liu and Marfurt (2007) for spectral decomposition. Each seismic trace is represented by a suite of event arrival times, wavelet center frequencies, and complex amplitudes (wavelet magnitude and phase), with the largest events being estimated during the initial iteration, and smaller magnitude residual events being estimated during subsequent iterations. At each iteration, the complex wavelet at time t(x) is simply copied and accumulated within an output trace to its corresponding NMO-corrected traveltime t_0. In this manner, the traveltimes between events are stretched, while the wavelets are not. In Figure 5.2 we show a synthetic comparison between migration and MPNMO from Zhang et al. (2013).

APPLICATION

The Diamond M data set consists of approximately 25 mi^2 of seismic data with a high signal to noise ratio located in Scurry County, TX. We have available 12 wells with density, P-wave sonic and fast and slow S-wave sonic logs (Figure 5.3). We also have well tops for the reservoir interval as well as surfaces picked from the 3D prestack time-migrated and stacked seismic data volume. Using these data we compare the

impact of the MPNMO to the conventional migration technique in three categories: wavelet response, well-seismic ties and simultaneous pre-stack inversion.

Wavelet response and Seismic well-ties

After conventional processing we apply a data conditioning flow to the time migrated gathers that included dip-azimuth consistent structure-oriented filtering to common offset volumes, followed by removal of the migration velocity using reverse NMO, thereby squeezing the data stretch associated with prestack time migration. With the data positioning and signal-to-noise ratio improved by both migration and structure-oriented filtering, we repicked a detailed velocity field and applied the MPNMO algorithm to the gathers (Figure 5.4). At this point our analysis mimics a conventional prestack simultaneous inversion workflow. Figure 5.5 shows a generalized workflow for the well tie process. We create angle gathers and extract angle dependent statistical wavelets for both the conventional migration and the MPNMO data (Figure 5.6) and tie the well data to the seismic data. First we extracted a statistical wavelet for a 6-20° angle stack on the conventional migration and the MPNMO data. We will refer to this stack as full stack. Then, we tied the wells using this statistical wavelet to the full stack for both the conventional migration and the MPNMO data (Figure 5.7 and Figure 5.8). We find that for the full stack there is not much difference between the conventional migration and the MPNMO data.

Next, using the angle dependent statistical wavelets (Figure 5.5 and Figure 5.6) we QC our well-ties for the particular angle ranges on the conventional NMO and on the MPNMO gathers (Figure 5.9). The pre-stack data shows a significant improvement on the correlation coefficients for the MPNMO data compared to the conventional

NMO data for the well-ties. Table 5.1 shows the correlation coefficients for the well-ties in this step.

Simultaneous pre-stack inversion

We use four interpreted horizon surfaces and nine of the available wells to build a low frequency background P-impedance, S-impedance, and density models prior to simultaneous model-based inversion (Figure 5.10). The background model step is important for our inversion results since we have steep dips present in the middle of our section that correspond to the San Andres Formation. Wells A, H and L are not used in building the model in order to blind test our subsequent simultaneous inversion results. We cross-plot the density and S-impedance logs versus the log derived P-impedance for the Horseshoe Atoll reservoir interval (Figure 5.11) and find that in both cases we are able to match the logarithm of P-impedance, S-impedance, and density with linear relationships, as required by the solution technique (Hampson et al., 2005).

Next, we test the inversion parameters on a well by well basis and compare the results with a synthetic derived from our model using the previously computed angle dependent wavelets. Figure 5.12 shows the inversion analysis results for well G using the conventional migration and the MPNMO data. Figure 5.13 shows the RMS error gathers calculated from the conventional NMO and the MPNMO corrected data. The MPNMO corrected data shows lower amplitude RMS errors compared to the conventional NMO corrected data. Table 5.2 shows the correlation coefficients for the inversion analysis for all the wells. We found a decrease in the correlation coefficient for the MPNMO data compared to the conventional data. On the other hand, the visual correlation favors the MPNMO data where we find better match of the inverted results

to the well data (Figure 5.12), this is the case for most of the wells. We attribute this decrease of the correlation coefficient on the inversion analysis to the increase of frequency content of the MPNMO data.

Figure 5.14 to Figure 5.16 show the inversion results comparison from the conventional and the MPNMO gathers. Figure 5.17 shows horizon slices of P-impedance, S-impedance and density extracted at the top of the Horseshoe Atoll reservoir. Figure 5.18 shows the RMS amplitude and the RMS error maps extracted at the top of the Horseshoe Atoll reservoir. We observe an overall increase of detail in the MPNMO compared to the conventional data. This increase in resolution is due to our ability to better tie the well data to the different angle range gathers and the stability of the angle dependent wavelets. The increased frequency, for the mid- and far-offsets in particular, gives us a better solution for S-impedance and density. The correlation coefficients between the inversion derived properties for the MPNMO data are between 75 and 81 %. The correlation coefficients between the inversion derived properties for the conventional migration are between 68 and 73 %.

CONCLUSIONS

When data quality permits, simultaneous inversion can be our most powerful quantitative seismic interpretation tool. We have demonstrated that by using a spectral decomposition based non-NMO stretch technique for correcting seismic data we are able to improve the bandwidth of the simultaneous inversion results for S-impedance and density. MPNMO improves the well tie correlation both in the stack and the pre-stack domain. Pre-stack simultaneous inversion analysis shows a better match between the original and the inverted density and S-impedance log from the MPNMO seismic

data. Inverted MPNMO P-, S-impedance and density display more detail and provide better correlation with the log data than the conventional NMO corrected data. The MPNMO RMS amplitude error map shows a better match to the synthetic than the conventional NMO corrected data. We have developed a workflow that combines MPNMO technique with simultaneous inversion in order to produce reliable S-impedance and density predictions from pre-stack seismic data. Finally, we have demonstrated how the MPNMO technique improves the S-impedance and density estimation from pre-stack simultaneous inversion.

ACKNOWLEDGEMENTS

Seismic processing was done using ProMAX, interpretation using Petrel, inversion using Strata, and log analysis and integration using Transform software. All these companies provided software licenses to OU for use in research and education. We thank Parallel Petroleum LLC for providing a license to the Diamond M dataset. Financial support was provided by the industry sponsors of the OU Attribute-Assisted Seismic Processing and Interpretation consortium. Finally we would like to thank Andrea Miceli, J. Tim Kwiatkowski, Carl Sondergeld, and Bradley C. Wallet for their help and technical guidance. The computing for this project was performed at the Oklahoma University Supercomputing Center for Education & Research (OSCER).

LIST OF FIGURES

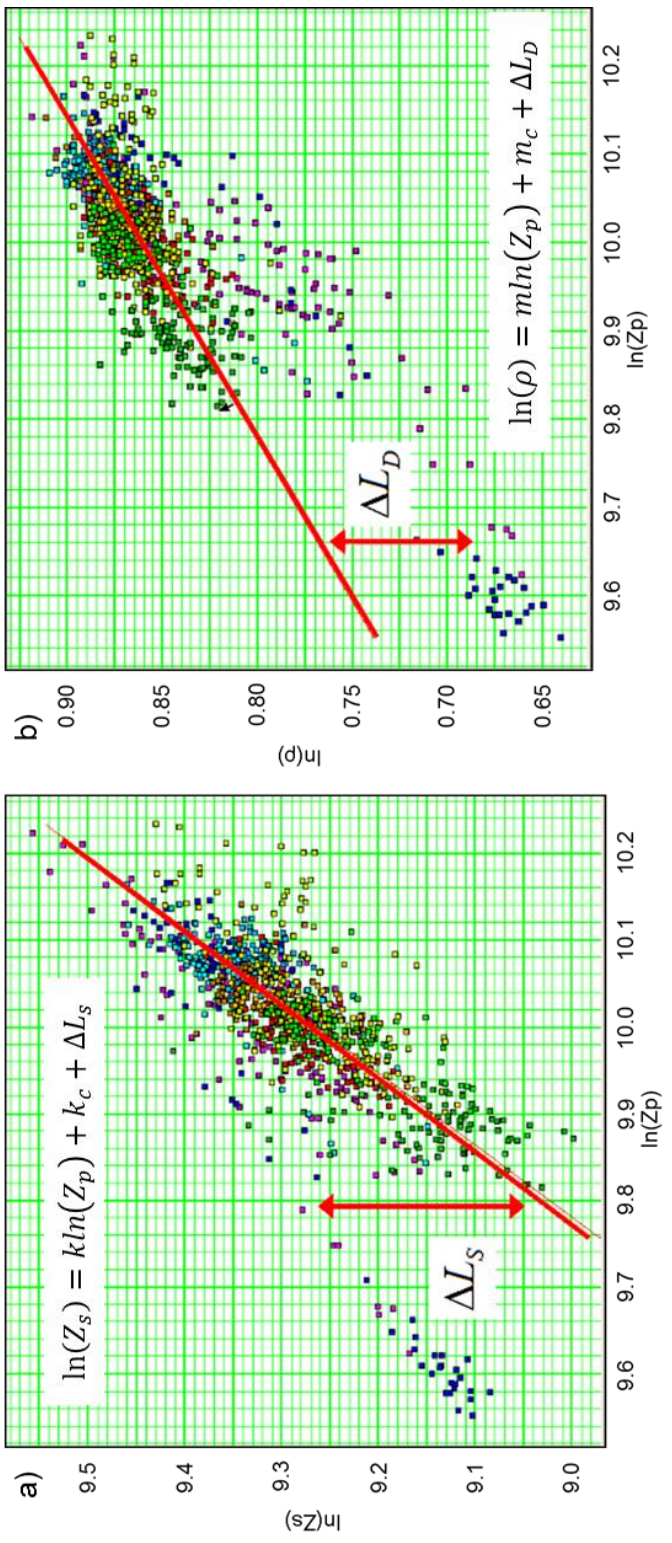

Figure 5.1: Crossplots of (a) $\ln(Z_s)$ versus $\ln(Z_p)$ and (b) $\ln(\rho)$ versus $\ln(Z_p)$. The principal assumption for the simultaneous prestack inversion is that $\ln(Z_s)$ versus $\ln(Z_p)$ and $\ln(\rho)$ versus $\ln(Z_p)$ hold a linear relationship. ΔL_D and ΔL_S are deviations from the background trend that may represent fluid anomalies (Modified from Hampson et al. 2005)

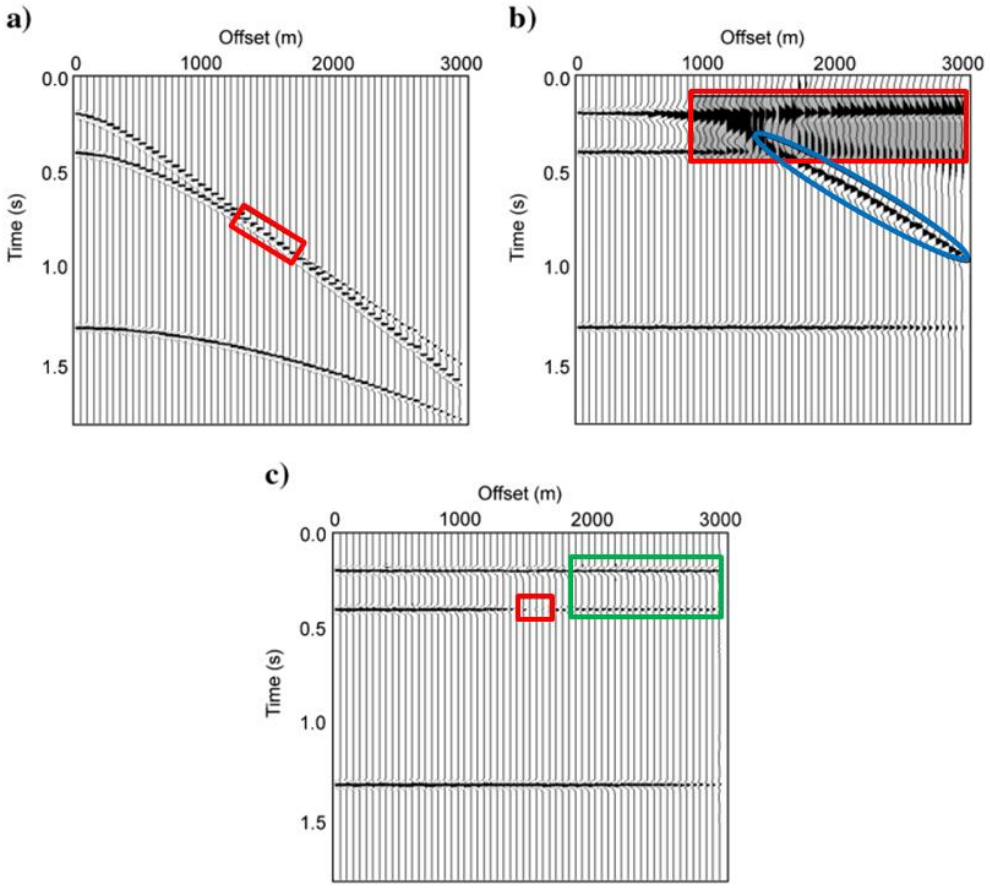

Figure 5.2: (a) CDP gathers, (b) conventional NMO-corrected gather and (c) MPNMO-corrected gather. (a) Red box indicates crossing events at the far offsets. (b) Effects of crossing events on the NMO-corrected gathers are indicated in by the red box and the blue ellipse. Note the decrease in frequency content at offsets of 900 m and higher (red box) and the wavelet repetitions due to the crossing events (blue ellipse). (c) The MPNMO technique moves the data wavelet by wavelet and avoids the NMO stretch (green box). Crossing event in (c) is incorrectly moved out to a different to time by the MPNMO technique thus giving rise to the low amplitude anomaly (red box).

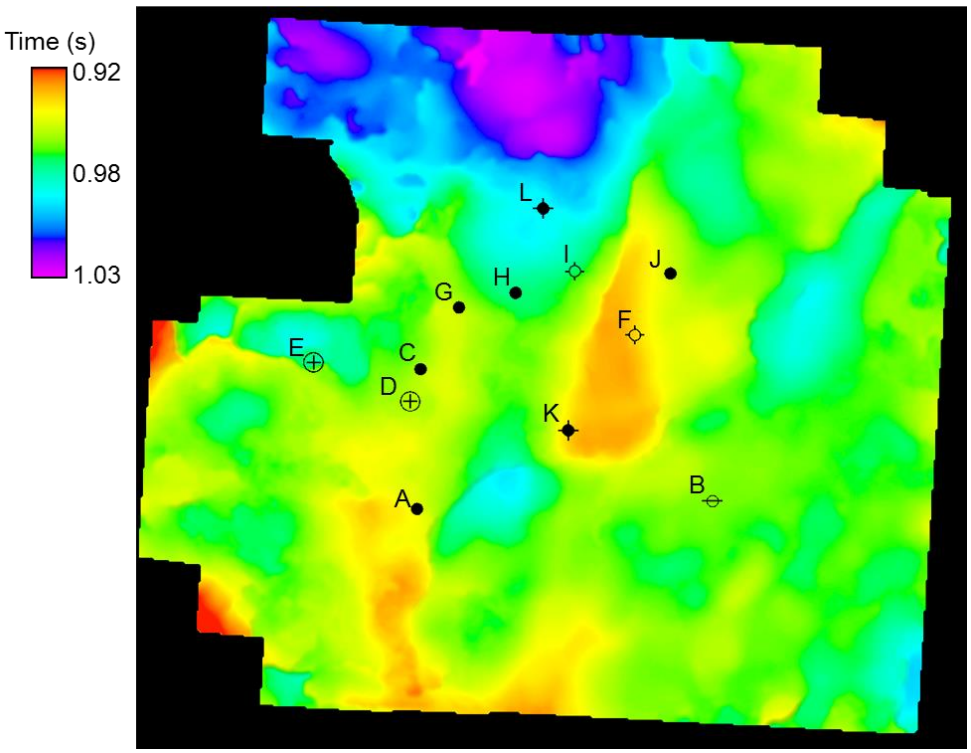

Figure 5.3: Time structure map of the top Horseshoe Atoll reservoir with the posted well locations used in this study.

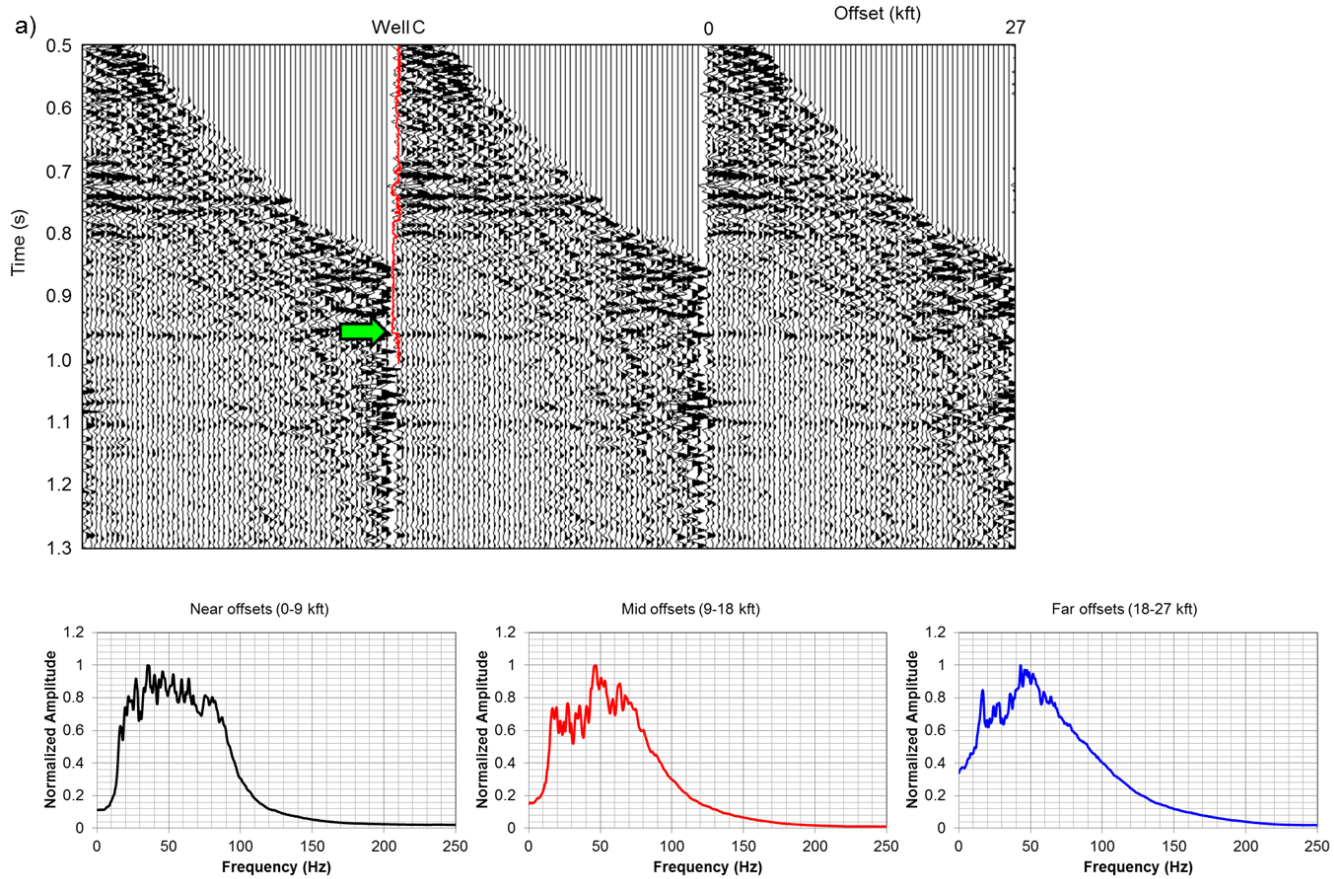
a)
Well C
0
Offset (kft)
27
Time (s)
0.5
0.6
0.7
0.8
0.9
1.0
1.1
1.2
1.3
Near offsets (0-9 kft)
Mid offsets (9-18 kft)
Far offsets (18-27 kft)
Normalized Amplitude
Frequency (Hz)
0
0.2
0.4
0.6
0.8
1
1.2
50
100
150
200
250

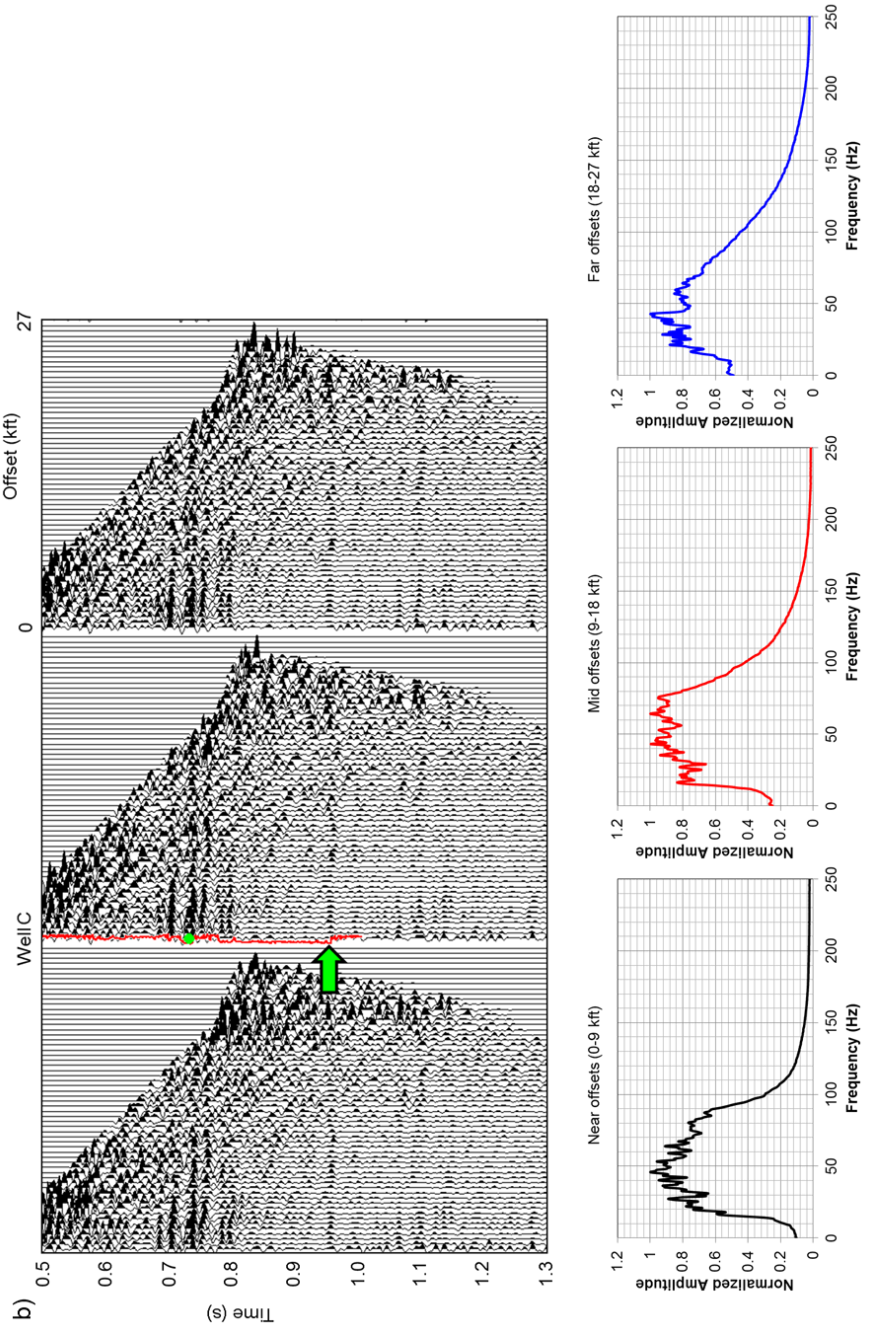
b)
Time (s)
0.5
0.6
0.7
0.8
0.9
1.0
1.1
1.2
1.3
Offset (kft)
0
27
Well C
Near offsets (0-9 kft)
Mid offsets (9-18 kft)
Far offsets (18-27 kft)
Normalized Amplitude
0
0.2
0.4
0.6
0.8
1
1.2
Frequency (Hz)
0
50
100
150
200
250

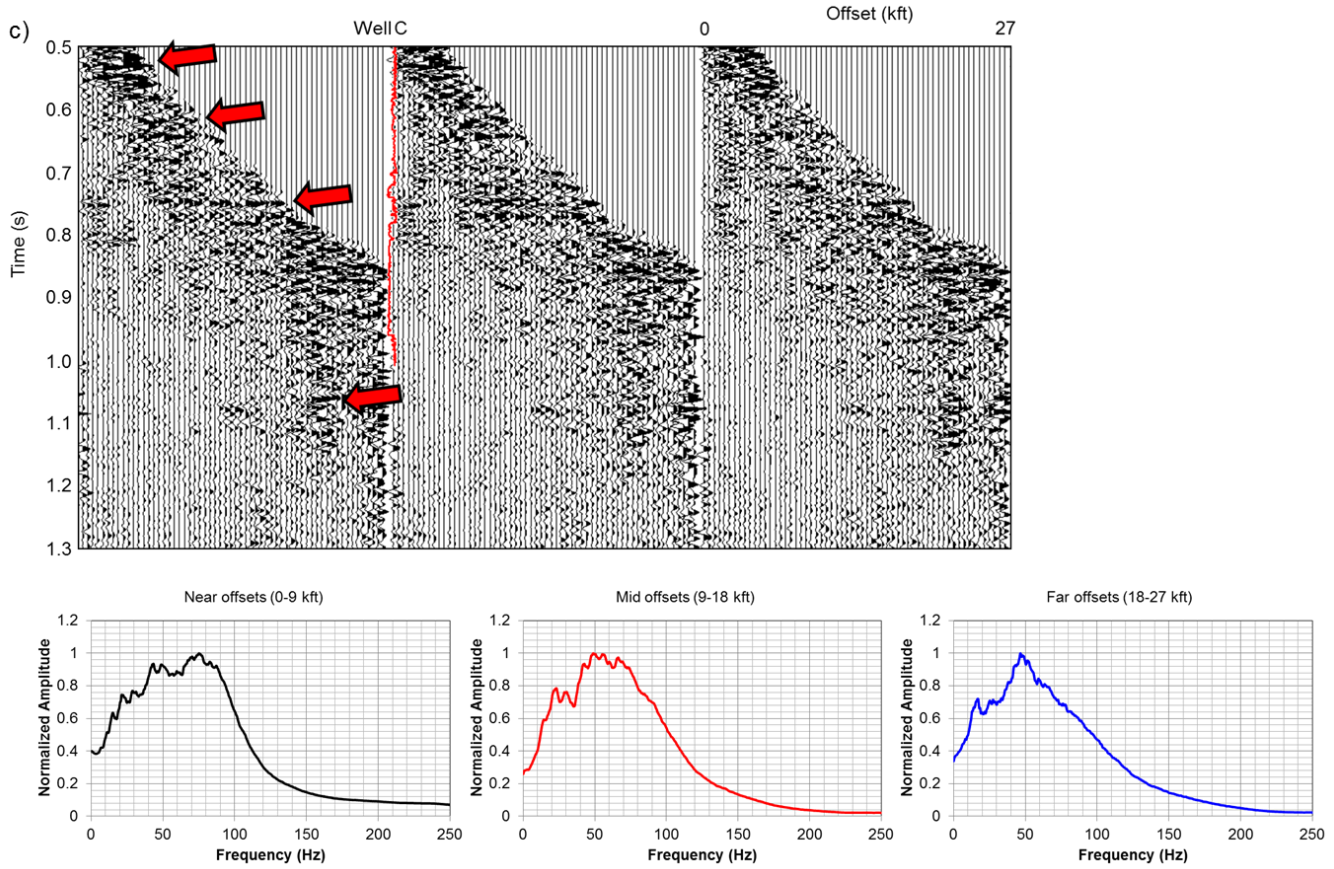

Figure 5.4: Representative (a) time-migrated, (b) MPNMO corrected gathers. (c) Difference between (a) and (b). Amplitude spectra in (b) show a more balanced behavior with respect to offsets when compared to the amplitude spectra on (a).(c) Red arrows indicate zones where the NMO-stretch has decreased the frequency of the data. Green arrows indicate the Horseshoe Atoll top reflector in figures (a) and (b).

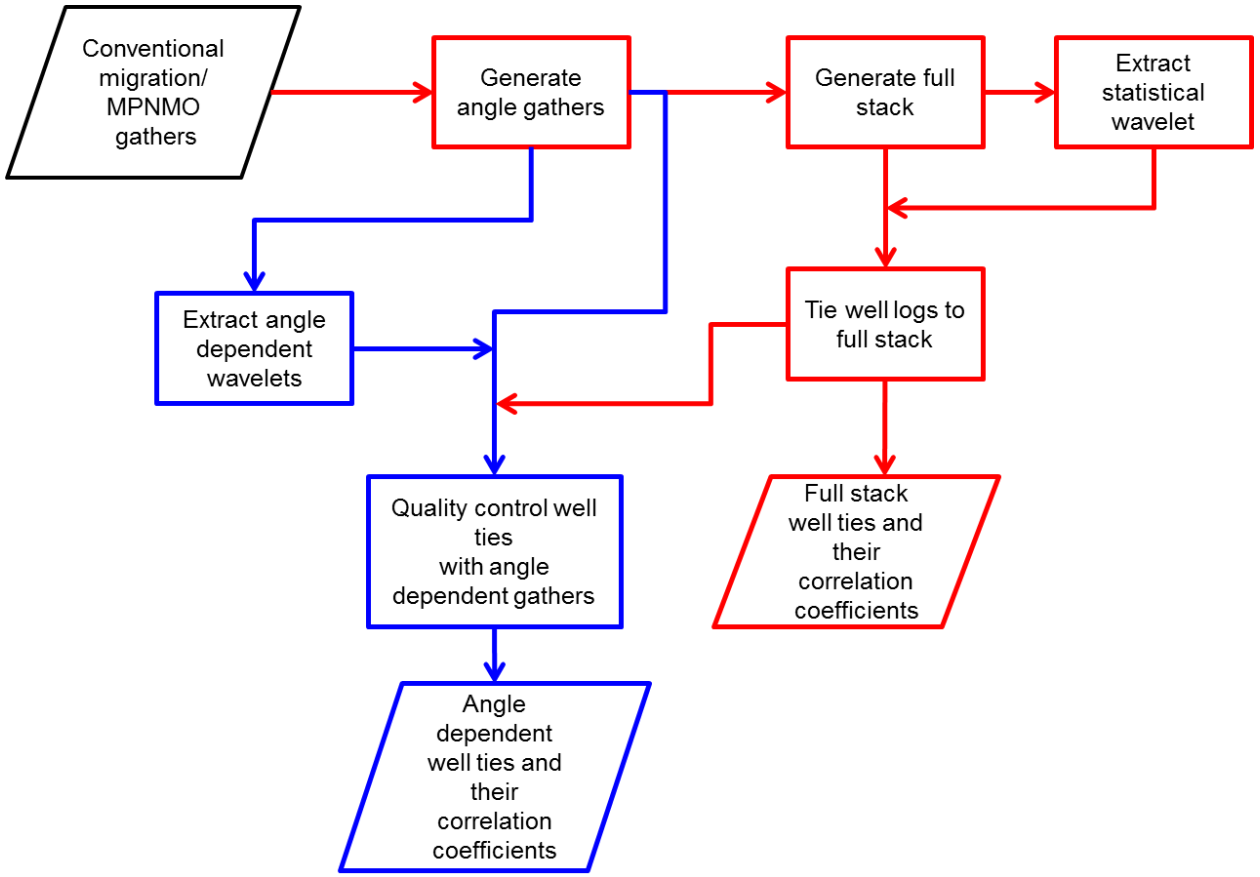

Figure 5.5: General flowchart for calibrating well logs to prestack seismic data used in this work. Colored steps are dependent on the type of analysis being performed. Red steps are for well-ties using post-stack data. Blue steps are for well-ties using the angle dependent wavelets and angle dependent data.

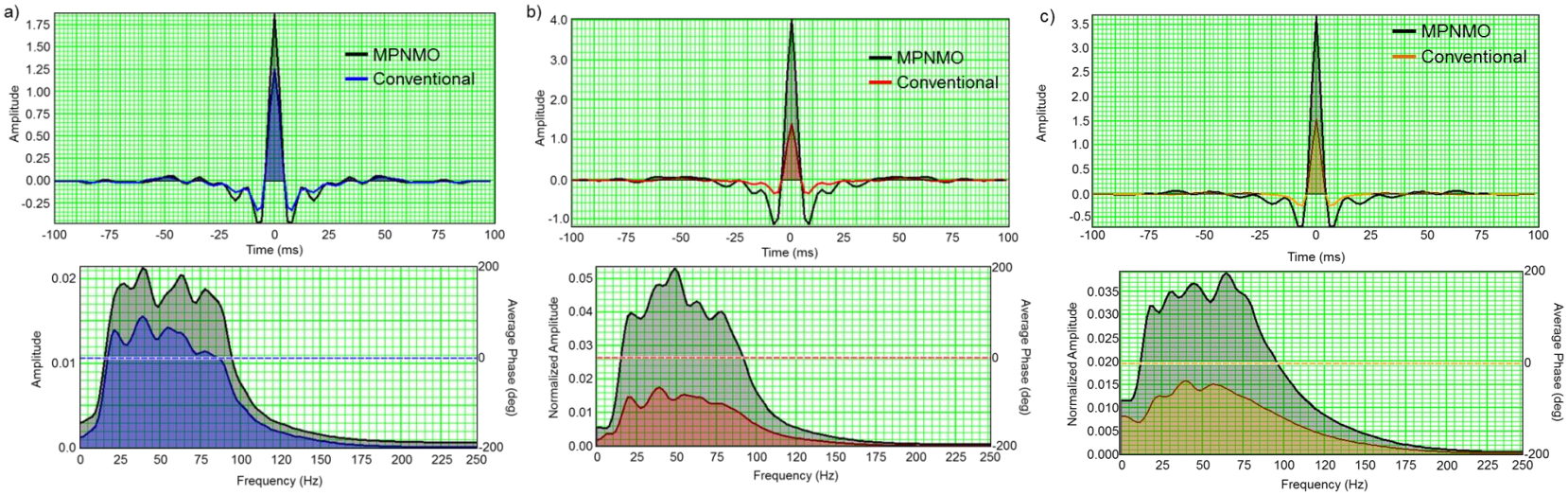

Figure 5.6: Extracted (a) near, (b) mid and (c) far angle gather statistical wavelets for the migrated (color) and the MPNMO corrected (black) data. Note the increase in low frequencies on the amplitude spectra of (b) and (c). For the MPNMO corrected data, the wavelets have a similar amplitude spectra behavior.

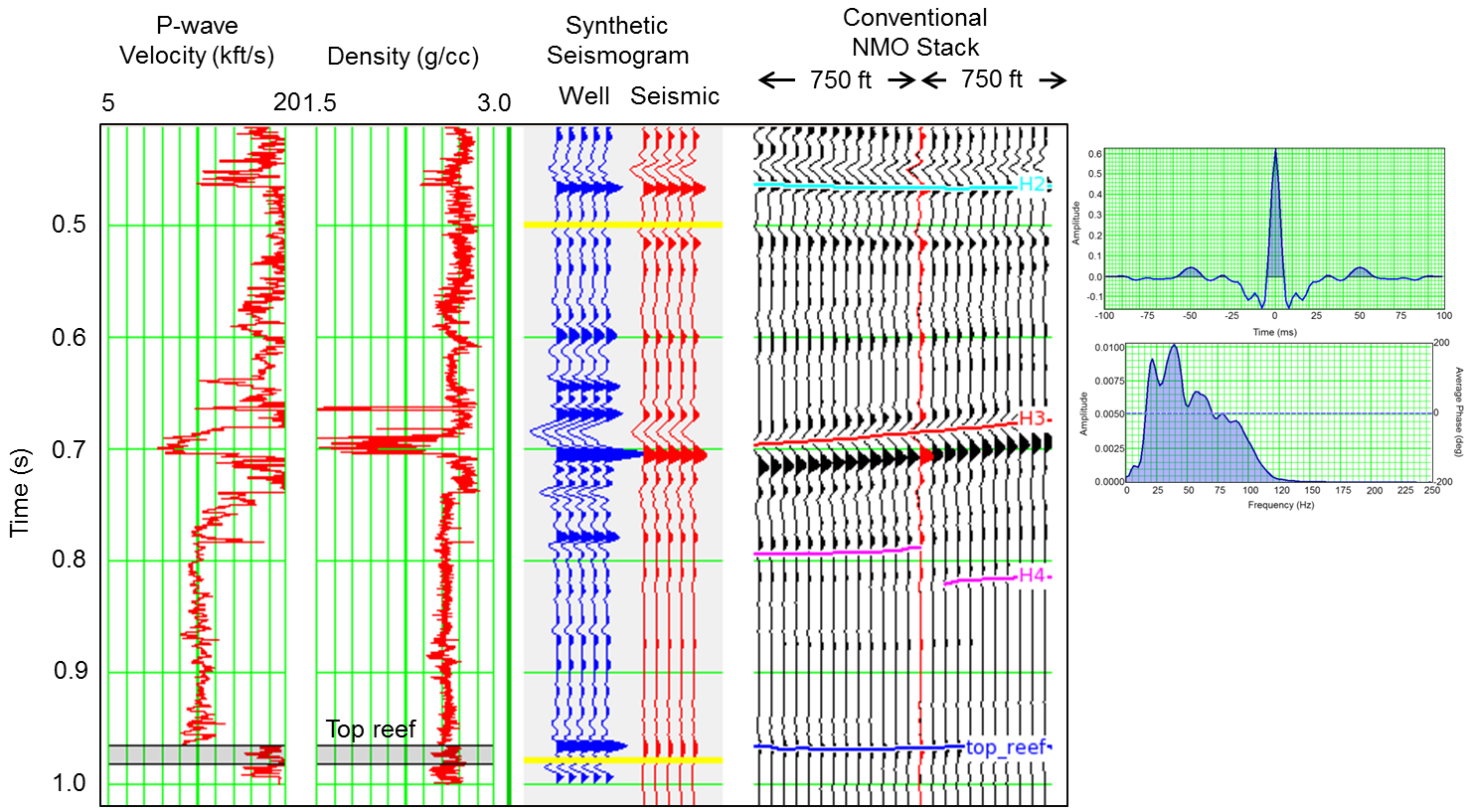

Figure 5.7: Well H synthetic seismogram using the conventional migration full stack. The correlation was done using a 500 ms window centered at 750 ms. The correlation coefficient is 82%. Blue marker on the seismic data corresponds to the Horseshoe Atoll reservoir. Note that the extracted statistical differs from the near angle wavelet shown in Figure 5.6a, displaying lower frequency content.

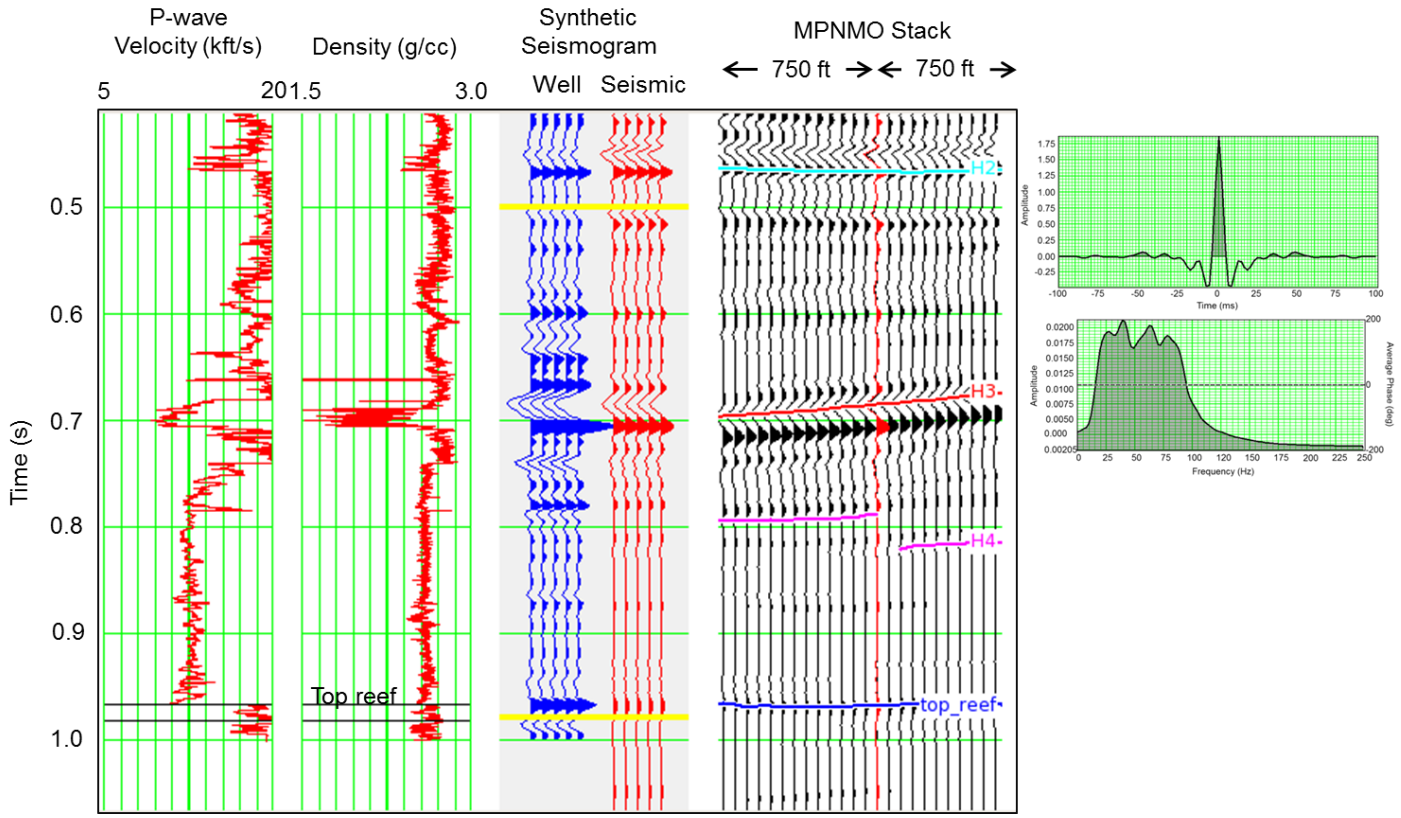

Figure 5.8 : Well H synthetic seismogram using the MPNMO corrected full stack. The correlation was done using a 500 ms window centered at 750 ms. The correlation coefficient is 84%. Blue marker on the seismic data corresponds to the Horseshoe Atoll reservoir. Note that the extracted statistical wavelet is identical to the near angle wavelet shown Figure 5.6a.

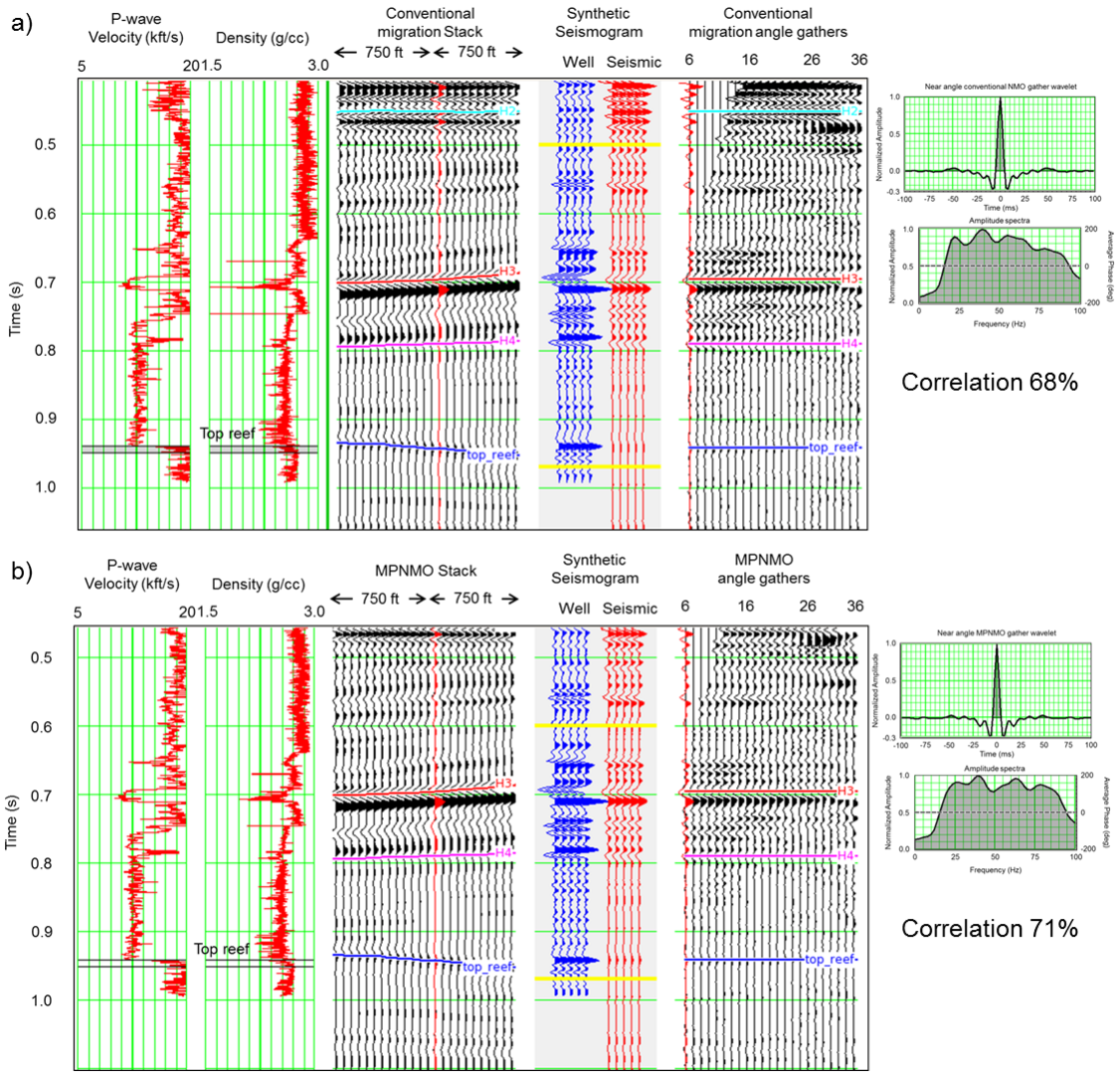
a)
P-wave Velocity (kft/s)
Density (g/cc)
Conventional migration Stack
750 ft
750 ft
Synthetic Seismogram
Well
Seismic
Conventional migration angle gathers
5
201.5
3.0
6
16
26
36
Time (s)
0.5
0.6
0.7
0.8
0.9
1.0
H2
H3
H4
top_reef
Top reef
Near angle conventional NMO gather wavelet
Normalized Amplitude
Time (ms)
Amplitude spectra
Frequency (Hz)
Amplitude Phase (deg)
Correlation 68%
b)
P-wave Velocity (kft/s)
Density (g/cc)
MPNMO Stack
750 ft
750 ft
Synthetic Seismogram
Well
Seismic
MPNMO angle gathers
5
201.5
3.0
6
16
26
36
Time (s)
0.5
0.6
0.7
0.8
0.9
1.0
H3
H4
top_reef
Top reef
Near angle MPNMO gather wavelet
Normalized Amplitude
Time (ms)
Amplitude spectra
Frequency (Hz)
Amplitude Phase (deg)
Correlation 71%

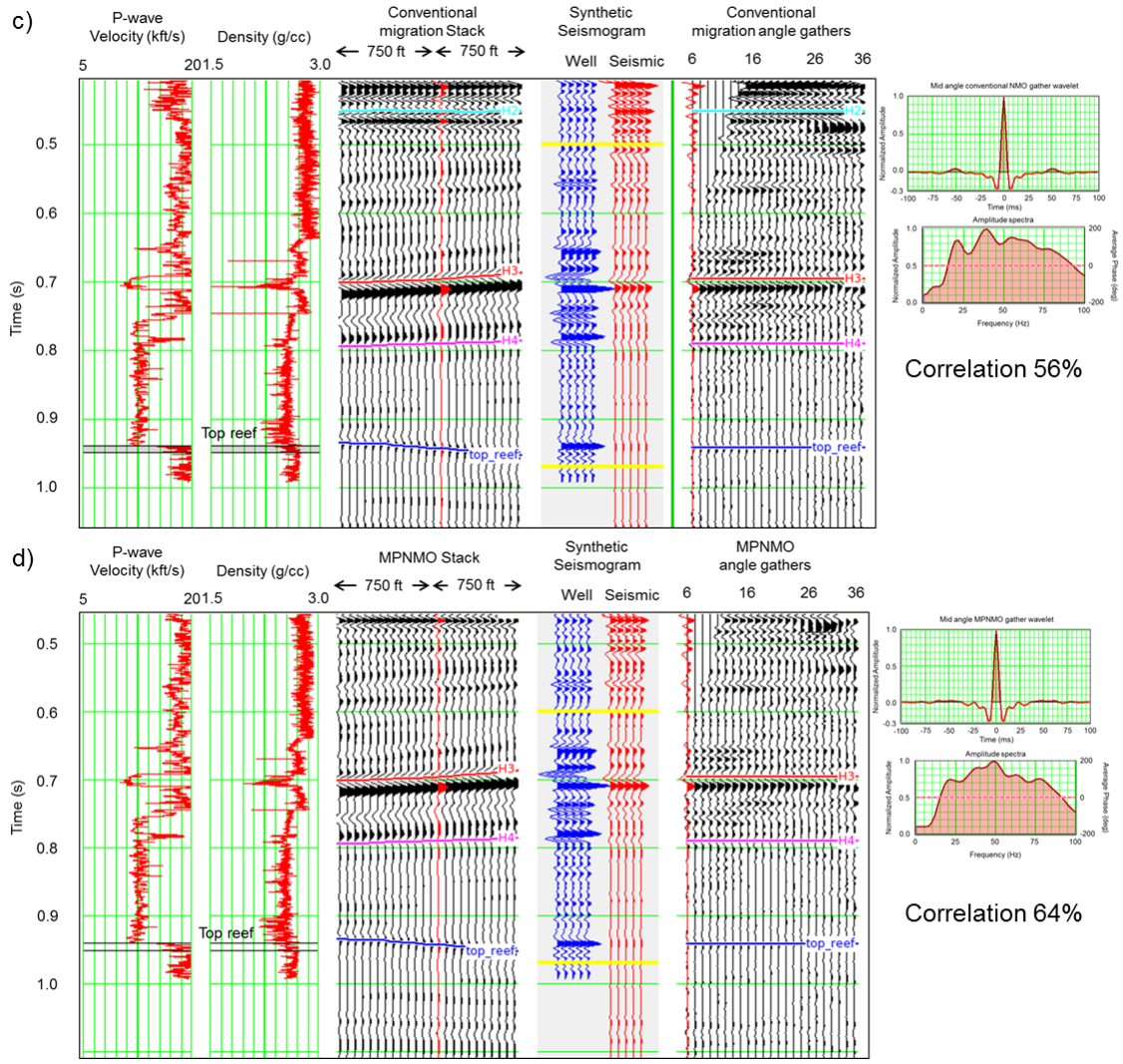
c)
P-wave Velocity (kft/s)
Density (g/cc)
Conventional migration Stack
750 ft
750 ft
Synthetic Seismogram
Well
Seismic
Conventional migration angle gathers
5
201.5
3.0
6
16
26
36
Time (s)
0.5
0.6
0.7
0.8
0.9
1.0
H2
H3
H4
Top reef
top_reef
Mid angle conventional NMO gather wavelet
Normalized Amplitude
Time (ms)
Amplitude spectra
Frequency (Hz)
Average Phase (deg)
Correlation 56%
d)
P-wave Velocity (kft/s)
Density (g/cc)
MPNMO Stack
750 ft
750 ft
Synthetic Seismogram
Well
Seismic
MPNMO angle gathers
Mid angle MPNMO gather wavelet
Correlation 64%

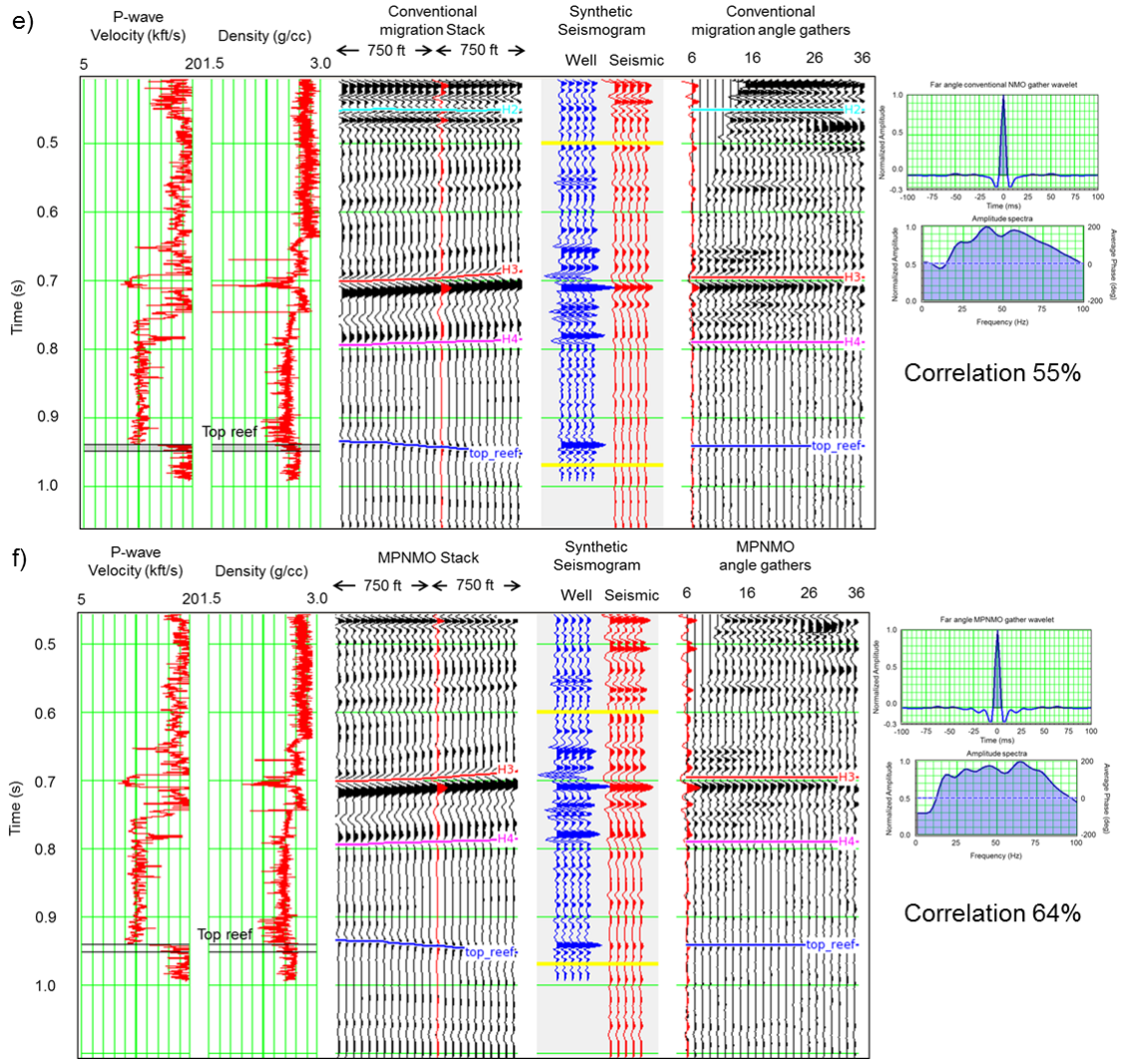

Figure 5.9: Well A well synthetic seismogram using (a) conventional migration, (b) MPNMO corrected near angle gathers, (c) conventional migration, (d) MPNMO corrected mid angle gathers, (e) conventional migration, and (f) MPNMO corrected far angle gathers. The correlation was done using a 500 ms window centered at 750 ms. Blue marker on the seismic data corresponds to the Horseshoe Atoll reservoir. We used the respective wavelets shown in Figures 4 and 5. Conventional migration data compared to the MPNMO data show a lower correlation coefficient for the near, mid and far angle gathers. We attribute this difference to the frequency content on the wavelets that after MPNMO better matches the log frequency response.

Table 5.1: Correlation coefficients for the well ties using conventional migration and the MPNMO corrected gathers for the full and the angle limited stack data. We observe a higher correlation coefficient between the well synthetics and the MPNMO corrected data. Also note that the near, mid, and far angle gather well-ties show more consistency in the correlation coefficients behavior than the conventional migration data.

	conventional migration				MPNMO corrected			
Well	full stack	near angle	mid angle	far angle	full stack	near angle	mid angle	far angle
A	81	64	56	55	86	71	64	64
B	75	61	59	58	81	73	71	71
C	79	65	66	64	80	65	65	65
D	74	60	59	41	78	69	67	66
E	51	44	35	32	48	43	43	43
F	71	64	58	53	70	62	62	61
G	74	65	61	41	80	67	65	66
H	82	61	65	54	84	70	68	68
I	64	32	42	49	74	61	61	61
J	71	56	57	55	67	58	58	58
K	72	51	47	41	70	60	58	58
L	75	54	55	51	75	71	70	70

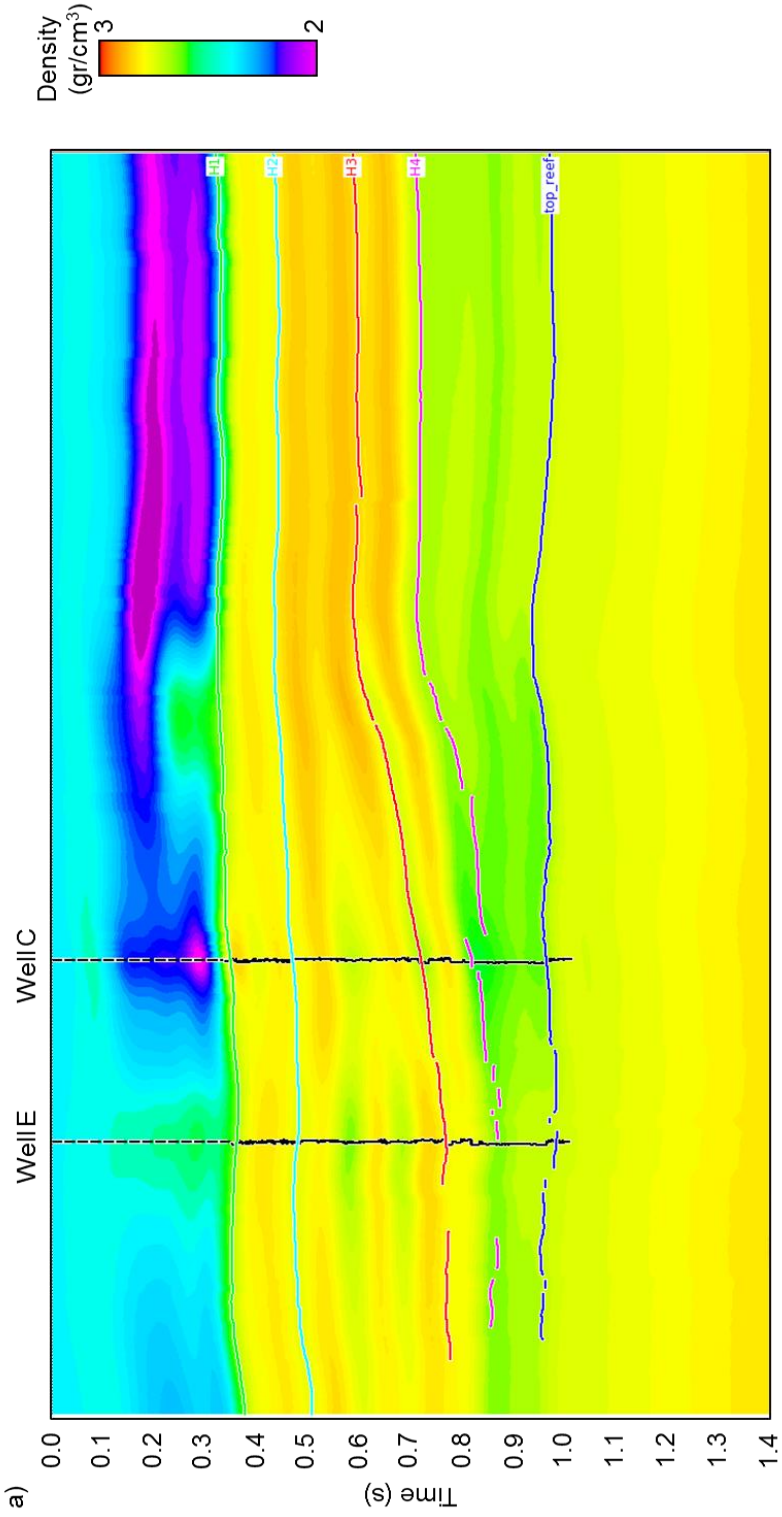
a)
Density (gr/cm3)
3
2
WellE
WellC
H1
H2
H3
H4
top_reef
Time (s)
0.0
0.1
0.2
0.3
0.4
0.5
0.6
0.7
0.8
0.9
1.0
1.1
1.2
1.3
1.4

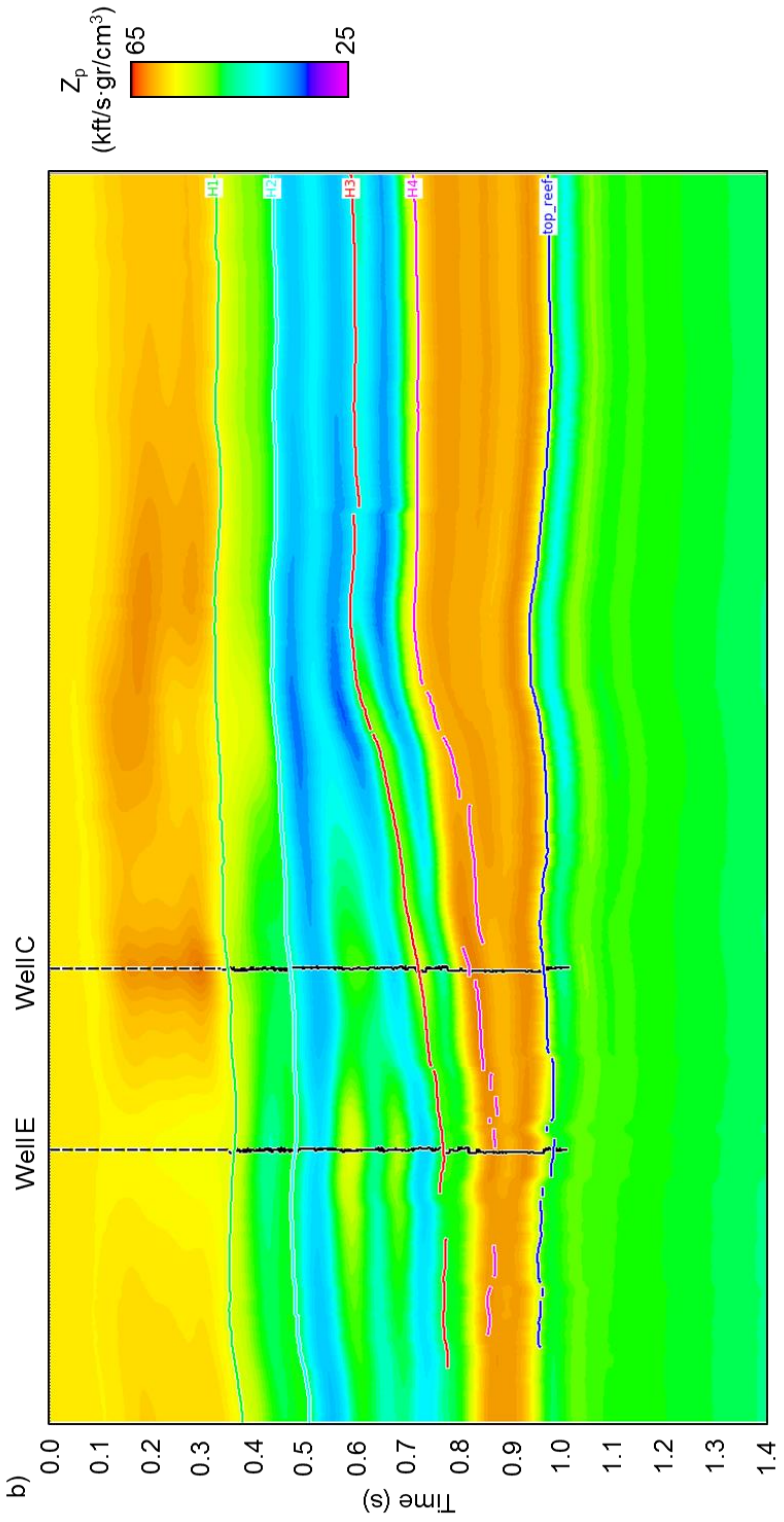
b)
WellE
WellC
H1
H2
H3
H4
top_reef
Time (s)
0.0
0.1
0.2
0.3
0.4
0.5
0.6
0.7
0.8
0.9
1.0
1.1
1.2
1.3
1.4
Z_p
(kft/s·gr/cm³)
65
25

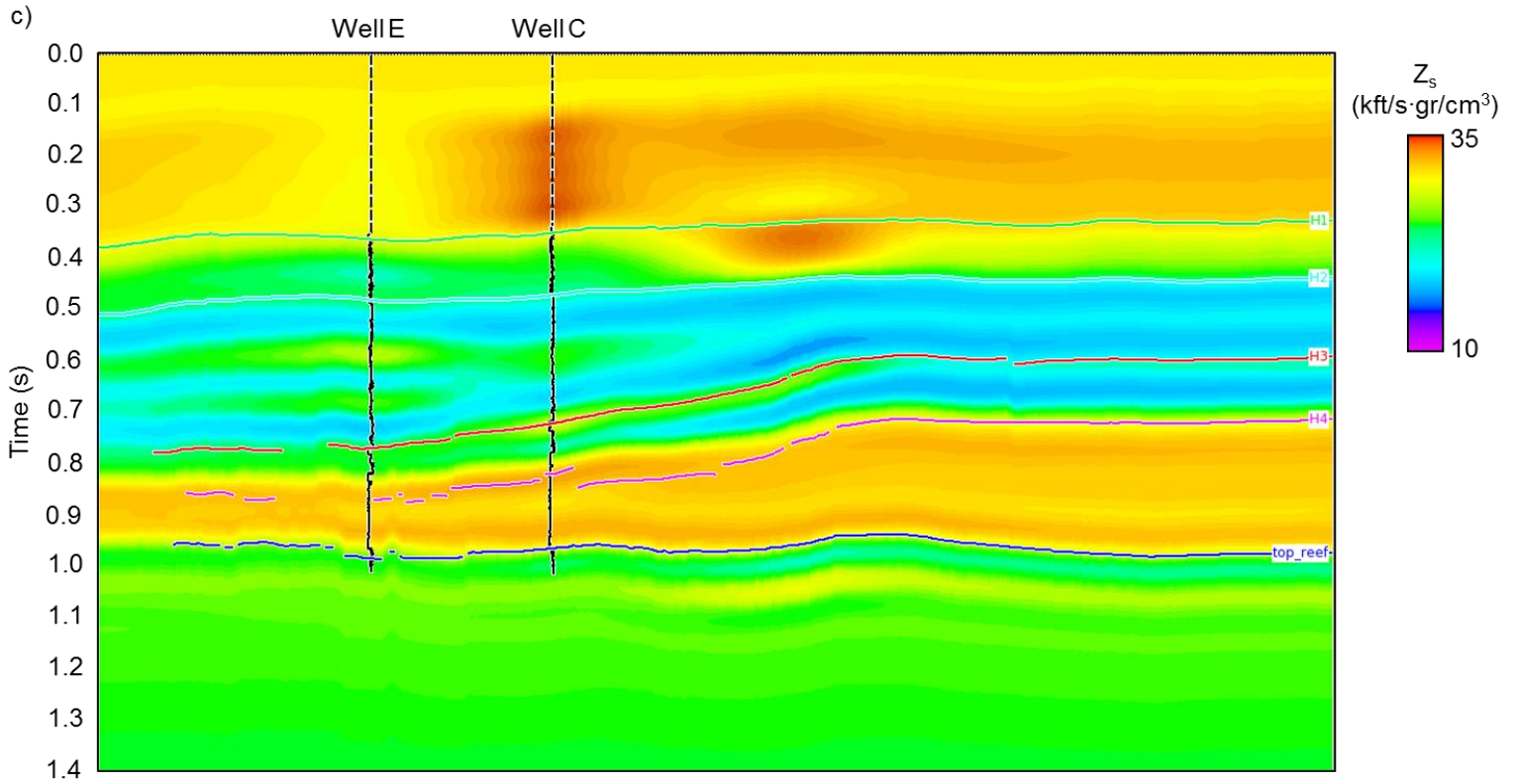

Figure 5.10: Vertical slice X-X' (Figure 2) through low-frequency background models for (a) density, (b) P-impedance and (c) S-impedance displaying wells B and E. Our model is driven by the stratigraphic relationship between horizons H1 trough H4 and the top of the Horseshoe Atoll (top_reef).

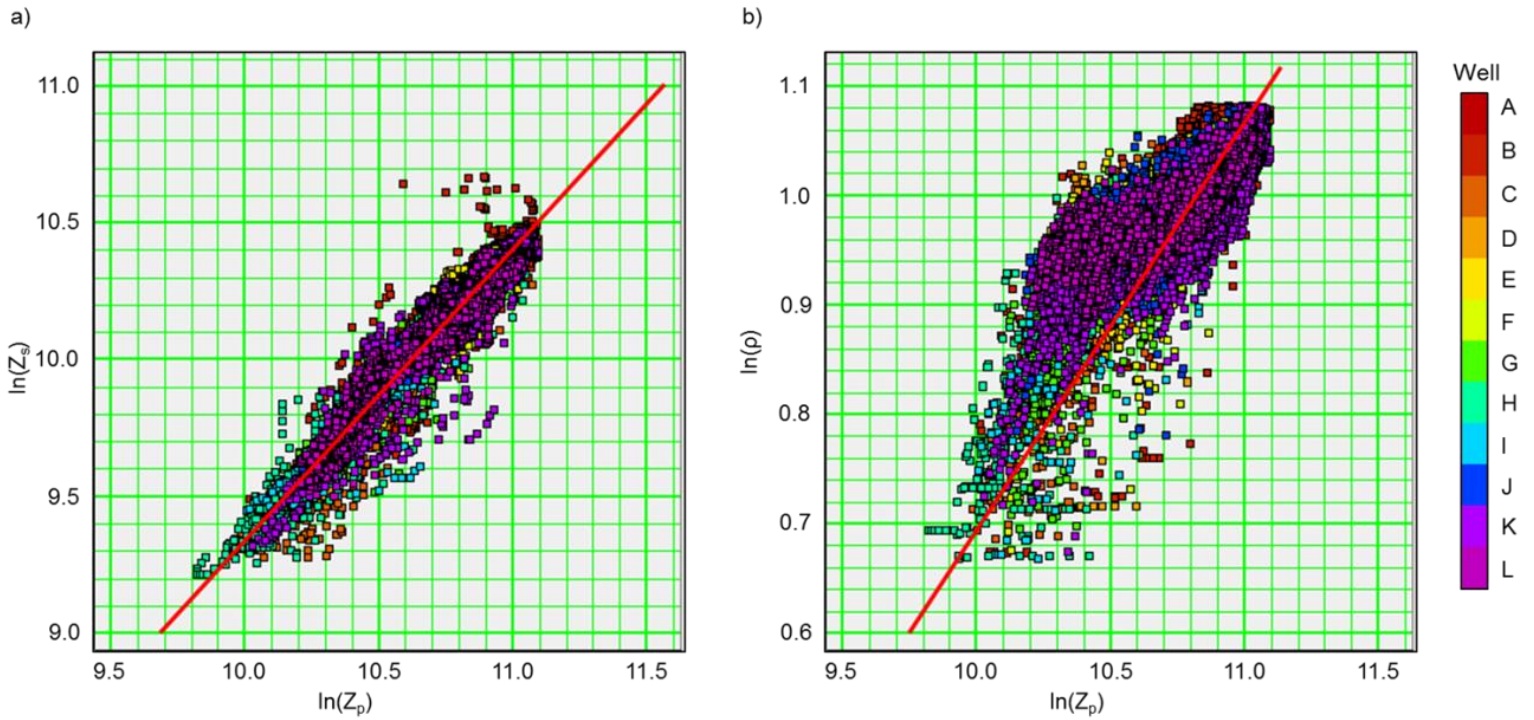

Figure 5.11: (a) S- versus P-impedance and (b) density versus P-impedance cross-plots on a log-log base. Both the S-impedance and the density have a linear relationship with the P-impedance.

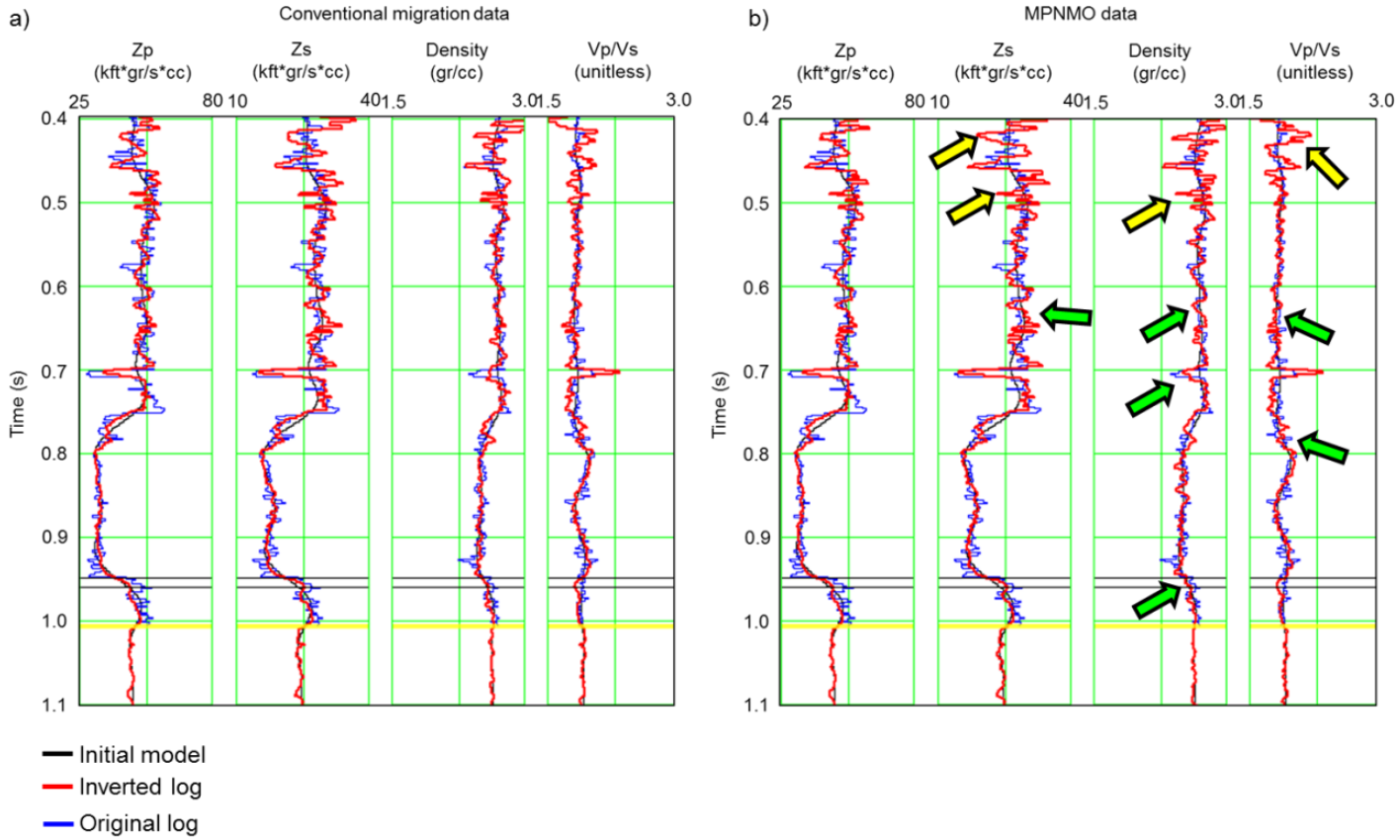

Figure 5.12: Inverted P-impedance, S-impedance, density and Vp/Vs ratio from (a) conventional migrated and (b) MPNMO corrected gathers. MPNMO significantly improves the resolution of the S-impedance, density, and Vp/Vs ratio inversion. The impact of MPNMO on P-impedance log is minimal since it is more sensitive to the near angle traces. (b) Green arrows indicate areas with improvement with respect to (a), yellow arrows indicate areas where the MPNMO

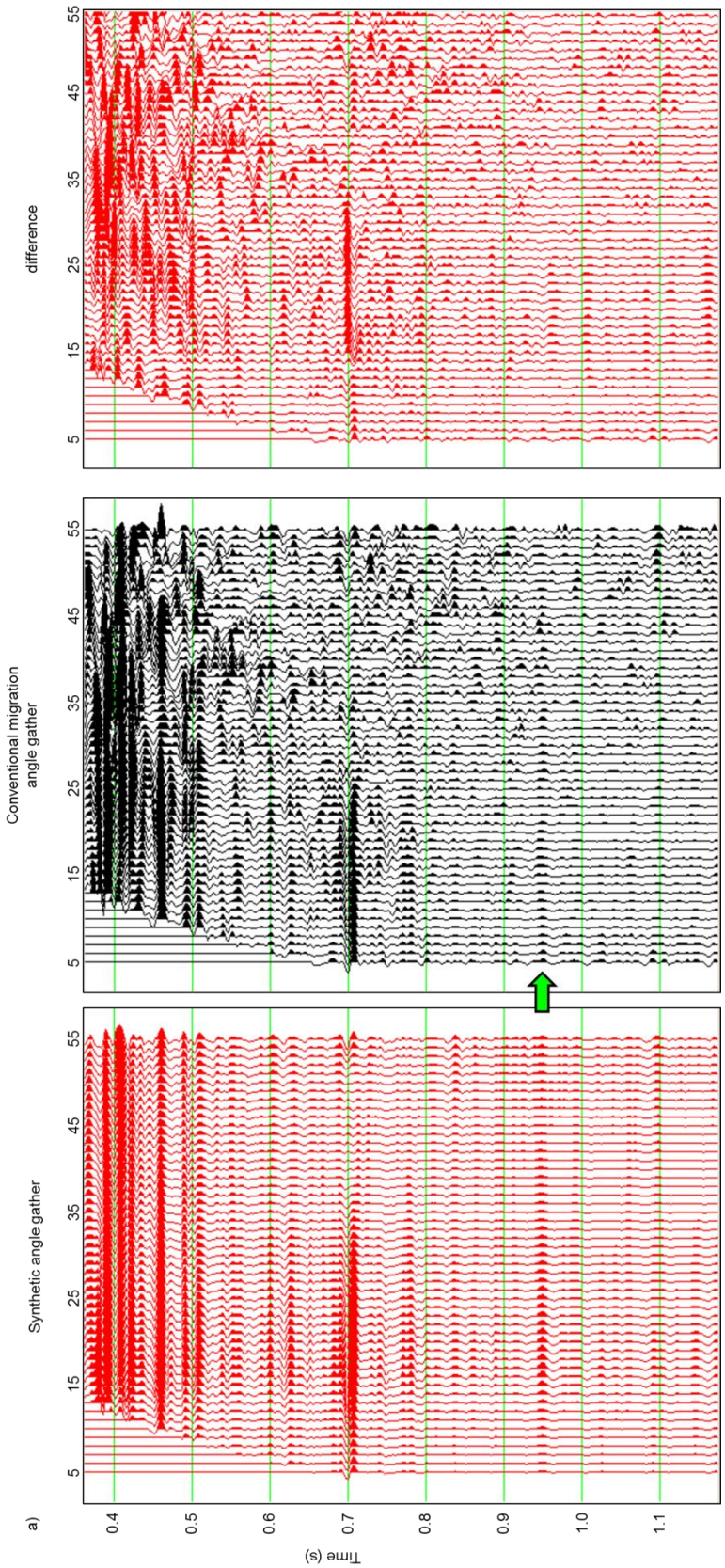
a)
Synthetic angle gather
Conventional migration
angle gather
difference
5
15
25
35
45
55
0.4
0.5
0.6
0.7
0.8
0.9
1.0
1.1
Time (s)

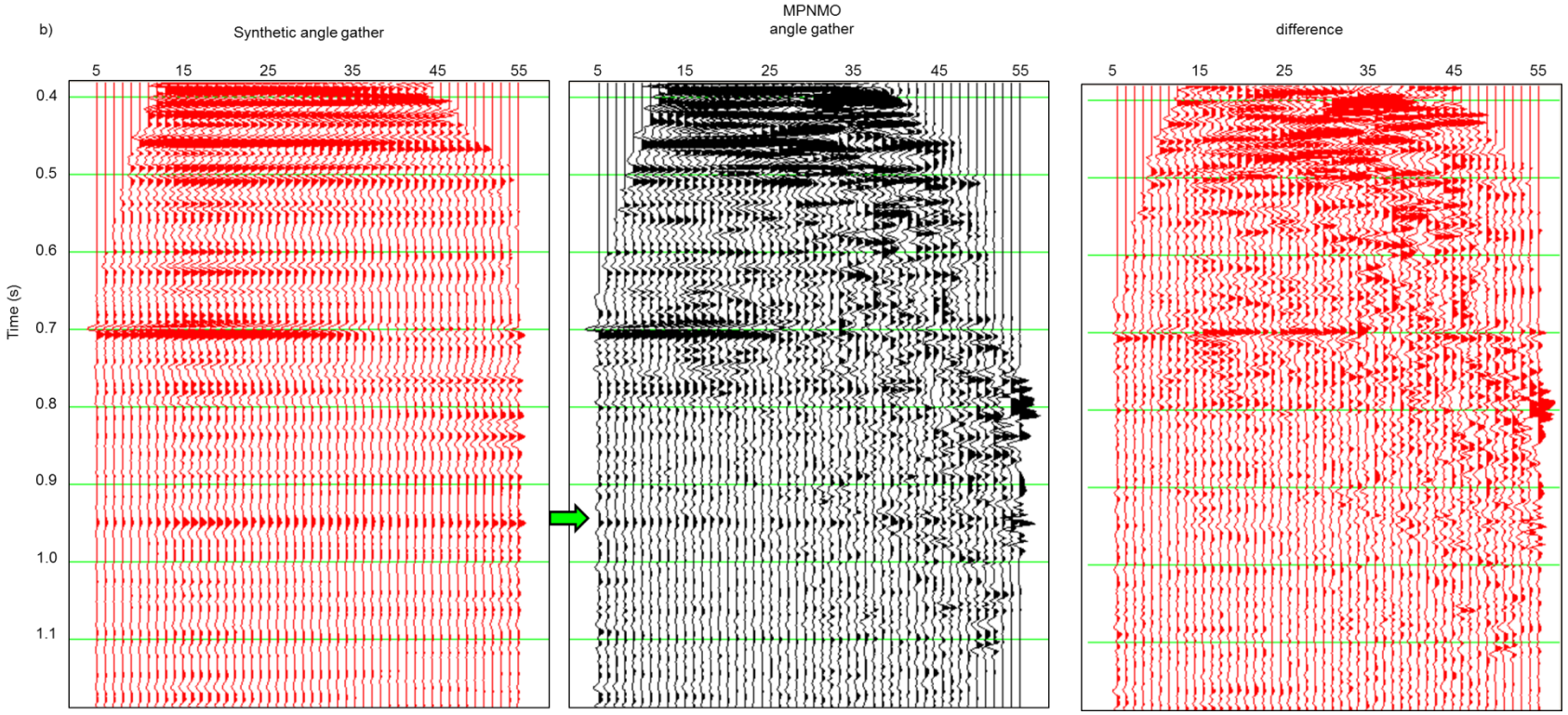

Figure 5.13: Synthetic, seismic data and difference between seismic data and synthetic about well H for (a) conventional migration and (b) MPNMO corrected gathers used to obtain the results in Figure 11. Green arrow indicates the Horseshoe Atoll top reflector

Table 5.2: Correlation coefficients of the inversion analysis for the conventional migration and the MPNMO data.

Well	Conventional migration	MPNMO corrected
A	82	78
B	73	70
C	80	72
D	75	75
E	76	76
F	75	64
G	84	84
H	76	76
I	77	73
J	79	78
K	77	76
L	78	73

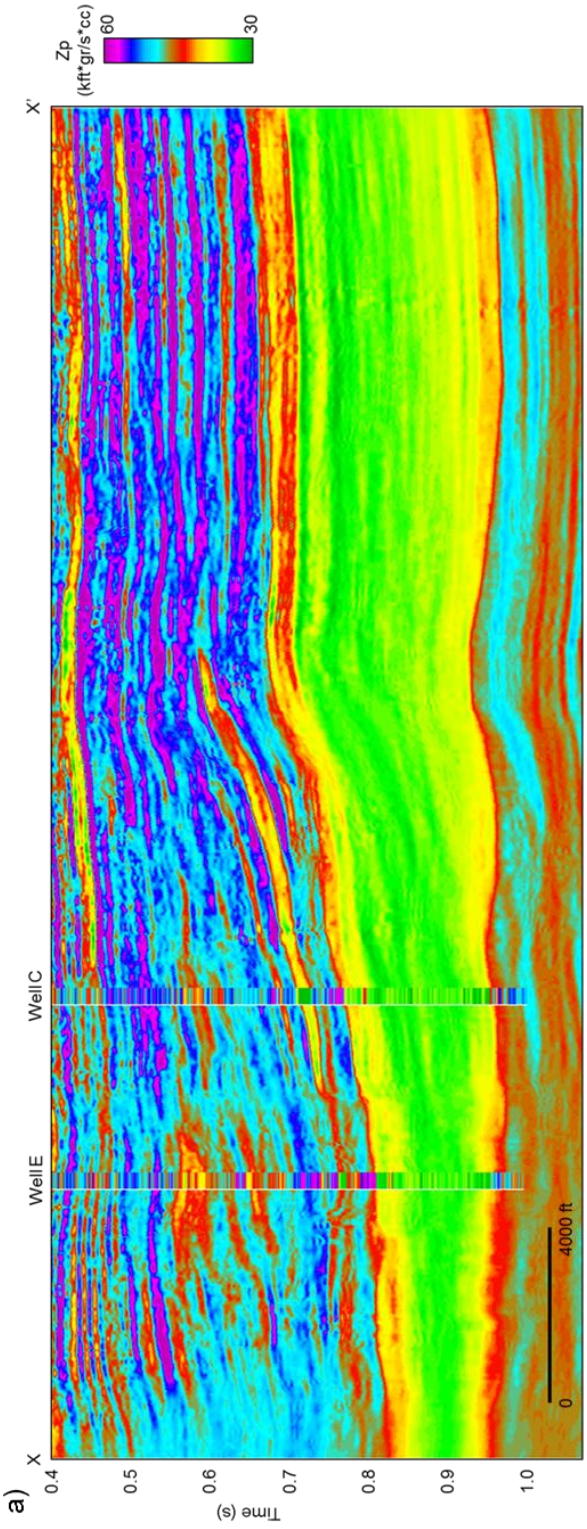
a)
X
X'
WellE
WellC
Zp
(kft*gr/s*cc)
60
30
Time (s)
0.4
0.5
0.6
0.7
0.8
0.9
1.0
0
4000 ft

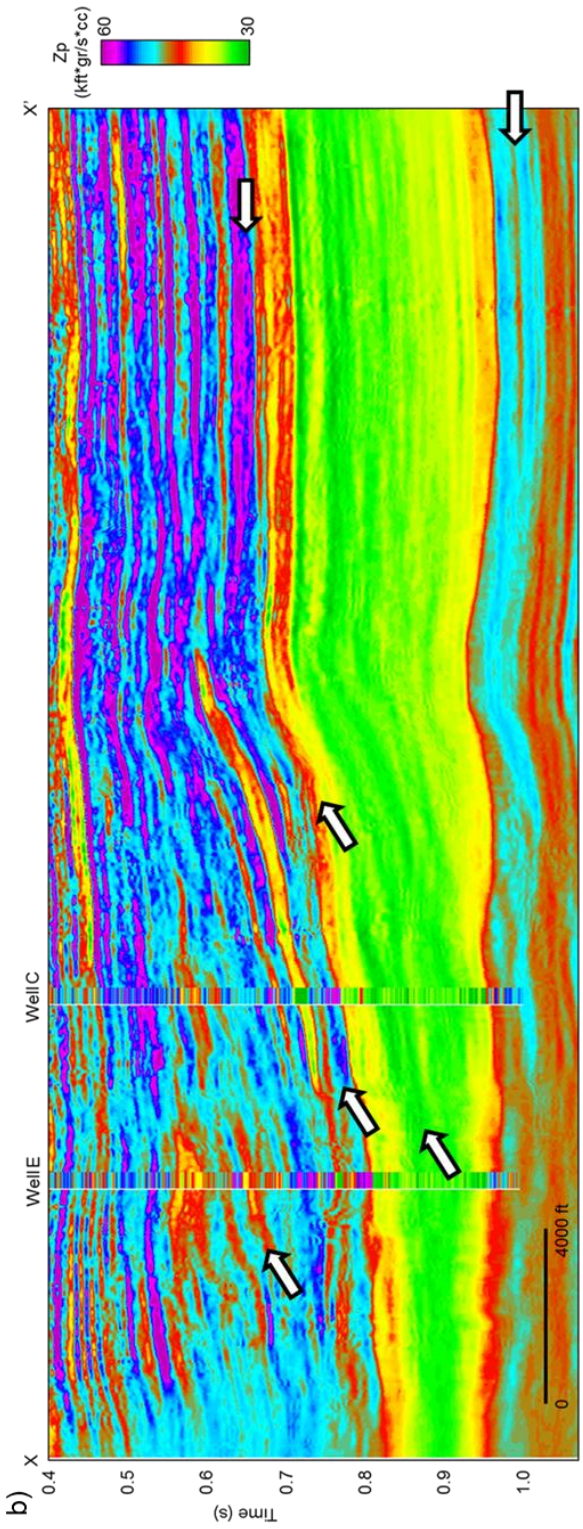
b)
X
X'
Zp
(kft*gr/s*cc)
60
30
Well E
Well C
Time (s)
0.4
0.5
0.6
0.7
0.8
0.9
1.0
0
4000 ft

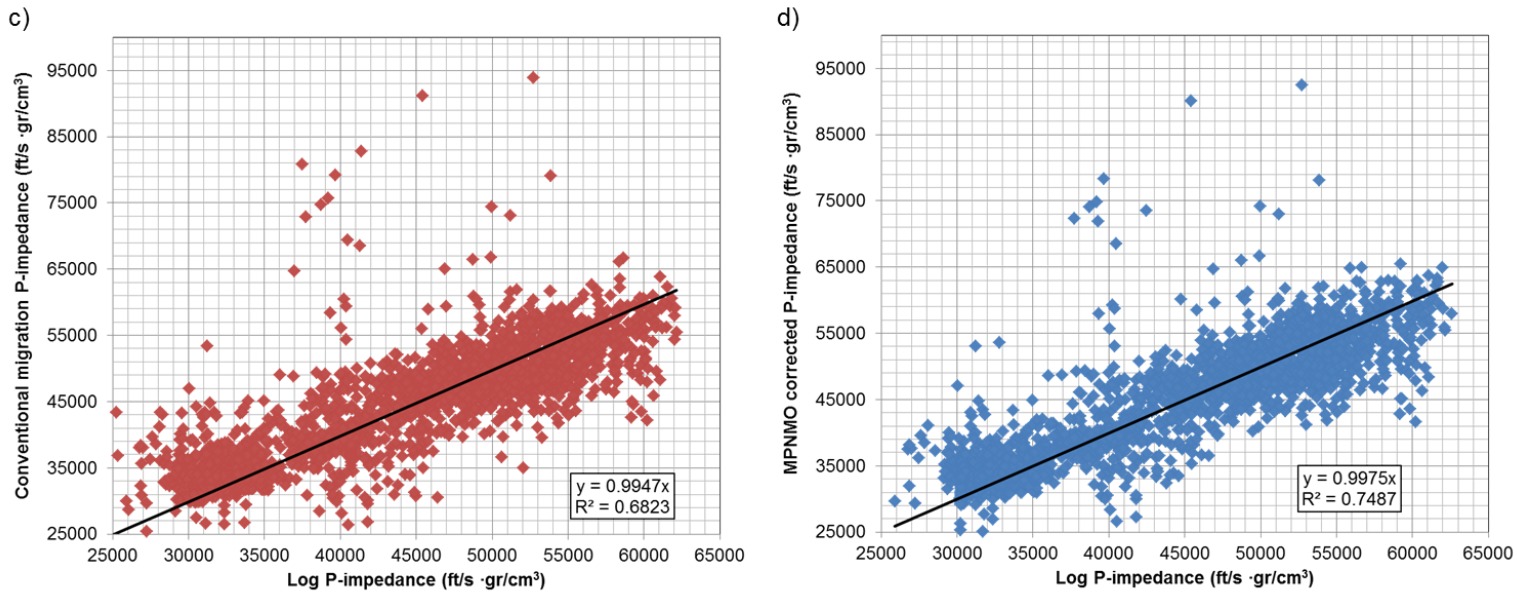

Figure 5.14: Cross-section X-X' through P-impedance volume using (a) conventional migration and (b) MPNMO corrected gathers. (c) Cross-plot of P-impedance from inversion using the conventional migration data versus P-impedance calculated from log data. (d) Cross-plot of P-impedance from inversion using the MPNMO corrected data versus P-impedance calculated from log data. (b) White arrows indicate zones where the P-impedance inversion results have improved by using the MPNMO technique. Cross-plotting the inverted P-impedance versus the log derived P-impedance shows that MPNMO corrected data has a better match to the log derived P-impedance. The black line represents the 1:1 trend in the cross-plots.

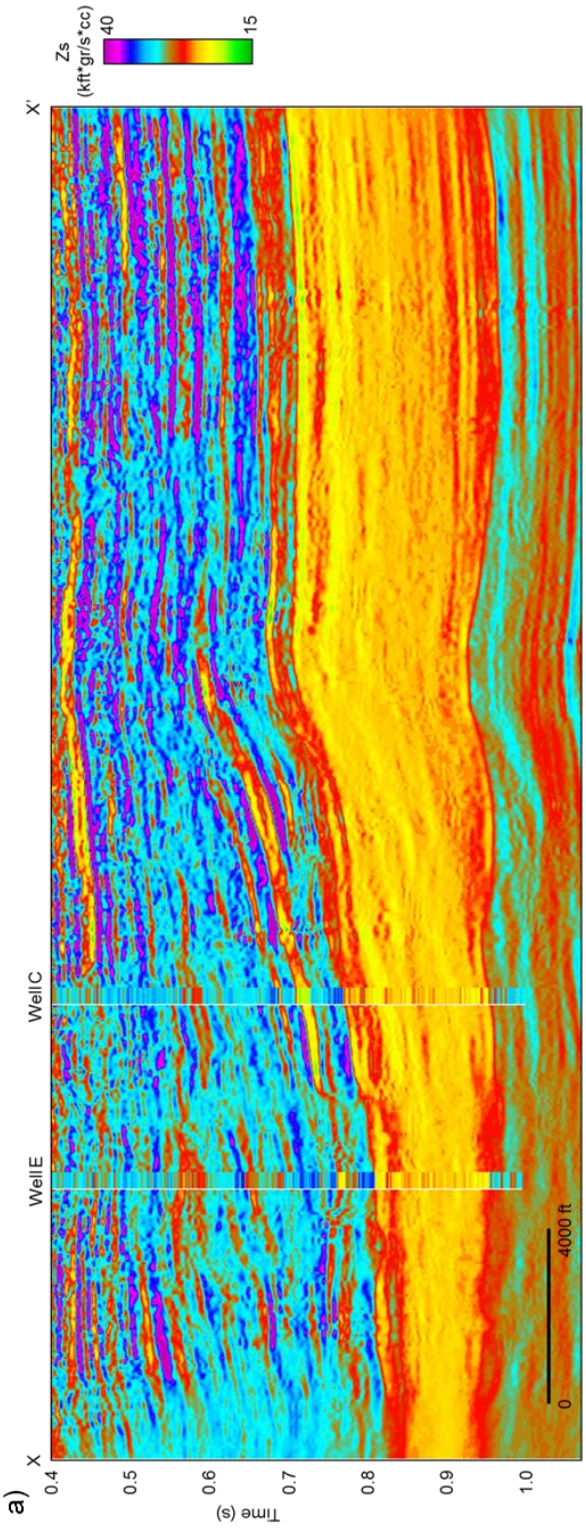
a)
X
X'
WellE
WellC
Zs
(kft*gr/s*cc)
40
15
Time (s)
0.4
0.5
0.6
0.7
0.8
0.9
1.0
0
4000 ft

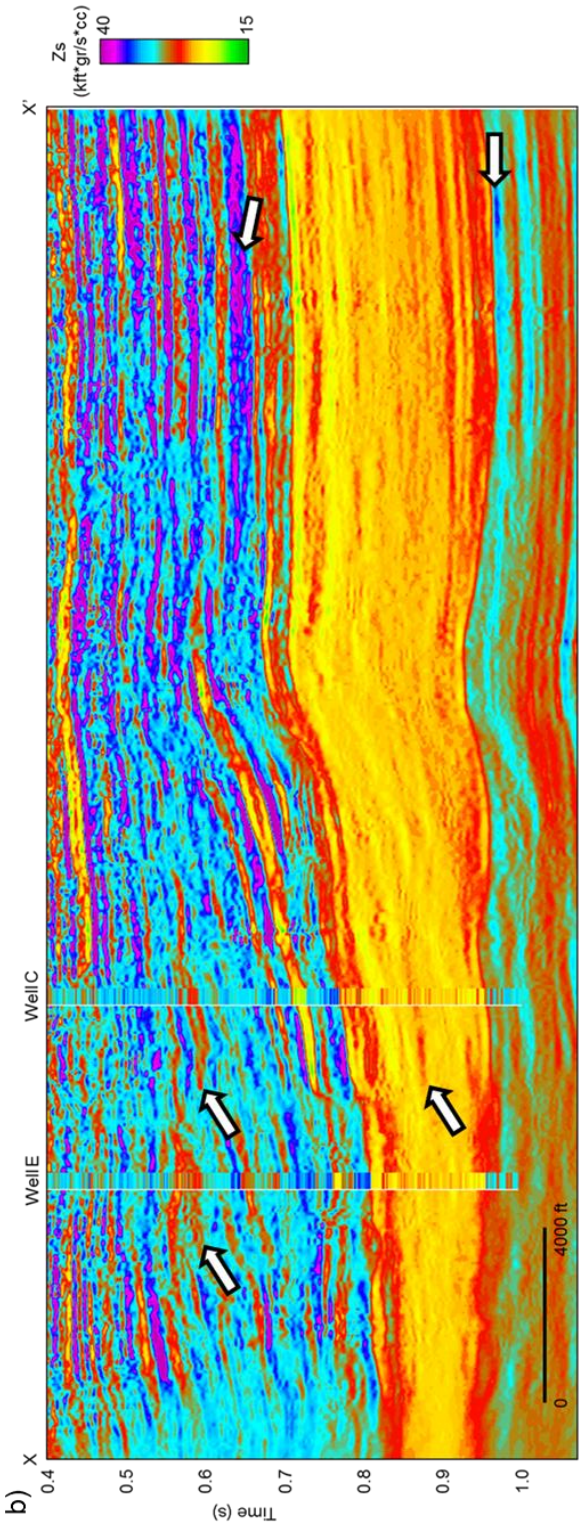
b)
X
X'
Well E
Well C
Time (s)
0.4
0.5
0.6
0.7
0.8
0.9
1.0
0
4000 ft
Zs
(kft*gr/s*cc)
40
15

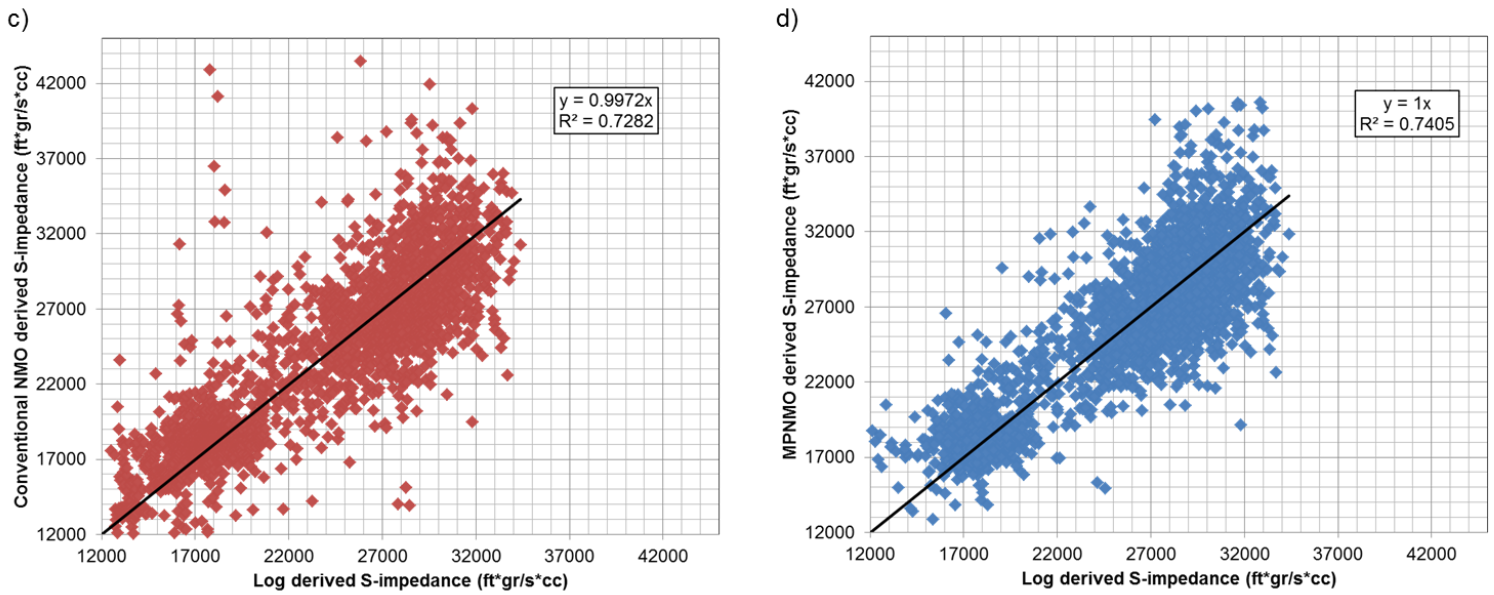

Figure 5.15: Cross-section X-X' through S-impedance volume using (a) conventional migrated and (b) MPNMO corrected gathers. (c) Cross-plot of S-impedance from inversion using the conventional migration data versus S-impedance calculated from log data. (d) Cross-plot of S-impedance from inversion using the MPNMO corrected data versus S-impedance calculated from log data. (b) White arrows indicate zones where the S-impedance inversion results have slightly improved by using the MPNMO technique. Cross-plotting the inverted S-impedance versus the log derived S-impedance shows similar correlation between the conventional migration and the MPNMO data. The black line represents the 1:1 trend in the cross-plots.

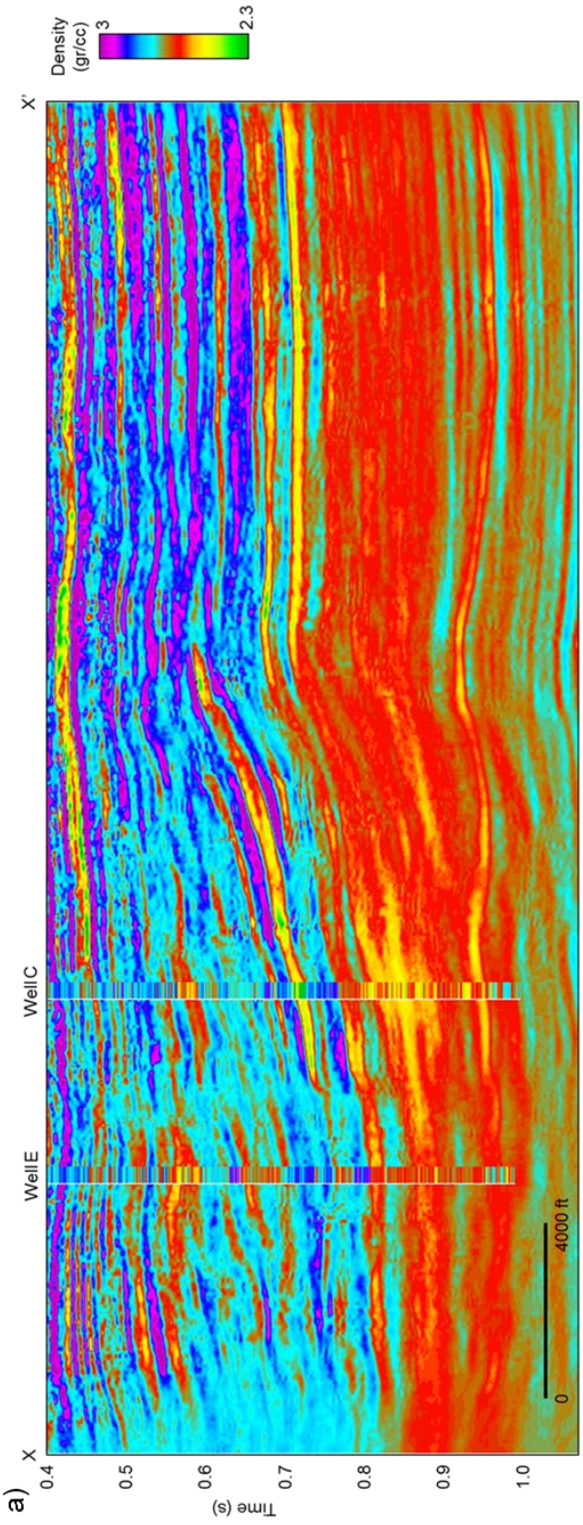
a)
X
X'
Well E
Well C
Density (gr/cc)
3
2.3
Time (s)
0.4
0.5
0.6
0.7
0.8
0.9
1.0
0
4000 ft

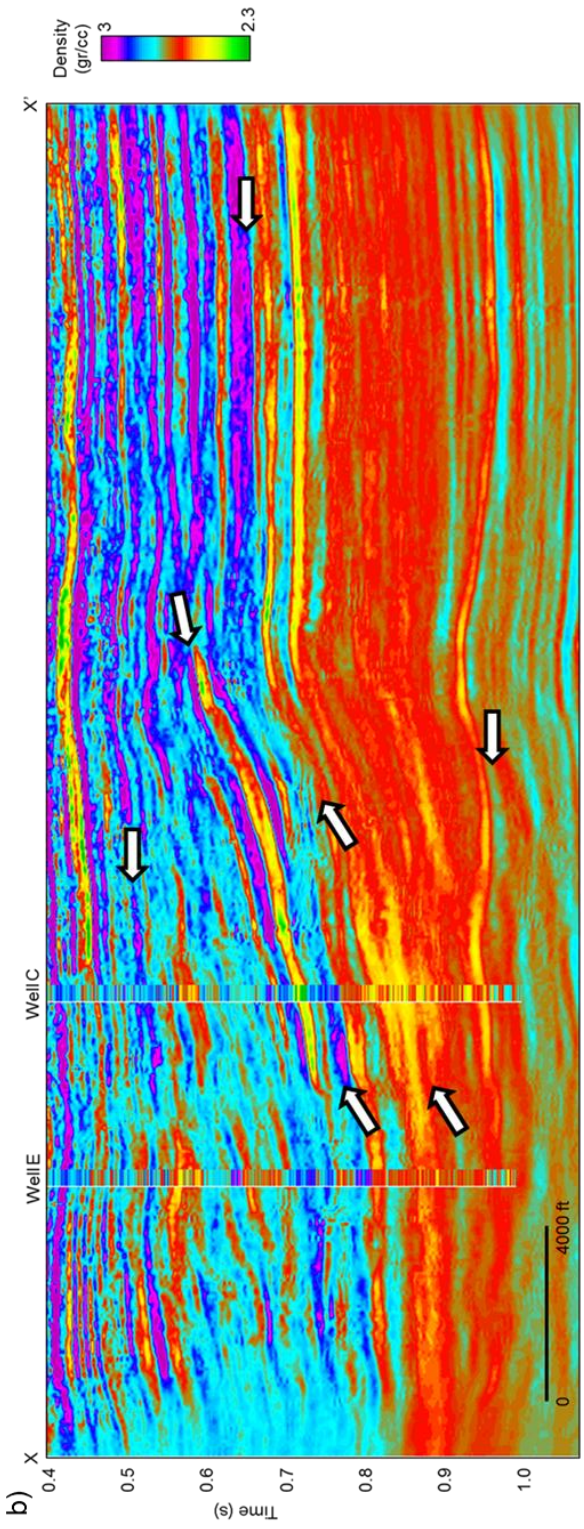
b)
X
X'
Well E
Well C
Time (s)
0.4
0.5
0.6
0.7
0.8
0.9
1.0
0
4000 ft
Density (gr/cc)
3
2.3

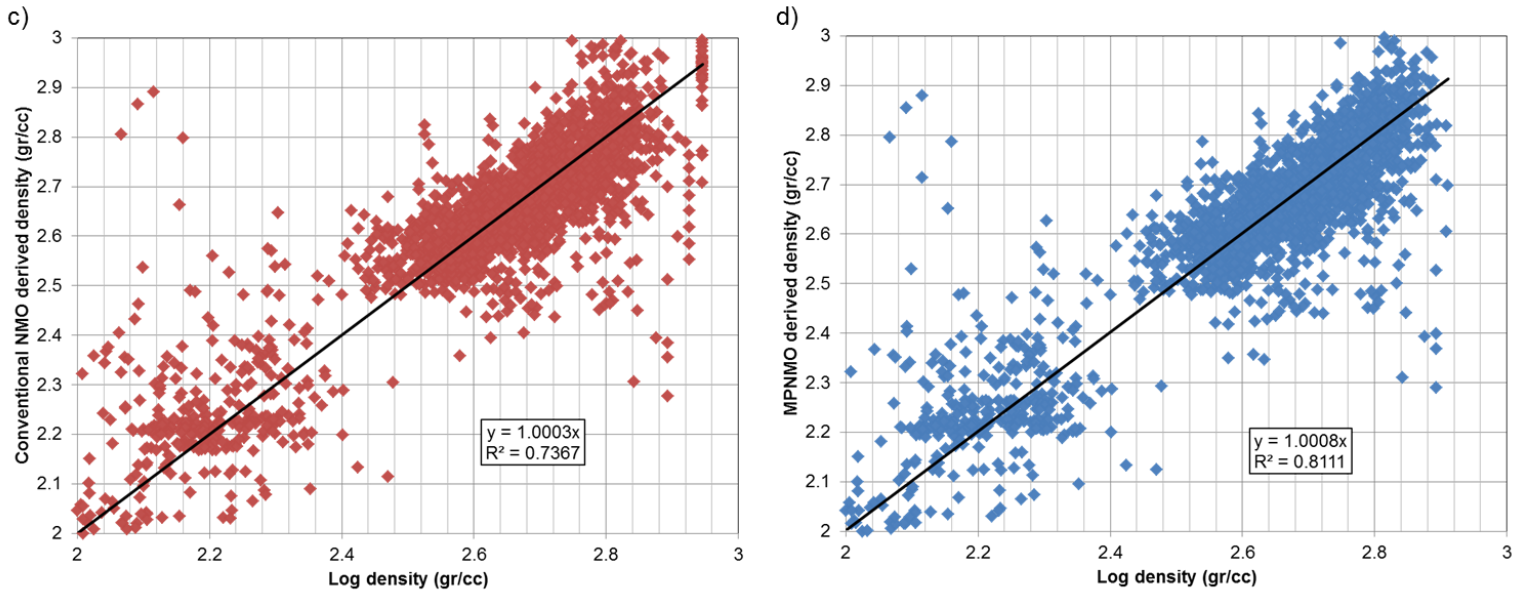

Figure 5.16: Representative cross-section through density volume using (a) conventional NMO and (b) MPNMO. (c) Cross-plot of density from inversion using the conventional NMO data versus density log. (d) Cross-plot of density from inversion using the MPNMO data versus density log. (b) White arrows indicate zones where the density inversion results have improved by using the MPNMO technique. Cross-plotting the inverted density versus the log density shows a significant improvement in the density estimation by using the MPNMO corrected data. The black line represents the 1:1 trend in the cross-plots.

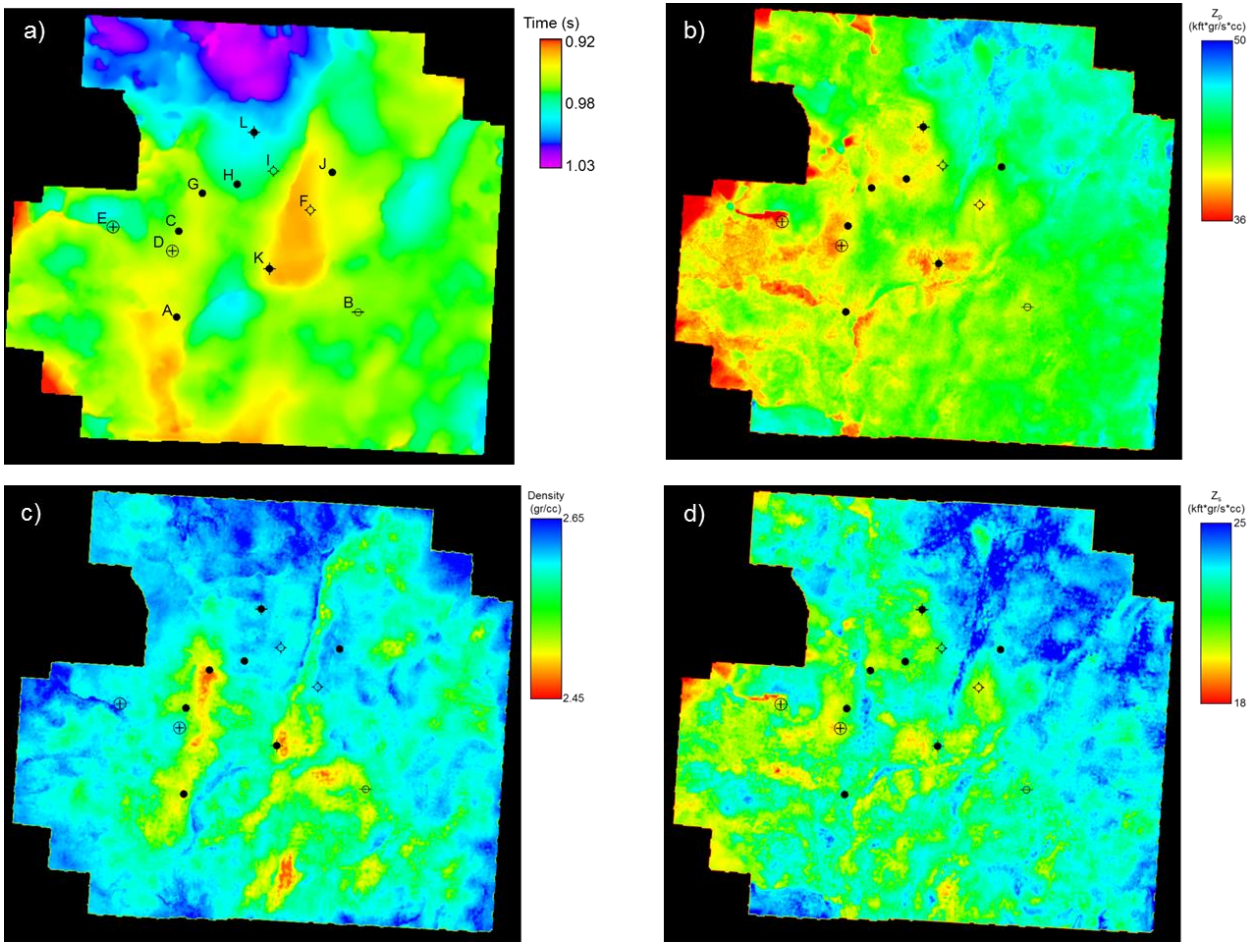

Figure 5.17: (a) Time structure map of the top Horseshoe Atoll reservoir with the posted well locations. (b) P-impedance, (c) density and (d) S-impedance extracted for the top of the Horseshoe Atoll reservoir using the MPNMO results shown in figures 14 to 16.

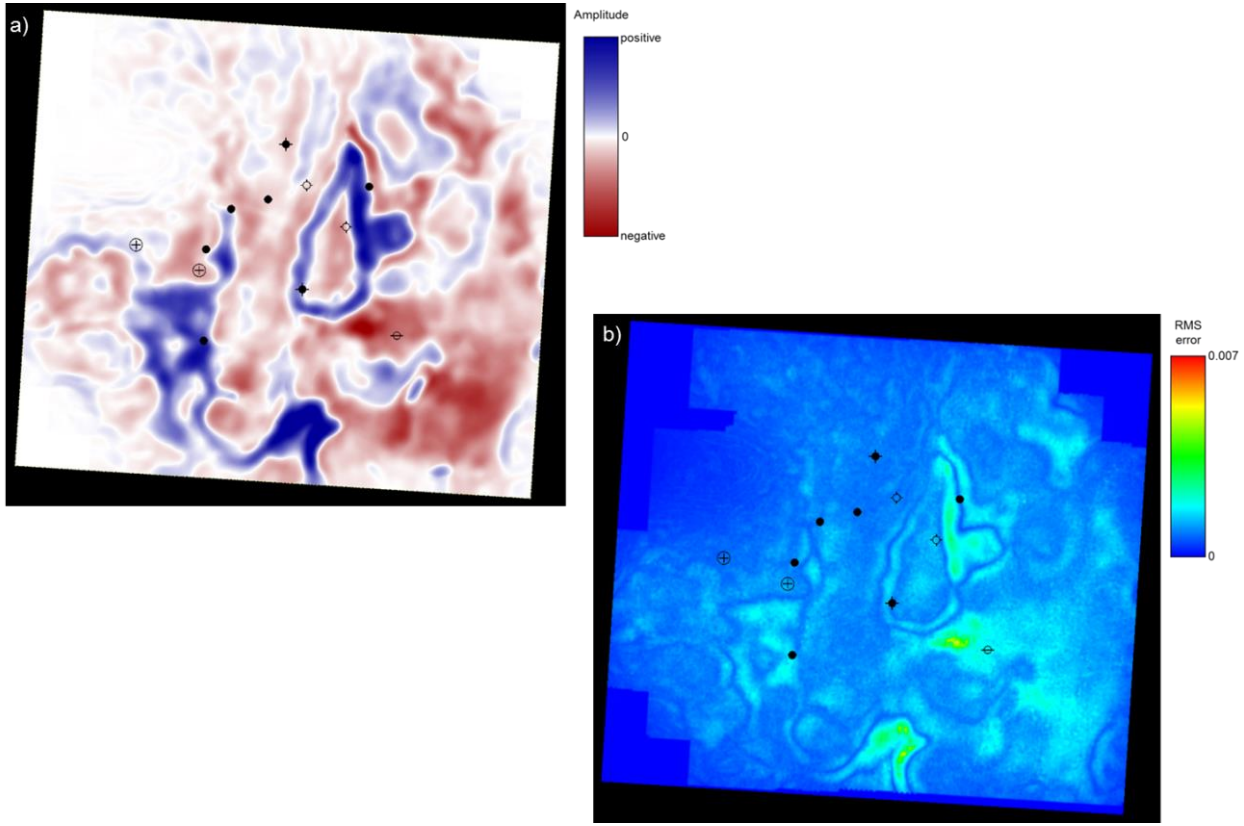

Figure 5.18: (a) Time slice at 0.94 s through MPNMO full stack. (b) RMS error computed using the synthetic and the MPNMO angle gathers shown in Figure 13.

REFERENCES

Aki, K., and P. G. Richards, 2002, Quantitative seismology, 2nd Edition: W. H. Freeman and Company.

Fatti, J., G. Smith, P. Vail, P. Strauss, and P. Levitt, 1994, Detection of gas in sandstone reservoirs using AVO analysis: a 3D Seismic Case History Using the Geostack Technique: Geophysics, 59, 1362-1376.

Hampson, D. P., B.H. Russell and B. Bankhead, 2005, Simultaneous inversion of pre-stack seismic data: 75th Annual International Meeting of the SEG, Expanded Abstracts, 1633-1637.

Singleton, S., 2008, The effects of seismic data conditioning on pre-stack simultaneous impedance inversion: The Leading Edge, **28**, 398–407.

Swan, H., 1991, Amplitude versus offset measurement errors in a finely layered medium: Geophysics, **56**, 41–49.

Swan, H., 1997, Removal of offset-dependent tuning in AVO analysis: 68th Annual International Meeting of the SEG, Expanded Abstracts, 175-178.

Singleton, S., M. Taner, and S. Treitel, 2006, Q estimation using Gabor Morlet joint time frequency analysis techniques: SEG Technical Program Expanded Abstracts 2006: 1610-1614.

Zhang, B., K. Zhang, S. Guo, and K. J. Marfurt, 2013, Nonstretching NMO correction of pre-stack time-migrated gathers using a matching-pursuit algorithm: Geophysics, 78, U9–U18.

6. 3D Alford rotation analysis for the Diamond M field, Midland Basin, Texas

Oswaldo Davogustto[1], J. Timothy Kwiatkowski, Kurt J. Marfurt[1] and J.W. Thomas[2]

[1] University of Oklahoma, School of Geology and Geophysics

[2]Dawson Geophysical Company

ABSTRACT

2C by 2C "shear wave" surveys generated significant excitement in the mid-1980s, but then fell out of favor when the shear wave splitting initially attributed to fractures was also found to be associated with an anisotropic stress regime. In general, 2C by 2C data requires more expensive acquisition and more processing effort in order to obtain images of comparable to single component "compressional wave" data acquired with vertical component sources and receivers. Since shear moduli are insensitive to fluids, and hence the water table, the effective shear wave weathering zone is greater than that for compressional waves, making statics more difficult. Shear wave splitting due to anisotropy complicates residual statics and velocity analysis as well as the final image. Shear wave frequencies and shear wave moveout are closer to those of contaminating ground roll than compressional waves.

Since Alford's introduction of shear wave rotation from survey coordinates to the principal axes in 1986, geoscientist and engineers retain their interest in fractures but are also keenly interested in the direction and magnitude of maximum horizontal stress. Simultaneous sweep and improved recording technology have reduced the acquisition cost to approximate that of single component data. Alford's work was applied to 2C by 2C post stack data. In this work we extend Alford rotation to prestack

data using a modern high fold 2C by 2C survey acquired over a fractured carbonate reservoir in the Diamond M field, Texas. Through careful processing, the resulting images are comparable and in many places superior to that of the contemporaneously acquired single component data. More importantly, we find a good correlation between our derived fracture azimuth map and the fracture azimuth log data from wells present in the field.

INTRODUCTION

Multicomponent seismic data is a powerful tool for reservoir characterization. The introduction of high bandwidth 3-component accelerometers based on either piezoelectric or MEMS technology transducers has not only reduced the cost of "converted-wave" (P to S) recording to approach that of conventional single component data but also provides additional data for P- and S-wave impedance inversion (Guliev and Michelena, 2010). Converted wave data are relatively insensitive to fluids in the overburdens (gas clouds) (Knapp et al, 2002) but are also particularly sensitive to fractures (Shekar and Tsvankin, 2011). However, converted wave processing is particularly difficult, with the weakest point being the need to estimate both, a P- and S-wave velocity field, P- and S- wave statics, and preprocessing using the common conversion point approximation (Gaiser et al., 1997).

In contrast to converted wave processing, the statics and velocity solutions as well as the imaging condition for 2C by 2C data, where we have two orthogonally polarized horizontal vibrators shaking into two orthogonally polarized receivers, is nearly identical to that of conventional single component "P-wave" data. Furthermore, recent innovations in slip sweep simultaneous recording, along with multicomponent

receivers, have reduced the field time of 2C by 2C data to approach that of single component data.

The key to both 2C by 2C and converted wave imaging is addressing the shear wave splitting. Alford (1986) recognized the necessity of aligning multicomponent multisource data into the principal axes of anisotropy in order to properly image fractured reservoirs and facilitate the interpretation of shear seismic data recorded on an azimuthally anisotropic medium. His method consisted of pre- and post-multiplication of the recorded data by the Bond rotation matrix (Auld, 1973) given by:

$$\begin{bmatrix} D_{11} & D_{12} \\ D_{21} & D_{22} \end{bmatrix} = \begin{bmatrix} \cos\theta & \sin\theta \\ -\sin\theta & \cos\theta \end{bmatrix} \begin{bmatrix} d_{yy} & d_{yx} \\ d_{xy} & d_{xx} \end{bmatrix} \begin{bmatrix} \cos\theta & -\sin\theta \\ \sin\theta & \cos\theta \end{bmatrix} \qquad (1)$$

where D_{yy}, D_{yx}, D_{xy}, and D_{xx} are the data recorded in field coordinates, D_{11}, D_{12}, D_{21} and D_{22} are the data rotated to be aligned with the principal axis of anisotropy and θ is the azimuth of the principal axis of anisotropy. Sondergeld and Rai (1992) using laboratory measurements on isotropic, anisotropic and inhomogeneous anisotropic materials and rock samples corroborated Alford's (1986) observations for seismic data. They found that in the presence of a single set of fractures in the medium only two shear velocities are observed. Fast and shear velocities being orthogonal to each other. In the presence of more than one set of fractures, they observed a complicated sequence of arrivals due to the multiple-splitting in the medium. Simmons and Backus (2001) described the importance of radial-transverse rotation of shear data. They demonstrate how the field data are a linear combination of *P*, *SH* and *SV* energy and summarize the critical differences between *SH* and *SV* modes. Simmons and Backus (2002) presented a full integrated study on shear wave data radial - transverse rotation. They find that for their data set radial – transverse rotation is sufficient to correctly orient the shear wave

propagation vectors. They also suggest that Alford rotation on prestack data should not be applied since the effect of the geometry is greater than the actual effect of shear wave splitting on their data. They recommend that Alford rotation should be applied to pre-stack data only at small offsets where the normal incidence assumption can be made.

We begin our paper with the formulation for an Alford rotation approach to a 2C by 2C multicomponent dataset. Our derivation will automatically calculate the direction of principal axis of anisotropy and use this calculated direction to align the data in such direction. For simplicity we will refer to the average principal axis of anisotropy direction as the hypothesized fracture direction. We apply this technique to a high fold 3D pre-stack 2C by 2C shear dataset from West Texas and show how our method is able to predict an average fracture direction. We conclude with a discussion of assumptions and limitations associated with this methodology.

AUTOMATIC ALFORD ROTATION USING LEAST SQUEARES MINIMIZATION

Our Alford rotation implementation is based on a least-squares technique for diagonalization and minimization of the left hand matrix of equation 1. Like Alford, who rolled out hard copy stacks every 10 degrees on the hallway floor of the Amoco Research Center (Marfurt, personal observation); our approach is a brute force approach. We do not analytically but rather numerically solve the min-max problem using a discrete angle search. Specifically, we numerically compute the direction that makes the energy of D_{12} and D_{21} minimum and D_{11} and D_{22} maximum simultaneously. We use Taner et al.'s (1979) formula for calculating the energy $e_{ij}\ (\theta)$ of the trace sample by sample

$$e_{ij}(\theta, t) = \left(D_{ij}(\theta, t) + D_{ij}^{H}(\theta, t)\right)^2 \qquad (2)$$

where D_{ij} is the amplitude of the source component *i* into receiver component *j*, D_{ij}^{H} is the Hilbert transform of D_{ij}. We then proceed to calculate the total energy of the trace by adding energy calculated at each sample. The total energy of the trace is then:

$$E_{ij}(\theta) = \sum_{n=1}^{N} e_{ii}(\theta, n\Delta t) \qquad (3)$$

where E_{ij} represents the total energy of the rotated traces and *n* is the time sample index. The equation for the simultaneous minimization of the D_{12} and D_{21}components and maximization of the D_{11} and D_{22} is given by:

$$\chi(\theta) = E_{12}(\theta) + E_{21}(\theta) - E_{11}(\theta) - E_{22}(\theta) \qquad (4)$$

where $\chi(\theta)$ is the minimization function. We then search for the global minimum of $\chi(\theta)$ and use the angle θ associated with the global minimum of function $\chi(\theta)$ value as an average fracture direction for each trace. Equation 4 is a joint energy minimization of the cross-diagonal terms and energy maximization of the diagonals.

APPLICATION OF THE AUTOMATED ALFORD ROTATION ALGORITHM TO THE DIAMOND M 2C BY 2C DATASET

The Diamond M data set consists of approximately 25 mi^2 of seismic data with a high signal to noise ratio located in Scurry County, TX (Figure 6.1). The target interval is focused on Cisco and Canyon formations of the Horseshoe Atoll. These carbonates formed during late Pennsylvanian to early Permian time when shallow water carbonate deposits dominated most of the deposition in the Permian basin. The reservoir is classified as a carbonate buildup and is composed mostly of rich biomicritic rocks with some packstone and grainstone occurrences (Fisher, 2005). The survey has an azimuth

of 3.64 degrees with respect to north. The data are 302 fold per component with frequencies between 4 and 40 Hz.

For simplicity we will refer to the inline direction for the source as *x* and the crossline direction for the same source as *y*. The same convention will be used for the receiver stations. For example, a trace recorded vibrator "shaking" in the *x* direction and on the inline component for the receiver stations will be denoted then as d_{xx}. We will refer to the fracture direction aligned data as D_{11} and its orthogonal direction as D_{22} (Figure 6.2). For comparison purposes we used a single average velocity field to migrate field and rotated S-wave components.

Field, Radial-Transverse, and Alford rotated data comparison

We applied a joint processing sequence for the four components of the dataset in order to avoid any amplitude alterations that would bias the Alford rotation process (Figure 6.3). Key processing steps include surface consistent deconvolution and surface consistent amplitude recovery. For the surface consistent deconvolution and surface consistent amplitude recovery we concatenated the traces from each component and computed deconvolution and scaling operators and applied them to the data. Figure 6.4 shows a representative shot gather before and after the surface consistent deconvolution and surface consistent amplitude recovery. We avoid the use of bandpass filters and AGC functions in order to keep most of the frequency content and true amplitude of the data. Next, we sort the data into CDP gathers and input the four components into our rotation algorithm. In order to apply Alford rotation to the migrated radial – radial, radial-transverse, transverse-radial, and transverse-transverse components, we migrate all four volumes using a single V (t, x, y) velocity volume (Figure 6.5). In this way we

do not favor either of the rotation techniques by having an improved velocity field. Figure 6.6 shows the field data results.

We compared the results from radial – transverse rotation with the field data. Although the "crosstalk" noise of the D_{rt} and D_{tr} components are less than those in the measured d_{yx} and d_{xy} components, we still observe some signal. (Figure 6.7). The signal present at the D_{rt} and D_{tr} components suggests the presence of fractures that do not align with the source – receiver azimuth pairs for most of the traces in each CDP bin.

Next we rotate the data using the automatic Alford rotation algorithm. From the algorithm we obtain the fracture direction for each trace and we calculate an average fracture direction for each CDP bin using a limited range of offsets in order to avoid noise contamination in our fracture direction estimation. Figure 6.8 shows the results for the stacked Alford rotated data. Note that the Alford rotated components D_{12} and D_{21} are uncorrelated noise whereas d_{yx} and d_{xy} components display both signal and noise.

Alford fracture azimuth map

We have oriented dipole sonic logs in four well locations in the Diamond M survey (Figure 6.1) that we use to corroborate the average fracture direction estimation from our automatic Alford rotation algorithm. Our Alford rotation implementation allows us to select what set of offset ranges to use for the Alford rotation and for the fracture direction estimation. Figure 6.9 shows the difference between using the near offsets (0-6000 ft.), the near and mid offsets (0-13500 ft.) and the full offset range for estimating the average fracture direction from the Alford rotation. The regional maximum stress direction is about 60 degrees from north (Figure 6.10). We assume that fractures parallel to this orientation are going to be open and fractures perpendicular to

this direction are going to be closed. In order to estimate the fracture direction from the shear components we compute a near offset derived Alford fracture azimuth map (Simmons and Backus, 2001). We found that our fracture direction estimation from seismic data is close to that of the fracture direction measured from the log data (Figure 6.11). The strong correlation we find with the azimuth direction derived from the log data suggests that the shear wave direction is a mixture of both regional stress and fractures present in the Horseshoe Atoll reservoir (Wielemaker et al., 2005) (Figure 6.12).

Processing considerations after pre-stack automatic Alford rotation

In order to improve the quality of the pre-stack Alford rotated data we input the rotated components into velocity analysis and refine the fast (V_{S1}) and slow (V_{S2}) velocity fields. We then migrated components D_{11} and D_{22} (Figure 6.3) using their respective corrected velocity fields. Figure 6.13 displays the final migrated D_{11} and D_{22} components using the V_{S1} and V_{S2} velocity fields. Using these refined versions of D_{11} and D_{22} we estimated the time lag between them at three different levels (Figure 6.14). Time differences that are reported as negative imply the amount of shift that D_{22} must be shifted upwards to match D_{11}. Time differences that are reported as positive imply the amount of shift that D_{22} must be shifted upwards to match D_{11}. We find that the amount of time difference for level 1 is about -0.6 ms with an average correlation coefficient of 0.45 and an estimated error of ±9 ms (Figure 6.15). For level two we find an average time difference of -3.3 ms with an average correlation of 0.65 and average error of ±4 ms (Figure 6.16). For level three we find a time difference of -3.6 ms with an average correlation of 0.8 and an average error of ±5.3 ms (Figure 6.17). These

results indicate that the time lags can only be used in a qualitative way. Figure 6.18 shows a comparison of the time lags obtained from the seismic data to the shear scanner sonic anisotropy study for well I. We selected a 100 ft. log section for each level of the time difference analysis. We observe that the time differences on the log data are between 1 and 5 μs/ft. This observation supports the results we obtained from the time lag analysis despite the uncertainty observed.

CONCLUSIONS

With the renewed interest in fractures and new interest in estimated stress direction land multicomponent data has experienced renewed interest. Most recent surveys have been acquired using "converted wave" technology, with either dynamite or vertically polarized vibrator and 3-component accelerometers. More traditional "shear wave" 2C by 2C surveys are much less common, partly because the horizontally polarized vibrators were are more than 20 years old and slowly shaking themselves apart. We have introduced a method to implement an automated pre-stack Alford rotation. One of our main assumptions is that the fracture direction does not change drastically throughout the section. This seems to be a valid assumption from our results in Figure 6.11. We proposed a processing sequence pre- and post-rotation in order to better preserve the amplitudes and obtain the best results for this dataset. We have shown that although Alford assumes a zero offset trace, far offsets do not change the fracture azimuth calculation drastically. We used a range from 0 to 20 degrees to avoid noise contamination for the average fracture direction estimation. Our fracture direction interpretation matches the log data for the Canyon and Cisco formation in the area of study. Finally, we find that the anisotropy induced time difference is minimal and has a

fair amount of uncertainty although it agrees with the time anisotropy seen in the log data.

ACKNOWLEDGEMENTS

Seismic processing was done using ProMAX, interpretation using Petrel, inversion using Strata, log analysis using Techlog, and integration using Transform software. We thank Parallel Petroleum LLC for providing a license to the Diamond M dataset. We thank Schlumberger for donating Petrel and Techlog Software for use in research and education. We thank DrillingInfo for donating Transform Software for use in research and education. We thank CGG Veritas for donating Hampson-Russell Software for use in research and education. Finally we would like to thank Andrea Miceli, Steve Roche, Carl Sondergeld, and Bradley C. Wallet for their help and support. The computing for this project was performed at the OU Supercomputing Center for Education & Research (OSCER) at the University of Oklahoma (OU).

LIST OF FIGURES

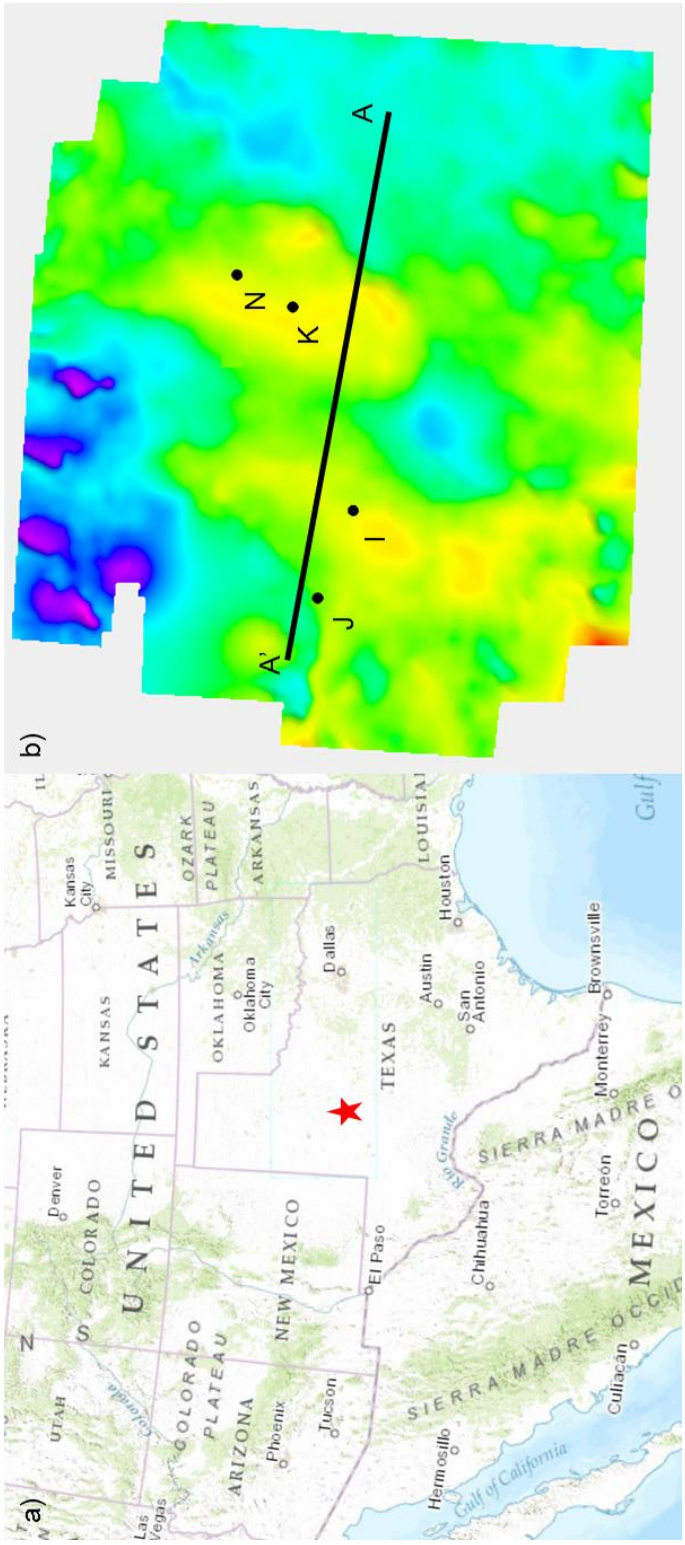

Figure 6.1: (a) Map displaying the location of the Diamond M field in Texas. (b) Time structure map of the Horseshoe Atoll indicating line AA' and the location of key wells.

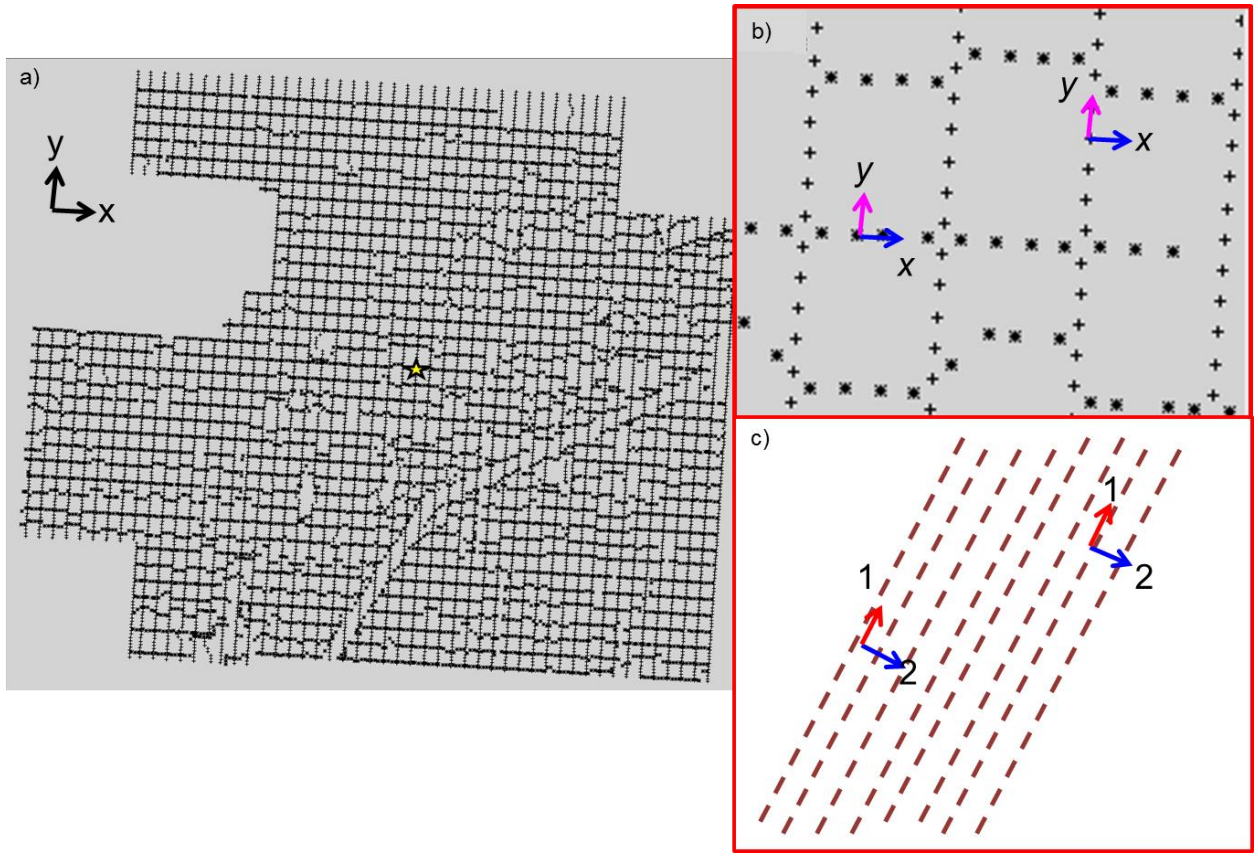

Figure 6.2: Diamond M multicomponent seismic survey layout. (a) Black arrows indicate the x and y directions of source and receiver components. (b) d_{yy} (magenta arrows) and d_{xx} (blue arrows) components also called field components. (c) D_{11} and D_{22} components also referred to as fast and slow shear components respectively. Hypothesized fractures are represented by the brown dashed lines.

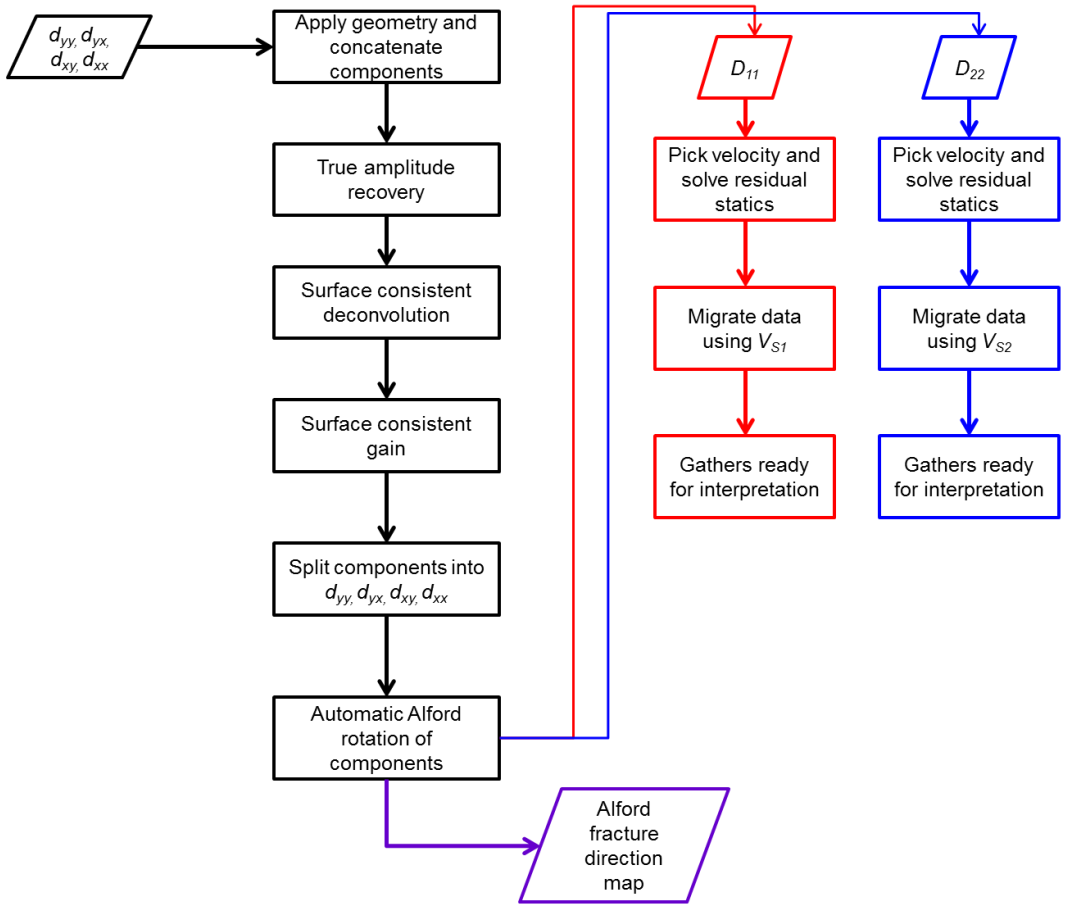

Figure 6.3: Seismic processing workflow of the Diamond M multicomponent seismic dataset. Processing steps in black are done before Alford rotation. These processes output three datasets, the Alford fracture direction map and rotated components D_{11} and D_{22}. Colored steps are dependent on the component being process. Red processing steps are applied to D_{11} and blue processing steps are applied to D_{22} components.

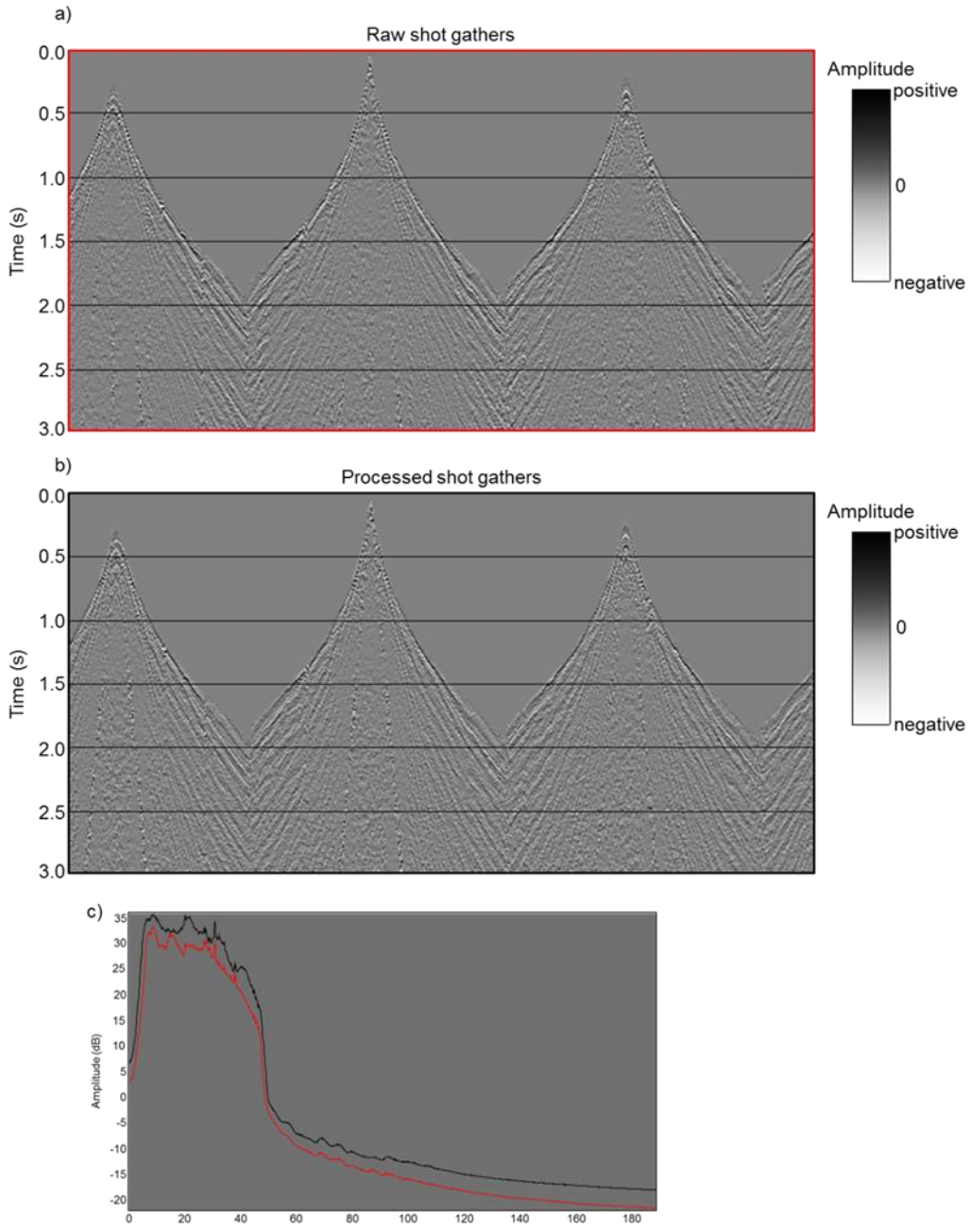

Figure 6.4: Three representative d_{yy} shot gathers (a) before and (b) after the processing flow described in Figure 3 previous to Alford rotation. (c) Frequency spectra for the raw (red) and processed (black) shot gathers. Note that surface consistent deconvolution and surface consistent gain have flattened the spectrum for the data. Location of the shot gathers indicated by a star in Figure 2a.

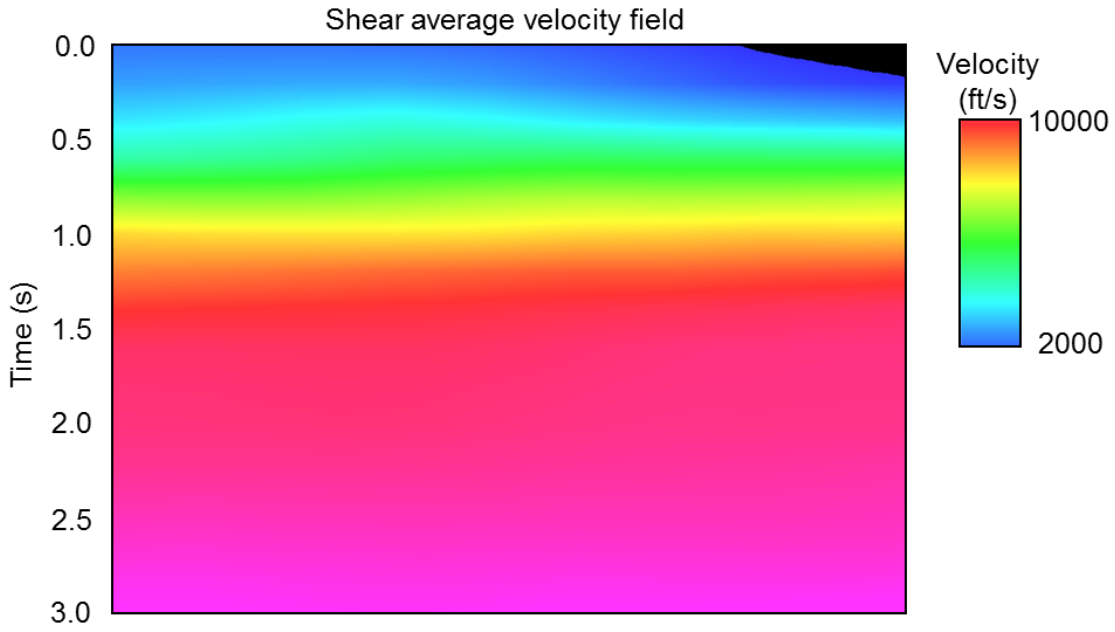

Figure 6.5: average velocity field used to compare field, radial-transverse and Alford rotation stacks.

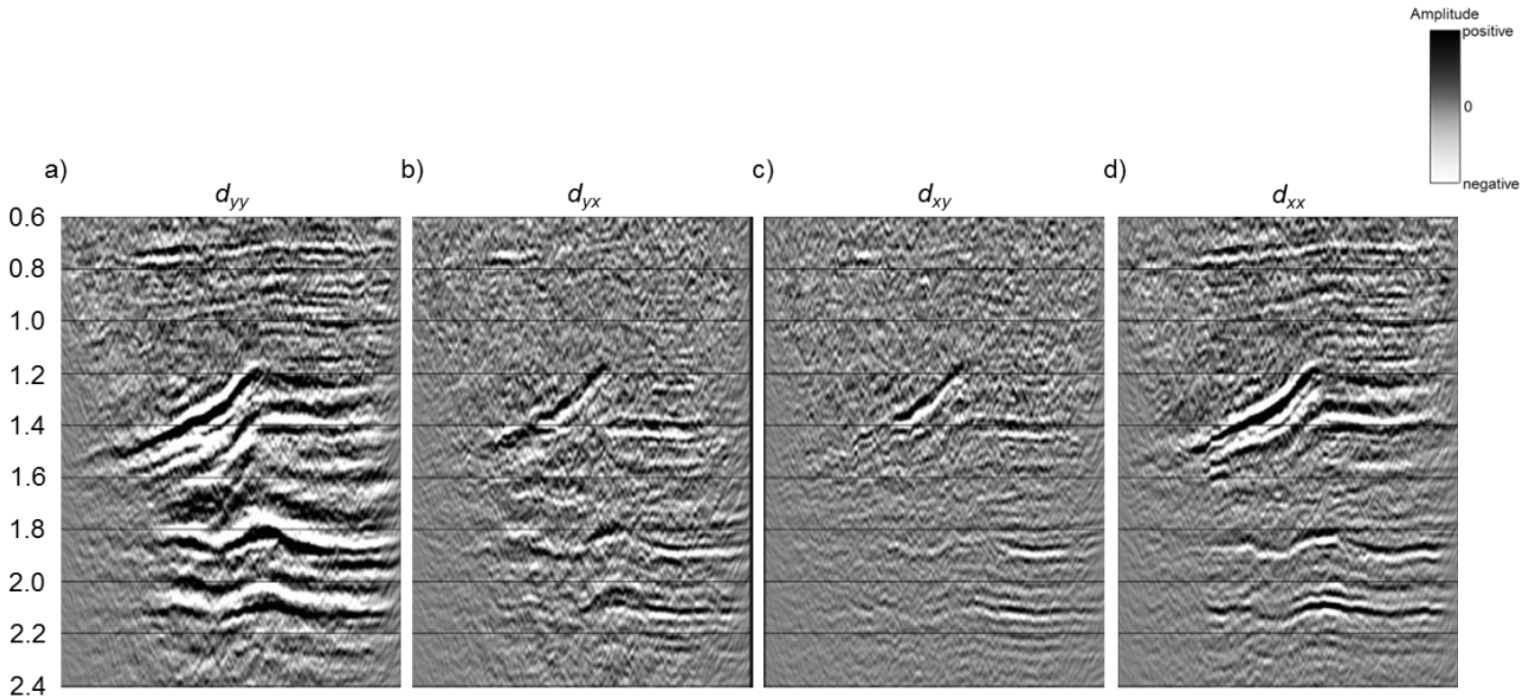

Figure 6.6: Vertical section A-A' through (a) d_{yy}, (b) d_{yx}, (c) d_{xy}, (d) d_{xx} component seismic amplitude. The four components display a similar image when stacked using the average picked velocity field. The signal in the cross-components, d_{yx}, and d_{xy}, indicates the principal axes of anisotropy are not aligned with the x and y axes. (a) The lower frequency observed in d_{yy} could be attributed to P-wave data contamination.

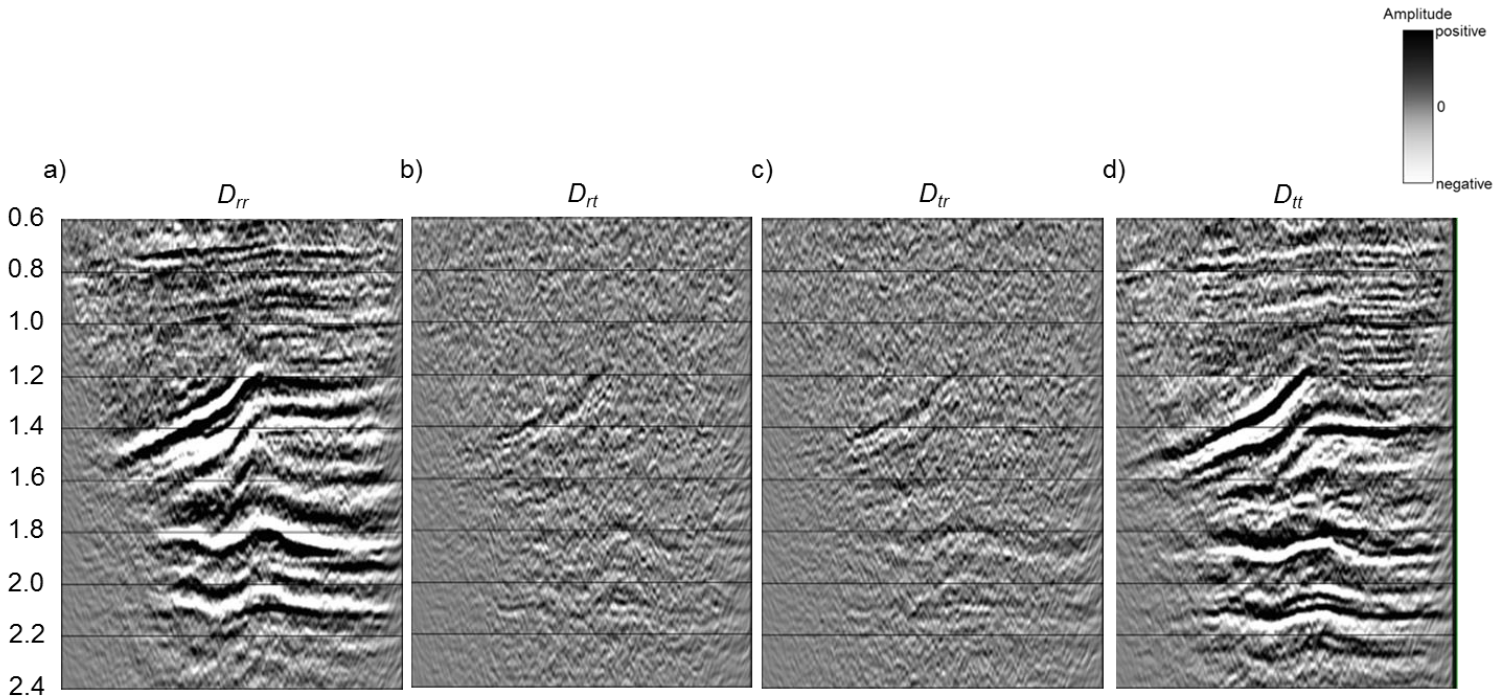

Figure 6.7: Vertical section A-A' through (a) D_{rr} (b) D_{rt}, (c) D_{tr}, (d) D_{tt} component seismic amplitude. (a) and (d) components display a similar image when stacked using the average picked velocity field with an offset in time. (b) and (c) show less amount of signal when compared to Figure 6 (a) and (b). The presence of signal in (b) and (c) indicates that the *r* and *t* axes are not aligned with the principal axes of anisotropy.

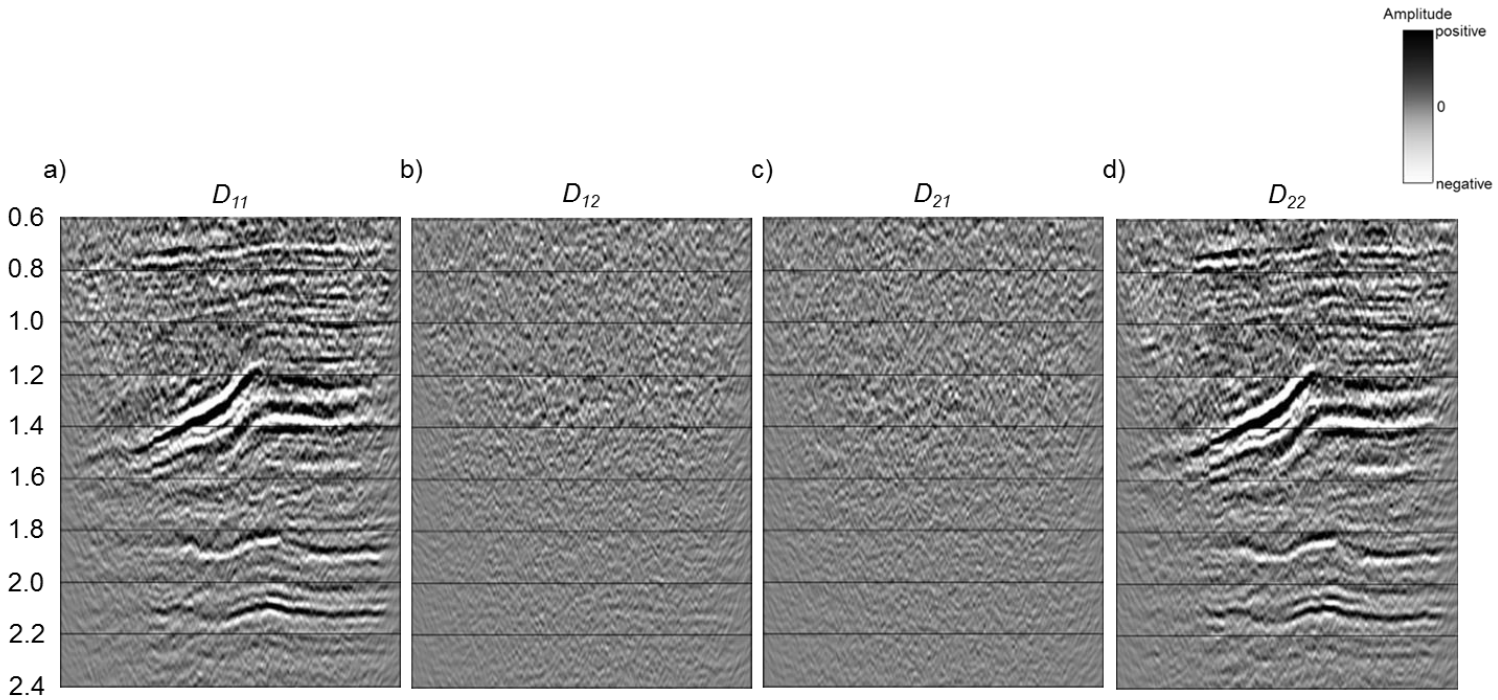

Figure 6.8: Vertical section A-A' through (a) D_{11} (b) D_{12}, (c) D_{21}, (d) D_{22} component seismic amplitude. (a) and (d) components display a similar image when stacked using the average picked velocity field. (b) and (c) show uncorrelated noise through the entire section, indicating that D11 and D22 are aligned with the principal axes of anisotropy which We interpret to be correlated with open fractures along the 22 direction. Note the increase in bandwidth in (a).

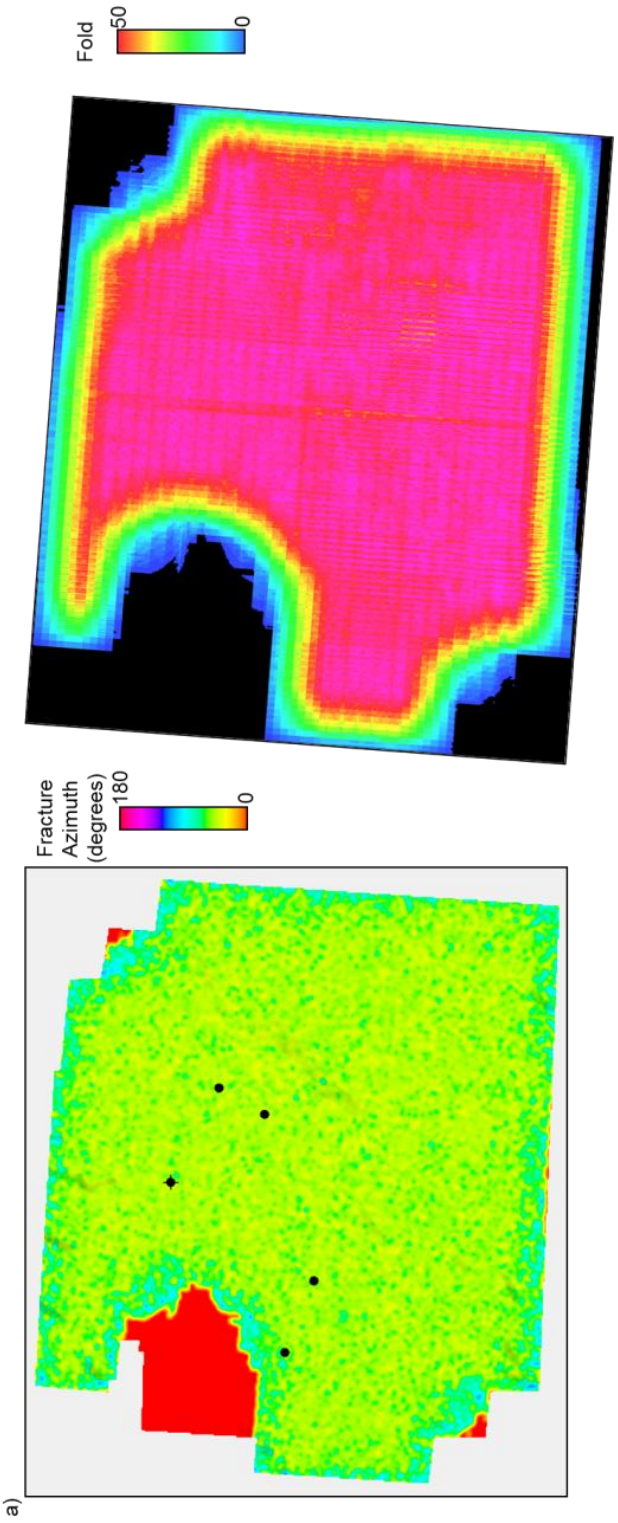
Fold
50
0
Fracture Azimuth (degrees)
180
0
a)

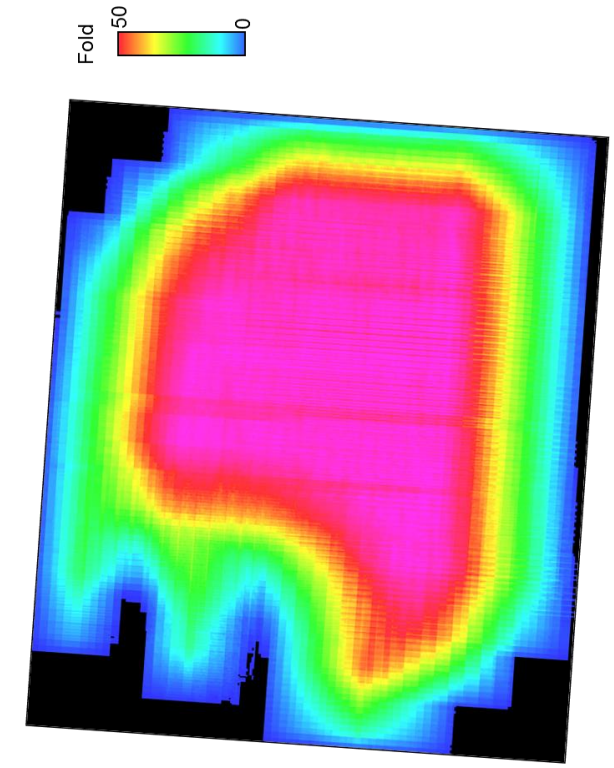

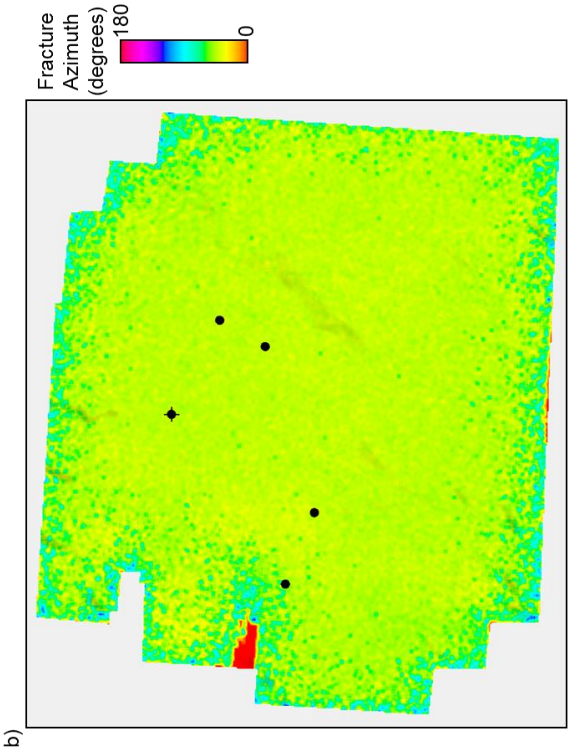

b)

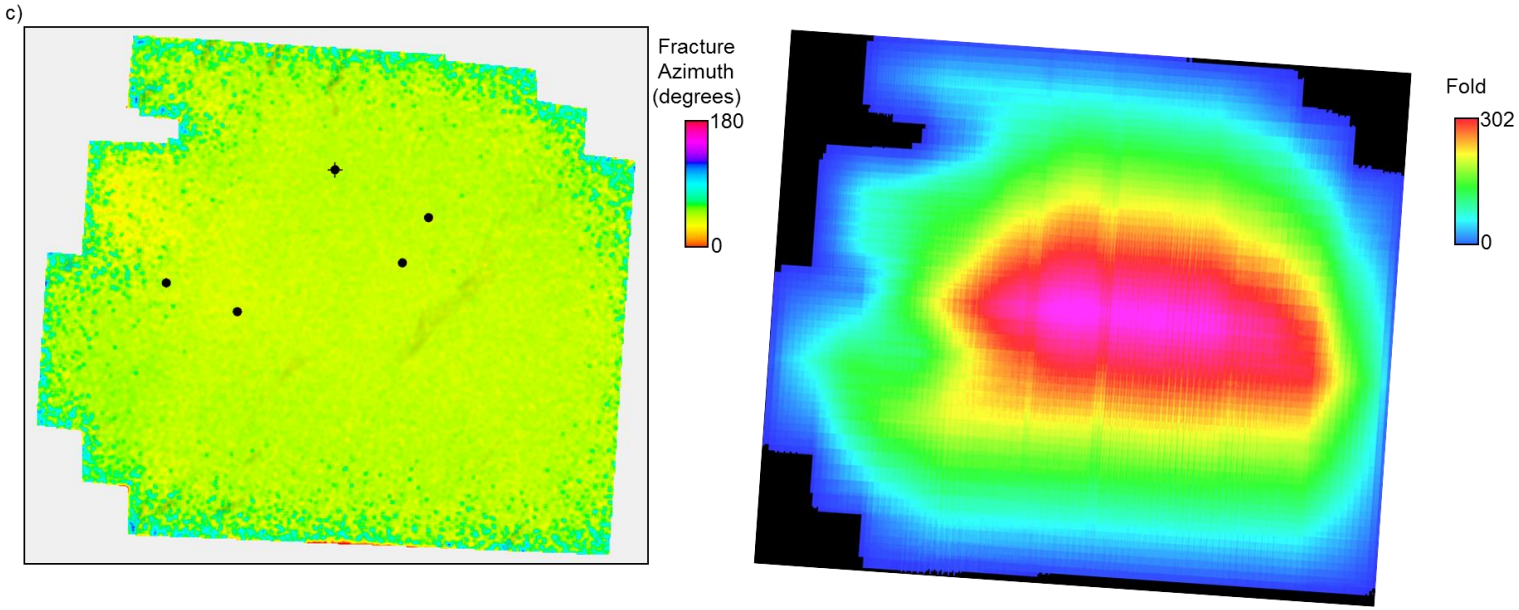

Figure 6.9: Alford anisotropy strike map for (a) near, (b) near-mid and (c) full offset range. The respective trace fold used for the anisotropy direction calculation is plotted on the side of the Alford fracture map. With increase of traces we observe a smoother strike calculation but we are also averaging over more complex travel paths. Since Alford rotation main assumption is that traces are zero offset we will use (a) as our estimate of fracture strike.

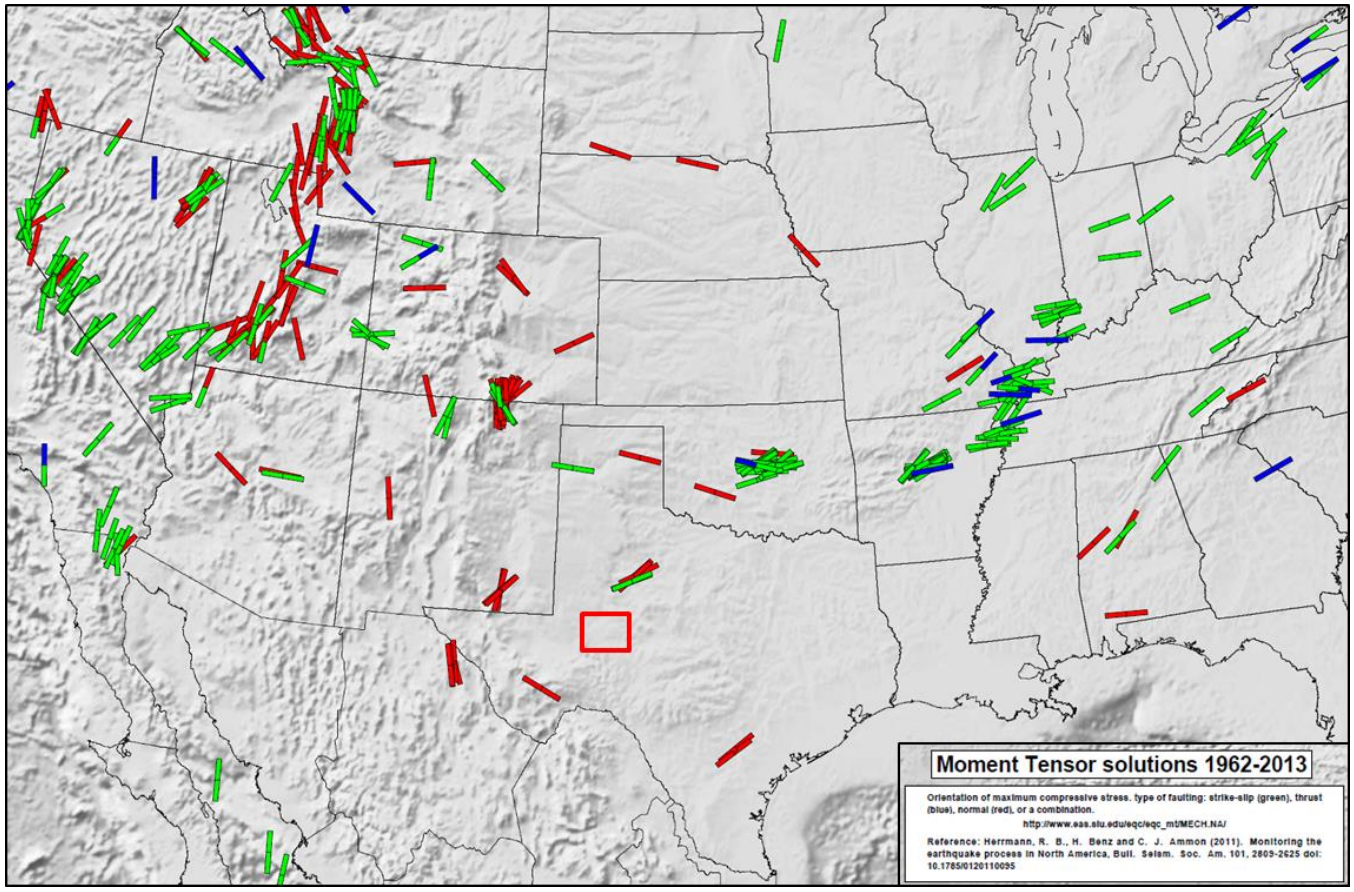

Figure 6.10: General stress direction for the state of Texas. The red square indicates the approximate location of the Diamond M field. The stress field for the area is about 60 degrees from north. Bar colors indicate the type of faulting: red, normal; blue, thrust, and green, strike-slip (Modified from Herrmann et al. 2011).

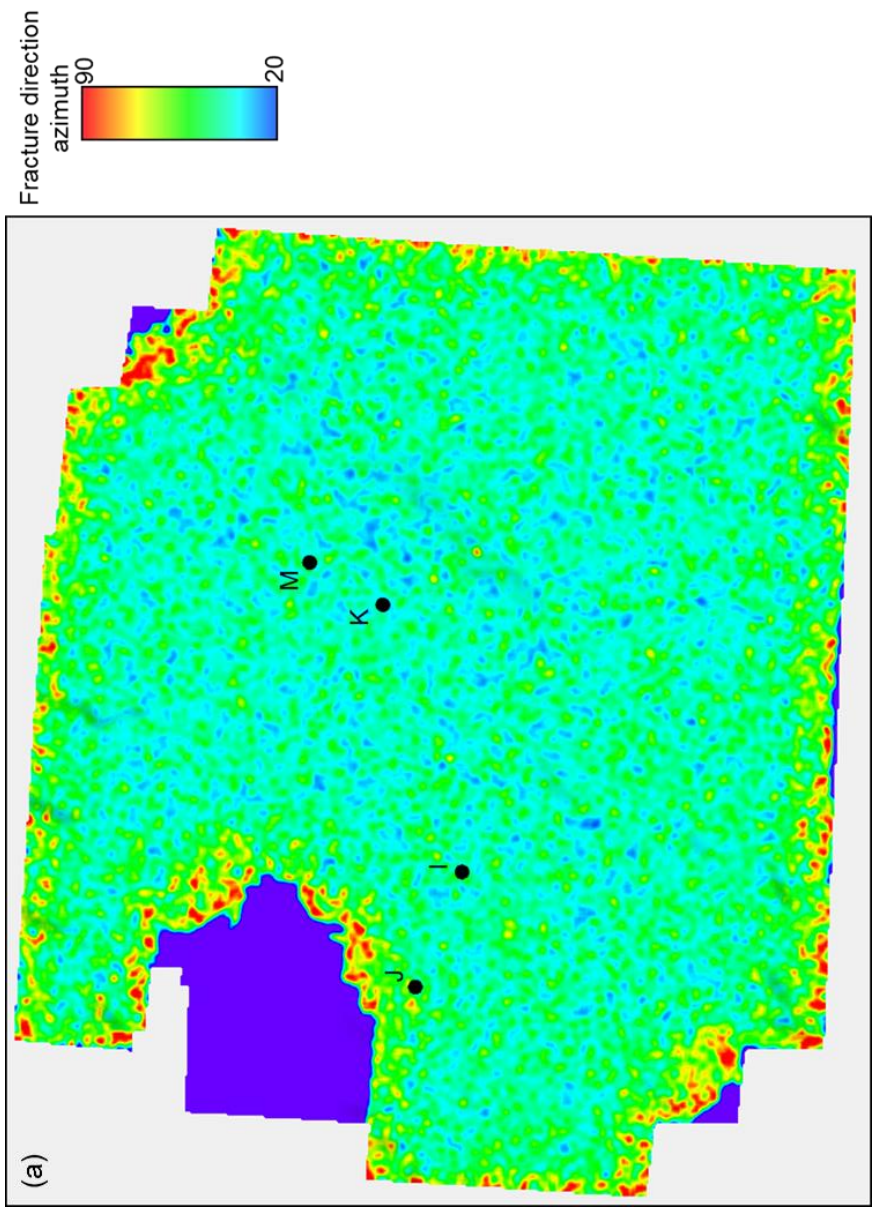
Fracture direction
azimuth
90
20
M
K
I
J
(a)

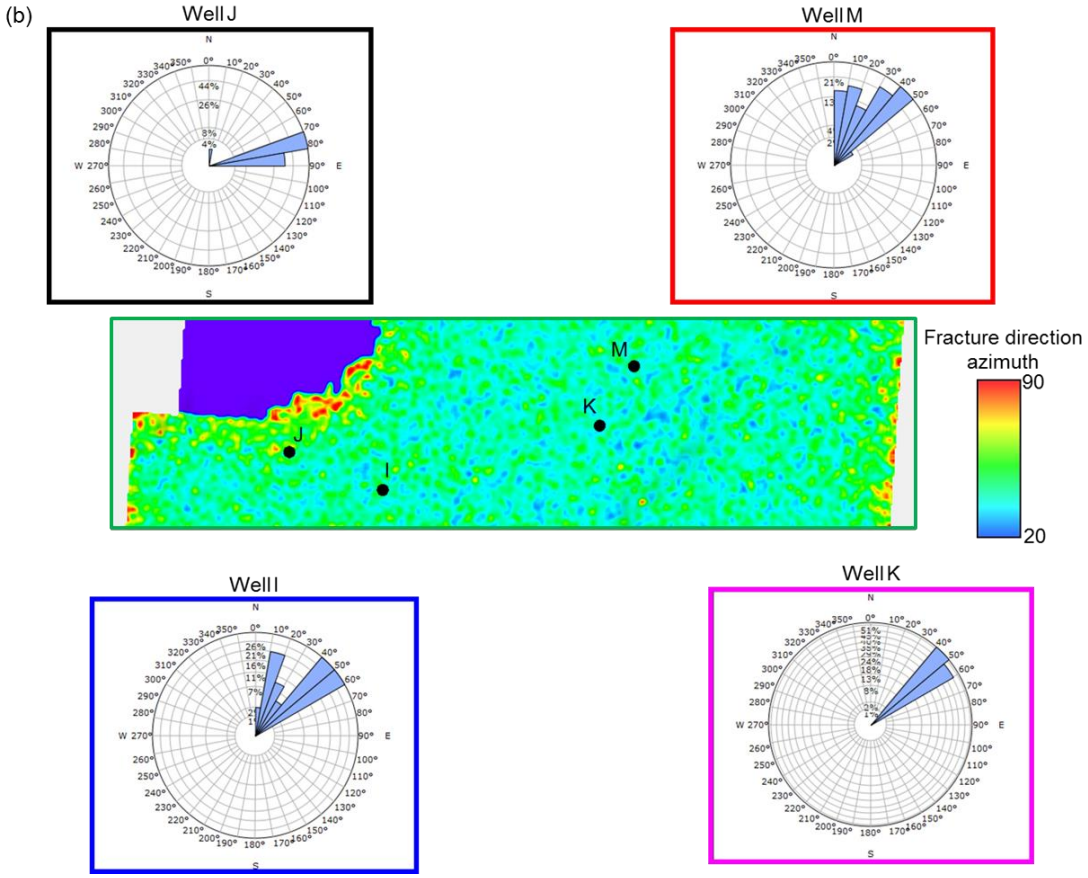

Figure 6.11: (a) Alford fracture strike map displaying azimuths between 20 and 90 degrees. From the histogram we interpret that the mean azimuth direction from derived from the seismic data is 50 degrees. This is showing a 10 degrees difference from the regional stress map shown in Figure 10. (b) Green box shows a zoomed section of the map in (a). We also display the fracture strike calculated from the dipole sonic logs on wells I, J, K, and M. The fracture strike calculated from the Alford rotation agrees with those calculated from the logs.

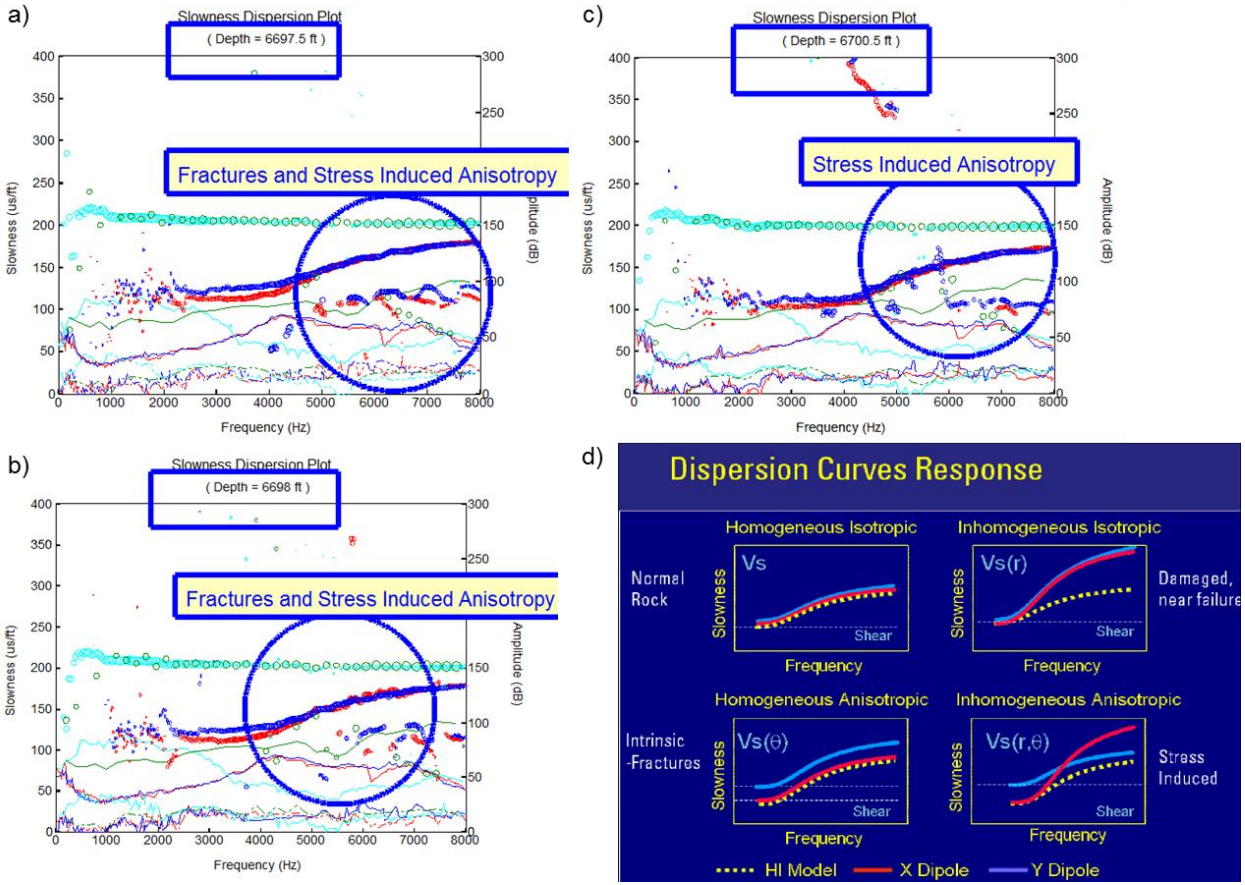

Figure 6.12: Full waveform dipole sonic slowness-frequency dispersion analysis plots for well M at (a) 6697.5 ft., (b) 6698.5 ft., and (c) 6700,5 ft. (d) Generic template for slowness-frequency dispersion curves interpretation (Wielemaker, et al., 2005). The reservoir interval in this well is between 6672 and 6836 ft.

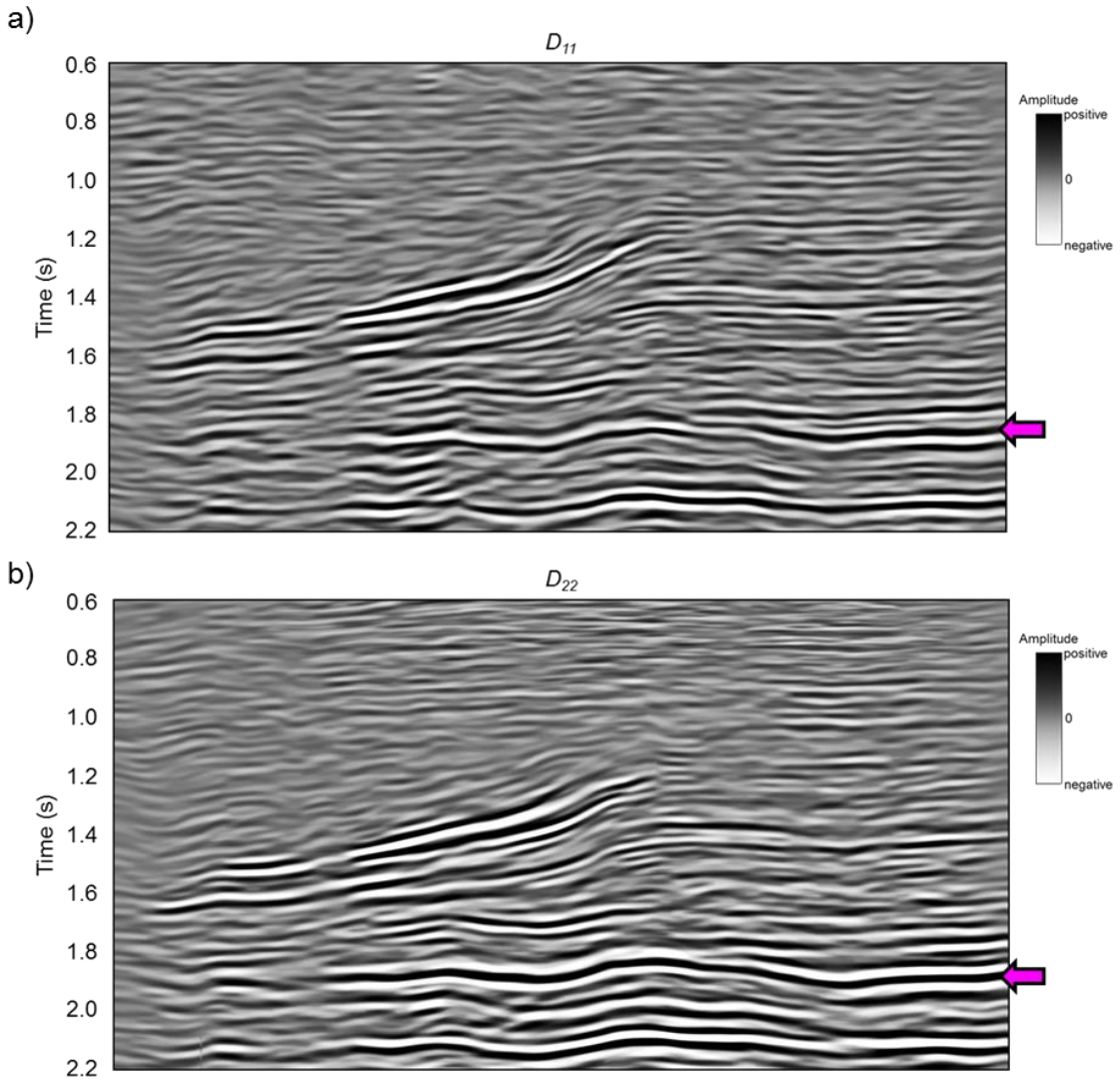

Figure 6.13: Cross-section AA' through (a) D_{11} and (b) D_{22} component after migration with their respective velocity fields. The improvement on the image compared to that of Figure 8 on D_{11} and D_{22} components is due to the improved velocities form migration and the aid of one pass of structure oriented filter on the pre-stack domain. Magenta arrows indicate the top of the Horseshoe Atoll horizon.

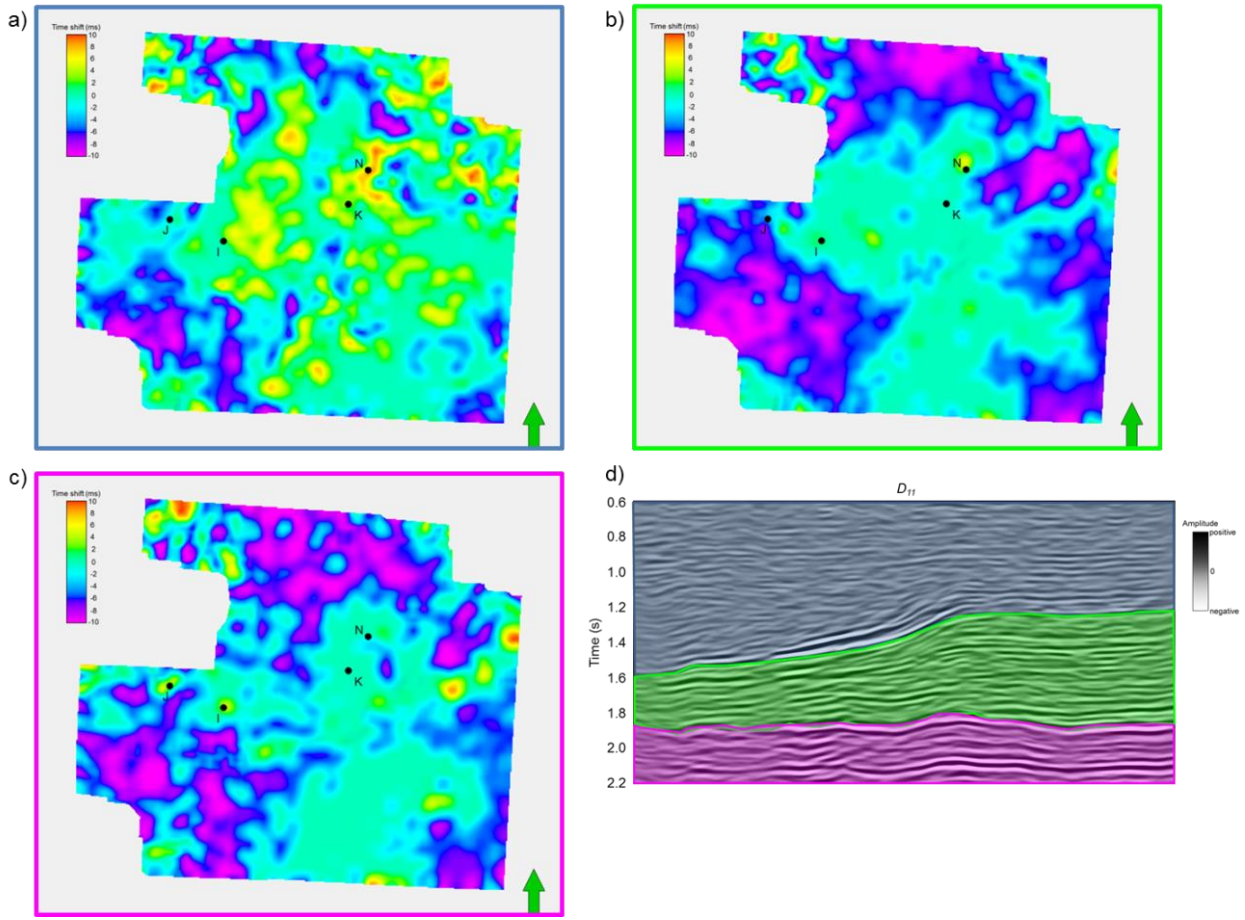

Figure 6.14: Time lag analysis results for (a) level 1, (b) level 2, and (c) level 3 between D_{11} and D_{22}. (d) Cross-section indicating the time windows used for each correlation level.

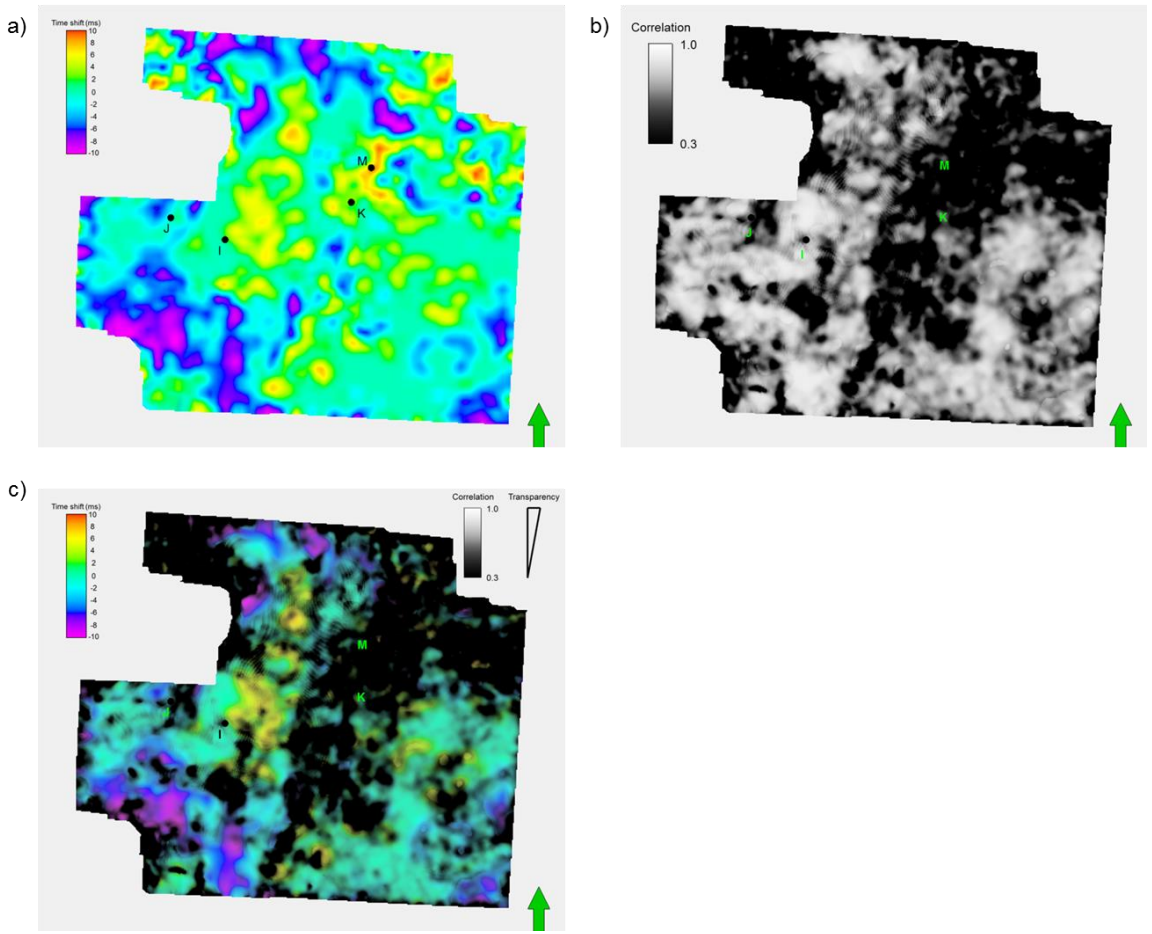

Figure 6.15: (a) Time lags between D_{11} and D_{22} for level 1 (Figure 14). (b) Correlation coefficients for the time lag analysis. (c) Time lag map correndered with the correlation analysis using transparency. We use the correlation coefficient as a quality measurement of the results in (a).

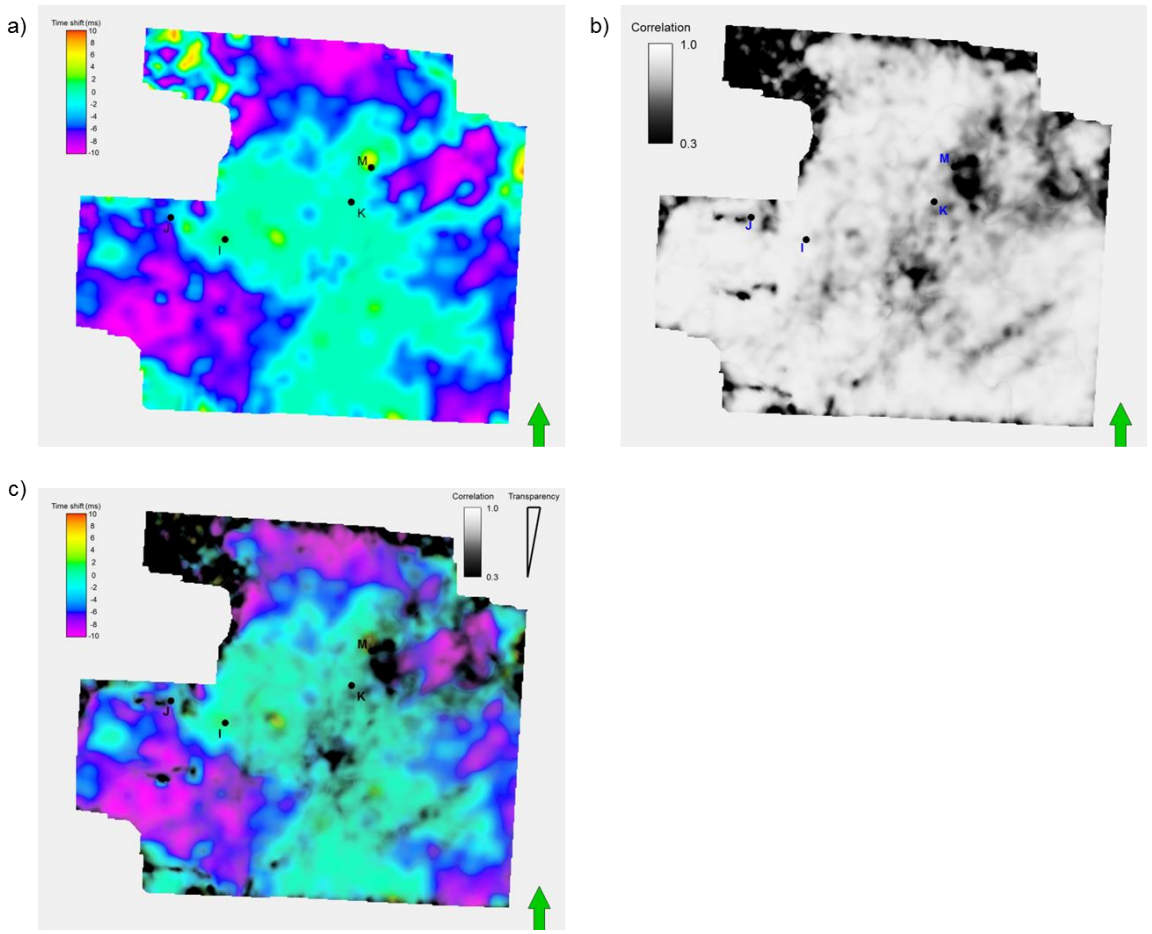

Figure 6.16: (a) Time lags between D_{11} and D_{22} for level 2 (Figure 14). (b) Correlation coefficients for the time lag analysis. (c) Time lag map correndered with the correlation analysis using transparency. We use the correlation coefficient as a quality measurement of the results in (a).

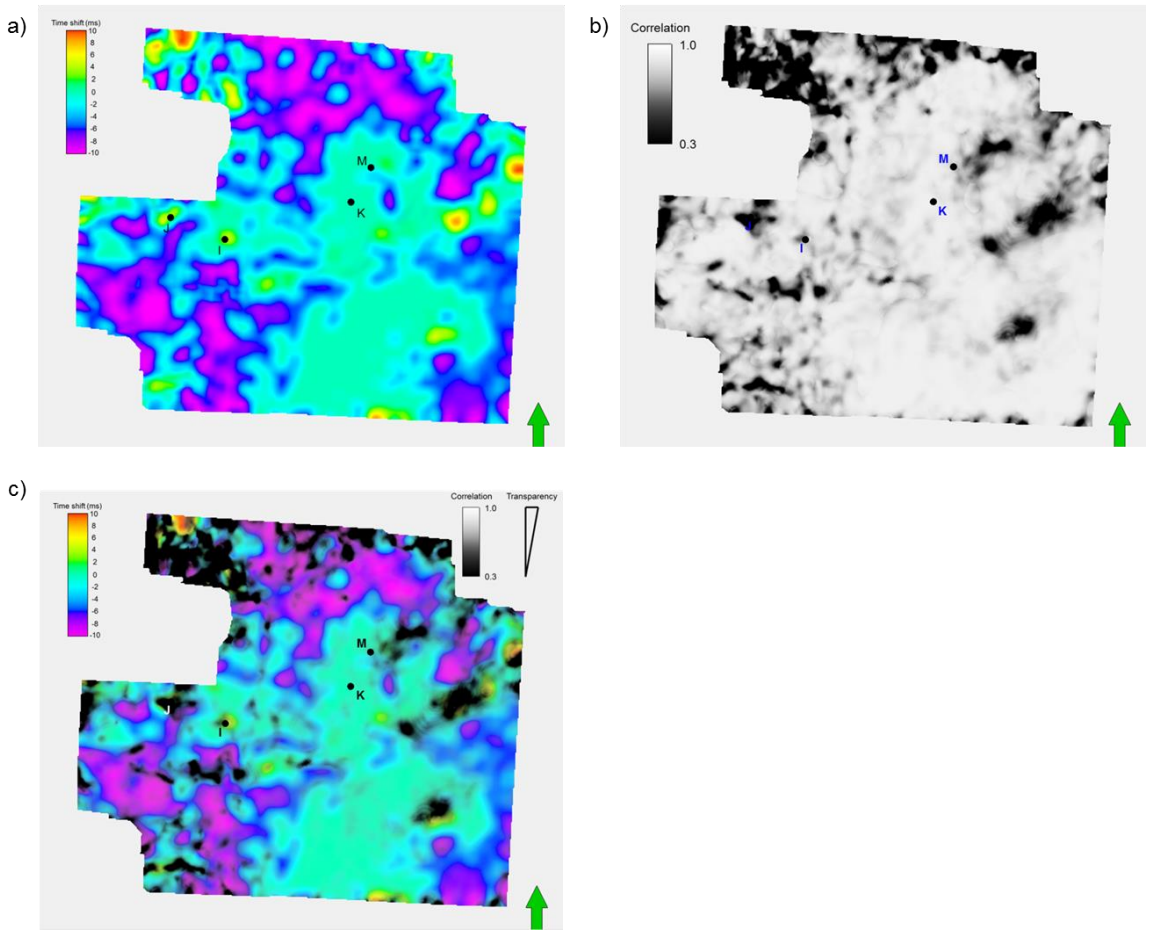

Figure 6.17: (a) Time lags between D_{11} and D_{22} for level 3 (Figure 14). (b) Correlation coefficients for the time lag analysis. (c) Time lag map correndered with the correlation analysis using transparency. We use the correlation coefficient as a quality measurement of the results in (a).

a)

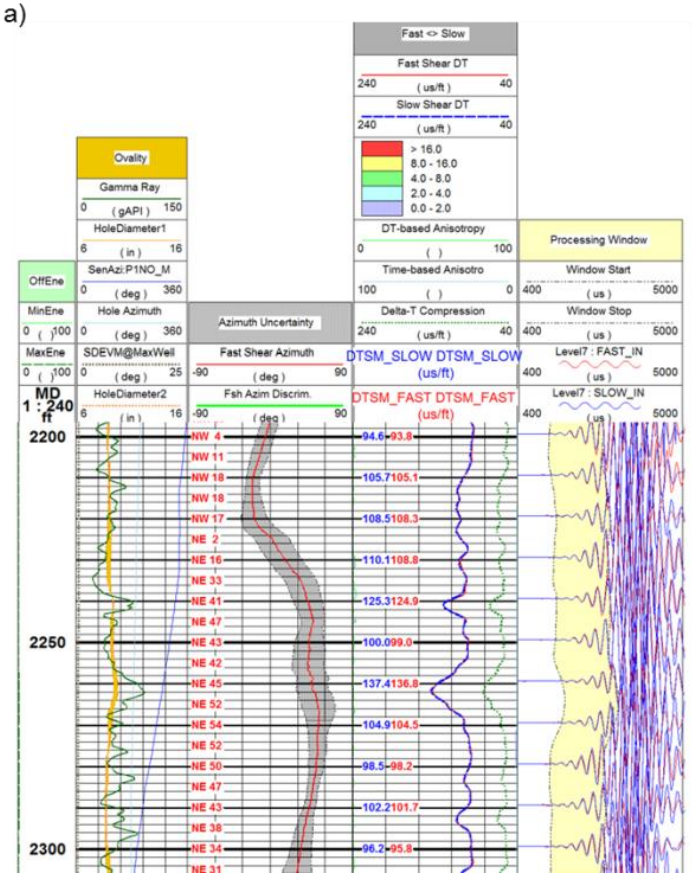
Fast <> Slow
Fast Shear DT
240 (us/ft) 40
Slow Shear DT
240 (us/ft) 40
> 16.0
8.0 - 16.0
4.0 - 8.0
2.0 - 4.0
0.0 - 2.0
Ovality
Gamma Ray
0 (gAPI) 150
HoleDiameter1
6 (in) 16
DT-based Anisotropy
0 ( ) 100
Processing Window
OffEne
SenAzi:P1NO_M
0 (deg) 360
Time-based Anisotro
100 ( ) 0
Window Start
400 (us) 5000
MinEne
Hole Azimuth
0 ( ) 100
0 (deg) 360
Azimuth Uncertainty
Delta-T Compression
240 (us/ft) 40
Window Stop
400 (us) 5000
MaxEne
SDEVM@MaxWell
0 ( ) 100
0 (deg) 25
Fast Shear Azimuth
-90 (deg) 90
DTSM_SLOW DTSM_SLOW (us/ft)
Level7 : FAST_IN
400 (us) 5000
MD 1 : 240 ft
HoleDiameter2
6 (in) 16
Fsh Azim Discrim.
-90 (deg) 90
DTSM_FAST DTSM_FAST (us/ft)
Level7 : SLOW_IN
400 (us) 5000
2200
2250
2300
NW 4
NW 11
NW 18
NW 18
NW 17
NE 2
NE 16
NE 33
NE 41
NE 47
NE 43
NE 42
NE 45
NE 52
NE 54
NE 52
NE 50
NE 47
NE 43
NE 38
NE 34
NE 31
94.6 93.8
105.7 105.1
108.5 108.3
110.1 108.8
125.3 124.9
100.0 99.0
137.4 136.8
104.9 104.5
98.5 98.2
102.2 101.7
96.2 95.8

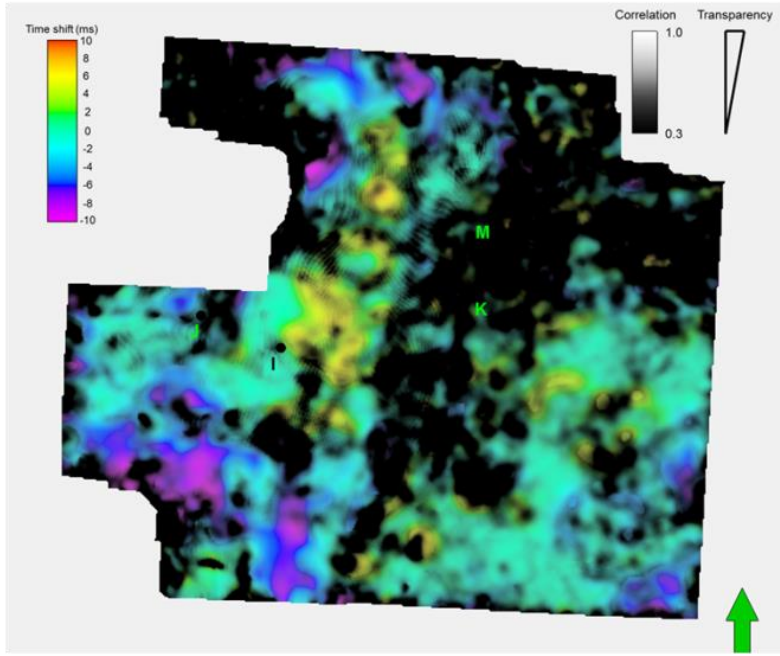
Time shift (ms)
10
8
6
4
2
0
-2
-4
-6
-8
-10
Correlation
1.0
0.3
Transparency
M
K
I
I

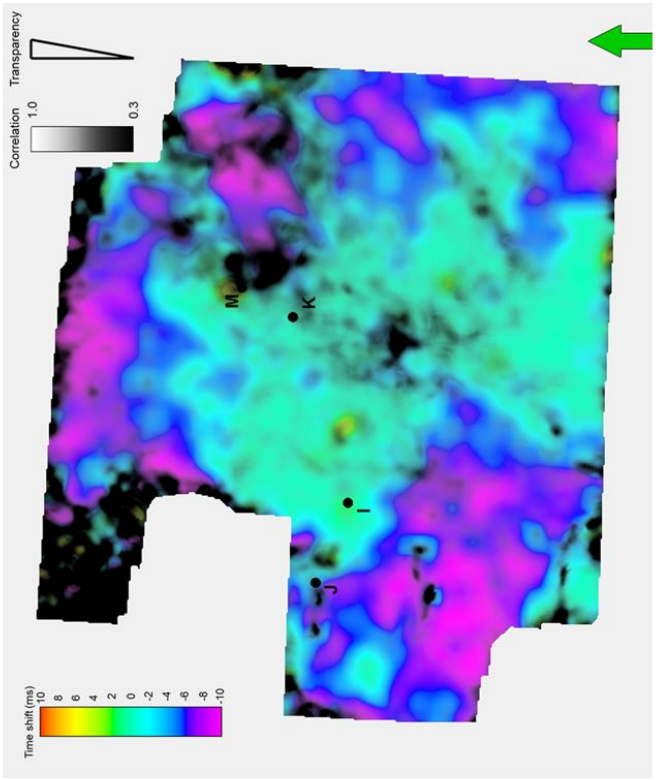
Correlation
1.0
0.3
Transparency
Time shift (ms)
10
8
6
4
2
0
-2
-4
-6
-8
-10
M
K
I
J

b)

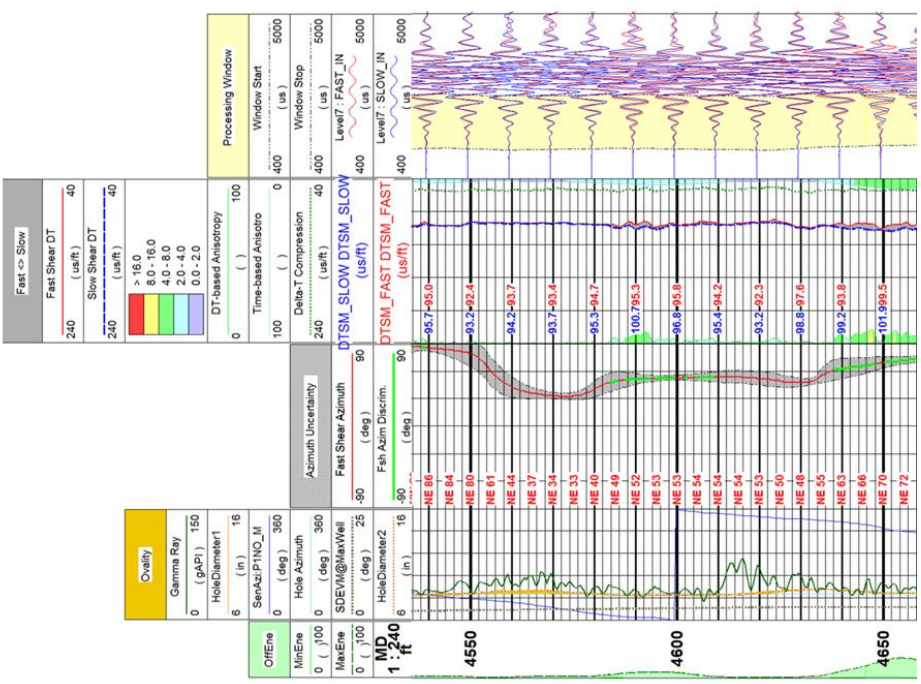
Fast <> Slow
Fast Shear DT
Slow Shear DT
DT-based Anisotropy
> 16.0
8.0 - 16.0
4.0 - 8.0
2.0 - 4.0
0.0 - 2.0
Processing Window
Time-based Anisotro
Window Start
Delta-T Compression
Window Stop
Azimuth Uncertainty
Fast Shear Azimuth
Fsh Azim Discrim.
DTSM_SLOW DTSM_SLOW
DTSM_FAST DTSM_FAST
Level7 : FAST_IN
Level7 : SLOW_IN
Quality
Gamma Ray
HoleDiameter1
SenAzi:P1NO_M
Hole Azimuth
SDEVM@MaxWell
HoleDiameter2
OffEne
MinEne
MaxEne
MD
1 : 240
ft
4550
4600
4650

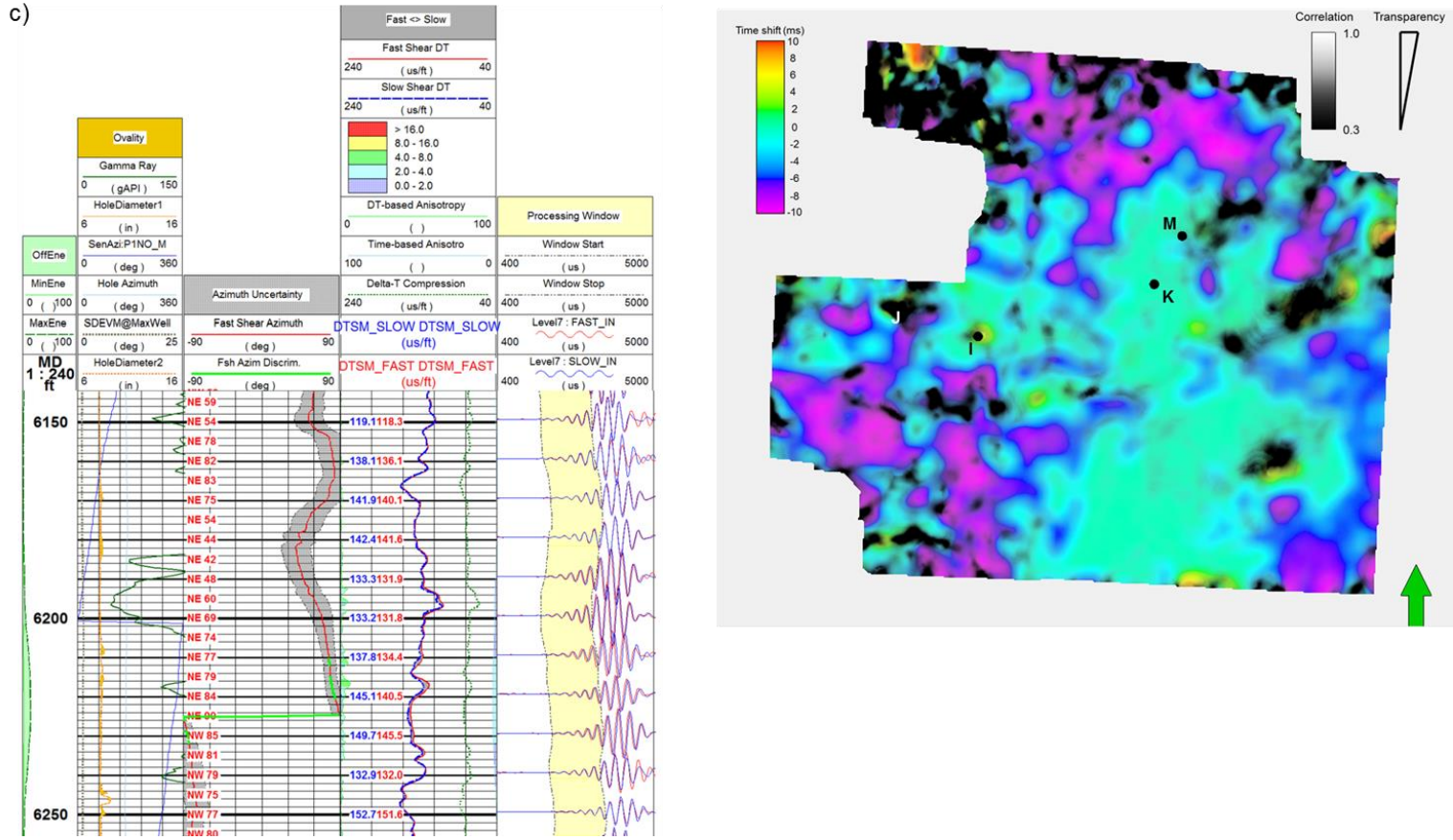

Figure 6.18: Comparison between log and seismic time lag differences for (a) level 1, (b) level 2, and (c) level 3. Although at different scales, we find that both measurements agree in the small amount of time differences between fast and slow shear.

REFERENCES

Alford, R.M., 1986, Shear data in the presence of azimuthal anisotropy: 56th SEG Annual International Meeting, Expanded Abstracts, 476–479.

Fisher, A. J., Predicting spatial distribution of critical pore types and their influence on reservoir quality, Canyon (Pennsylvanian) reef reservoir, Diamond M Field, Texas: Master's thesis, Texas A&M University.

Geaiser, J., P. Fowler, and A. Jackson, 1997, Challenges for 3-D converted wave processing: 67th SEG Annual International Meeting, Expanded Abstracts, 1199-1202.

Guliev, E. and R. Michelena, 2010, Inversion of converted PS data in the poststack domain for shear impedance: 80th SEG Annual International Meeting, Expanded Abstracts, 2789-2793.

Herrmann, R. B., H. Benz and C. J. Ammon, 2011, Monitoring the earthquake source process in North America: Bulletin of the Seismological Society of America, **101**, 2609-2625.

Knapp, S., S. Data, T. Medley, and B. Compani, 2002, Inversion of PP and PS multicomponent seismic volumes: A case history from the Gulf of Mexico: 72nd SEG Annual International Meeting, Expanded Abstracts, 1042-1044.

Shekar, B and I. Tsvankin, 2001, Estimation of shear-wave interval attenuation from mode-converted data: Geophysics, **76**, D11-D19.

Simmons, J., and M. Backus, 2001, Shear waves from 3-D-9-C seismic reflection data, Have we been looking for signal in all the wrong places?: The Leading Edge, **20**, 604-612.

Sondergeld C. and C. Rai, 1992, Laboratory observations of shear-wave propagation in anisotropic media: The Leading Edge, **11**, 38-43.

Taner, M. T., F. Koehler, and R. E. Sheriff, 1979, Complex seismic trace analysis: Geophysics, 44, 1041–1063.

Wielemaker, E., P. Saldungaray, M. Sanguinetti, T. Plona, and H. Yamamoto, 2005, Shear-wave anisotropy evaluation in Mexico's Cuilahuac field suing a new modular sonic tool: SPWLA 46th annual Logging Symposium.

7. Quantitative geophysical reservoir characterization at the Diamond M field, Texas

Oswaldo Davogustto[1], Kurt J. Marfurt[1] and Alison Small[2]

[1]University of Oklahoma, School of Geology and Geophysics

[2]Parallel Petroleum LLC

ABSTRACT

Diamond M field is one of several oil fields over the Horseshoe Atoll in the Midland Basin of Texas. Production began in the 1940s and continues through the present day with much of the focus on highly compartmentalized reservoir in the Cisco and Canyon formations. A recent infill drilling program has tagged previously unrecognized compartments and not only provided both core and a suite of modern logs but justified the acquisition of a wide azimuth surface "P-wave" seismic acquisition program as well as a 2C by 2C "S-wave" seismic acquisition programs.

We integrate these data at the core, well log, and surface seismic scale to map the carbonate buildup and diagenetically altered facies that form the reservoir. Through careful reprocessing of the 2C by 2C data into fast S_1 and slow S_2 shear wave volumes, we find a dominant NE-SW striking anisotropy at all levels of the data volume, consistent with the NE-SW trending maximum horizontal stress. We estimate fracture intensity by comparing time thickness maps of the reservoir from the S_1 and S_2 volumes as well as from the P-wave volume.

After reprocessing, the vertical resolution of the S_1 and S_2 volumes is comparable to that of the P-wave volume, but with a greater number of internal reservoir reflectors illuminated by S_1 and S_2, which we attribute to a greater variation in

shear wave impedance. Reprocessing of the P-wave data volume provided long offset data amenable to prestack inversion, providing high quality P-impedance, S-impedance, and density volumes. Using P-wave and dipole sonic logs as well as density and neutron-density porosity logs, we constructed a template to predict porosity from our surface seismic inversion.

Coherence volumes computed from the stacked data delineate the edges of carbonate buildups as well as internal low coherence anomalies which we interpret to indicate karsting seen in the nearby Reinecke Field. Volumetric estimates of shape delineate domes and ridges that show the structural control of the buildups. As in Reinecke Field, we anticipate that not all buildups have undergone the ideal length of subareal exposure to enhance and subsequently preserve porosity. We therefore cluster our two morphology attributes – coherence and shape, with the prestack inversion porosity and anisotropy intensity estimates to predict sweet spots to help prioritize subsequent infill drilling locations.

INTRODUCTION

P-wave derived attributes are routinely used in exploration and production of oil and gas with an overwhelming rate of success. P-wave data are most sensitive to changes in P-impedance, and with good quality, long offset acquisition, quite sensitive to changes in S-impedance and density. Despite this success there are cases when the P-wave data are insufficient to understand the behavior of a heterogeneous reservoir. Based on this thought several authors have demonstrated how combining P- and S-wave data can sometimes help reduce the uncertainty in the reservoir assessment. Pardus et al. (1990) demonstrate how the time differences between two know reflectors on P- and S-

wave data can be used to differentiate reservoir dolomite from non-reservoir limestone in Southern Michigan. The Pardus et al. (1990) technique is based on the relationship between the traveltime ratio $\Delta T_s/ \Delta T_p$ where ΔT_p and ΔT_s are the times required for the P- and S-wave to travel vertically through a defined stratigraphic interval of thickness ΔZ. This approach holds as long as the reflections between the interval times are exactly the same for both P- and S-wave data (Hardage et al., 2011). Garrota (1985) was able to identify porous from non-porous carbonates facies with the aid of a multicomponent VSP survey. Garrota (1985) found a difference in the V_s/V_p ratio of 20% between the two facies. Hardage et al. (2011) show that converted wave data can distinguish low-porosity carbonates from high porosity carbonates using a seismic facies analysis approach. Hardage et al. (2011) identify high amplitude sinuous anomalies in the P-SV RMS amplitude maps that correlate with the producing wells and that are not observed in the P-P RMS amplitude maps. Jianming et al. (2009) used estimates of anisotropy from wide-azimuth P-wave data and travel time thickness changes between P-S1 and P-S2 images to estimate fracture intensity in carbonate reservoir in Sichuan, China. They then combined these "quantitative" rock property estimates with more qualitative coherence and curvature geometric attributes that map structural deformation in a table that mimics that commonly used in risk analysis to predict fracture sweet spots.

Carbonates are characterized by high velocity, giving rise to relatively low vertical resolution. Carbonate on carbonate lithologies give rise to relatively low amplitude internal reflectivity. Finally, carbonate matrices are quite stiff, such that amplitudes are relatively insensitive to fluid content. In spite of all these difficulties,

seismic inversion to estimate porosity or to differentiate limestones from dolomites can be very successful in carbonate reservoirs (e.g. Tinker et al., 2004, Melville et al., 2004, Vahrenkamp et al., 2004, Pardus et al., 1990). Since porosity is a function of deposition and diagenesis, "softer" analysis workflows based on geologic processes can also be very effective. Pearson and Hart (2004) predict porosity in the Red River Formation through an understanding of depositional and post-depositional processes using property-prediction maps. Pearson and Hart (2004) base their study on the relationship among porosity thickness, spectral slope from peak to maximum frequency, and ratio of positive to negative samples. Pearson and Hart (2004) find that their predicted porosity is in agreement with the geological model for Red River Formation. Pranter et al. (2004) present an integrated approach to characterize the San Andres carbonate reservoir at the Vacuum field, NM. Pranter et al. (2004) develop techniques to identify heterogeneities in the San Andres Formation using stratigraphic, petrophysical and multicomponent seismic data. Neuhaus et al. (2004) perform a quantitative reservoir characterization study on the carbonate reservoir of Malanpaya field, Philippines. Neuhaus et al. (2004) use horizon extracted amplitudes to identify high porosity zones and optimize drilling success. Neuhaus et al. (2004) use variograms from log data and stochastic impedance inversion to generate a suite of multiple porosity scenarios to risk weight alternative development well locations.

Diamond-M Field in west Texas is one of several highly heterogeneous, but highly productive oil fields over the Horseshoe Atoll. A recent infill drilling program has justified the acquisition of modern 3D wide-azimuth P-wave and 2C by 2C S-wave seismic surveys, as well as core and dipole sonic logs in the newer wells. Our goal is to

use integrate these new data with historical production to high-grade targets for future infill drilling.

We begin our paper with a comparison between P- S_1- and S_2-wave volumes and estimate the amount of anisotropy present in the reservoir interval using the average thickness ratios between the top and base of our target zone. Using similarity and shape index attributes we describe the internal structure and confirm the depositional model for the Horseshoe Atoll at the Diamond M field. We then generate a template from our well logs that provides an accurate estimate of porosity from P-impedance, S-impedance, and density, which will then be used to compute a porosity volume from prestack P-impedance, S-impedance, and density inversion volumes. Finally we correlate the porosity model to production from 50 wells. We conclude with a discussion of assumptions and limitations for the workflows presented in this paper.

GEOLGICAL BACKGROUND

Our study is focused on Cisco and Canyon formations of the Horseshoe atoll in Midland Basin, Scurry County, TX (Figure 7.1). The carbonates of the Horseshoe Atoll formed during late Pennsylvanian to early Permian time when shallow water carbonate deposits dominated most of the deposition in the Permian Basin. The reservoir is classified as a carbonate buildup and is composed mostly of rich biomicritic rocks with some packstone and grainstone occurrences (Fisher, 2005). Using data from the nearby Reinecke field, TX (Figure 7.1), Saller et al. (2004) proposed that the Horseshoe Atoll formed in response to a sequence of sea level fluctuations. Saller et al. (2004) identify that sequence boundaries within the reservoir are characterized by soil and exposure related features. Saller et al. (2004) hypothesize that the relief of the Horseshoe Atoll at

the Reinecke field is due to differential growth of carbonate organisms, sub-aerial karstification and deep marine erosion. Figure 7.2 shows Saller et al.'s (2004) Horseshoe Atoll carbonate depositional model.

DATA DESCRIPTION

The Diamond M data set consists of approximately 25 mi^2 of multicomponent seismic data with a high signal to noise ratio located in Scurry County, TX. We have available for this study a multicomponent dataset consisting of a P-wave survey with 490 fold and frequencies between 5 and 96 Hz and a 2C by 2C S-wave survey with 302 fold per component with frequencies between 4 and 40 Hz. The survey has an azimuth of 3.64 degrees with respect to north. The P-wave data was processed using a conventional processing workflow to abate random noise and strong refraction events. A final step applied to the CDP gathers included a prestack structure oriented filtering and post-migration non-stretch NMO (Chapter 4) correction. The S-wave data was processed using a joint processing sequence for the four components of the dataset in order to avoid any amplitude alterations that would bias the Alford rotation process (Chapter 5). Then the components were Alford rotated to the inferred fracture strike, fast and slow velocity fields were estimated from the rotated data and the data were migrated using the refined velocity fields (Chapter 5).

TIME STRUCTURE MAPS AND ESTIMATED ANISOTROPY

We begin with a simple evaluation of the reservoir horizon based anisotropy using conventional seismic interpretation. Figure 7.3 shows a representative cross-section from the P-wave, the fast and the slow S-wave data. We will refer to the fast S-wave data as S_1 and to the slow S-wave data as S_2. We picked the top and the base of

the Horseshoe Atoll on the P-wave, S_1 and S_2 data. Figure 7.4 shows the synthetic well ties for the P-wave, S_1, and S_2 datasets. Figure 7.5 shows our time structure maps from the interpreted top and base of the Horseshoe Atoll. Next, we calculate the time isochron maps for the interpreted horizons (Figure 7.6). Then following the technique by Pardus et al. (1990) we calculated the ratios between S_1 and P-wave, S_2 and P-wave and S_1 and S_2 isochron maps. We find an estimated $\Delta T_{s1}/ \Delta T_p$ ratio of 1.8 on average and estimated shear wave anisotropy of 6% on average (Figure 7.7). The differences between S_1 and S_2 are a combination of the effect of fractures present in the reservoir and regional stress (Chapter 5).

GEOMETRIC ATTRIBUTE RESERVOIR DESCRIPTION

We computed volumetric shape index and curvedness (e.g. Bergbauer et al., 2003; Al-Dossary and Marfurt, 2006) and various coherence estimates from the P-wave volume. We take advantage of the shape index's detailed description of the geometric shape calculated at each point of the seismic volume and the Sobel filter similarity identification of discontinuities. Using shape index we confirm that the structural highs and lows in the time structure maps and seismic amplitude match those observed in the shape index attribute (Figure 7.8). Sobel filter similarity (Figure 7.9) time slices reveal several features that we interpret to be related to the internal growth of the Horseshoe Atoll carbonate as described by Saller et al (2004). In order to confirm our hypothesis we co-rendered the shape index attribute with the Sobel filter similarity. Using this joint interpretation we are able to map the dome and ridge shapes that correlate to "reef" buildups (Figure 7.10). Also we interpret the bowl shapes as zones that could have been

affected by karsting (Figure 7.10). This interpretation is in agreement with our hypothesized model.

INTEGRATION OF CORE, LOG DATA AND SEISMIC INVERSION DATA FOR POROSITY PREDICTION

For this study we had available 12 wells with log data in the study area. Of these wells, 2 had been cored and we have measured porosity, density, and acoustic velocities (V_p and V_s). We also have P- impedance, S-impedance and density seismic volumes derived from prestack seismic inversion. We wish to derive a 3D volumetric porosity estimate by combining the available core, log and seismic data.

Using this data we calculated P- and S-wave impedances, and V_p/V_s ratio. We then created cross-plots for the P-impedance, S-impedance, and the V_p/V_s ratio versus the measured porosity. We wish to identify any anomalies in the impedances that could relate to high porosity zones (Figure 7.11). Next, we generated P-impedance and S-impedance versus density cross-plots using the log data and find the similar trends to those we identified from the core measurements (Figure 7.12). The P-impedance and the S-impedance hold an inverse relationship with porosity and density. The linear character among impedances, density and porosity suggest that we can use a multi-linear regression model to predict porosity from seismic data based on the response of porosity based on its relationship to P-impedance, S-impedance and density (Table 7.1). Figure 7.13 shows the accuracy of our multi-linear regression porosity prediction from P-impedance, S-impedance and density logs. We then use this relationship to generate a porosity volume (Figure 7.14d) from the volumetric seismic inversion estimates of P-impedance, S-impedance and density (Figure 7.14a-c) In order to corroborate our

results we compare our model to that proposed by Hobson (1989) derived from log data. Note the similarity between Hobson's (1989) well-based high porosity streaks with our seismic inversion-based porosity streaks. Our porosity model also agrees with the porosity distribution model proposed by Saller et al. (2004) of Reinecke field where most of the porosity occurs in streaks resulting from sub-aerial exposure and meteoric diagenesis. Both of these processes helped preserve the intra-granular porosity by creating a framework resistant to compaction. Figure 7.15 shows a 3D analysis of the seismically derived porosity distribution at the Horseshoe Atoll in the Diamond M field.

CORRELATION OF ATTRIBUTES TO PRODUCTION DATA

The previous analysis of attributes allowed us to integrate the reservoir measurement at core and log to the seismic scale where we find that porosity is the main driver of the reservoir response to P-impedance, S-impedance and density. Our ultimate goal is to identify production sweet spots to help prioritize infill drilling locations and maximize reservoir performance. To achieve this goal we compare the production data from 50 wells with our horizon based anisotropy attributes (Figure 7.16). We also compared production with porosity threshold maps generated for the Horseshoe Atoll interval map (Figure 7.17 to Figure **7.19**). Figure 7.20 shows the percentage of porosity above 4% threshold map. White stars indicate potential drilling locations over undrilled areas that what we interpret to be porosity sweet spots.

CONCLUSIONS

Diamond M Field is representative of many west Texas carbonate oil fields that have seen 50-100 years of production. Relatively high oil prices, modern completion processes, and the potential to produce directly from source rock can justify reacquiring

3D seismic data using modern acquisition techniques. We were disappointed in our ability to map fracture sweet spots from shear wave splitting, although this finding was consistent with both core and dipole sonic measurements. In contrast, careful consideration of shear wave splitting resulted in S_1 and S_2 volumes that had vertical resolution (measured in ft) comparable to the more conventional P-wave volume. Furthermore, both well log synthetics and S1 and S2 seismic volumes show significantly greater internal reflectivity than on the P-wave synthetics and seismic data volume. This increased reflectivity has nothing to do with seismic data processing, but rather with the underlying geology and rock physics.

Geometric attributes are applied to post-stack data, require little special data preparation or skill to compute, and can effectively delineate major structural and stratigraphic features in a seismic volume. In the Diamond M survey we find that volumetric co-rendering Sobel filter similarity and shape index modulated by curvedness highlights structural domes and ridges not only along picked horizons but also between picked horizons, highlighting subtle carbonate buildups that may otherwise be overlooked.

The depositional model for the Horseshoe consists of diagenetically altered high porosity streaks in an otherwise low porosity matrix that occurred when structurally high buildups were subareally exposed. Core and log measures show an excellent correlation of porosity to a linear combination of P-impedance, S-impedance and density. Using this transform template, we generated volumetric estimates of porosity from our volumetric P-impedance, S-impedance and density prestack inversion volumes which allow us to map high porosity streaks within the reservoir. Core and log analysis

shows that production is correlated to porosities exceeding a threshold of 4%. We therefore compute net porosity exceeding 4% map of the reservoir and found a good visual correlation with historic production. Unfortunately, we neither find nor expect a strong quantitative correlation with production due to the evolution of completion processes over the past 60 years. Nevertheless we use these threshold maps to high grade future infill drilling locations that exhibit dome and ridge shape, high net porosity, and low coherence streak sweet spots.

ACKNOWLEDGEMENTS

Interpretation and integration was done using Petrel, inversion using Strata, Multi-linear analysis using Transform, and log analysis using Techlog. We thank Parallel Petroleum LLC for providing a license to the Diamond M dataset. We thank Schlumberger for donating Petrel and Techlog Software for use in research and education. We thank CGG Veritas for donating Hampsson-Russell Software for use in research and education. We thank DrillingInfo for donating Transform Software for use in research and education Finally we would like to thank Andrea Miceli, Steve Roche, and Carl Sondergeld, for their help and support. The computing for this project was performed at the OU Supercomputing Center for Education & Research (OSCER) at the University of Oklahoma (OU).

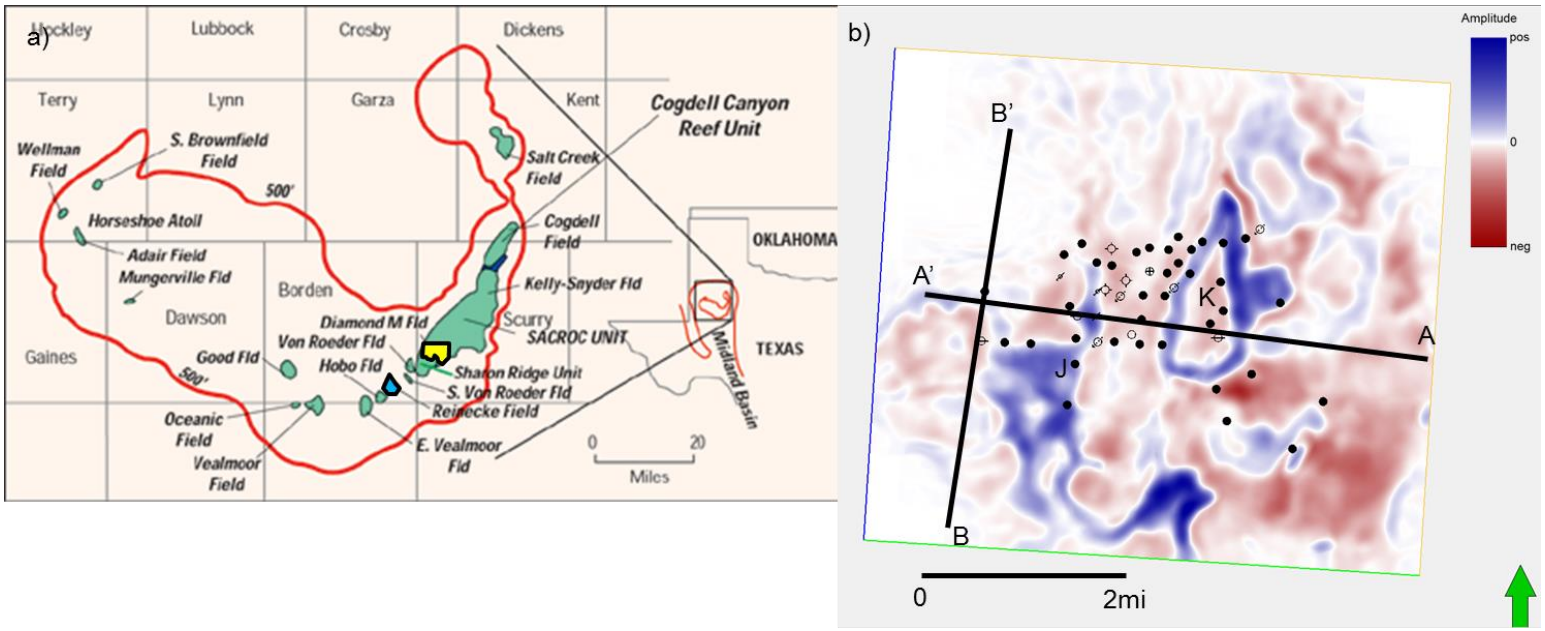

Figure 7.1: (a) Map displaying the location of the Diamond M field in Scurry County, Texas (Modified from Pennel and Melzer, 2003). Yellow polygon indicates the location of the Diamond M field. Blue polygon indicates the location of the Reinecke field. Red line indicates the outline of the Horseshoe Atoll. (b) Time structure map of the Horseshoe Atoll indicating lines AA', BB' and the location of wells with production data available. K is the well used to generate the well synthetic seismograms. J is the cored well. North is indicated by the green arrow.

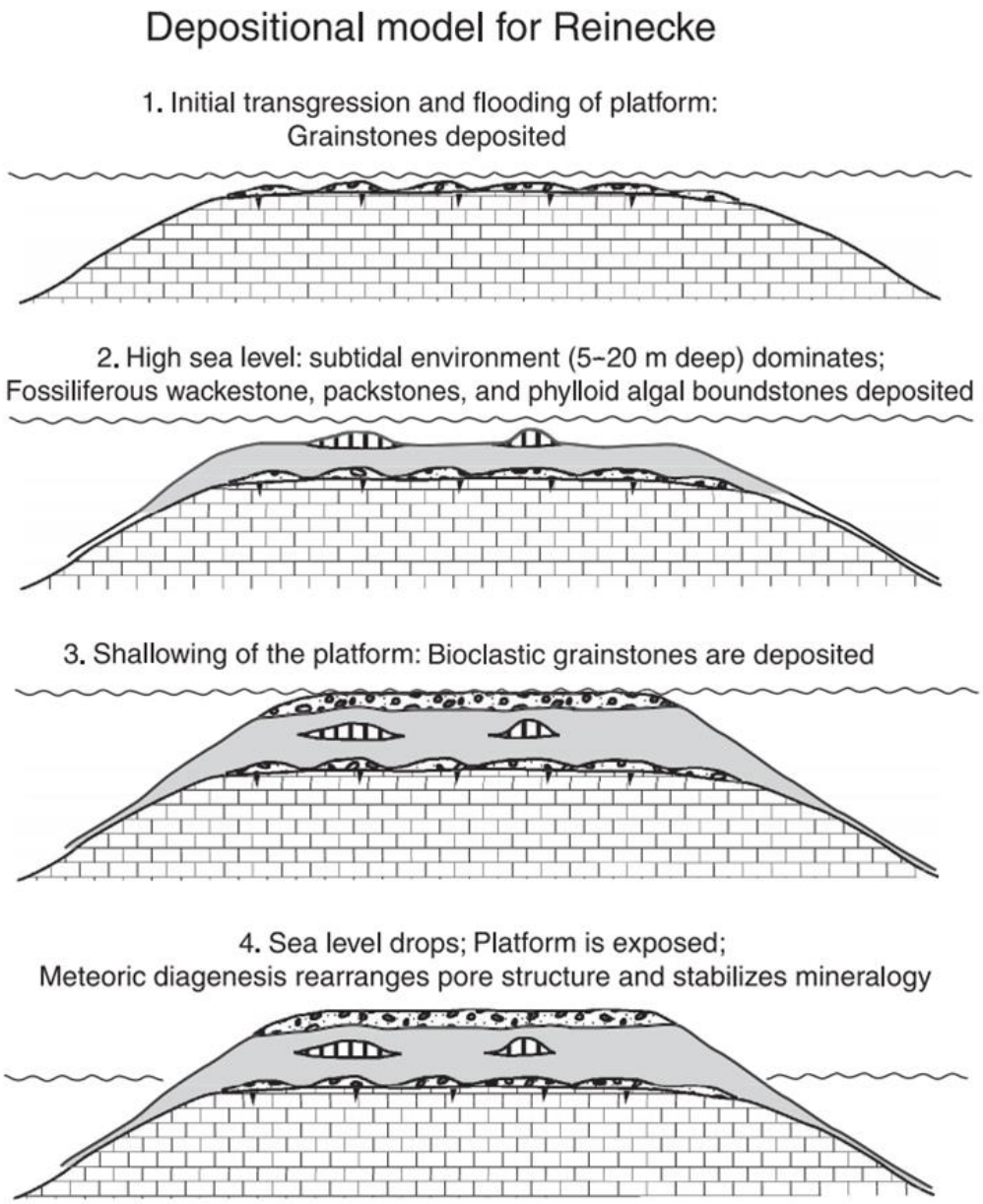

Figure 7.2: Depositional history of model for the Reinecke field (after Saller et al., 2004). Reinecke field is located approximately 20 miles south west of the Diamond M field. Exposure and drowning of the Horseshoe Atoll allowed the development of porosity in several episodes followed by "tight" streaks.


a)
A
A'
0.5
0.6
0.7
0.8
0.9
1.0
1.1
1.2
Time (s)
+
-

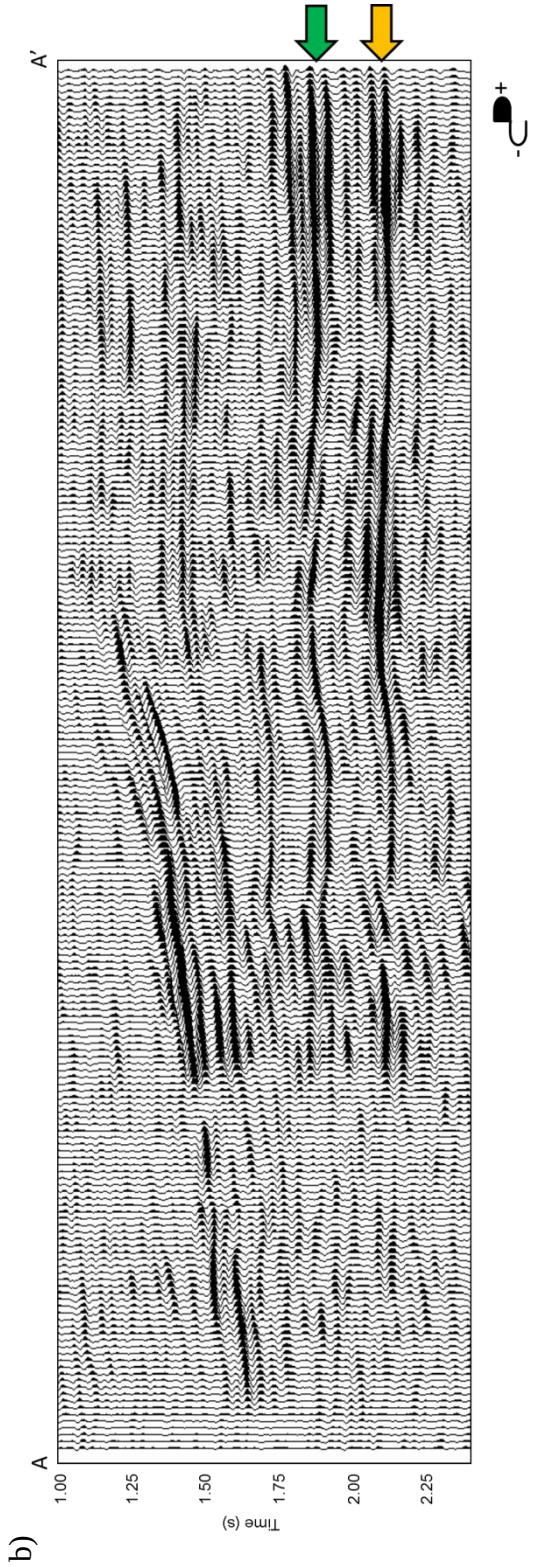
b)
A
A'
1.00
1.25
1.50
1.75
2.00
2.25
Time (s)
+
-

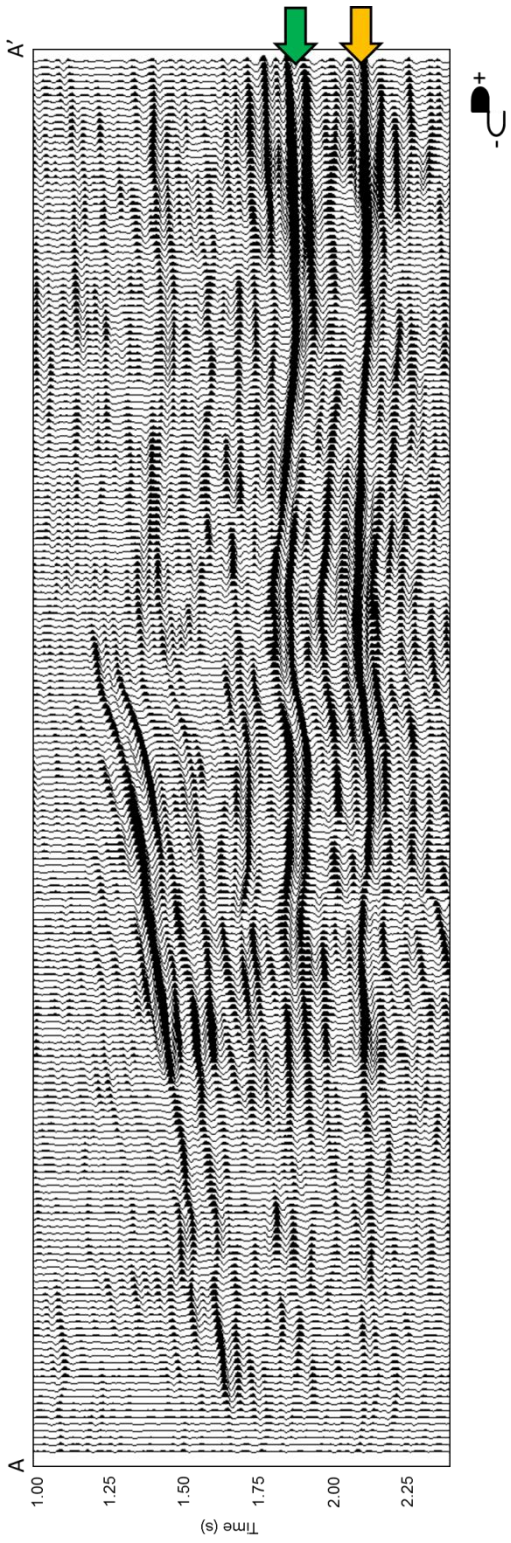
A'
A
+
-
1.00
1.25
1.50
1.75
2.00
2.25
Time (s)

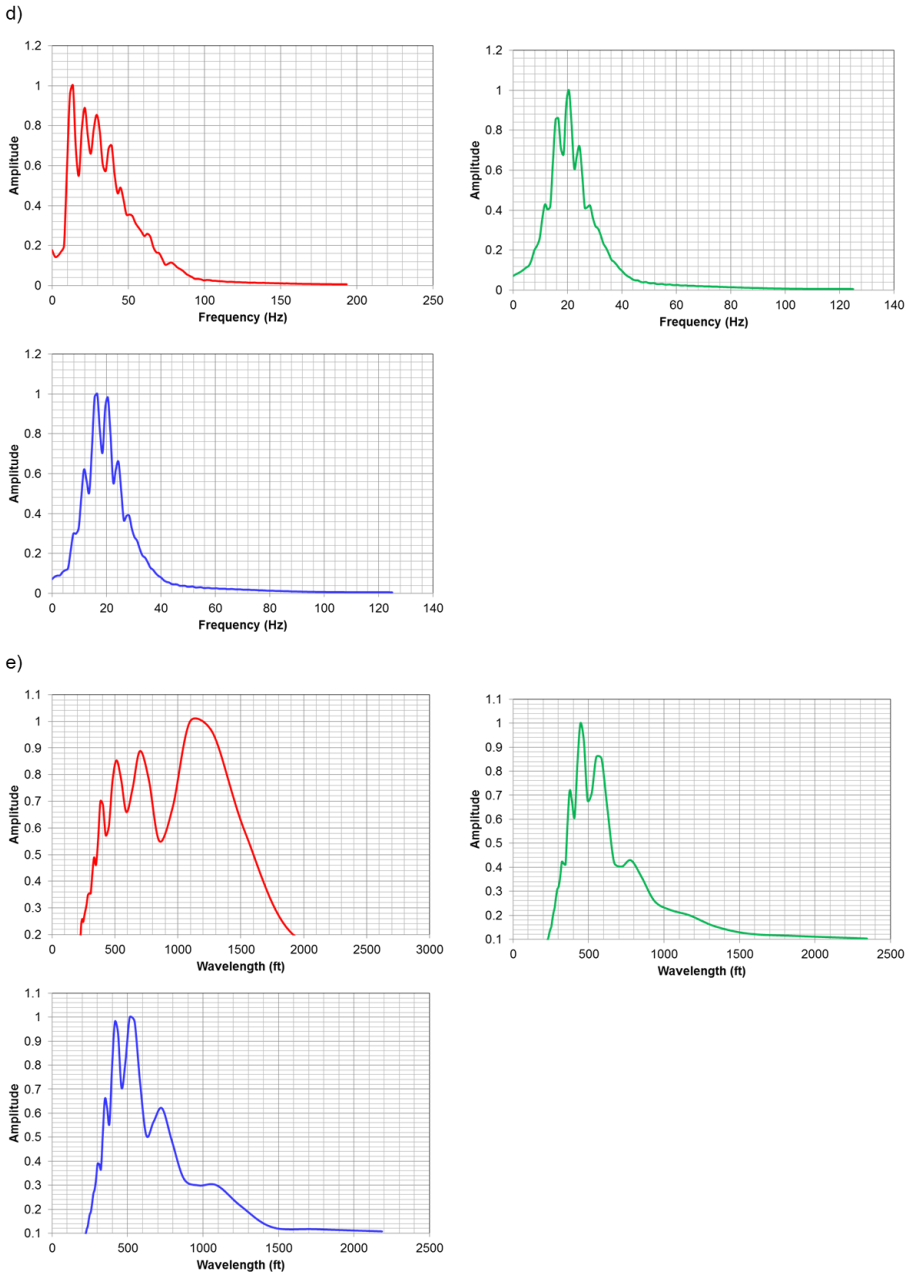

Figure 7.3: Vertical section A-A' through (a) P-wave data, (b) S_1 data and (c) S_2 data. (d) Amplitude spectra for P (red), S_1 (green), and S_2 (blue) data.(e) Amplitude spectra as a function of wavelength for P (red), S_1 (green), and S_2 (blue) data. (a-c) Green arrows indicate the top of the Horseshoe Atoll reservoir. Orange arrows indicate the interpreted base of the Horseshoe Atoll. Although the three vertical sections are similar it is important to notice that the shear data has a better response to the internal reflectors of the Horseshoe Atoll. (d -e) P data amplitude spectra spans 3 octaves. S_1 and S_2 data span two octaves. Although showing the same bandwidth, S_1 data shows higher frequency content than S_2 data. Location of line shown in Figure 7.1b.

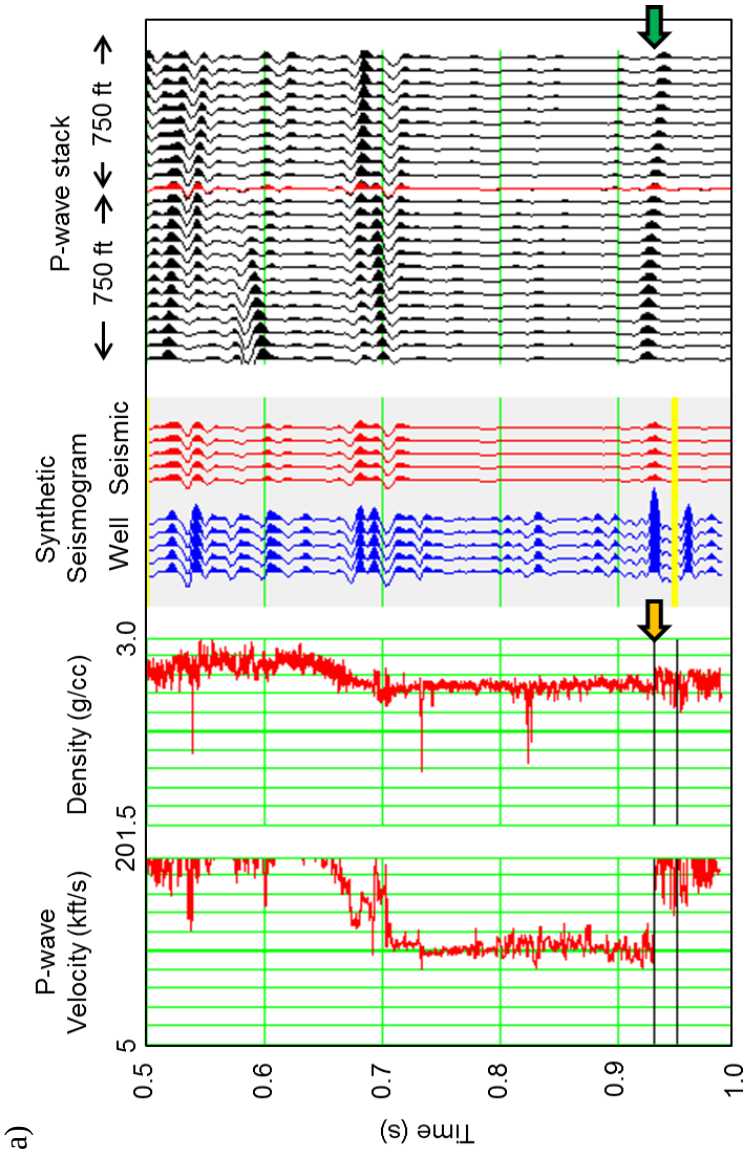
a)
P-wave stack
750 ft
750 ft
Synthetic
Seismogram
Well Seismic
Density (g/cc)
3.0
2
1.5
P-wave
Velocity (kft/s)
5
0.5
0.6
0.7
0.8
0.9
1.0
Time (s)

b)

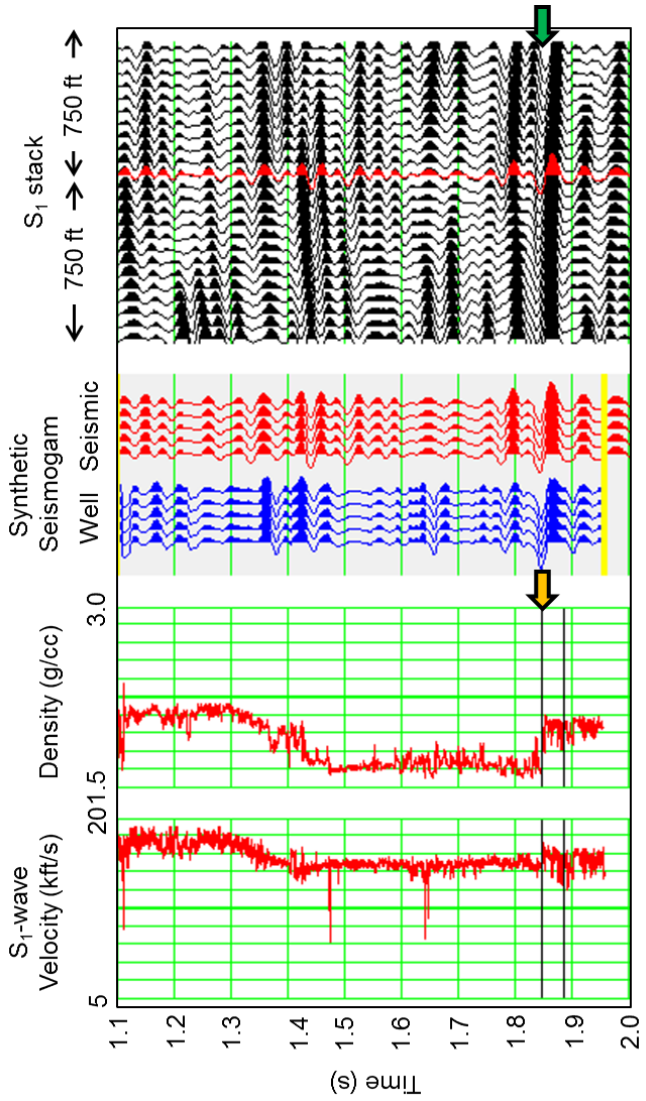
S1 stack
← 750 ft → ← 750 ft →
Synthetic Seismogam
Well Seismic
Density (g/cc)
2
1.5
3.0
S1-wave Velocity (kft/s)
5
1.1
1.2
1.3
1.4
1.5
1.6
1.7
1.8
1.9
2.0
Time (s)

c)

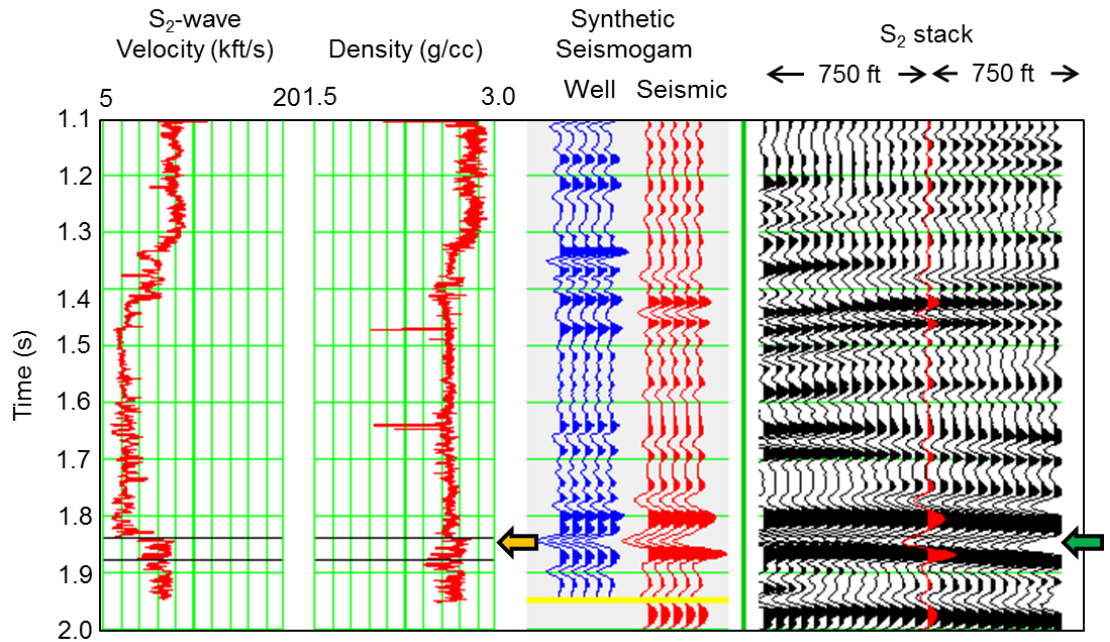

Figure 7.4: Well K synthetic seismograms for (a) P-wave, (b) S_1 and (c) S_2 stacks. The correlation for the P data was done using a 500 ms time window. The correlations for the S_1 and S_2 data were done using a 900 ms window. The correlation coefficients are 0.82, 0.65 and 0.62 for the P-wave, S_1, S_2 data respectively. Green arrow indicates the top of the Horseshoe Atoll reflector for the seismic data. Orange arrow top of the Horseshoe Atoll for the well logs.

a)

Top Horseshoe Atoll

Base Horseshoe Atoll

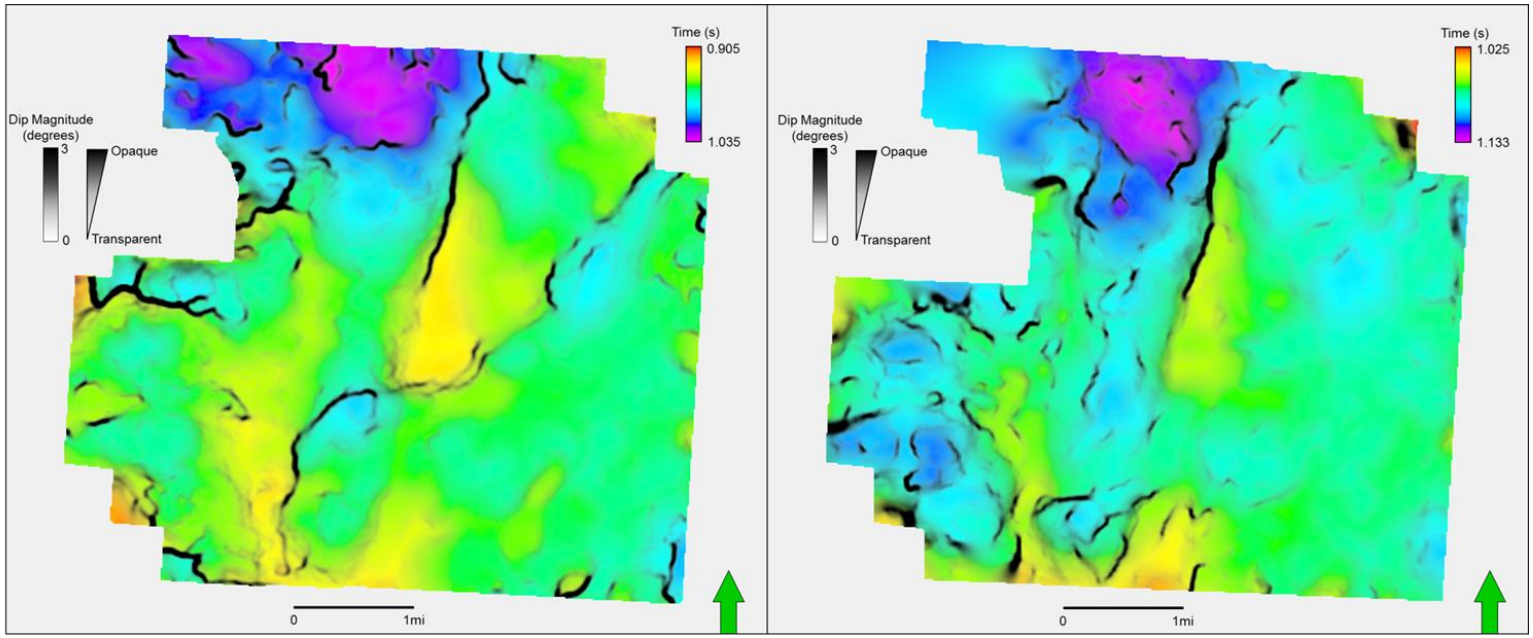

b)

Top Horseshoe Atoll

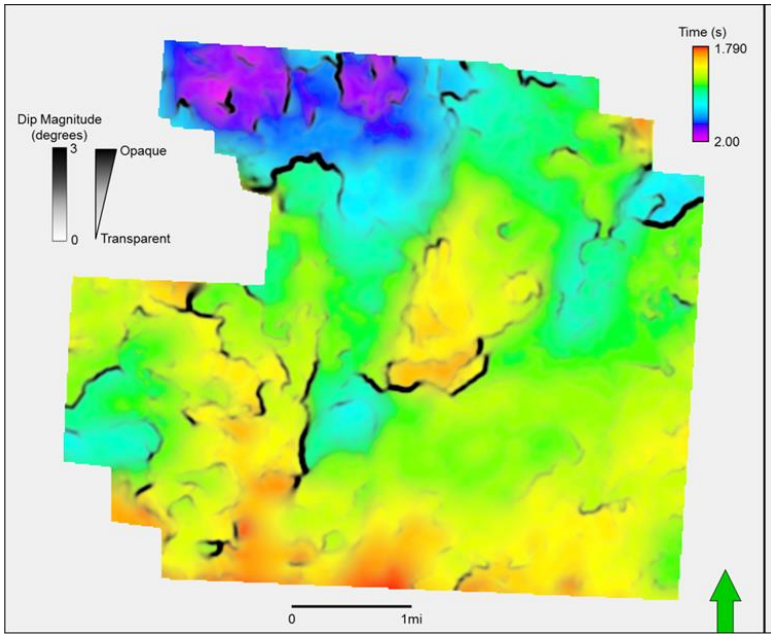

Base Horseshoe Atoll

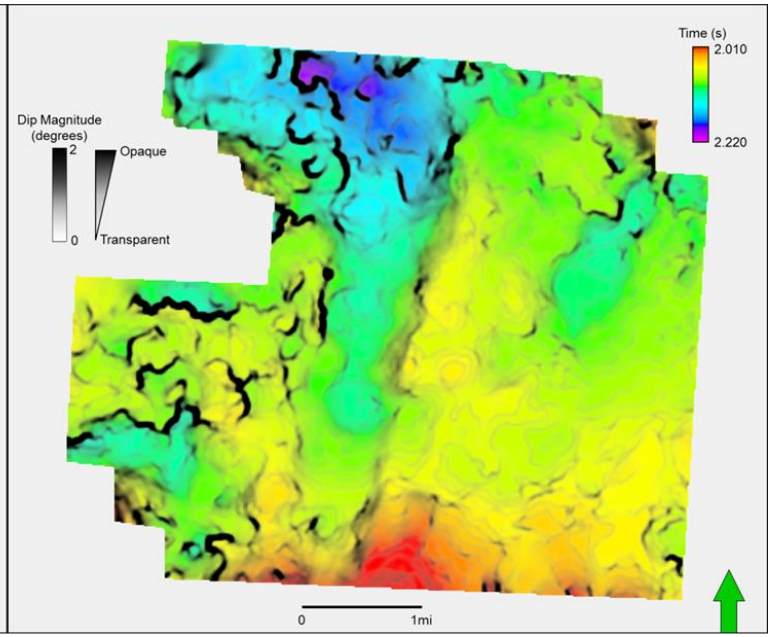

c)

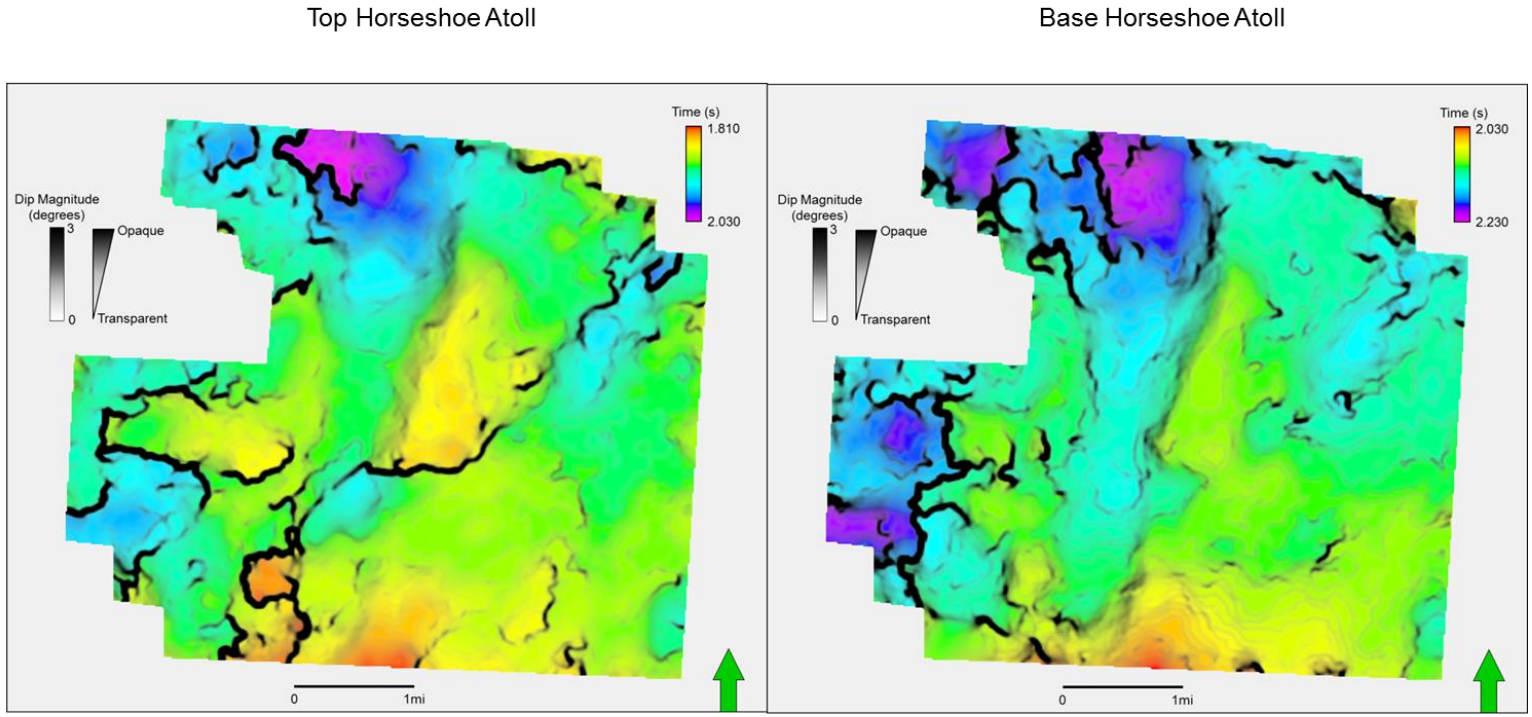

Figure 7.5: Time structure map of the top Horseshoe Atoll top (left) and base (right) for (a) P-wave, (b) S1, and (c) S2 data correndered with their respective horizon based dip magnitude. Although the maps share the same trend we observe differences that could relate to illumination differences depending on the type of data.

a)

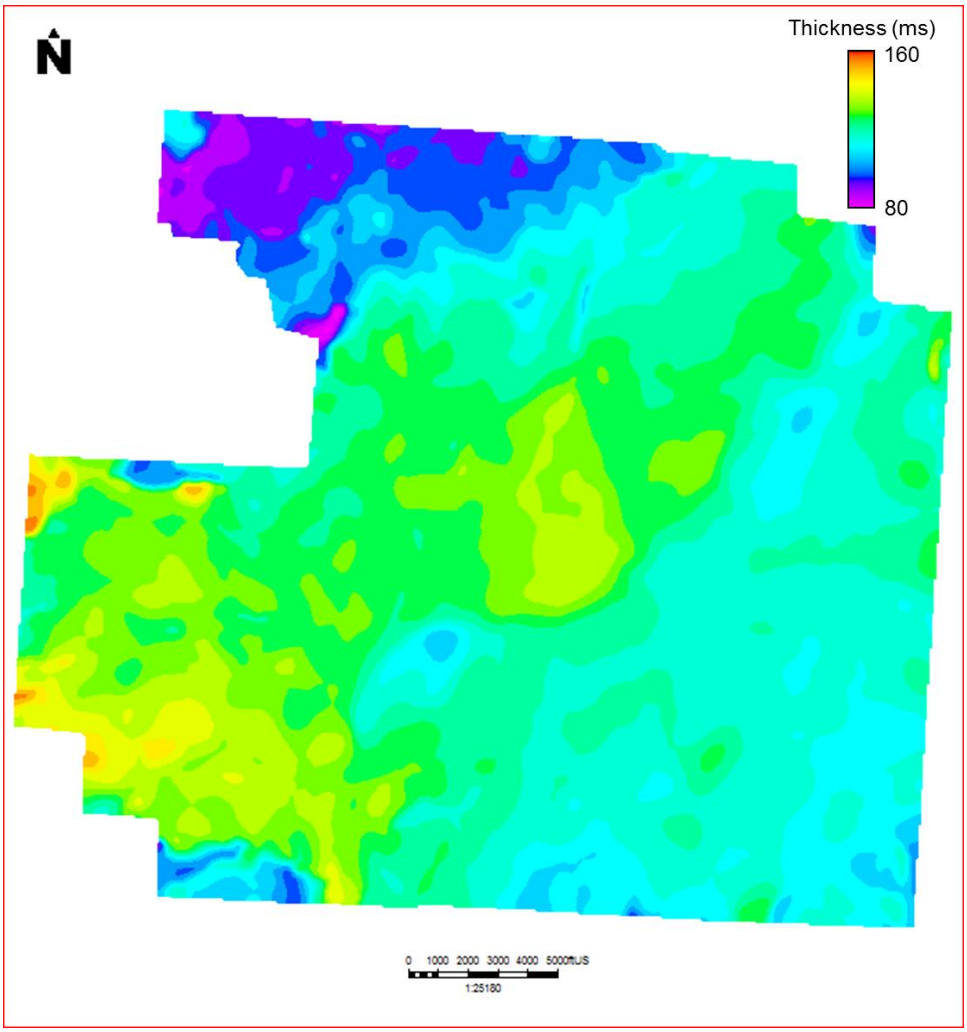

b)

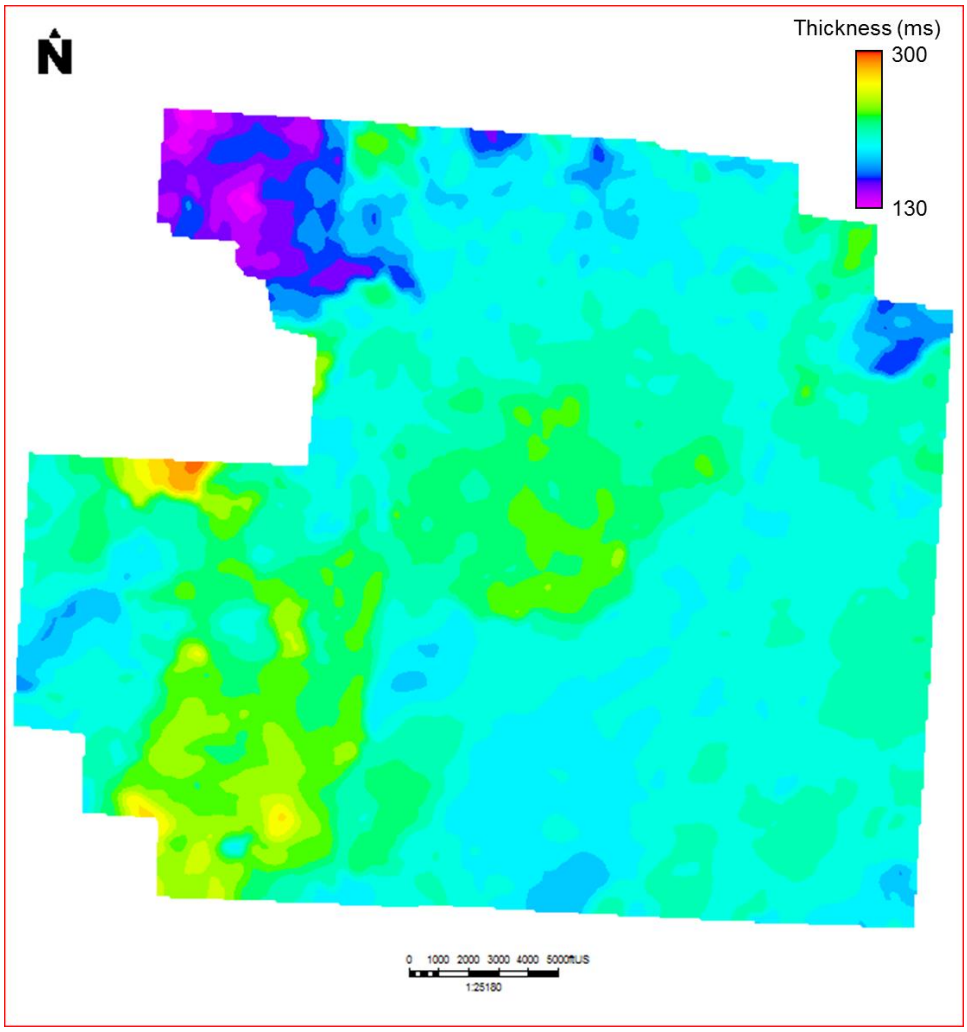

c)

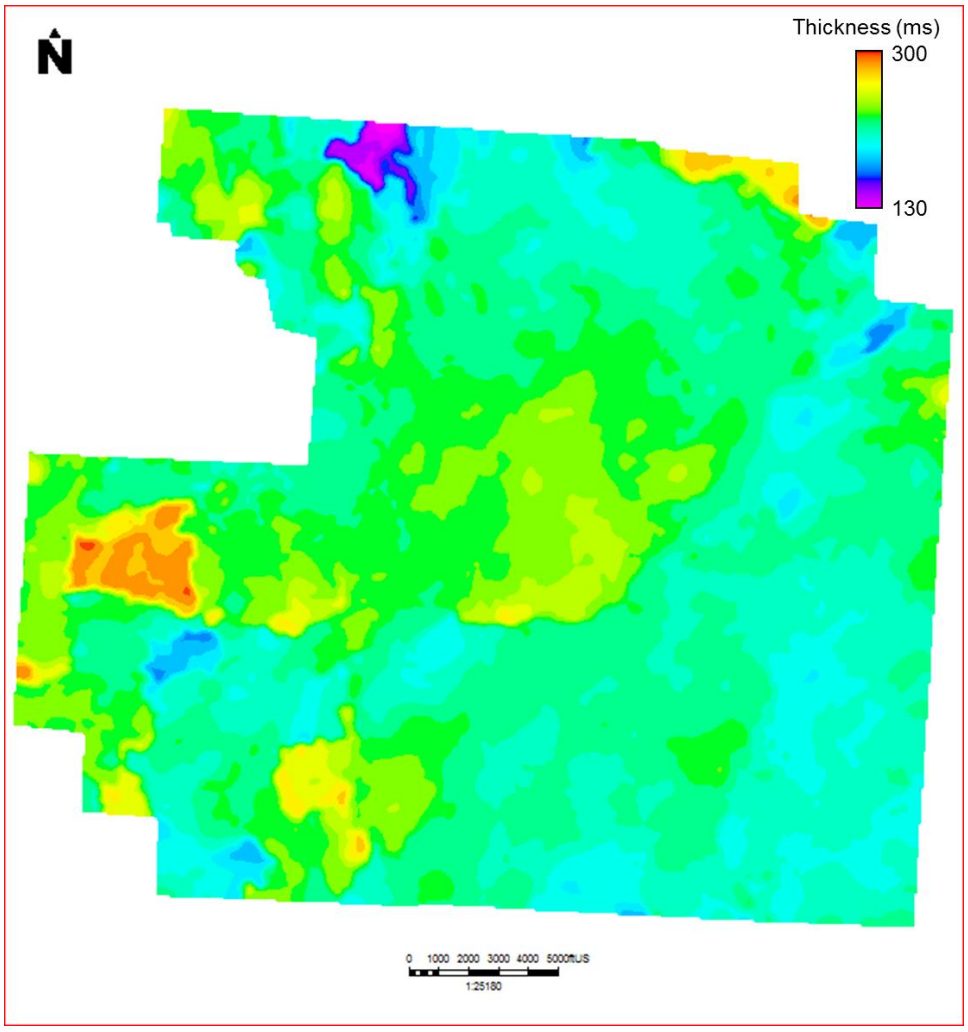

Figure 7.6: Two-way time thickness between the top and base of the Horseshoe Atoll time structure maps (Figure 4) for (a) P-wave, (b) S_1, and (c) S_2 data. These maps will be the input for the time anisotropy estimation and velocity ratios between the three datasets.

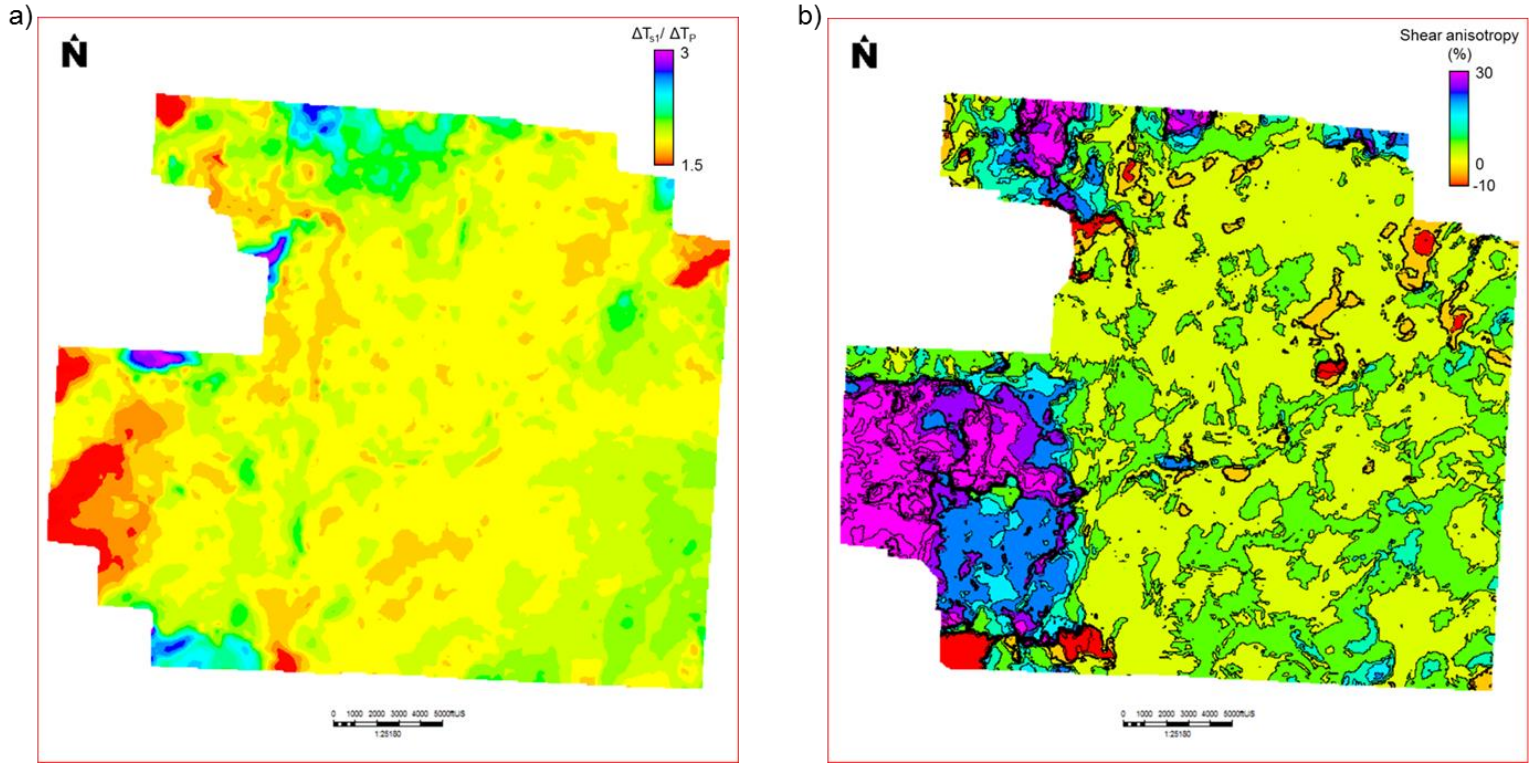

Figure 7.7: (a) $\Delta T_{s1}/\ \Delta T_p$ and (b) shear anisotropy maps. (a) Yellow and orange values indicate zone of low V_p/V_s ratios that could be associated with high porosity or fractures areas. We estimate a 1.8 V_p/V_s in average for the Horsehsoe Atoll. (b) We observe an average shear anisotropy of 6%. Zones where the shear anisotropy is negative are due to low signal to noise ratio that leads to uncertainty in the horizon interpretation process.

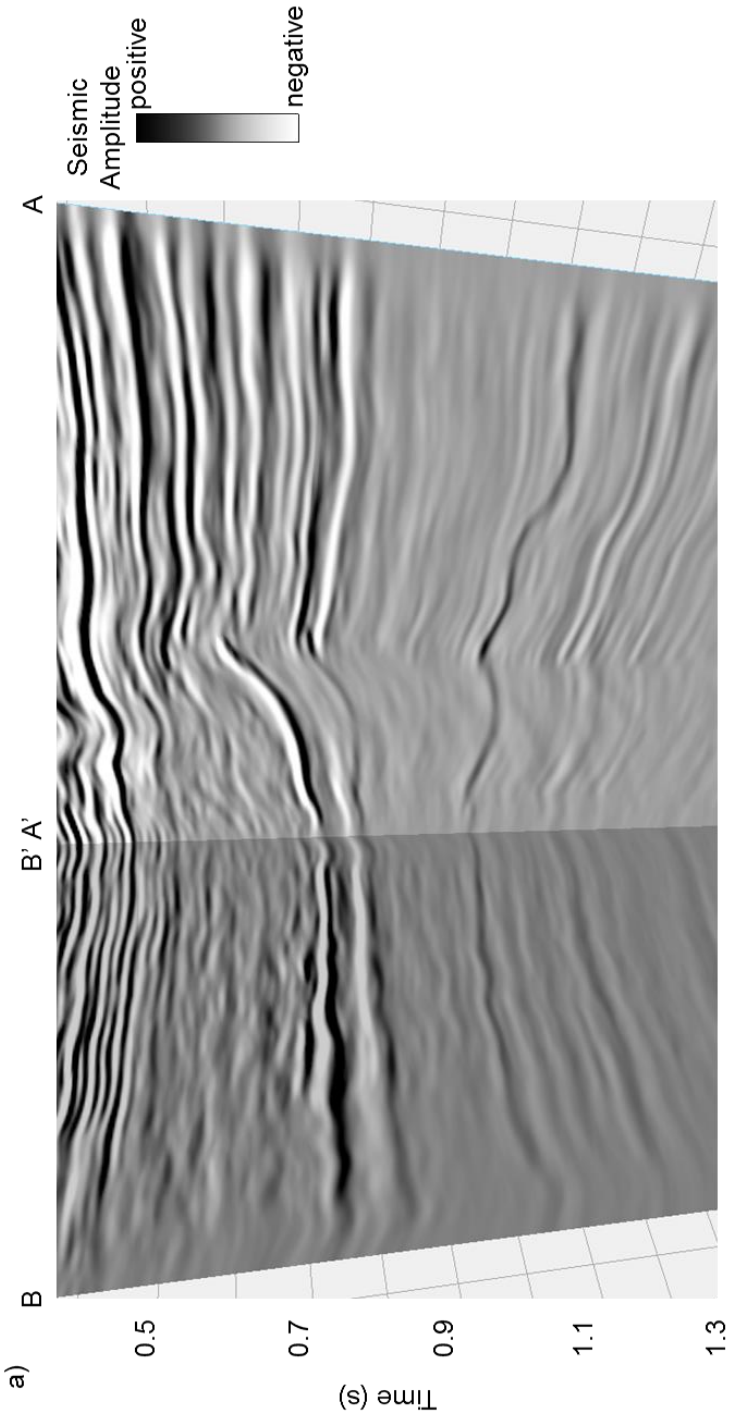
a)
B
B' A'
A
Seismic Amplitude
positive
negative
0.5
0.7
0.9
1.1
1.3
Time (s)

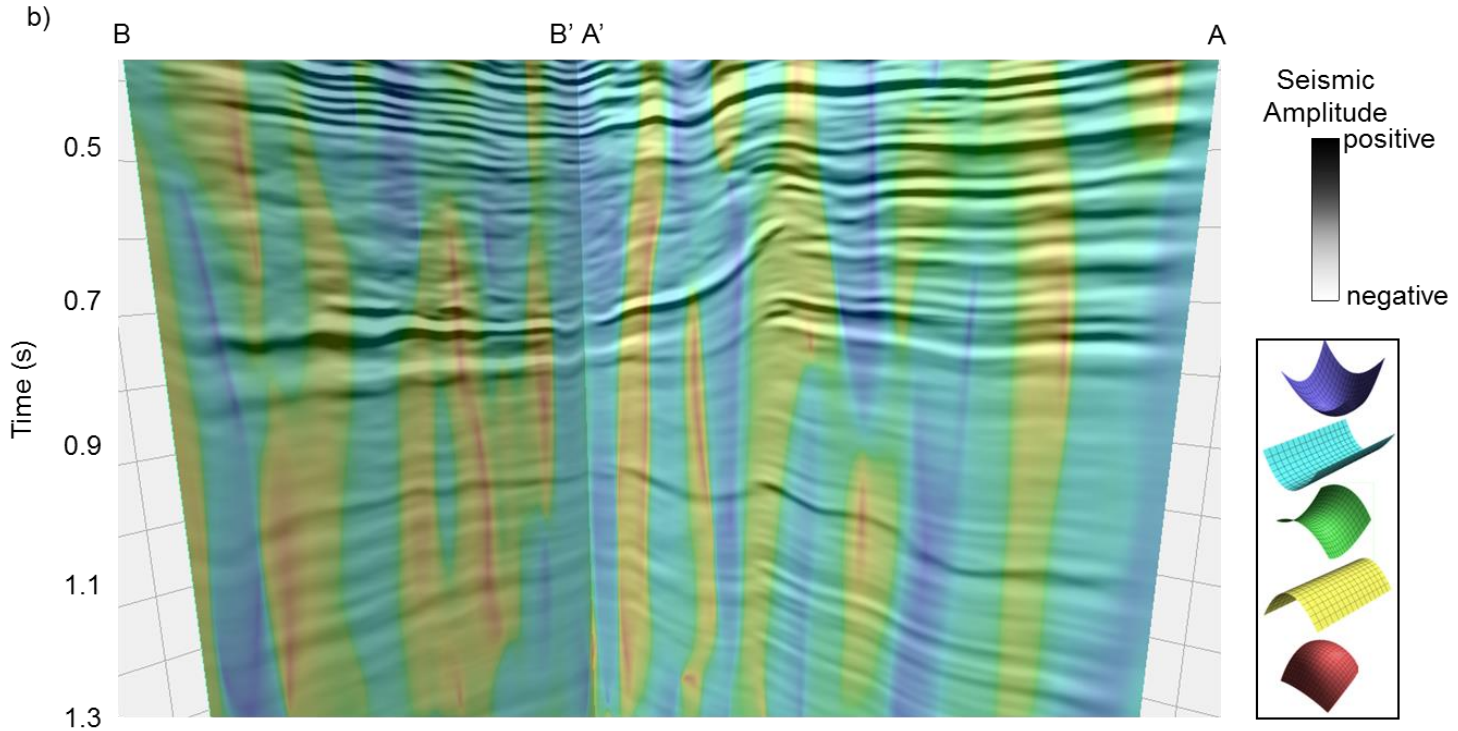
b)
B
B' A'
A
Time (s)
0.5
0.7
0.9
1.1
1.3
Seismic
Amplitude
positive
negative

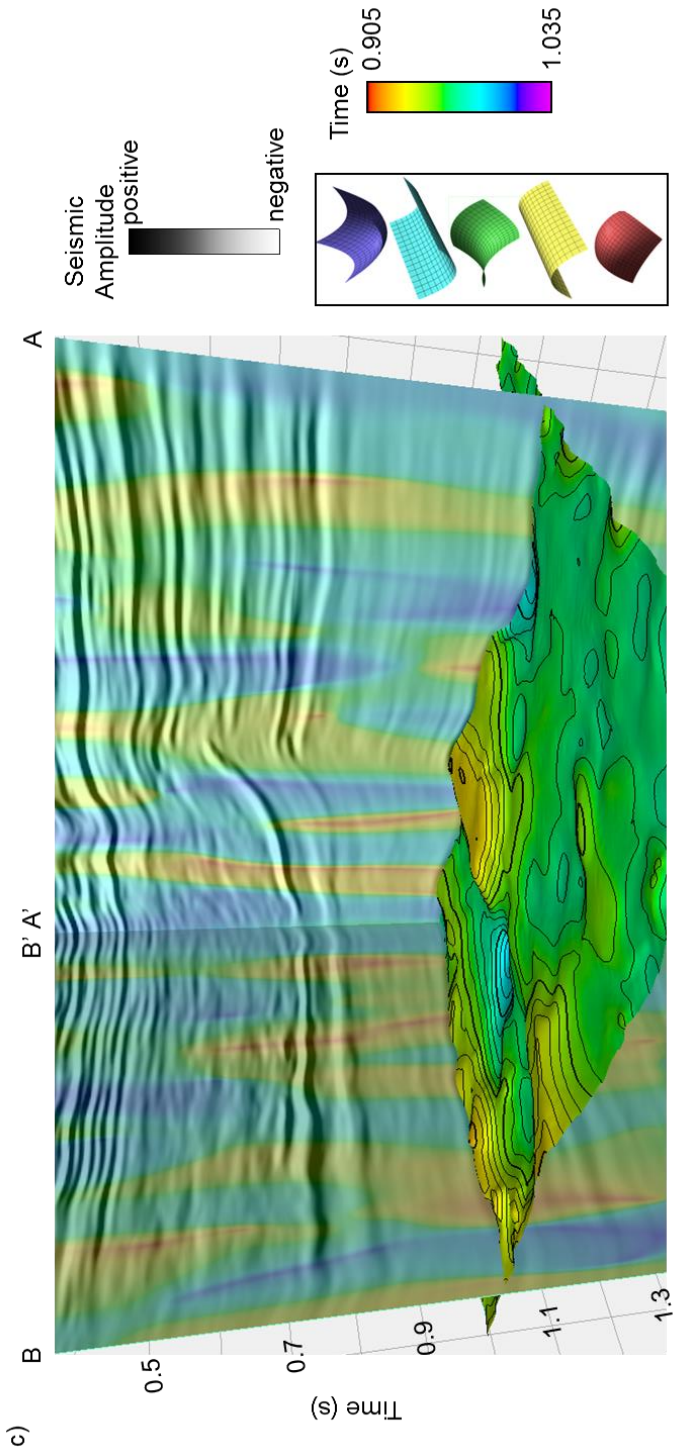
c)
A
B' A'
B
Time (s)
0.5
0.7
0.9
1.1
1.3
Seismic Amplitude
positive
negative
Time (s)
0.905
1.035

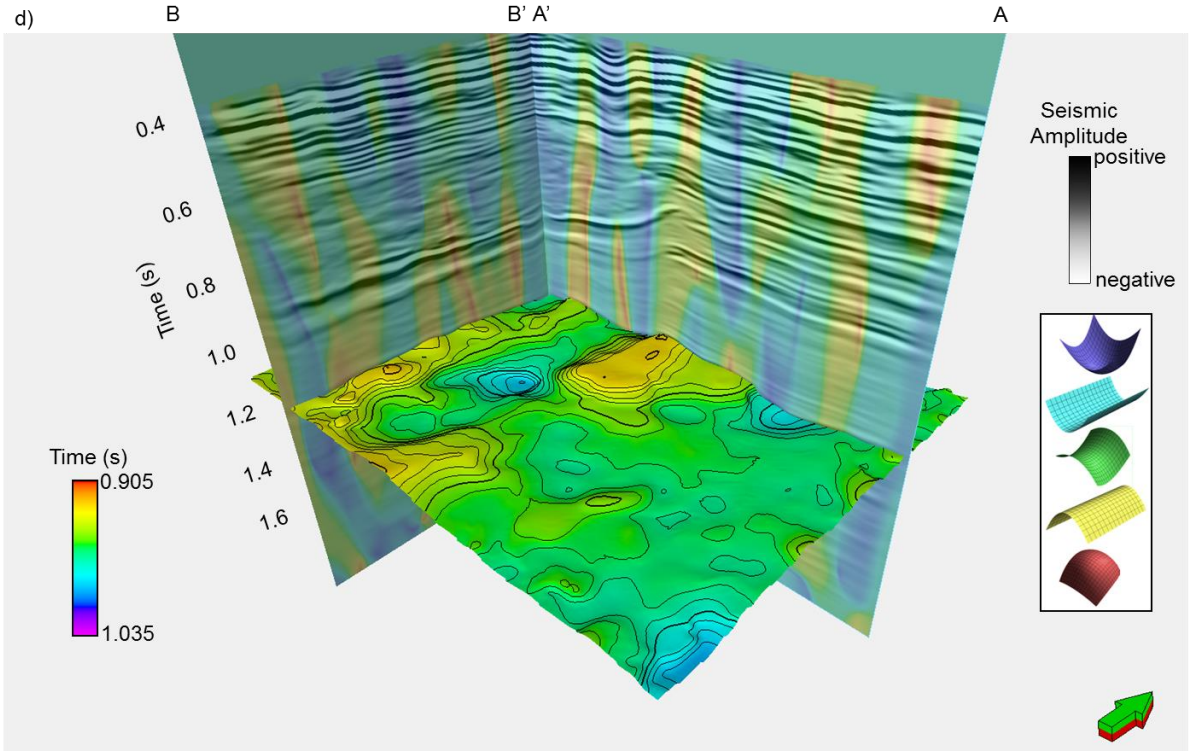

Figure 7.8: Chair diagram for lines AA' and BB' through (a) seismic amplitude, (b) seismic amplitude correndered with shape index modulated by curvedness using 20% transparency, and (c-d) seismic amplitude correndered with shape index displaying the top Horseshoe Atoll horizon. Shape index hot colors indicate dome and ridge structures. Cool colors indicate valley or saddle structures. According to the model in Figure 7.2, zones where data shows dome or ridge structure are more prone to develop porosity due to aerial exposure of the carbonate buildups during late Pennsylvanian to early Permian time. Green arrow is pointing north.

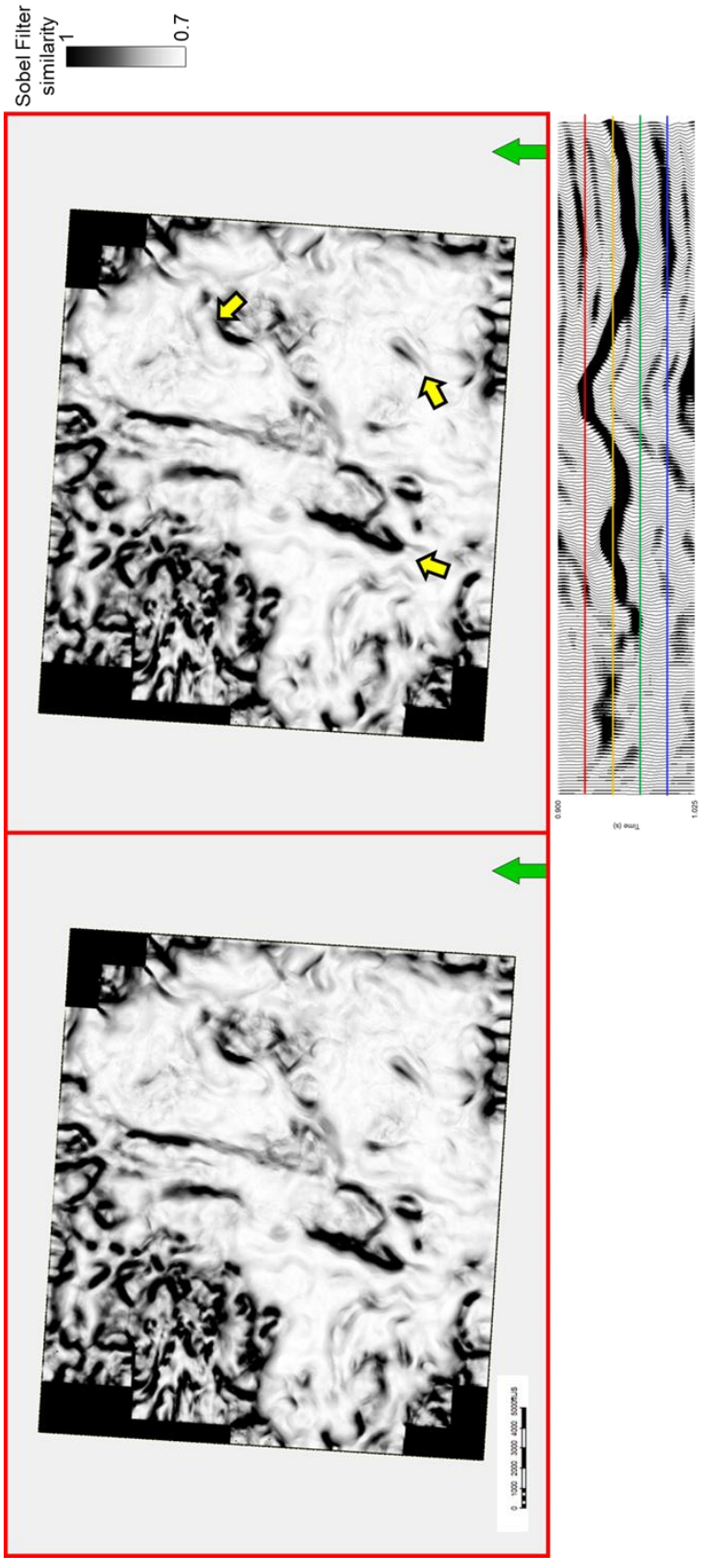
Sobel Filter similarity
1
0.7
Time (s)
0.600
1.025
0 1000 2000 3000 4000 5000Ft

a)

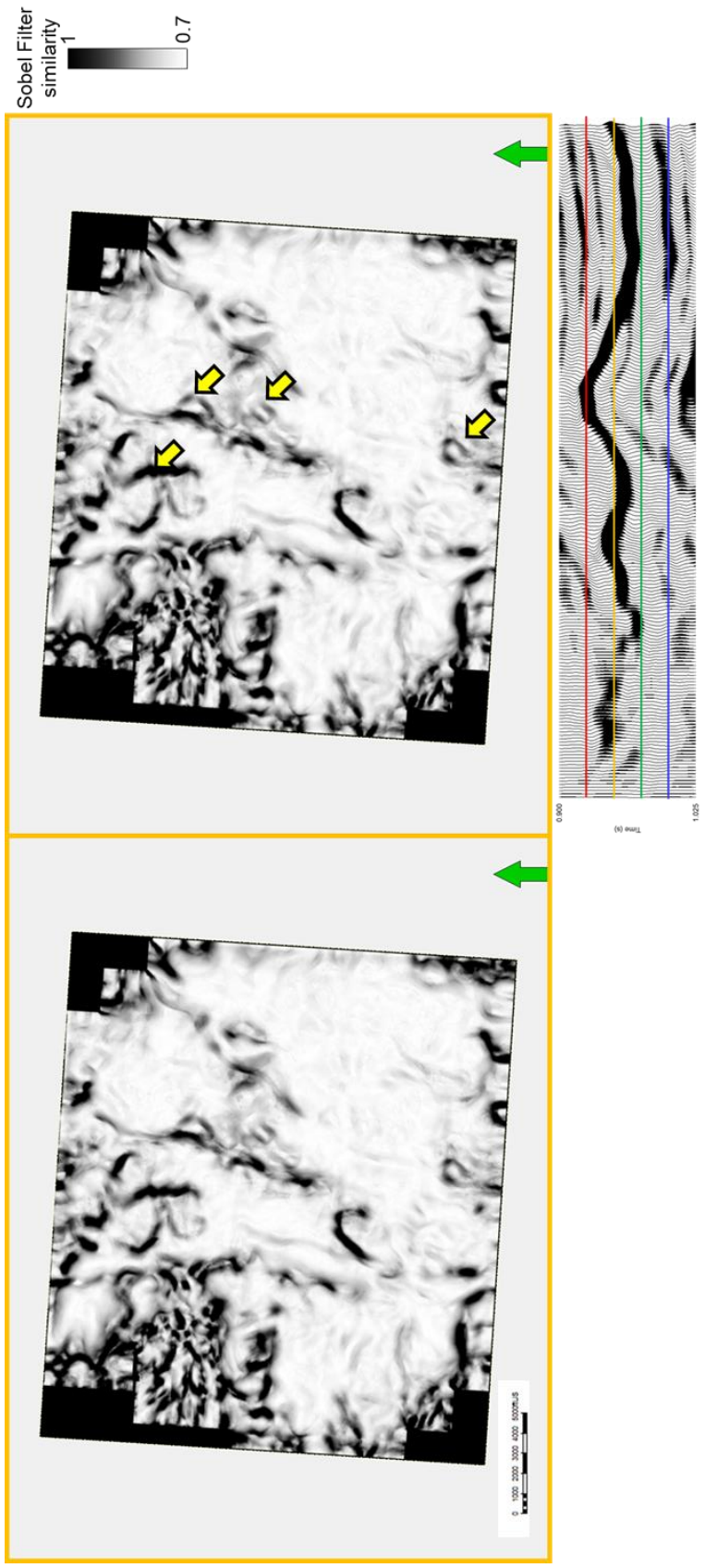

b)

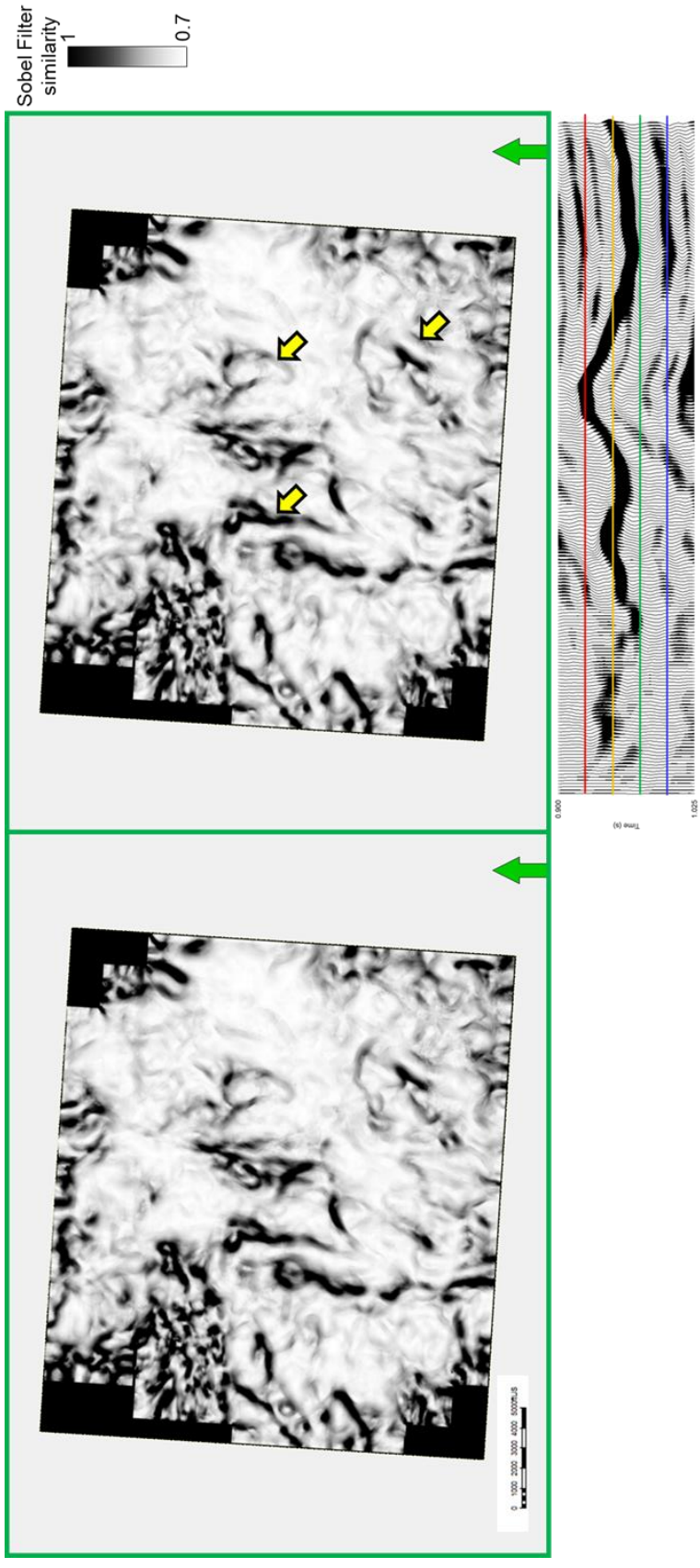
Sobel Filter similarity
1
0.7
Time (s)
0.900
1.025
0 1000 2000 3000 4000 5000mS

c)

d)

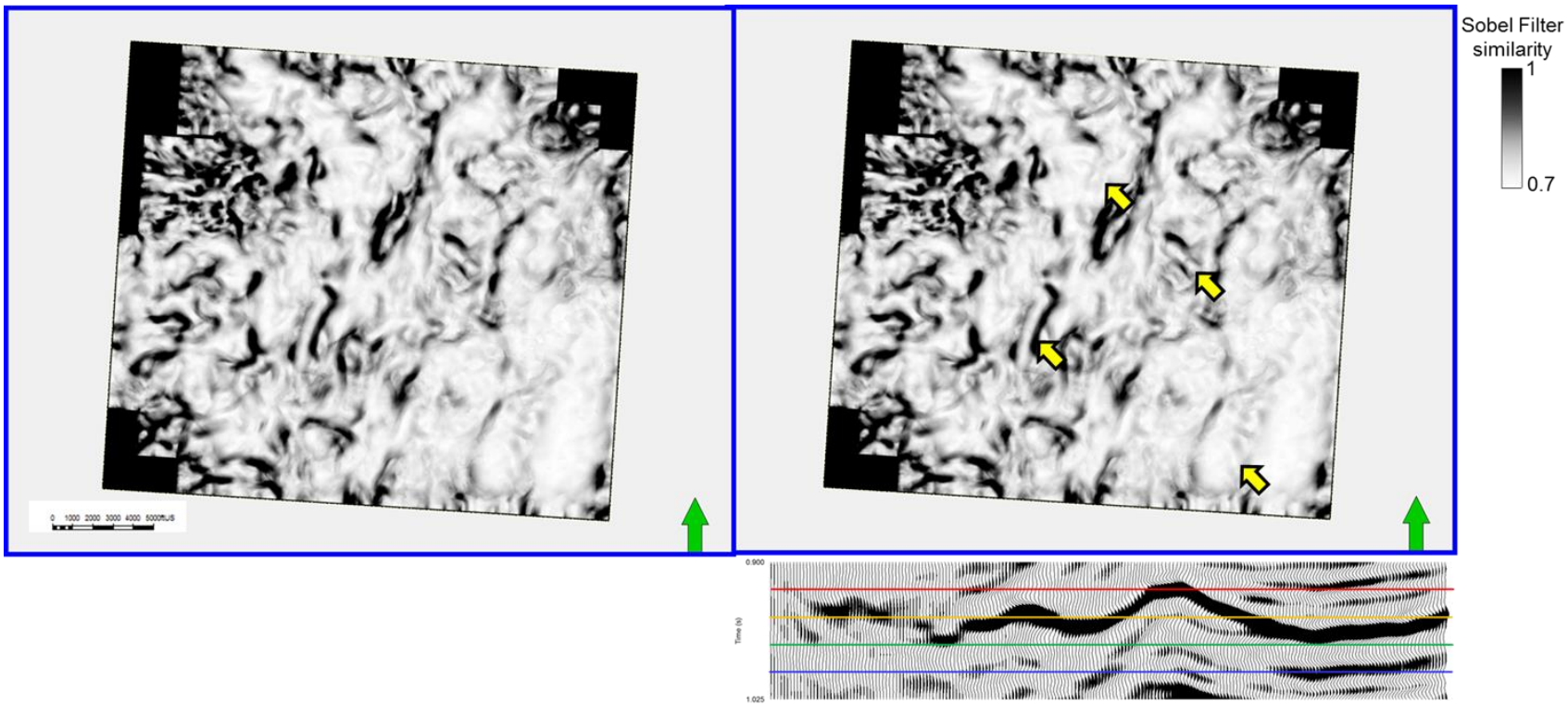

Figure 7.9: Time slice at (a) 0.945, (b) 0.965, (c) 0.985, and (d) 1.005 s through Sobel filter similarity computed from seismic amplitude. Yellow arrows indicate anomalies that could be interpreted carbonate buildups highlighted by the Sobel filter similarity. Green arrow is pointing north.

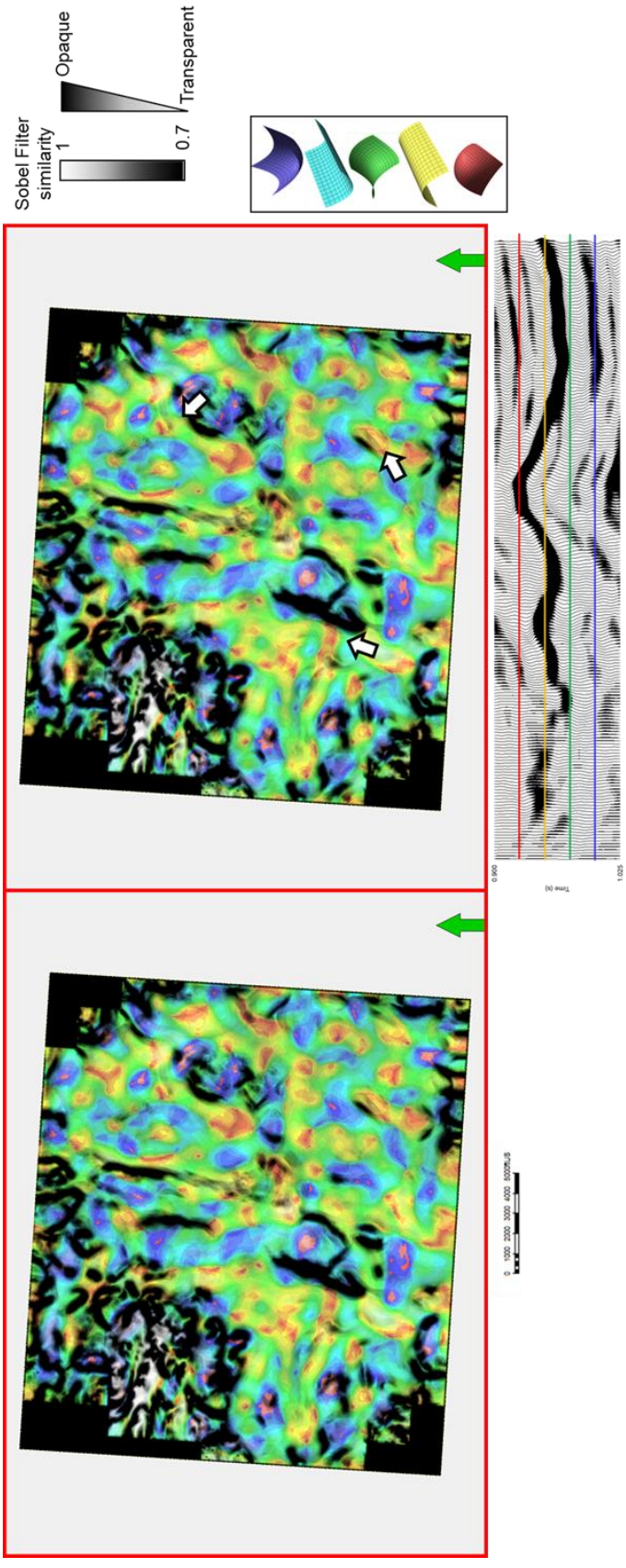

a)

b)

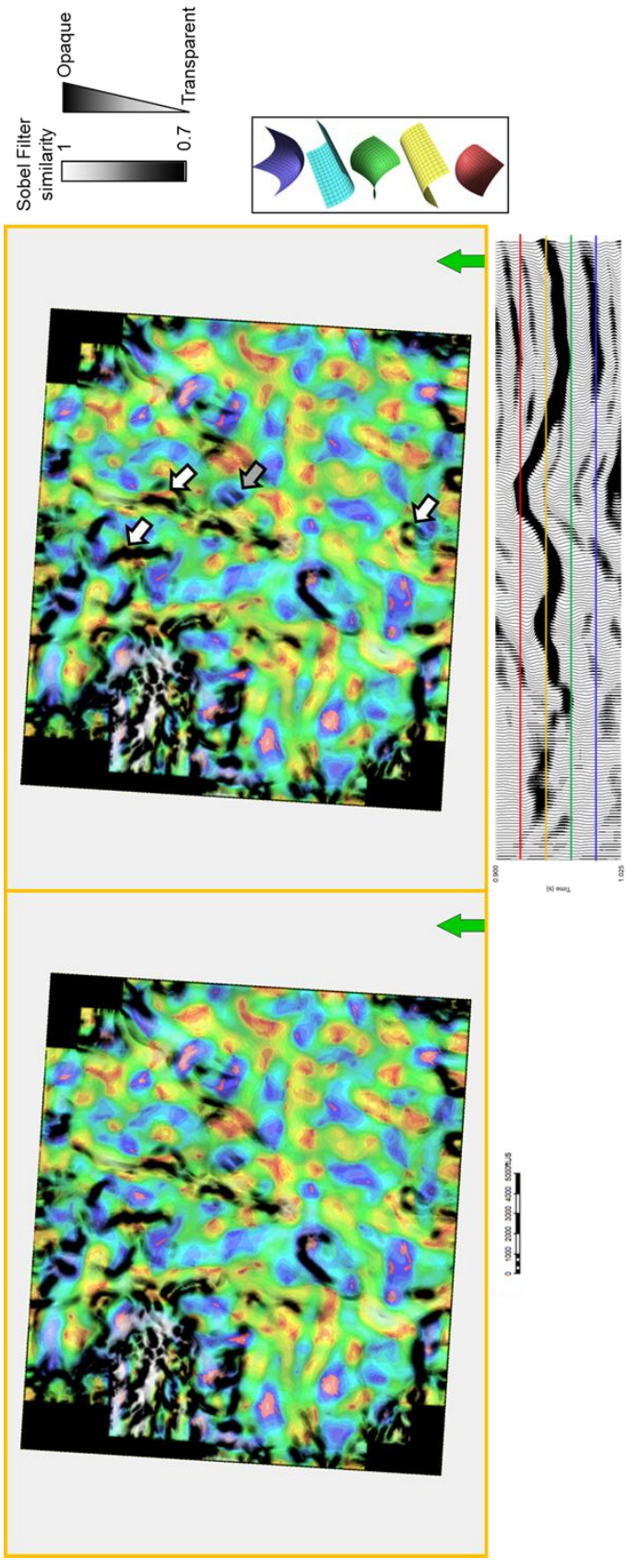

c)

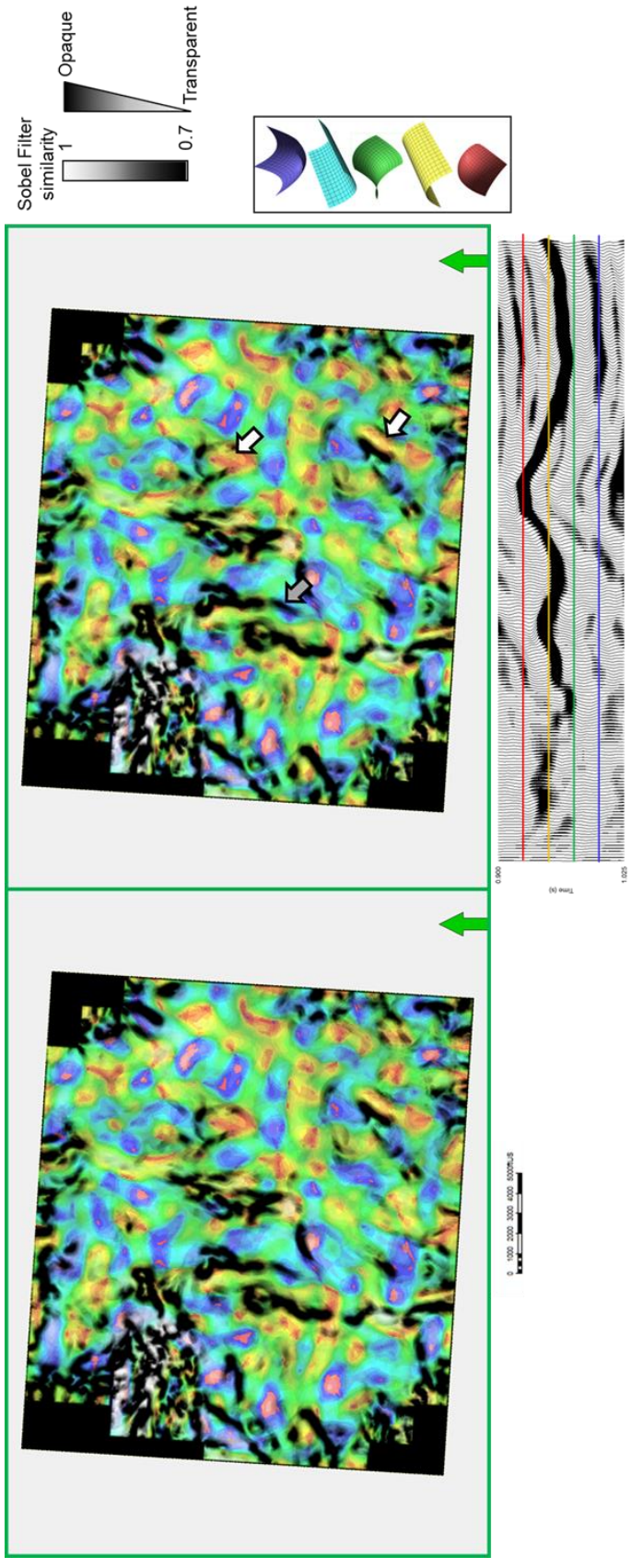
Sobel Filter similarity
1
0.7
Opaque
Transparent
0.900
1.025
Time (s)

d)

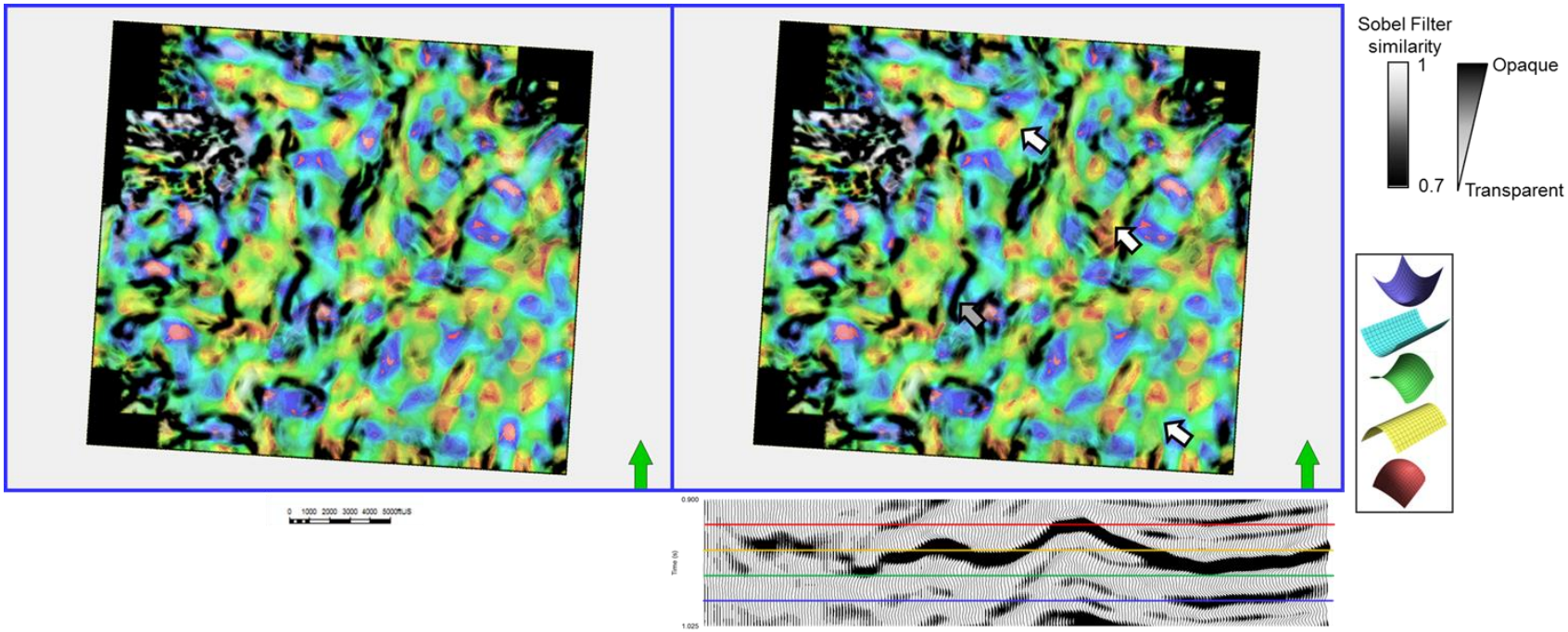

Figure 7.10: Time slice at (a) 0.945, (b) 0.965, (c) 0.985, and (d) 1.005 s through Sobel filter similarity computed from seismic amplitude correndered with shape index modulated by curvedness. We defined a proxy for carbonate buildups in areas of ridge or saddle shape index and surrounded by low Sobel filter similarity values based on the model in Figure 2. White arrows indicate anomalies are interpreted as carbonate buildups matching our interpretation in Figure 8. Grey arrows indicate anomalies that were interpreted as carbonate buildups in Figure 8 but do not agree with our proxy. Green arrow is pointing north.

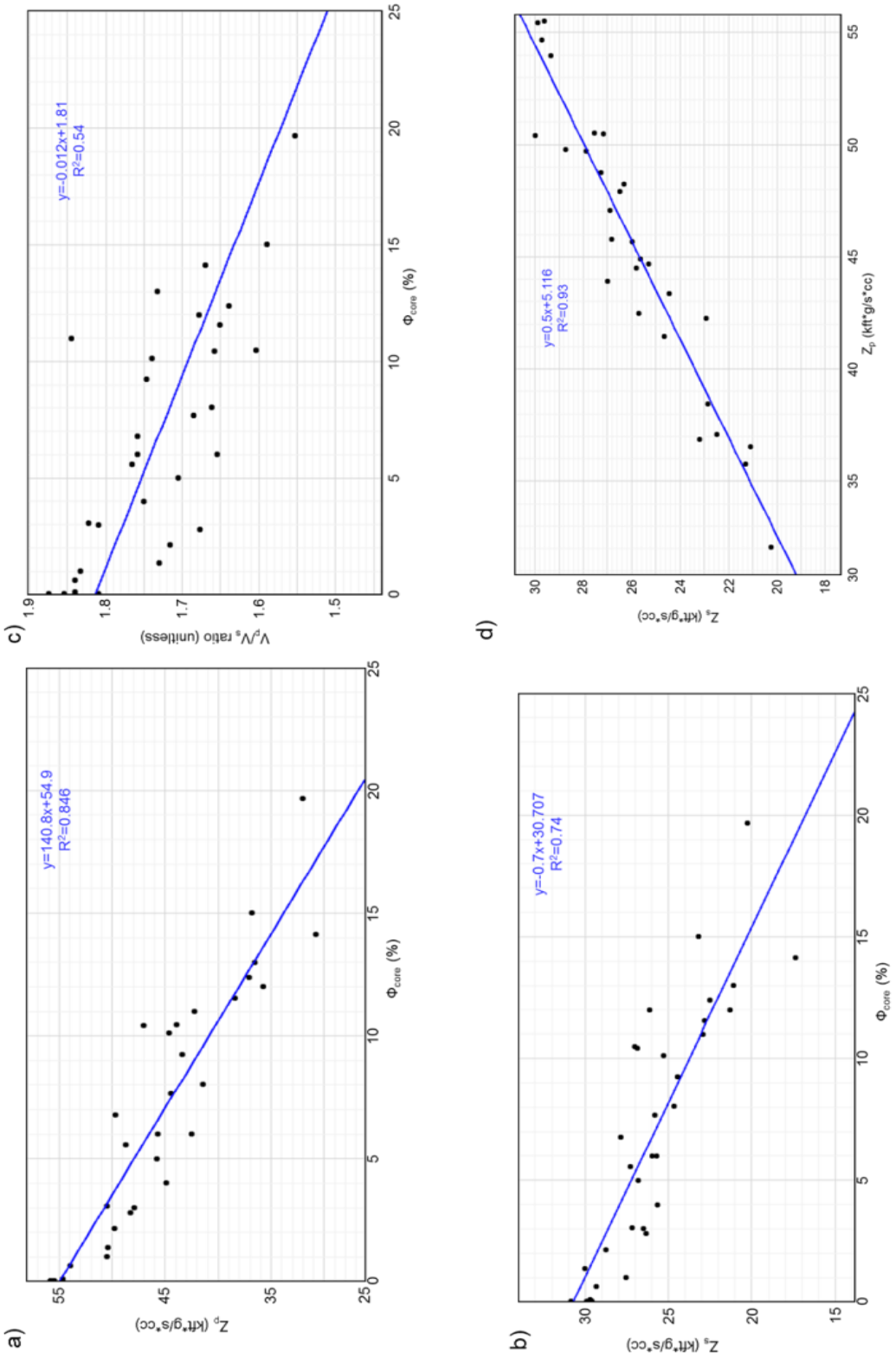
a)
y=140.8x+54.9
R²=0.846
Z_p (kft*g/s*cc)
Φ_core (%)
b)
y=-0.7x+30.707
R²=0.74
Z_s (kft*g/s*cc)
Φ_core (%)
c)
y=-0.012x+1.81
R²=0.54
V_p/V_s ratio (unitless)
Φ_core (%)
d)
y=0.5x+5.116
R²=0.93
Z_s (kft*g/s*cc)
Z_p (kft*g/s*cc)

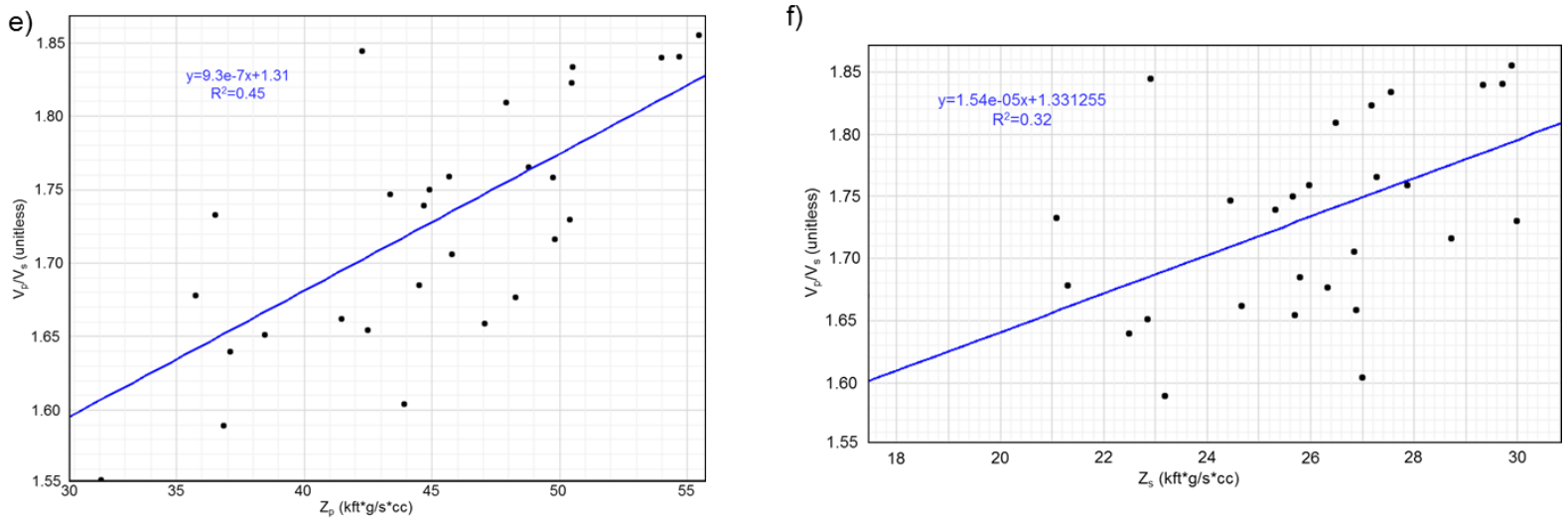

Figure 7.11: Crossplots showing (a) P-impedance versus core porosity, (b) S-impedance versus core porosity, (c) V_p/V_s ratio versus core porosity, (d) S-impedance versus P-impedance, (e) V_p/V_s ratio versus P-impedance and (f) V_p/V_s ratio versus S-impedance. Impedances and V_p/V_s ratios were calculated using acoustic velocities and densities measured using core plugs. P-impedance, S-impedance and V_p/V_s ratio show an inverse relationship with porosity. P-impedance and S-impedance show a direct relationship between them. V_p/V_s ratio only shows a fair correlation with the porosity measured from core. Blue line indicates the best fit trend

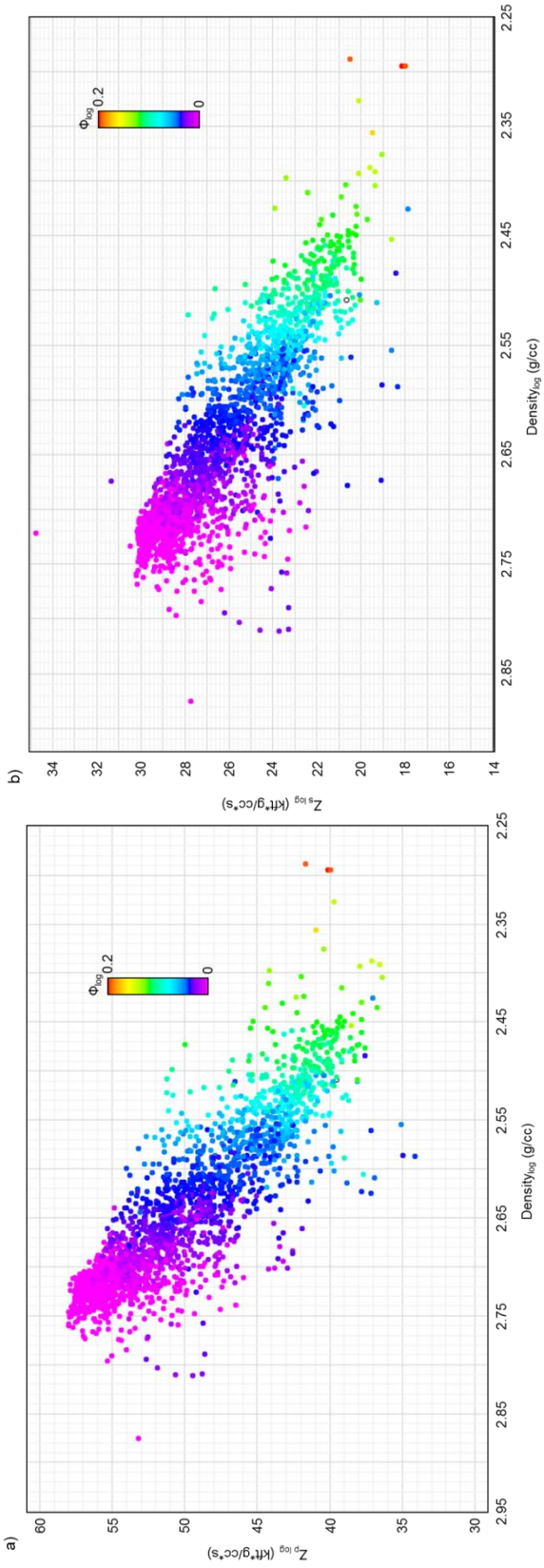
a)
b)
Φ_{log} 0.2
0
$Z_{p\ log}$ (kft*g/cc*s)
$Z_{s\ log}$ (kft*g/cc*s)
$Density_{log}$ (g/cc)

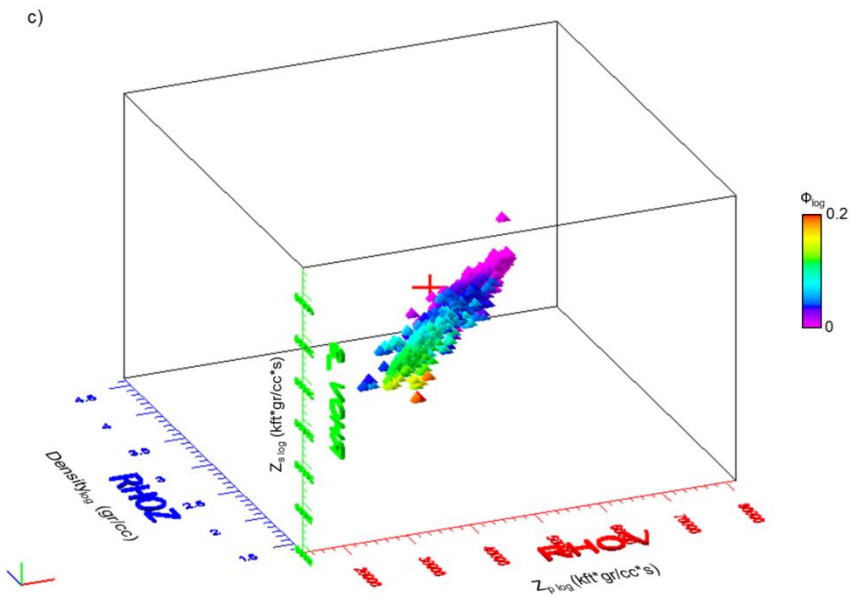

Figure 7.12: Cross-plots showing log (a) P-impedance versus density color coded by porosity and (b) S-impedance versus density color coded by porosity. (c) 3D crossplot of P-impedance versus S-impedance versus density. Colors in the 3D crossplot represent porosity. Impedances show a linear relationship with density values.

Table 7.1: Multi-linear regression for porosity prediction from P-impedance, S-impedance, and density correlation table.

Variable	Density	S-impedance	P-impedance	Porosity
Density	1	0.83	0.87	-0.95
S-impedance	0.83	1	0.96	-0.88
P-impedance	0.87	0.96	1	-0.91
Porosity	-0.95	-0.88	-0.91	1

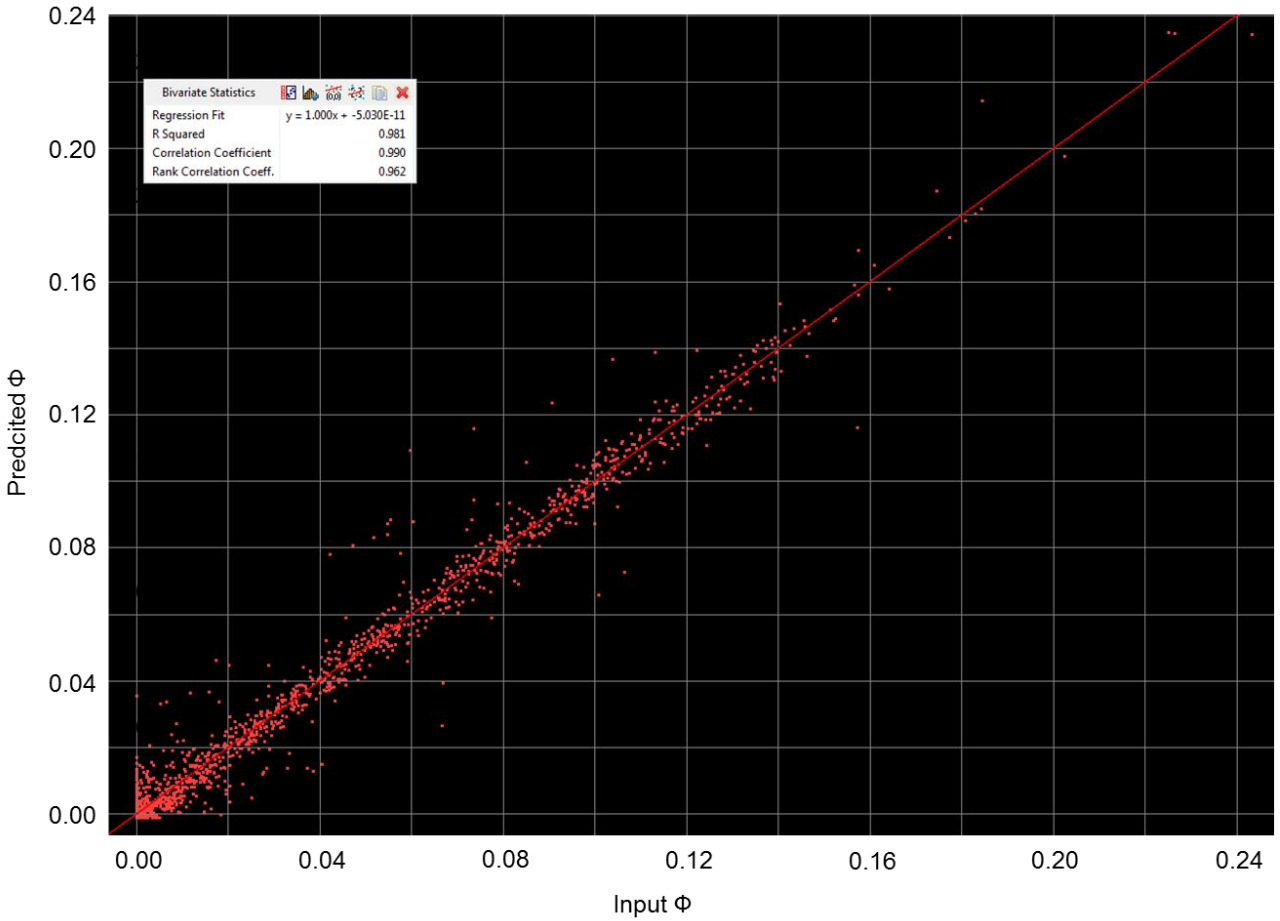

Figure 7.13: Multi-linear regression predicted versus measured porosity.

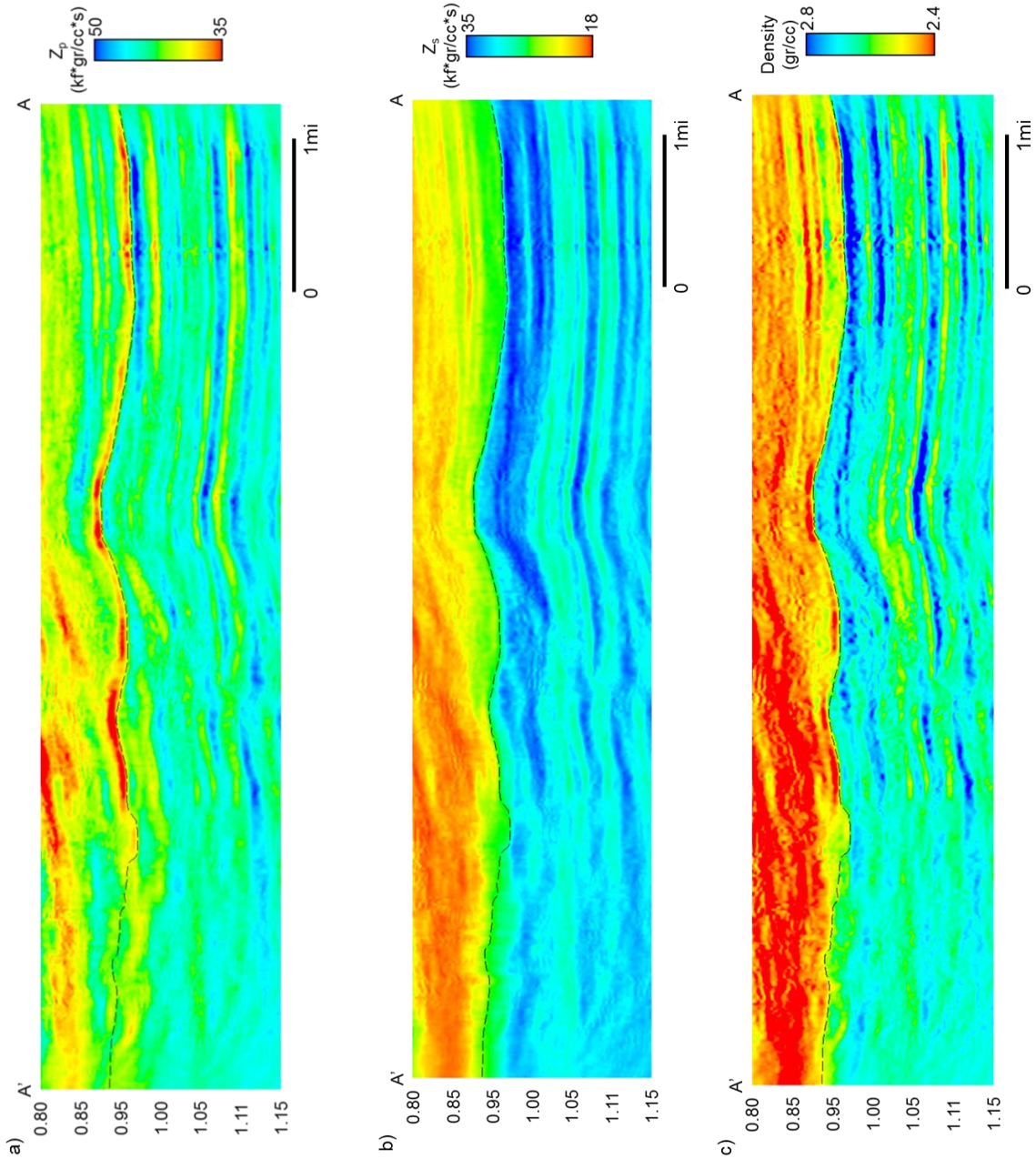
a)
A
A'
Z_p (kf*gr/cc*s)
50
35
1mi
0
0.80
0.85
0.95
1.00
1.05
1.11
1.15
b)
A
A'
Z_s (kf*gr/cc*s)
35
18
1mi
0
0.80
0.85
0.95
1.00
1.05
1.11
1.15
c)
A
A'
Density (gr/cc)
2.8
2.4
1mi
0
0.80
0.85
0.95
1.00
1.05
1.11
1.15

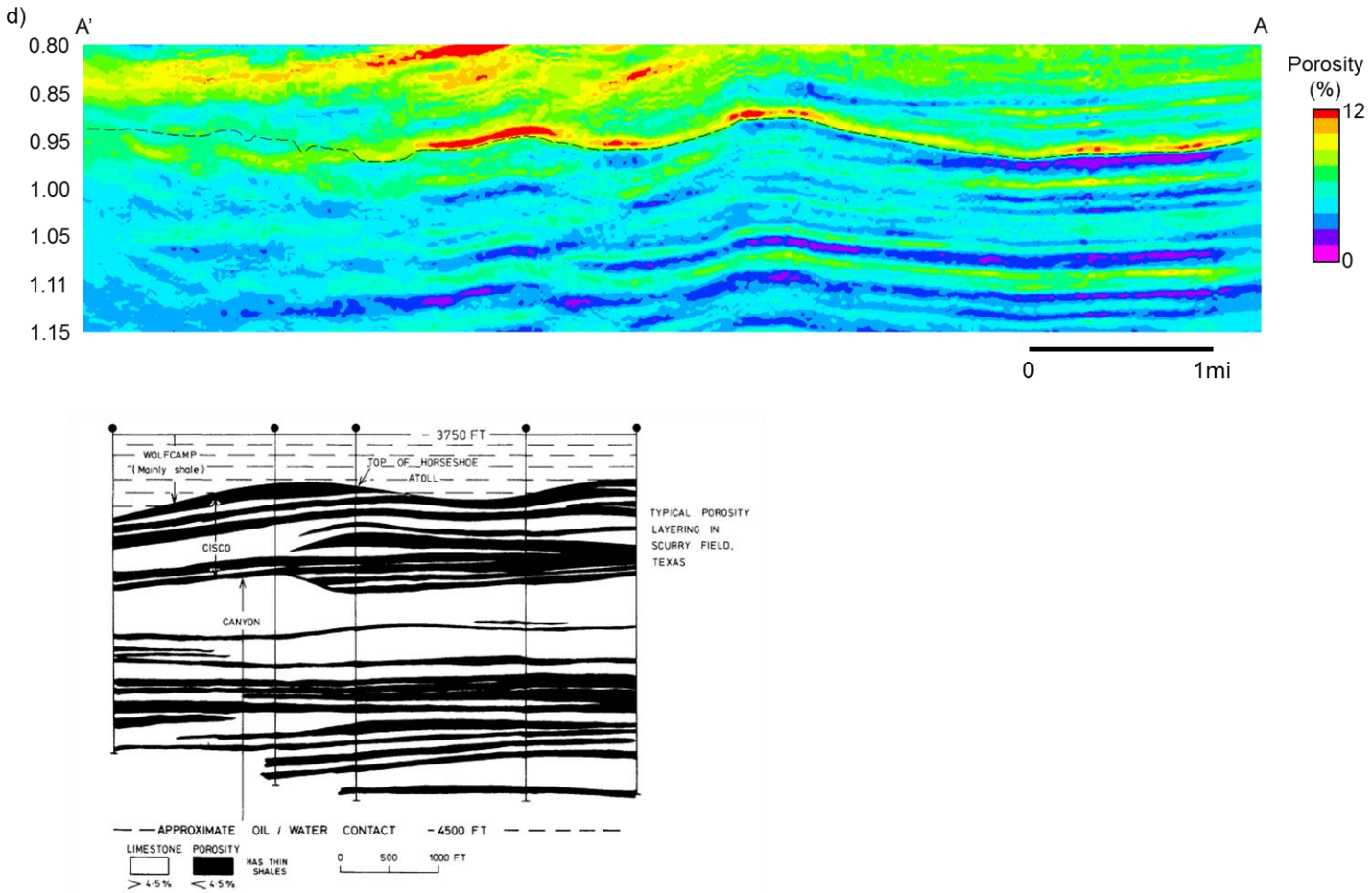

Figure 7.14: Vertical section A-A' through (a) P-impedance, (b) S impedance, (c) Density, and (d) derived porosity.(d) Although at a different scale, we identify porosity streaks that correlate with the model proposed by Hobson (1989). Dashed line indicates top of the reservoir.

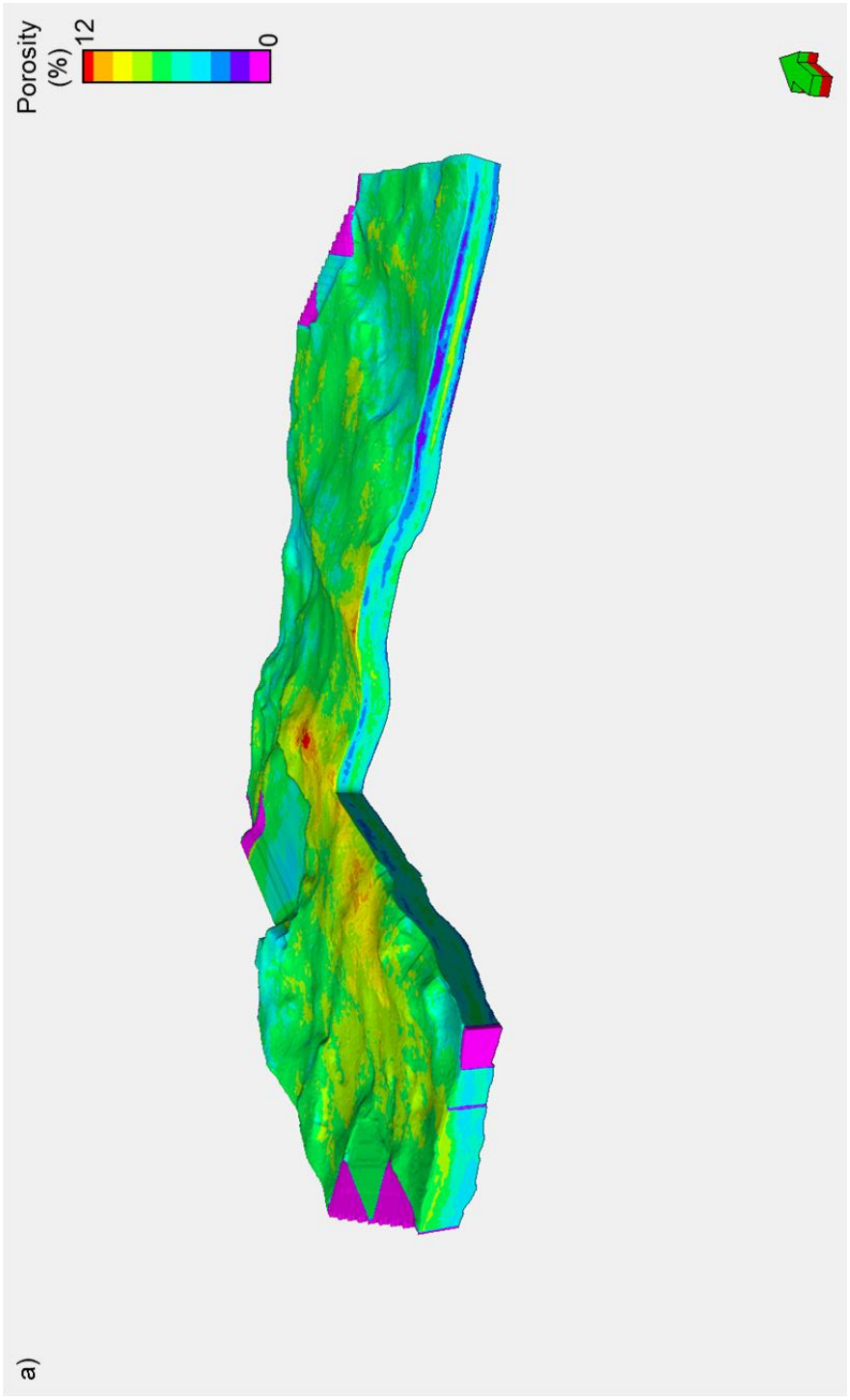
Porosity (%)
12
0
a)

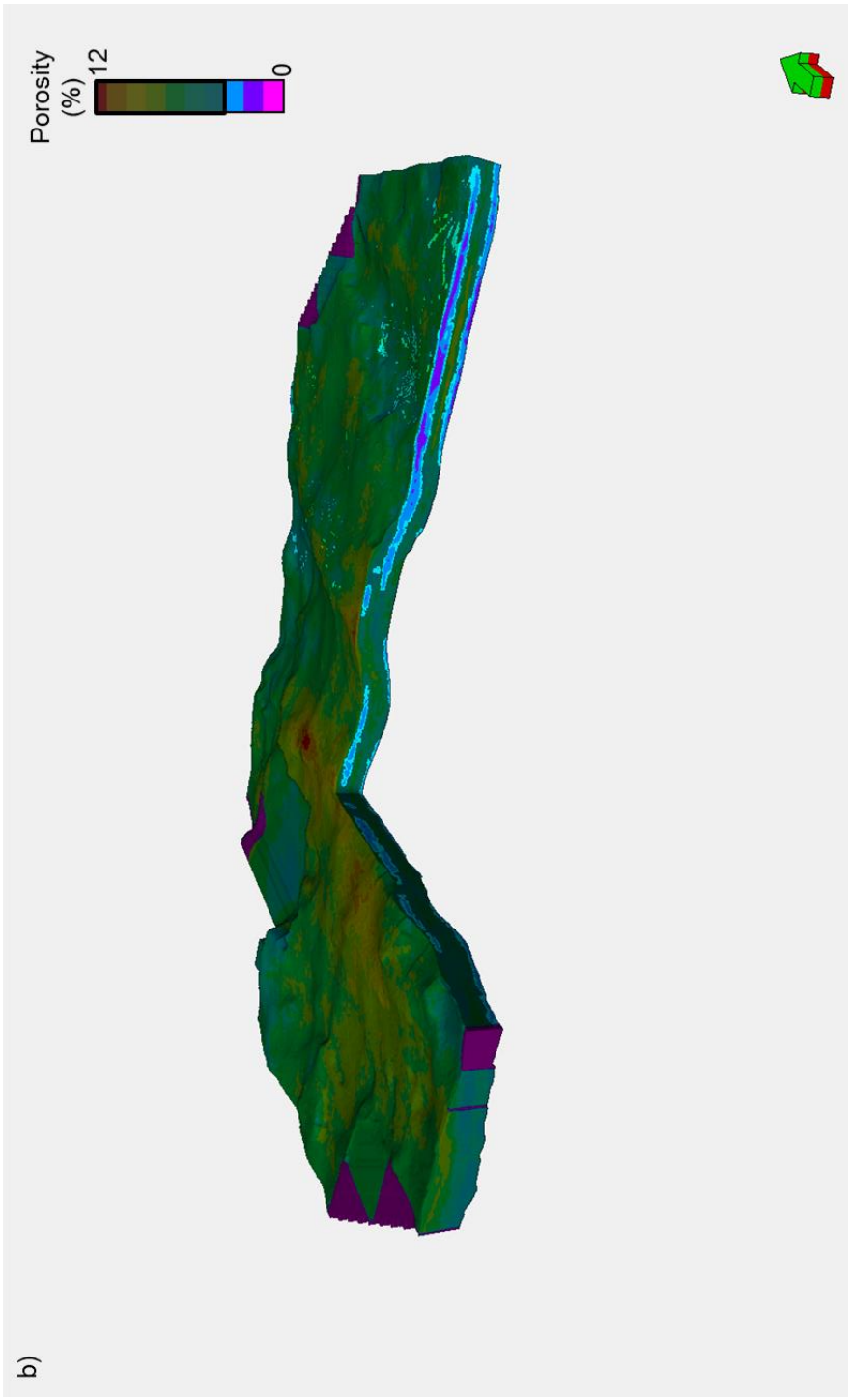
Porosity (%)
12
0
b)

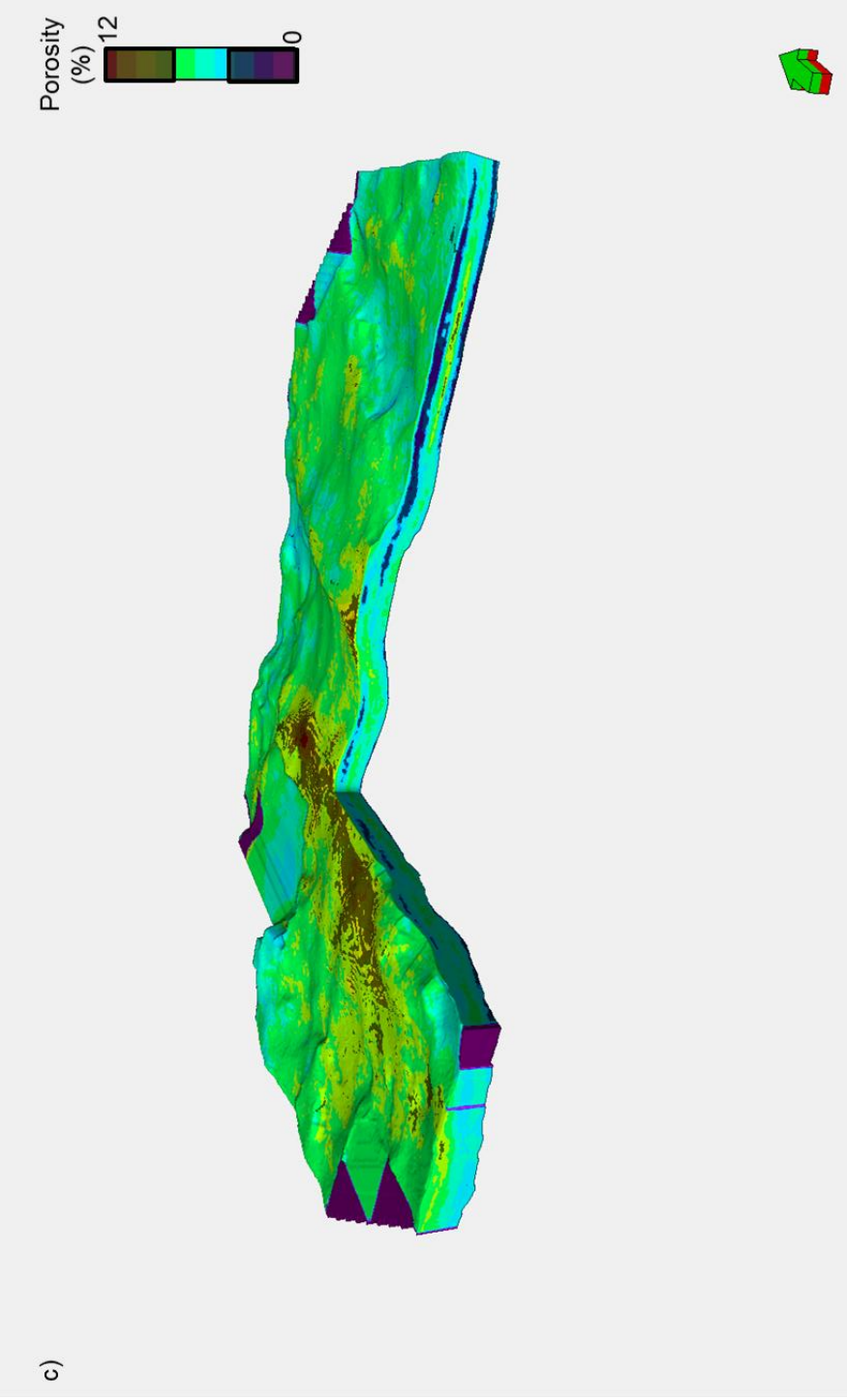
Porosity (%)
12
0
c)

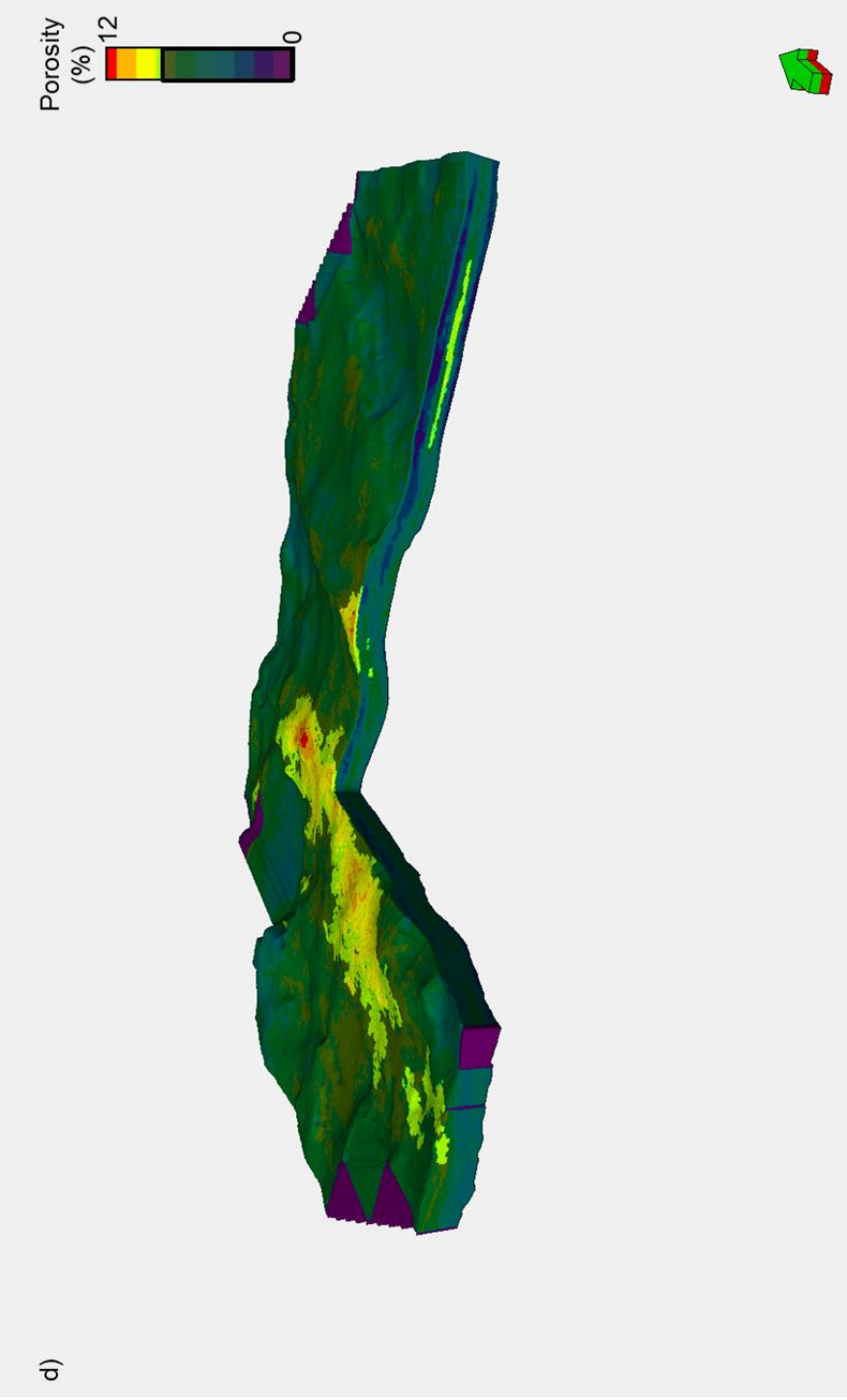
Porosity (%)
12
0
d)

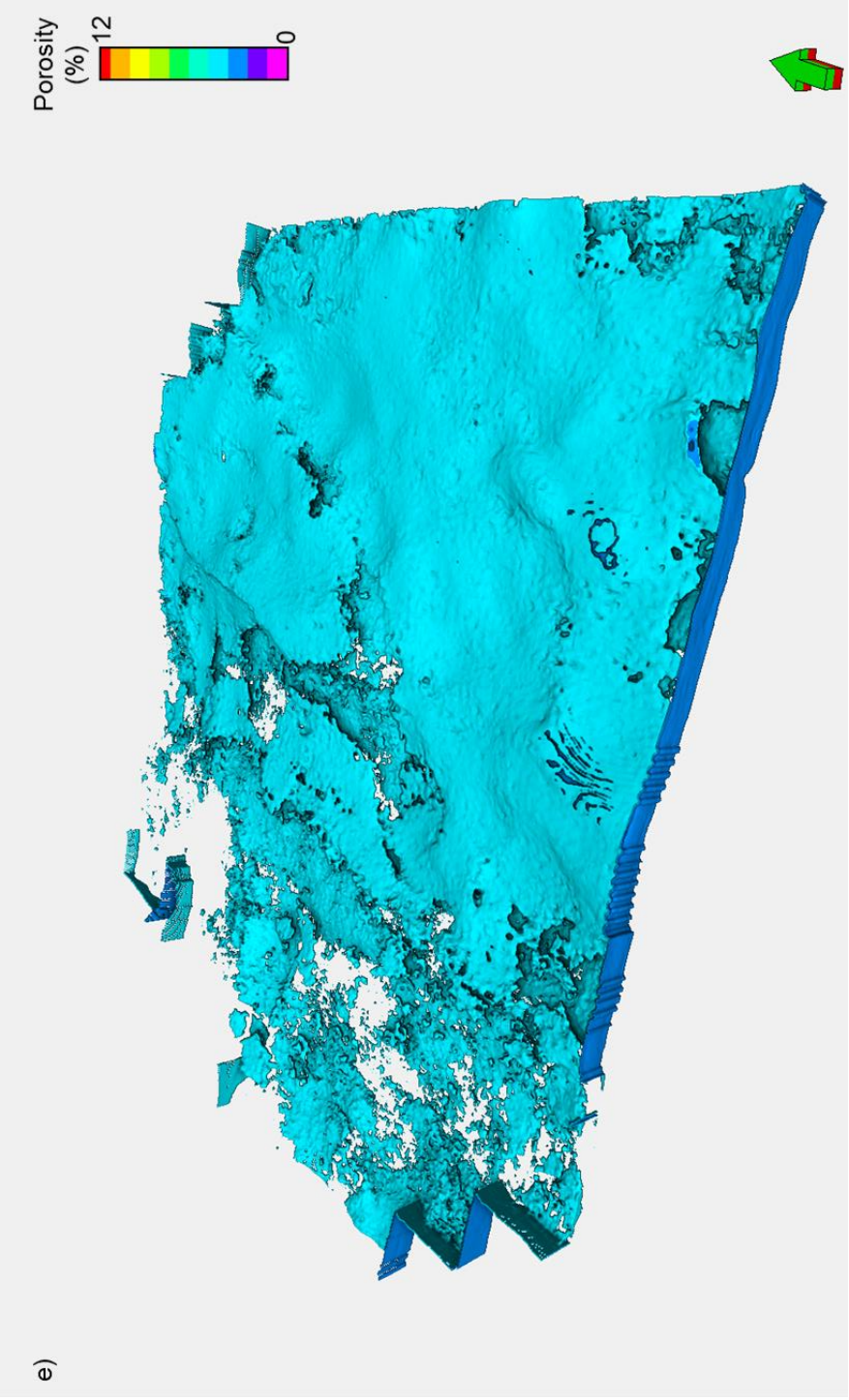
Porosity (%)
12
0
e)

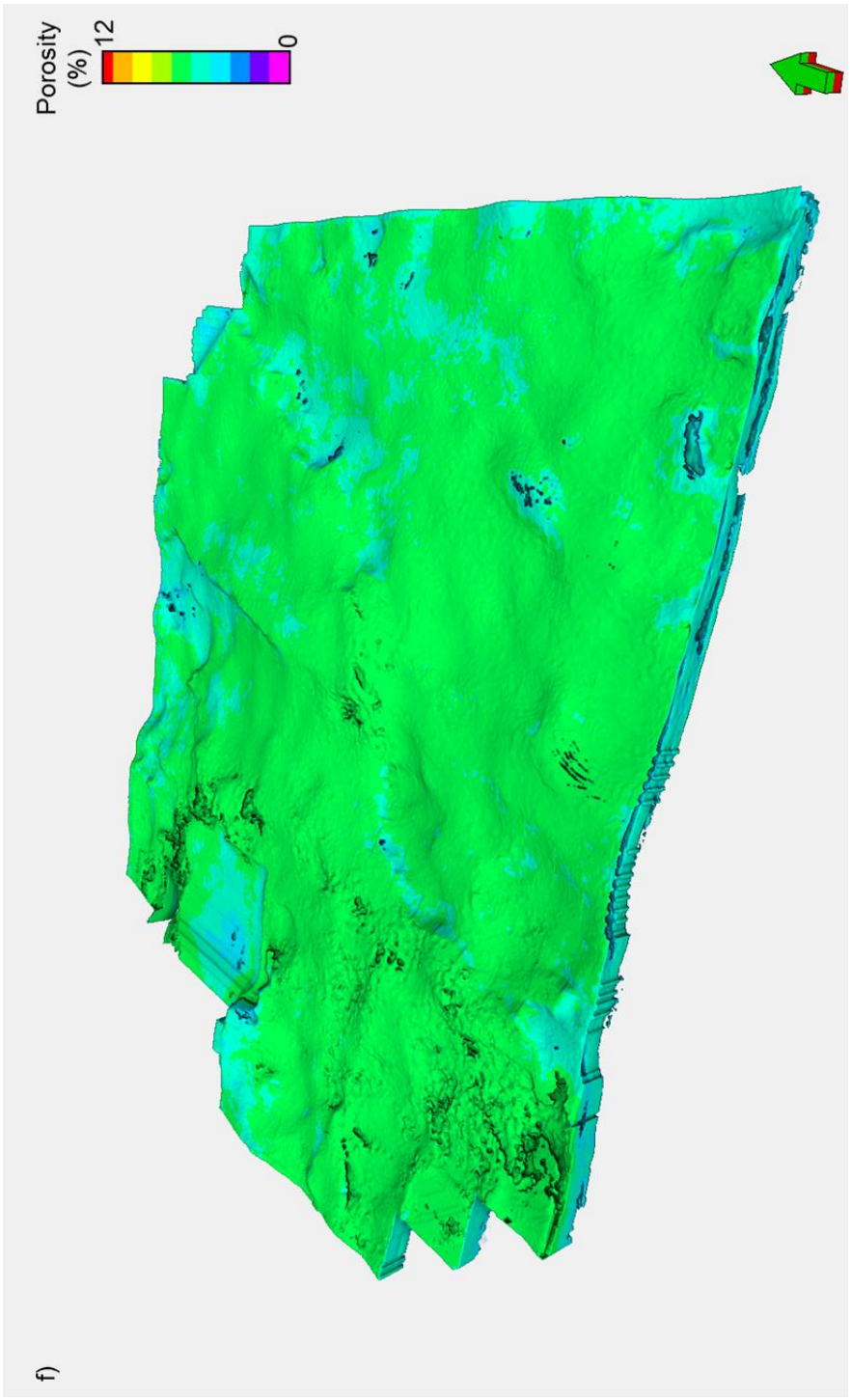
Porosity
(%)
12
0
f)

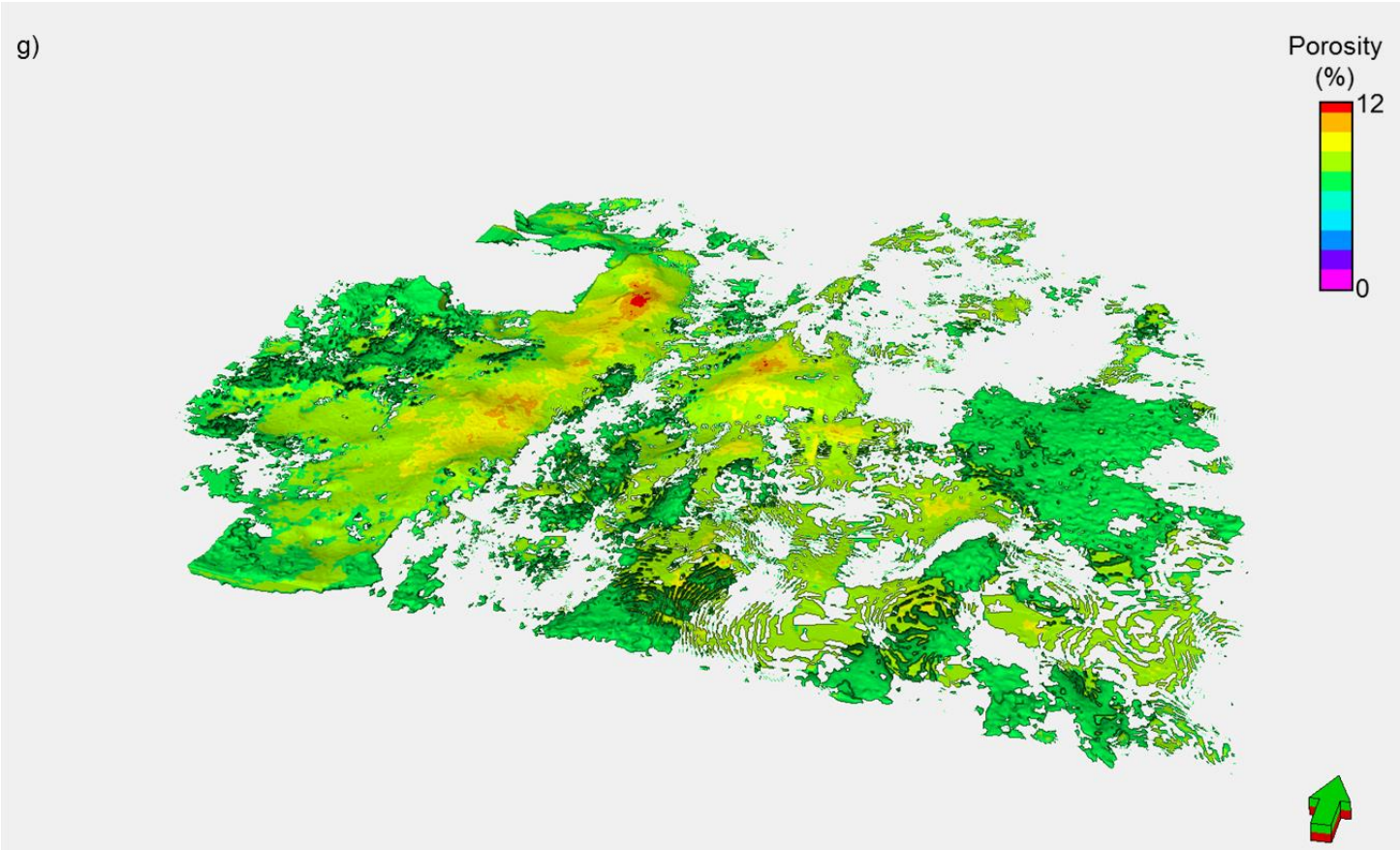

Figure 7.15: 3D horizon probe view of (a) porosity volume, (b) porosities below 4%, (c) porosities between 4 and 8%, and (d) porosities above 8%. (b-d) Bright colors show threshold porosities. (e-g) Porosity distribution geobodies obtained from the analysis threshold porosities analysis. (e) Extracted geobody for porosities below 4%. (f) Extracted geobody for porosities between 4 and 8%. (g) Extracted geobody for porosities above 8%. Horizon probe was generated using the top of the Horseshoe Atoll time structure map (Figure 7.5a) and a stratal slice half way between the top and the base of the Horseshoe Atoll (Figure 7.5). (b-d) Bright colors show threshold porosities.

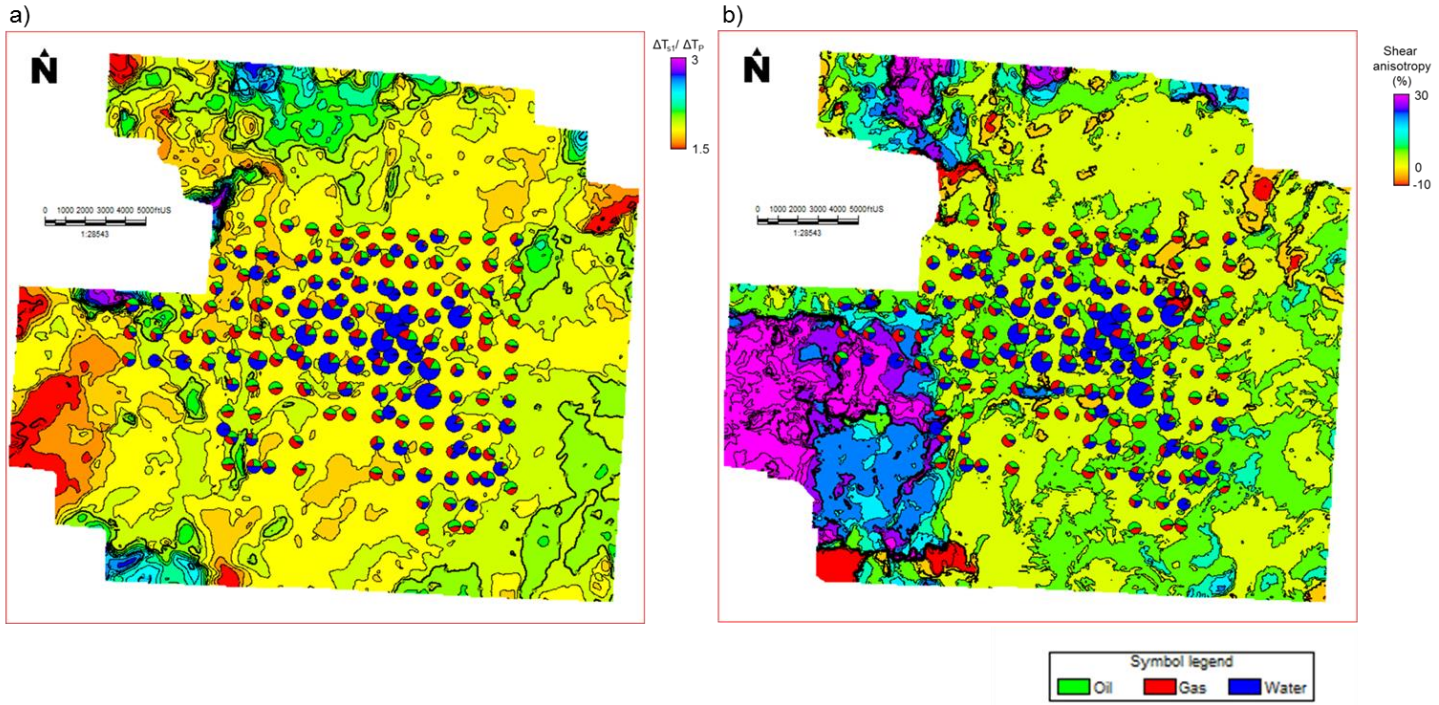

Figure 7.16: (a) $\Delta T_{s1}/\ \Delta T_p$ and (b) shear anisotropy maps with first 90 days production overlaid. Production and horizon based anisotropy do not show a clear correlation. In a broad sense the bulk of the production is located at the center of the survey. Most of the horizon based anisotropy variation is also present at the center of the survey. Production pie chart size is relative to the amount of production.

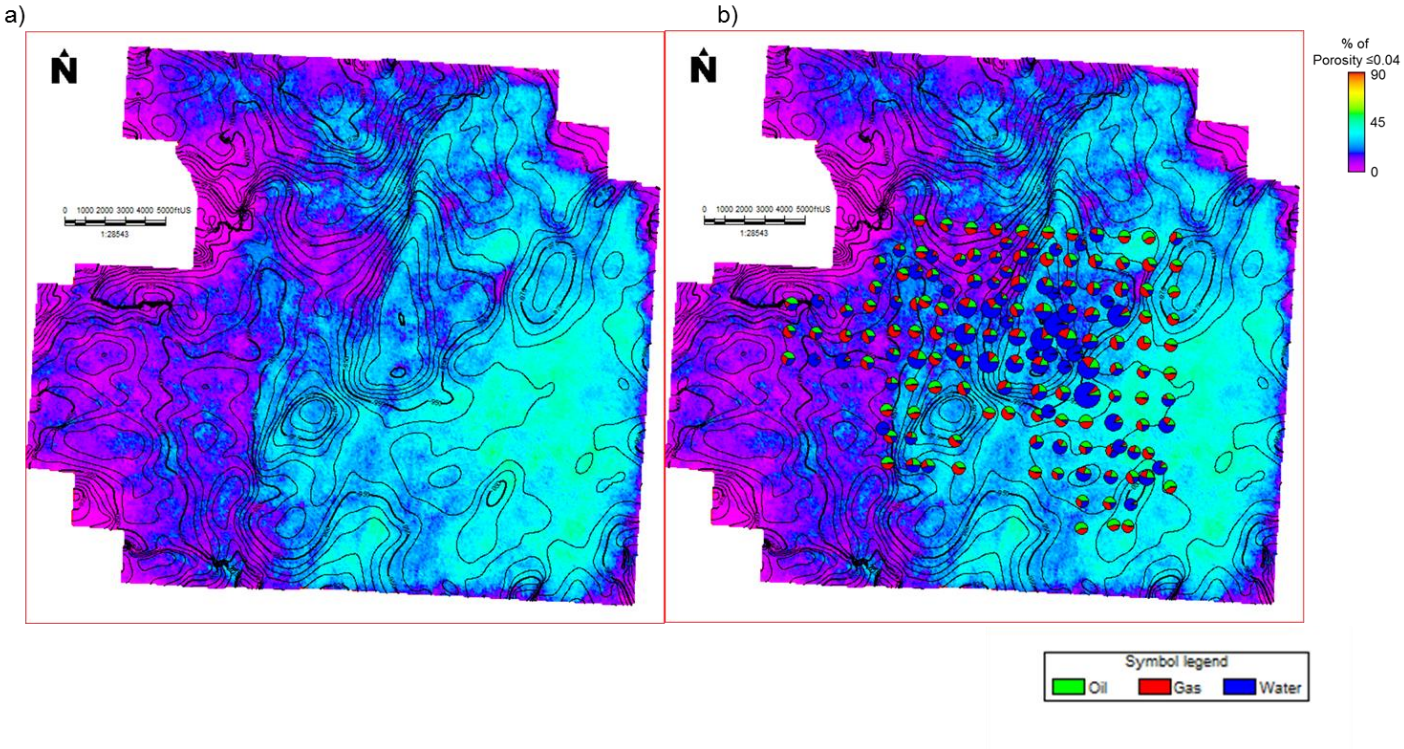

Figure 7.17: (a) Percentage of porosity below 4% for the porosity horizon probe shown in Figure 7.15. (b) Percentage of porosity below 4% for the porosity horizon probe shown in Figure 7.15 with production data overlaid. As we expected, low zones do not show a strong correlation with production. Production pie chart size is relative to the amount of production.

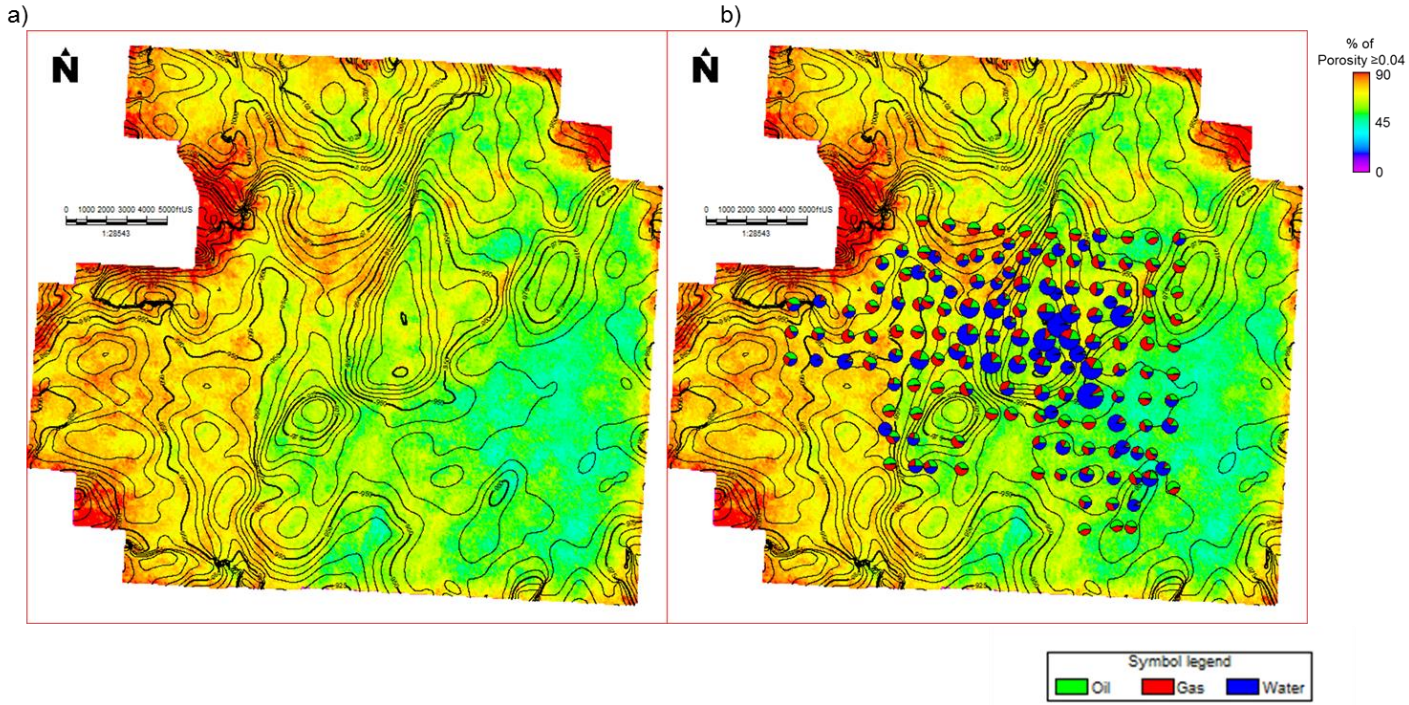

Figure 7.18: (a) Percentage of porosity above 4% for the porosity horizon probe shown in Figure 7.15. (a) Percentage of porosity above 4% for the porosity horizon probe shown in Figure 7.15 with production data overlaid. There is a strong correlation between very good producer wells and high porosity zones. This indicates that production is mainly driven by porosity. Production pie chart size is relative to the amount of production.

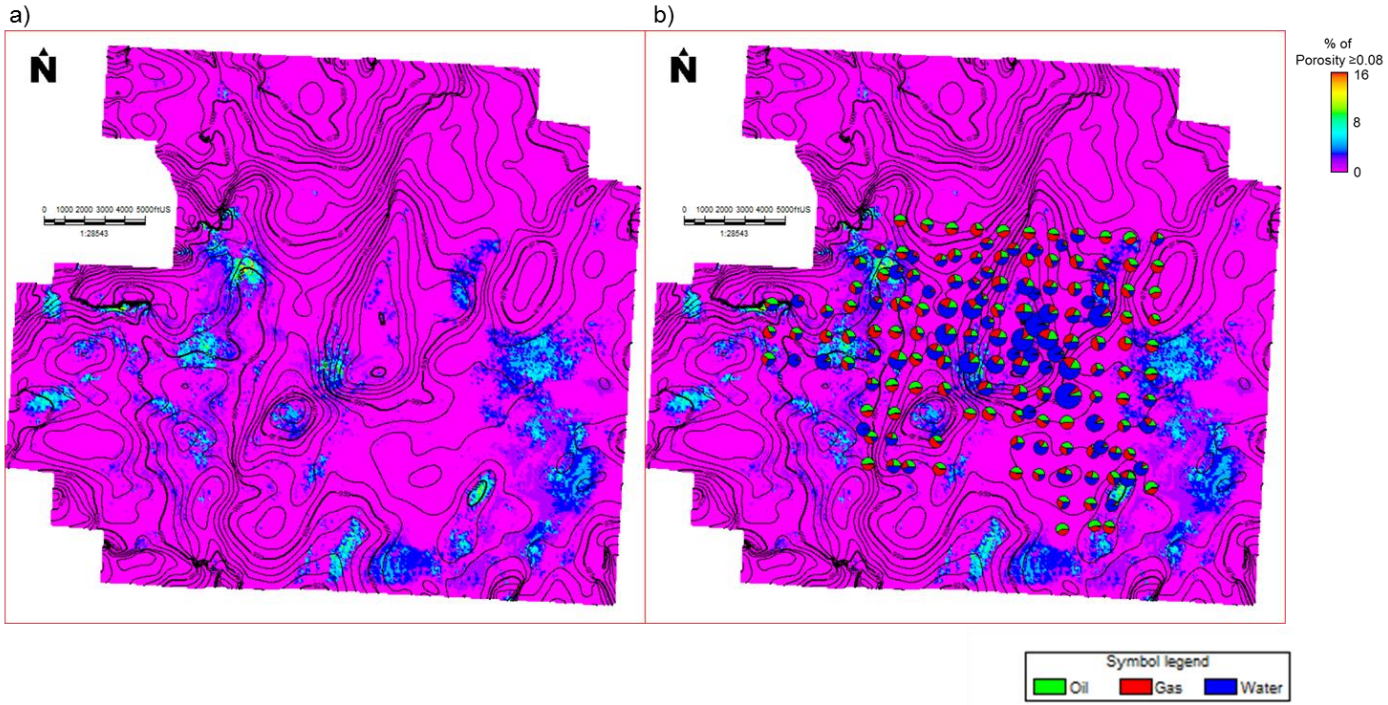

Figure 7.19: (a) Percentage of porosity above 8% for the porosity horizon probe shown in Figure 7.15. (a) Percentage of porosity above 8% for the porosity horizon probe shown in Figure 7.15 with production data overlaid. High porosity zones show a correlation with oil and gas production. Most of the wells located in a high porosity zone have a relative higher hydrocarbon production to water production. Production pie chart size is relative to the amount of production.

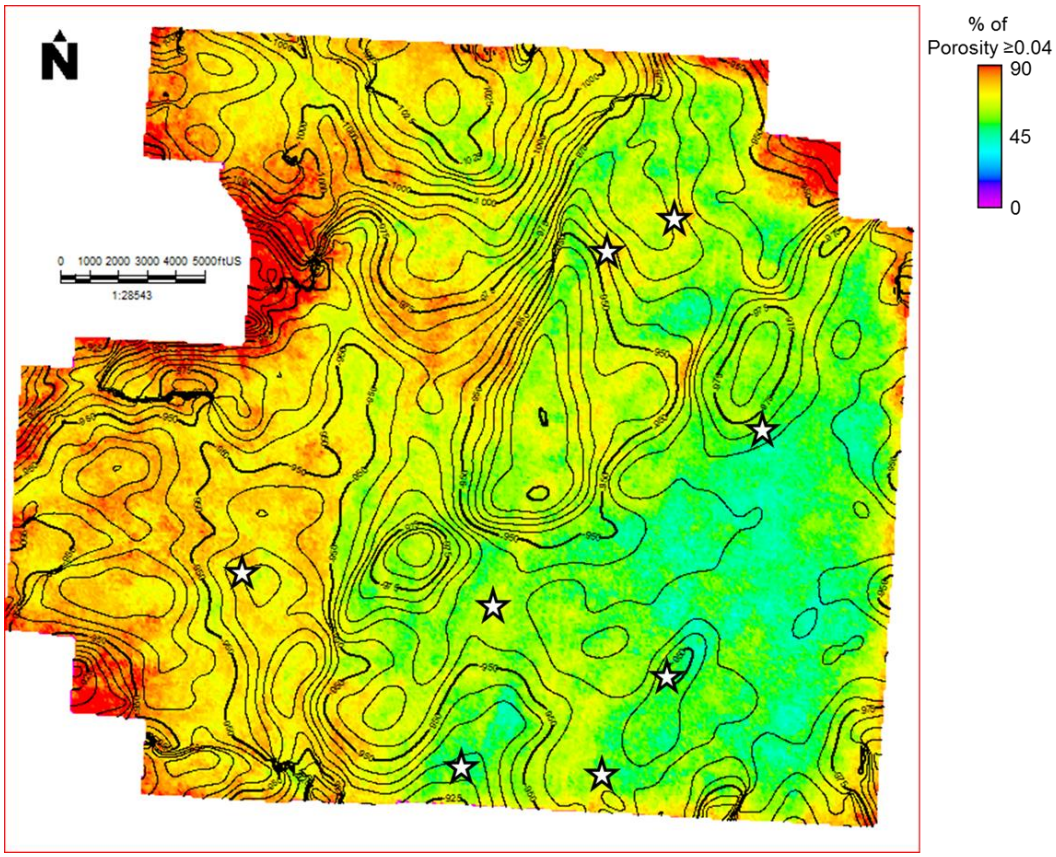

Figure 7.20: Percentage of porosity above 4% for the porosity horizon probe shown in Figure 7.18. Proposed drilling locations are indicated by white stars.

REFERENCES

Al-Dossary, S., and K. J. Marfurt, 2006, Multispectral estimates of reflector curvature and rotation: Geophysics, **71**, P41-P51.

Bergbauer, S., T. Mukerji, and P. Hennings, 2003, Improving curvature analyses of deformed horizons using scale-dependent filtering techniques: AAPG Bulletin, 87, 1255-1272.

Fisher, A. J., 2005, Predicting spatial distribution of critical pore types and their influence on reservoir quality, Canyon (Pennsylvanian) reef reservoir, Diamond M Field, Texas: Master's thesis, Texas A&M University.

Hardage, B., M. V. DeAngelo, P. E. Murray, and D. Sava, 2011, Multicomponent Seismic Technology, 1st Edition: Society of Exploration Geophysicists.

Hobson, G.D., 1989, Production from carbonate reservoirs, Oil field development techniques: AAPG Studies in Geology No. 28, 193-207.

Jianming, T., H. Yue, X. Xiangrong, J. Tinnin, and J. Hallin, 2009, Application of converted-wave 3D/3C data for fracture detection in a deep tight-gas reservoir: TLE, 28, 826-837.

Garotta, R., 1985, Observation of shear waves and correlation with P events, in G. Dohr, ed., Seismic shear waves, Part B: Applications, Chapter 1: Geophysical Press, 1–86.

Melville, P., O. Al Jeelani, .S. Al Menhali, and J. Grötsch, 2004, Three-dimensional seismic analysis in the characterization of a giant carbonate field, onshore Abu Dhabi, United Arab Emirates, in Seismic imaging of carbonate reservoirs and systems: AAPG Memoir **81**, p. 123-148.

Neuhaus, D., J. Borgomano, J.-C. Jauffred, C. Mercadier, S. Olotu, and J. Grötsch, 2004, Quantitative seismic reservoir characterization of an Oligocene–Miocene carbonate buildup: Malampaya field, Philippines, in Seismic imaging of carbonate reservoirs and systems: AAPG Memoir **81**, p. 169–183.

Pardus, Y. C., J. Conner, N. R. Schuler, and R. H. Tatham, 1990, VP/VS and lithology in carbonate rocks: A case history in the Scipio Trend in southern Michigan: 60th Annual International Meeting of the SEG, Expanded Abstracts, 169–172.

Pearson, R. A., and B. S. Hart, 2004, Three-dimensional seismic attributes help define controls on reservoir development: Case study from the Red River Formation, Williston Basin, *in* Seismic imaging of carbonates reservoirs and systems: AAPG Memoir **81**, 43–57.

Pranter, M. J., N. F. Hurley, and T. L. Davis, 2004, Sequence-stratigraphic, petrophysical, and multicomponent seismic analysis of a shelf-margin reservoir: San Andres Formation (Permian), Vacuum field, New Mexico, United States, *in* Seismic imaging of carbonate reservoirs and systems: AAPG Memoir **81**, 59–89.

Saller, A. H., S. Walden, S. Robertson, R. Nims, H. Hagiwara, and S. Mizohata, 2004, Three-dimensional seismic imaging and reservoir modeling of an upper Paleozoic ‘‘reefal’’ buildup, Reinecke field, west Texas, United States, *in* Seismic imaging of carbonate reservoirs and systems: AAPG Memoir **81**, 107–122.

Tinker, S., D. H. Caldwell, D. M. Cox, L. C. Zahm, and L. Brinton, 2004, Integrated Reservoir Characterization of a Carbonate Ramp Reservoir, South Dagger field.

New Mexico: Seismic data are only part of the story, in Seismic imaging of carbonate reservoirs and systems: AAPG Memoir **81**, p. 59-90.

Vahrenkamp, V. C., F. David, P. Duijndam, M. Newall and P. Crevello, 2004, Growth architecture, faulting, and karstification of a middle Miocene carbonate platform, Luconia province, offshore Sarawak, Malaysia, in Seismic imaging of carbonate reservoirs and systems: AAPG Memoir **81**, p. 329-350.

8. Resolving subtle stratigraphic features using spectral ridges and phase residues

Oswaldo Davogustto[1], Marcílio Castro de Matos[1], Carlos Cabarcas[1], Toan Dao[1] and Kurt J. Marfurt[1]

[1] University of Oklahoma, School of Geology and Geophysics,

ABSTRACT

Seismic interpretation is dependent on the quality and resolution of seismic data. Unfortunately seismic amplitude data are often insufficient for detailed sequence stratigraphy interpretation. In this work, we review a method to derive high resolution seismic attributes based upon complex Continuous Wavelet Transform (CWT) pseudo-deconvolution and phase-residue techniques. The pseudo-deconvolution method is based upon an assumption of a blocky earth model that allows us to increase the frequency content of seismic data that for our data better matches the well log control. The phase residue technique allows us to extract information not only from thin layers but also from interference patterns such as unconformities from the seismic amplitude data. Using data from a West Texas carbonate environment, we show how pseudo-deconvolution can be used not only to improve the seismic well ties but also to provide sharper sequence terminations. Using data from an Anadarko Basin clastic environment we show how phase residues delineate incised valleys seen on the well logs but difficult to see on vertical slices through the original seismic amplitude.

INTRODUCTION

Fourier spectral analysis is a key component of seismic data processing. Random and coherent noise filtering, spectral balancing, wavelet shaping and Q compensation are all based on spectral analysis. Spectral analysis techniques are also useful in seismic interpretation. Using a running window spectral analysis, also called a short window discrete Fourier transform (SWDFT), Partyka et al. (1999) computed the spectra for overlapping windows thereby producing a 4D time-frequency data volume. These 4D frequency data volumes can be used to detect lateral changes in thickness. In addition to the SWDFT, one can use transforms based on a library of wavelets, giving rise to the continuous wavelet transform (CWT) and matching pursuit (MP) algorithms (Castagna et al., 2003).

Taner et al. (1979) introduced complex trace attributes such as quadrature, envelope, phase and instantaneous frequency, attributes that are well known amongst the geophysical community. Taner et al. (1979) noted that the instantaneous frequency, *f*, suffered discontinuities associated with abrupt changes in phase, which in turn were associated with waveform interference located at envelope, *e*, minima. To remove these discontinuities, Taner et al. (1979) introduced a weighted average frequency, f^{avg}, at time $t=k\Delta t$ as:

$$f_k^{avg} = \frac{\sum_{j=-K}^{+K} e_{k-j} f_{k-j}^{inst} L_j}{\sum_{j=-K}^{+K} e_{k-j} L_j}$$

where *e* is the envelope (also called reflection strength), f^{inst} is the instantaneous frequency, and L is a low pass filter.

Combining the concepts of instantaneous and weighted average frequency, Taner (2000) introduced a “thin bed indicator” attribute by removing the weighted

average frequency from the instantaneous frequency thereby enhancing zones where wavelet destructive interference takes place. The thin bed indicator is given by:

$$f^{thin} = f^{inst} - f^{avg}$$

These zones of destructive interference are referred to as frequency spikes. In Figure 8.1 we show an example of the instantaneous frequency, weighted average frequency and thin bed indicator attributes.

Zeng (2010) used synthetic models and field data to correlate frequency spikes with geological information, defining two types of frequency spikes. Type I spikes are related to the destructive interference of the top and base layer reflection of a wedge. Type II spikes are more indicative of thin beds. Zeng (2010) show Type II spikes occur at wavelengths less than 1/5 of a wavelength (Figure 8.2).

Liner et al. (2004) introduced a technique based on the Hough transform to detect singularities in the CWT magnitude spectra. Using Liner et al's. (2004) algorithm Smythe et al. (2004) showed that discontinuities in the CWT of the underlying impedance model are preserved as discontinuities seen in band-limited seismic amplitude data.

In general, seismic data amplitudes are not as well preserved as seismic phases. Matos et al. (2011) therefore introduced an alternative spectral discontinuity method based on the phase of the CWT components. Since instantaneous frequency is the time derivative of the instantaneous phase, there is a direct relationship between Matos et al.'s (2011) phase discontinuity and earlier work by Taner (2000) and Zeng (2010). Likewise there is a similarity between (Matos et al., 2011) pseudo deconvolution and "spectral whitening" deconvolution operators implemented in the frequency domain.

We begin our paper with a review of spectral decomposition to generate pseudo-deconvolution and phase residues attributes. We then apply these methods to a carbonate system from West Texas and show how these algorithms can help accelerate interpretation of thin reflectors. Then we apply these algorithms to a Red Fork incised valley system from the Anadarko Basin and show how phase residues correlate to sequence boundaries seen on logs. We conclude with a discussion of assumptions, processing workflows and limitations associated with these two attributes.

METHODOLOGY REVIEW

Spectral Ridges and Pseudo-deconvolution

The CWT is simply the cross-correlation between the seismic trace and dilated versions of a symmetric "mother" wavelet (Grossman and Morlet, 1984). Since the "mother" wavelet is symmetric, we can compute the CWT by convolving the seismic trace with the time-reversed scaled version of the basic wavelet (Figure 8.3c). Since convolution in the time domain is equivalent to multiplication in the frequency domain, we can also interpret the CWT as a suite of band pass filters resulting in spectral components. Each seismic trace is represented by a time (depth) versus frequency band (or "scale") complex matrix. This matrix represents how well the seismic trace correlates to each dilated wavelet at each instant of time (Matos and Marfurt, 2011).

Mallat and Zhong (1992) showed that the CWT ridges along the frequency bands are associated with signal inflection points that characterize much of the signal (Figure 8.3d). They also showed that we can reconstruct a non-unique but very good approximation of the seismic trace by using only the CWT ridges (Figure 8.3e), which they called Wavelet Transform Modulus Maxima Line Amplitudes (WTMML). Tu and

Hwang (2005) later proved that the same concept can be applied using complex wavelets. Grossman and Morlet (1984) showed that the complex CWT magnitude represents the average magnitude of each spectral component (dilated wavelet) at each instant of time. Likewise, the maximum averages, or the ridges, along the scales (WTMMLA) show the existence of consistent signal transitions.

Borrowing CWT spectral ridge (WTMMLA) ideas from Mallat and Zhong (1992) and Tu and Hwang (2005), several authors have shown how CWT spectral ridges can be associated with reflectivity series (Hermann and Stark, 2000; Matos et al., 2011; Liner et al. 2004, Devi and Schwab, 2009). Matos and Marfurt (2011) showed how to enhance seismic resolution by using complex Morlet CWT spectral ridges and reconstructing the seismic trace using broader band wavelets than those used in the original analysis giving a result they call pseudo-deconvolution (PD). This process is schematically shown in Figure 8.3.

Figure 8.4a shows a single 2D synthetic seismic response of a channel with thicknesses varying from 0 to 50 ms. Figure 8.4b shows the pseudo-deconvolution result. We can clearly see the improvement in the seismic resolution. Figure 8.4c shows the relative acoustic impedance computed from Figure **8.4**b. This high-resolution seismic representation can be considered a reflectivity approximation, which can be integrated to estimate the relative acoustic impedance (RAI) (Berteussen and Ursin, 1983). The RAI computation consists of three steps:

1. Rescale the high resolution trace, by keeping the magnitude much smaller (we suggest 10 times) than one,

2. Integrate the trace using the procedure designed by Peacock (1979) for discrete integration, and
3. High pass filter (we suggest $f > 10$ Hz) the integrated data to provide RAI.

We assume that the earth impedance model is blocky thus giving rise to a suite of sparse spikes that we convolve with a narrow-band seismic wavelet giving rise to conventional seismic data. We can replace these wavelets, frequency by frequency, with their broad-band equivalents thereby generating a broadband signal. The process relies on the original frequency information of the narrow-band wavelets; hence the frequencies not sampled will not be reconstructed. We validate all these assumptions by tying the broadband data to well synthetic seismograms.

Spectral Discontinuities and Phase Residues

Although the complex CWT phase can be used to reconstruct the high-resolution trace, Bone (1991) showed that a shifted and dilated wavelets can interfere with another wavelet creating a signature in the phase spectra. This interference or inconsistency is called a phase residue. Matos et al. (2011) showed how one can detect phase discontinuities in the Morlet complex wavelet transform phase component. They implement the technique developed by Ghilgia and Pritt (1998) for detecting phase anomalies using a rectangular window and looking for inconsistent phase values when unwrapping these phase components. Matos et al. (2011) use phase residues to map wavelet interference patterns that correlate with stratigraphic discontinuities as well as inconsistencies in seismic data quality. To demonstrate this concept we generated a three layer synthetic wedge model embedded in a shale background. We used a Ricker

wavelet with a peak frequency of 46 Hz and 100 ms length. In Figure 8.5 we show the spectral magnitude and spectral phase for 15, 30 and 70 Hz frequencies for our wedge model. We are able to identify the phase discontinuities described by Ghilgia and Pritt (1987) within each magnitude-phase pane for each frequency. Figure 8.6 shows the phase residues generated using the model shown in Figure 8.5.

Note the discreet type I and type II spikes seen in Figure 8.6 appear as a more continuous anomaly in the phase residue seen in Figure 8.6c allowing one to track the discontinuity laterally. Cohen (1993) showed that instantaneous attributes estimate the average properties of the seismic wavelet, such as the instantaneous frequency of an isolated wavelet. Note that both type I and type II discontinuities appear at approximately 60 Hz (green). Examining Figure 8.6c we note the phase residue at these two locations also occurs at 60 Hz (green). Rather than "probing" for discontinuities at the average frequency, the phase residue algorithm probes at a suite of frequencies on CWT spectral components, thereby giving rise to a laterally continuous anomaly.

Comparing Figure 8.4 and Figure 8.6 we see the complementary nature of CWT phase-residues, high-resolution spectral ridges and relative acoustic impedance and their potential use in seismic interpretation. Specifically, spectral ridges enhance individual reflectors while phase residues enhance unconformities and pinchouts.

APPLICATION OF CWT ATTRIBUTES TO IMPROVE RESERVOIR GEOMETRY INTERPRETATION

Carbonate environment example (Midland Basin, TX)

The Diamond M data set consists of approximately 25 mi^2 of seismic data with a high signal to noise ratio located in Scurry County, TX (Figure 8.7). We computed the

pseudo-deconvolution and relative acoustic impedance attributes to determine if they better define the stratigraphic sequences of interest. Figure 8.7 shows the location of the composite seismic line and the location of two wells used for the interpretation. Figure 8.8 and Figure **8.9** show representative synthetic seismograms used to tie well data to the original seismic data and pseudo-deconvolution data respectively. The original data show a minimum phase character whereas the bandwidth extension process not only enhances the resolution of the data but also converts it to zero-phase. Examining composite line AA' we compare the original seismic data with the pseudo-deconvolution data in our integrated interpretation with the well data (Figure 8.10). We identify reflector terminations on Figure 8.10b in the vicinity of well 2 that on Figure 8.10a appear as a continuous reflector. Further evaluation using the well logs allows us to interpret the sequence as a highstand to transgressive systems track progression (Figure 8.10c). We compared the PD and seismic amplitude data and found that the PD data shows a better defined progradational sequence with internal onlap and downlap terminations for the identified sequence (Figure 8.10c-d). We proceed to evaluate the relative acoustic impedance character of this clinoform using a seismic probe and are able to extract the top and the base of the clinoform sequence and convert them to seismic horizons (Figure 8.11). We display our relative acoustic impedance created horizons on the original seismic data and the pseudo-deconvolution (Figure 8.12a) data and corroborate that the top and base horizons correspond to the previously identified highstand systems tract sequence. Finally we compare the relative acoustic impedance result with the acoustic impedance log finding a strong correlation (Figure 8.12b). This result demonstrates the reliability of the relative acoustic impedance using the CWT

method in areas where little or no well control is available. Equally important, generating the horizons using PD, RAI, and geobody extraction took 30 minutes versus 3 hours using the conventional "auto-tracker" seismic interpretation.

Clastic environment example (Anadarko Basin, OK)

Red Fork sands are a prominent gas producer in the Anadarko Basin. The Red Fork stratigraphy consists of regional deltaic deposits that endured five stages of fluvial incision during a sea level low stand. Such fluvial incisions are informally called "invisible channels" since they cannot be identified on stacked seismic data but are encountered by subsequent drilling to deeper targets (Peyton, et al. 1998, Suarez et al., 2008; Barber, 2010).

Figure 8.13 shows a map with the location of the seismic data of the Watonga field, well locations and composite line locations and Peyton et al. (1998) interpretation of the Red Fork incised valleys using semblance, 30 Hz spectral magnitude and well data. Collaborating with Chesapeake Energy geoscientists we show an updated version of Peyton et al.'s (1998) cross-section AA' using the exact same well data (Figure 8.14). Figure 8.15 and Figure **8.16** show the synthetic seismograms for wells R and S respectively. These are the only wells with sonic and density logs in the survey. Well R penetrates the regional Red Fork sequence. Well S penetrates incision stage V. Time to depth curves differ depending on the geologic section a well penetrates. We found that wells that penetrate the regional Red Fork share a similar time to depth relationship while wells that penetrate any of the incision stages share a different time to depth relationship. By using these two different time to depth curves we were able to tie most wells on Peyton et al.'s (1998) AA' cross-section with our seismic amplitude and phase

residue data. Composite line AA' through the seismic data shows one of these incisions (Figure 8.17). Once we have tied all the wells in Figure 8.14 with the seismic data we compared the well tops from the regional Red Fork and the incision stages with anomalies observed in the seismic data. In the seismic amplitude section we are able to correlate only the Pink Lime, Inola Limestone and Stage V tops (Figure 8.17b-c). Using phase residues and the regional Red Fork and incision stage tops from Figure 8.14, we not only identify the Stage V incision as in Figure 8.17, but are also able to identify two additional phase residue anomalies that correspond to the other stages of incision that were invisible on the seismic data (Figure 8.18b-c). We proceed to interpret the phase residues attribute in a conventional way and generate surfaces from the Pink Lime and stages I-V (Figure 8.19). Using these interpreted surfaces we create a 3D geocellular model and compare it to Peyton et al.'s (1998) original interpretation (Figure 8.20). Figure 8.21 shows a 3D perspective of the regional Red Fork and each incision stage. Each stage occurred in a different depositional environment with stage I having lag deposits and Stage V filled by a shale plug (Suarez et al. 2008). Separating each stage from the regional Red Fork facilitates geologic modeling each stage to estimate reservoir properties consistent with the depositional environment.

Conclusions

Spectral analysis has long been used in seismic processing and interpretation. We have demonstrated how CWT pseudo-deconvolution (PD), relative acoustic impedance (RAI) and phase residues can be effectively applied to reveal and enhance stratigraphic features that are buried in conventional seismic amplitude data. PD enhances reflector terminations, facilitating seismic sequence stratigraphy

interpretation. RAI computed for PD when used as a geobody extraction and interpretation tool, accelerates the interpretation of clinoforms and complex features. Phase residues extends the well-established thin bed indicator and instantaneous frequency spike interpretation workflows, providing more continuous discontinuities, as well as the magnitude and frequency at which they occur. We have developed a workflow that combines seismic amplitude with CWT attributes in order to produce a high frequency seismic stratigraphy framework for seismic interpretation. Finally, we have demonstrated how by combining CWT attributes with detailed seismic stratigraphy, sequences can be extracted from the seismic data as an input for detailed reservoir characterization.

ACKNOWLEDGEMENTS

The authors would like to thank Chesapeake Energy Corporation for providing a license to well data and the original version of the seismic data and Mark Falk and Al Warner for their contribution to understand the complex geology of the Red Fork formation. We wish to thank CGG Veritas for providing a license to the reprocessed data that forms part of a mega merge survey. We thank Parallel Petroleum LLC for providing a license to the Diamond M dataset and Alison Small for her invaluable help on interpretation of the Diamond M data. We thank Schlumberger for donating Petrel Software for use in research and education. We thank Dr. Hongliu Zeng, Dr. Dengliang Gao, Dr. Bruce Hart, and Dr. Yonghe Sun whose careful reviews and detailed comments helped improve this paper. Finally we would like to thank Andrea Miceli, Dr. J. Tim Kwiatkowski, Bradley C. Wallet, Richard Brito and Roger Slatt for their help and support.

LIST OF FIGURES

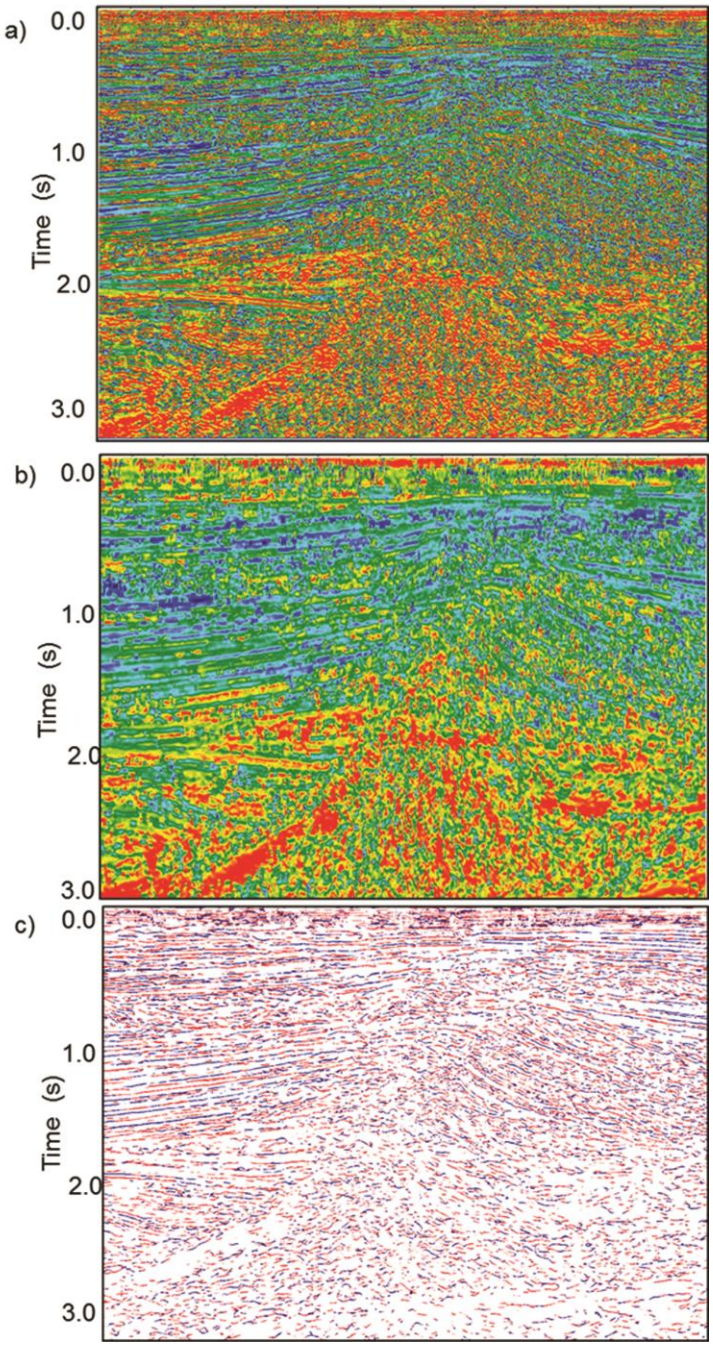

Figure 8.1: Vertical slices through (a) instantaneous frequency, f^{inst}, (b) envelope weighted average frequency, f^{avg}, and (c) thin-bed indicator, $f^{thin}=f^{inst}-f^{avg}$, obtained as the difference between the (a) and (b). (c) Is plotted using a color bar that highlights the extreme values (After Taner, 2000).

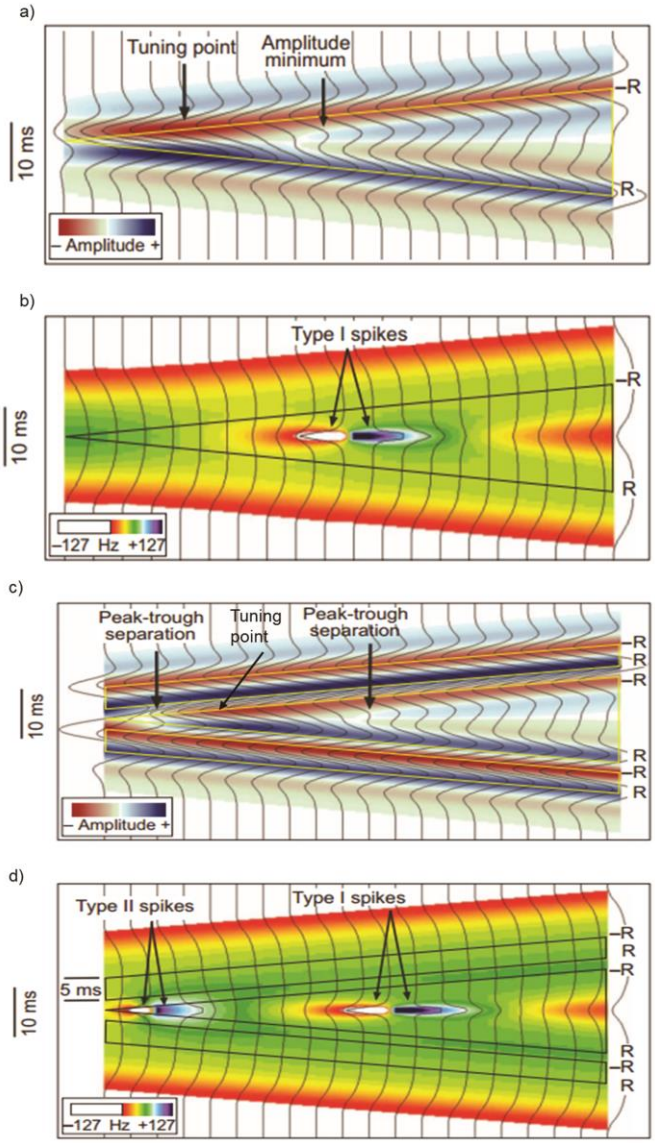

Figure 8.2: Zeng's (2010) (a) seismic amplitude and (b) corresponding instantaneous frequency from a three-layer model giving rise to a reflector coefficient of –R and +R for the first and second interface. Note the "type I" spikes within the center layer. (c) Seismic amplitude and (d) corresponding instantaneous frequency for a seven layer model giving rise to a suite of –R, +R, –R, +R, -R, +R, reflection coefficients between interfaces. On these model two types of frequency spikes can be identified. (b) Zeng (2010) defines the anomaly observed at the center of the model as a Type I spike. Note that the spike appears at wavelengths larger than tuning wavelength. (d) Zeng (2010) finds that type II spikes are associated with thin beds, they depend on the impedance contrast of the layers, and the predominant wavelet frequency in which they occur is inversely proportional to the thickness of the beds.

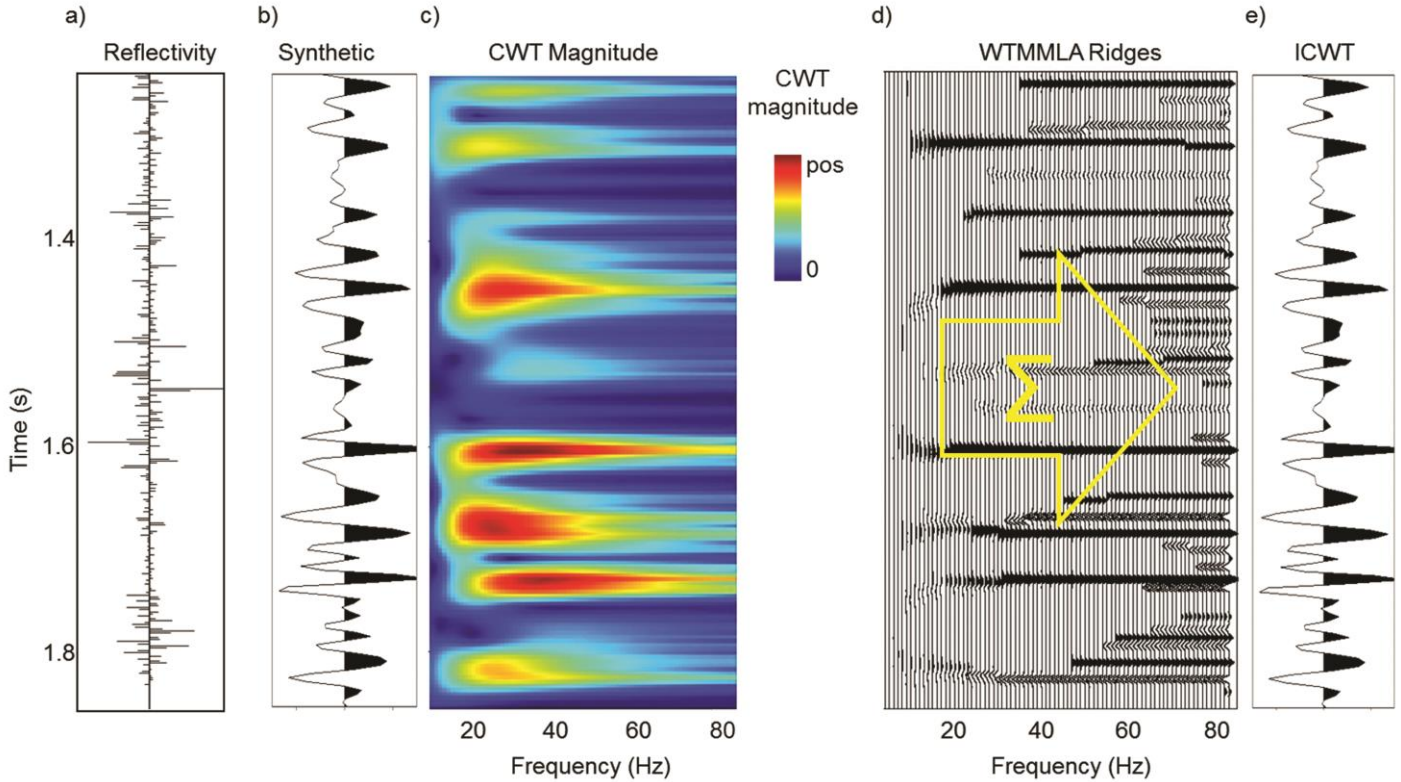

Figure 8.3: Schematical representation of the pseudo-deconvolution process (After Matos and Marfurt, 2011). (a) Time reflectivity series for a representative seismic trace. (b) Synthetic seismogram generated by convolving (a) with a 30 Hz Ricker wavelet. (c) CWT magnitude of (a). (d) WTMMLA ridges computed from (c). (e) Reconstructed data using (d) and a 30 Hz Ricker wavelet.

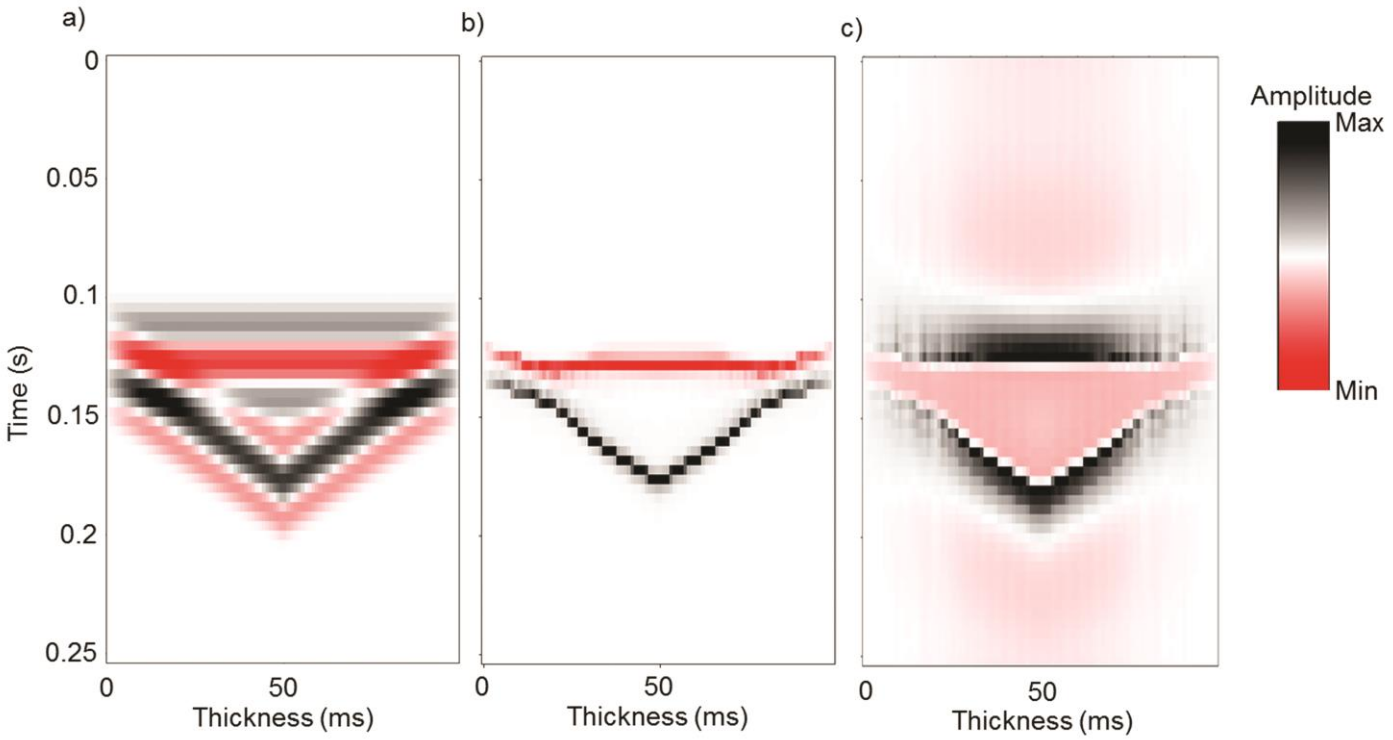

Figure 8.4: (a) Synthetic channel model, (b) enhanced resolution result after PD process and (c) relative acoustic impedance computed from (b).

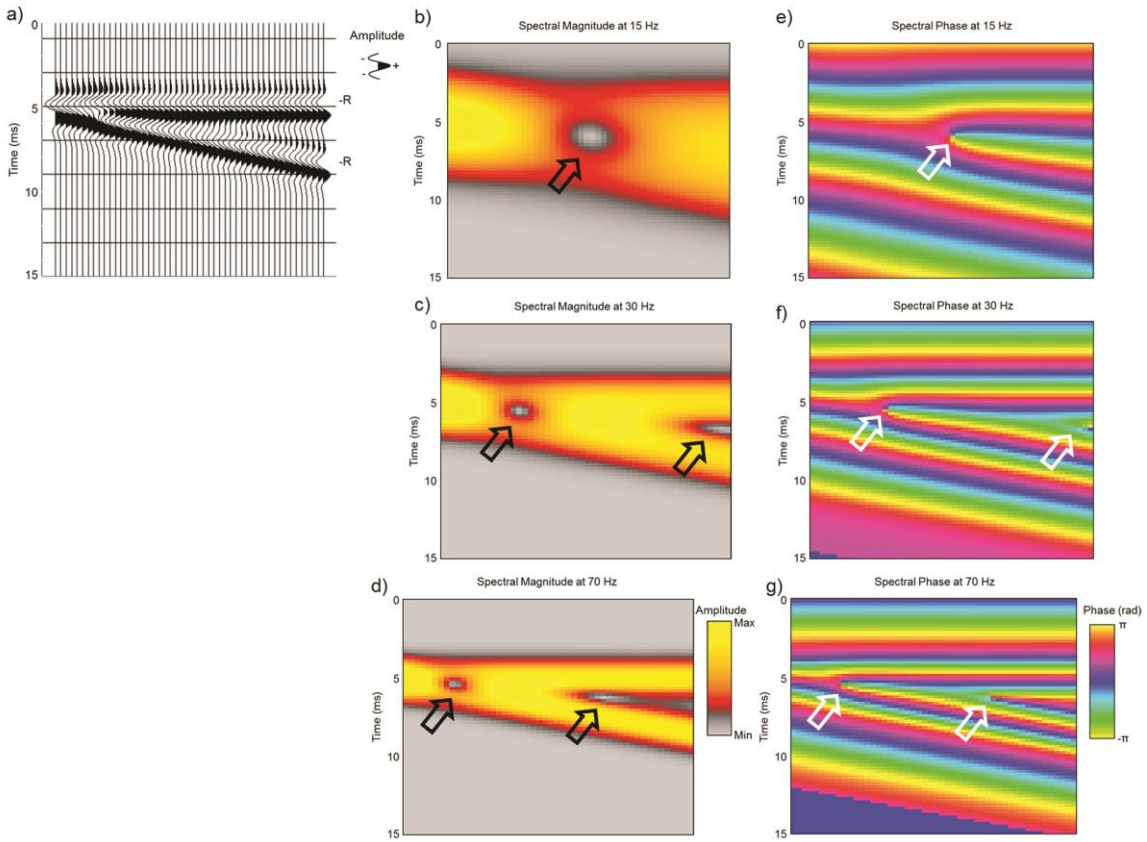

Figure 8.5: (a) Amplitude from a 3 layer synthetic wedge model. Corresponding CWT spectral magnitude response at (b) 15, (c) 30 and (d) 70 Hz and phase response at (e) 15, (f) 30 and (g) 70 Hz. We identify phase anomalies in the spectral phase (white arrows) and magnitude (black arrows). This is the phenomena first described by Ghiglia et al. (1998). Note that the anomaly location is frequency dependent.

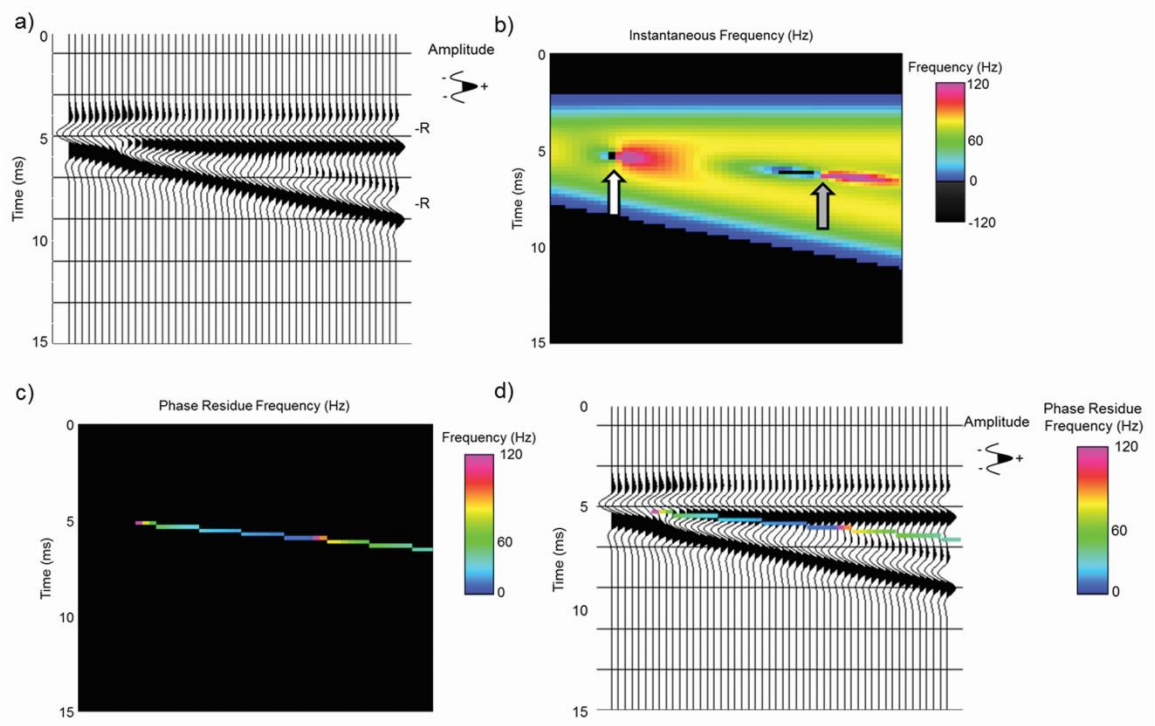

Figure 8.6: (a) 3 layer synthetic wedge model shown previously in Figure 5. (b) corresponding instantaneous frequency exhibiting type I and type II discontinuities. (c) phase residue where the color indicates the frequency at which the residue (discontinuity) occurs. Anomalies on (b) and (c) occur at the same wedge thicknesses and are generated by the same interference pattern in the data. (b) grey arrow indicates type I spike and white arrow indicates type II spikes (Zeng, 2010). (d) Phase residues give a more continuous anomaly allowing it to be more easily mapped.

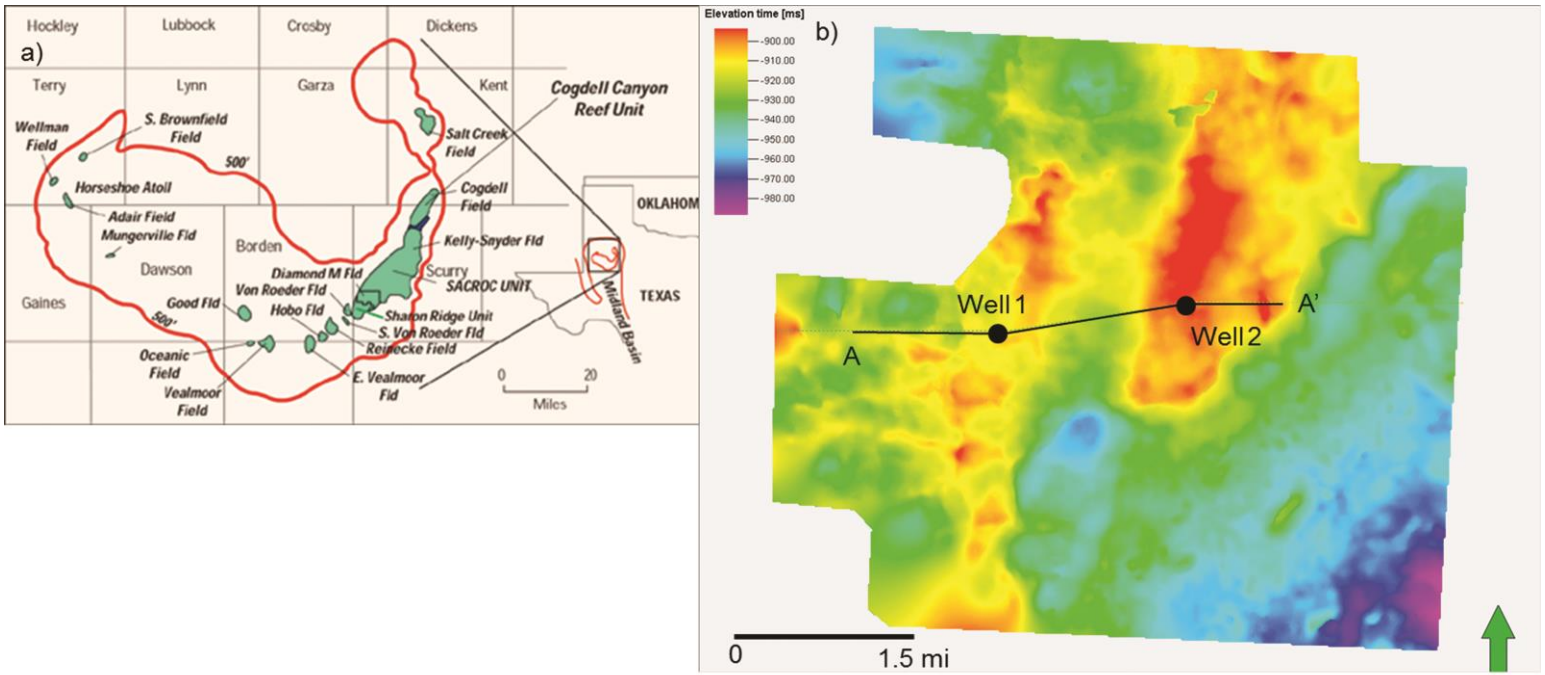

Figure 8.7: (a) Map displaying the location of the Diamond M field in Scurry County, Texas (Modified from Pennel and Melzer, 2003). (b) Time structure map along the top reef pick showing the location of line A-A'.

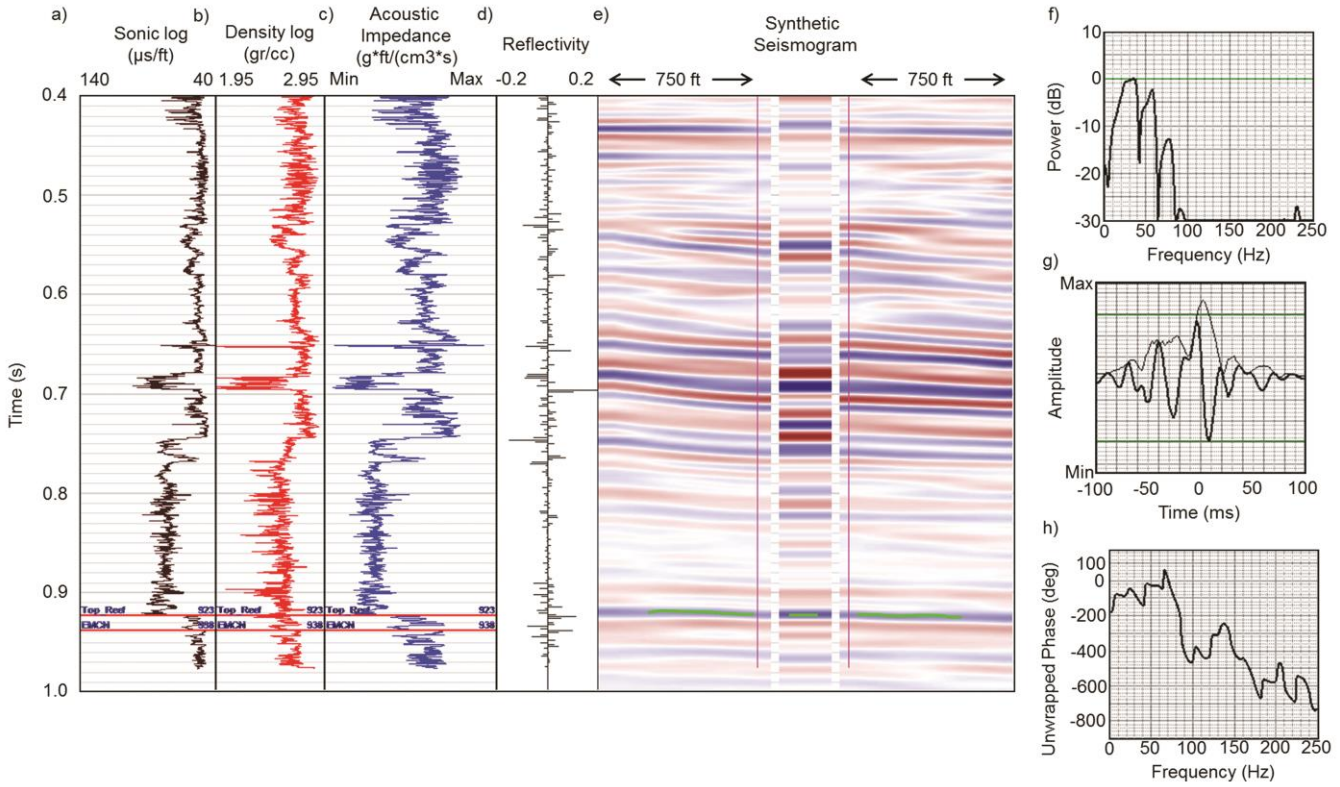

Figure 8.8: Well 2 synthetic seismogram using the seismic amplitude data. The correlation was done using a 250 ms window centered at 870 ms. The correlation coefficient is 68%. The green marker in the synthetic window corresponds to the top of the Horseshoe Atoll reef. Note that the extracted wavelet is minimum phase.

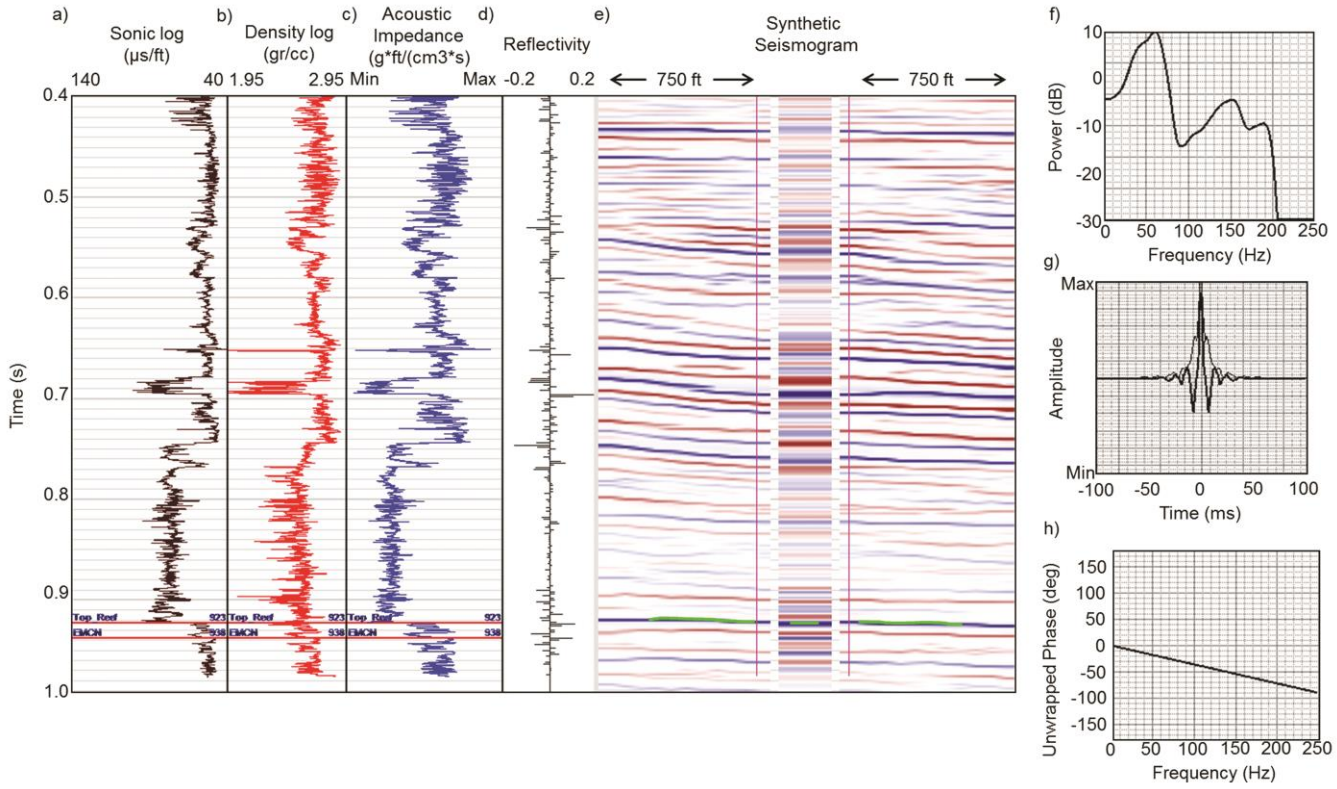

Figure 8.9: Well 2 synthetic seismogram using the PD data. The correlation was done using a 250 ms window centered at 870 ms. The correlation coefficient is 79%. The green marker in the synthetic window corresponds to the top of the Horseshoe Atoll reef. Note that the extracted wavelet is zero phase.

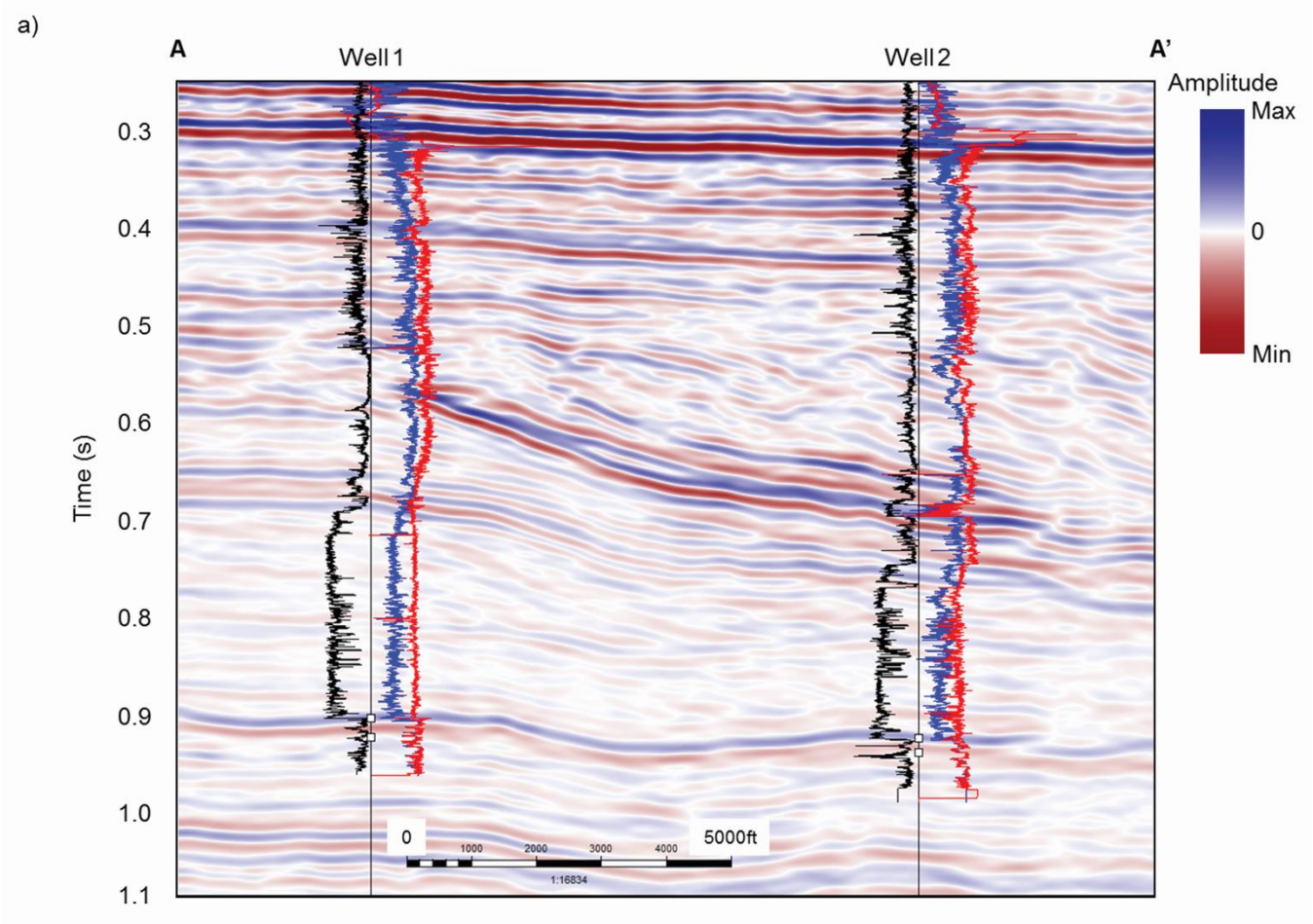
a)
A
Well 1
Well 2
A'
Amplitude
Max
0
Min
Time (s)
0.3
0.4
0.5
0.6
0.7
0.8
0.9
1.0
1.1
0
1000
2000
3000
4000
5000ft
1:16834

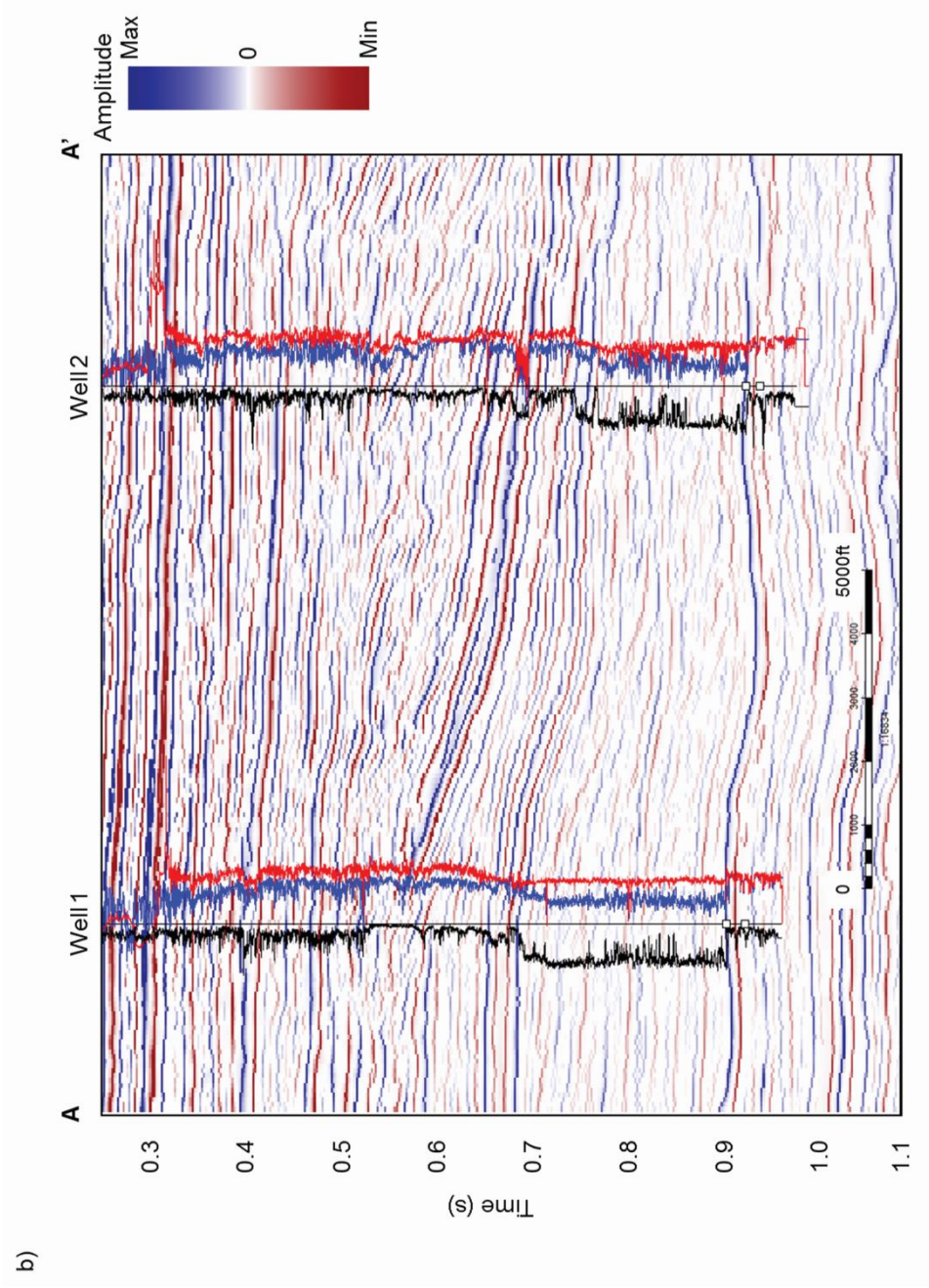
b)
A
A'
Well1
Well2
Amplitude
Max
0
Min
Time (s)
0.3
0.4
0.5
0.6
0.7
0.8
0.9
1.0
1.1
0
5000ft

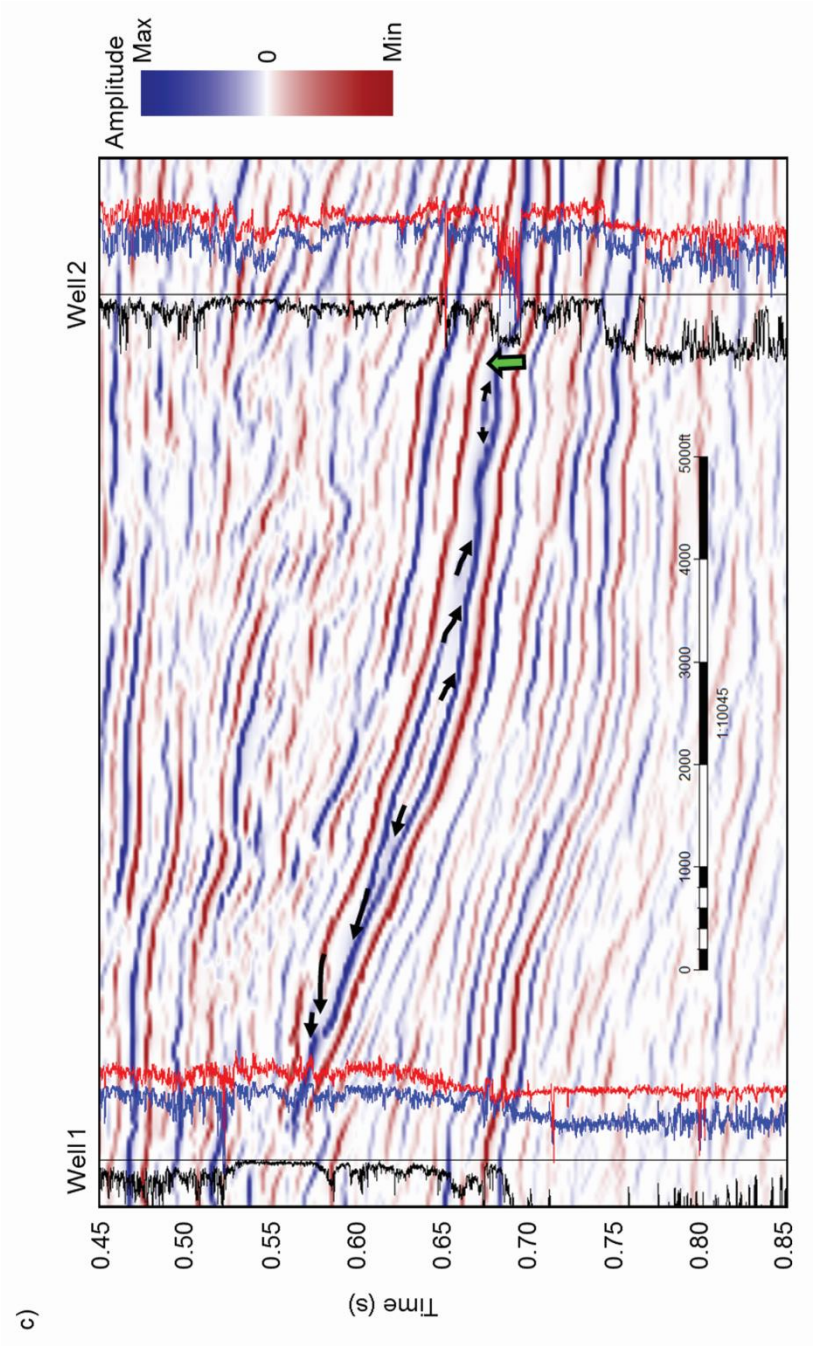
Amplitude
Max
0
Min
Well 2
Well 1
5000ft
4000
3000
2000
1000
0
1:10045
0.45
0.50
0.55
0.60
0.65
0.70
0.75
0.80
0.85
Time (s)
c)

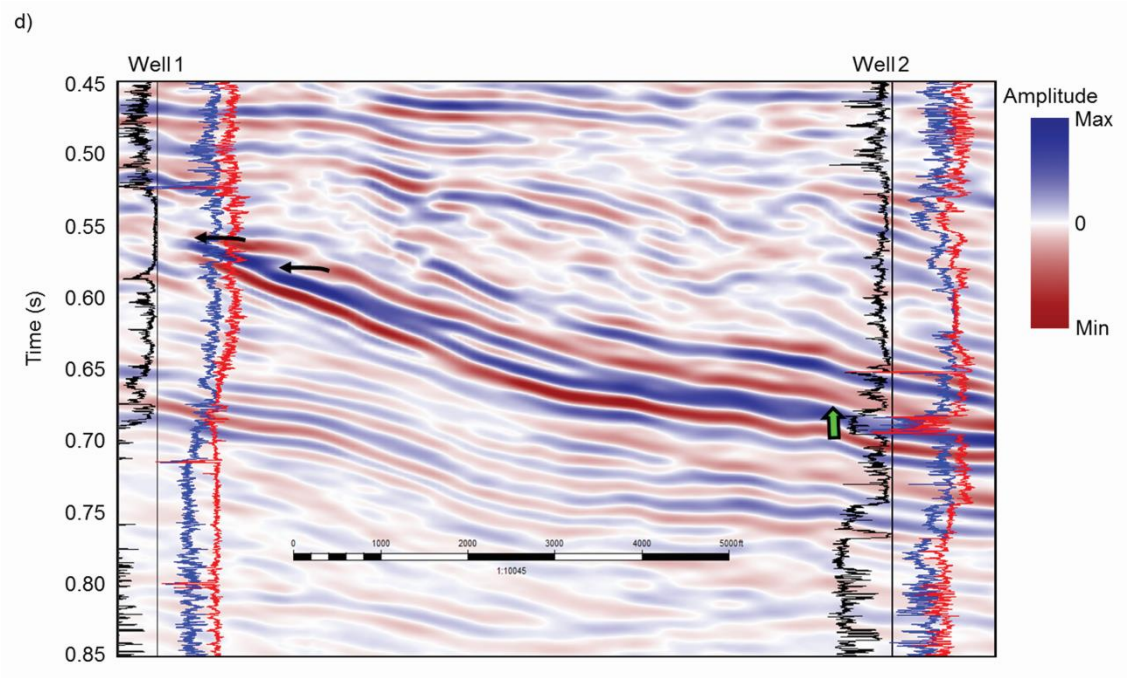

Figure 8.10: Cross-section A-A' displaying wells 1 and 2 converted to time using the time to depth relationship from the pseudo-deconvolution seismic well tie (Figure 9). (a) Although the time to depth relationships were created using the PD data, these relationships work well with the seismic amplitude data too. Log curves on the wells are gamma ray (black), bulk density (red) and neutron porosity (blue). The gamma ray values increase to the left and the bulk density and neutron porosity values increase to the right. (b) PD data cross-section A-A' displaying wells A and B converted to time the time to depth relationship from the pseudo-deconvolution seismic well tie (Figure 9). With the PD data it is easier to identify onlaps, toplaps, downlaps and reflector truncations than with the seismic amplitude data. (c) PD data cross-section A-A' zoomed on the clinoform interval. Black arrows indicate downlap or onlap features identified in the internal structure of the clinoform. On well 2 we identify a highstand to transgressive systems track sequence (green arrow) that correlates with our onlap and downlap features. Note that the same event is not identified on well 1, indicating that well 1 is closer to the shelf. (d) Seismic amplitude data cross-section A-A' zoomed on the clinoform interval. Besides the onlap features close to well 1 it is difficult to identify any other clear reflector terminations in the seismic amplitude data.

Max
Relative Acoustic Impedance
Min
0
100
Opacity
Well B
Well A
a)

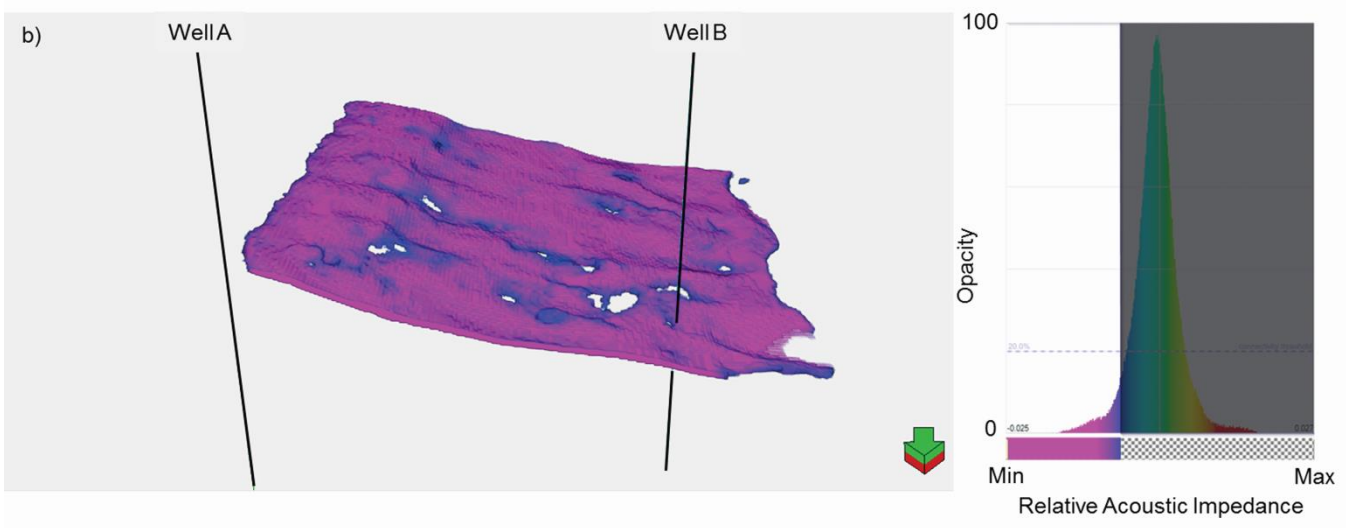
b)
Well A
Well B
100
Opacity
0
Min
Max
Relative Acoustic Impedance

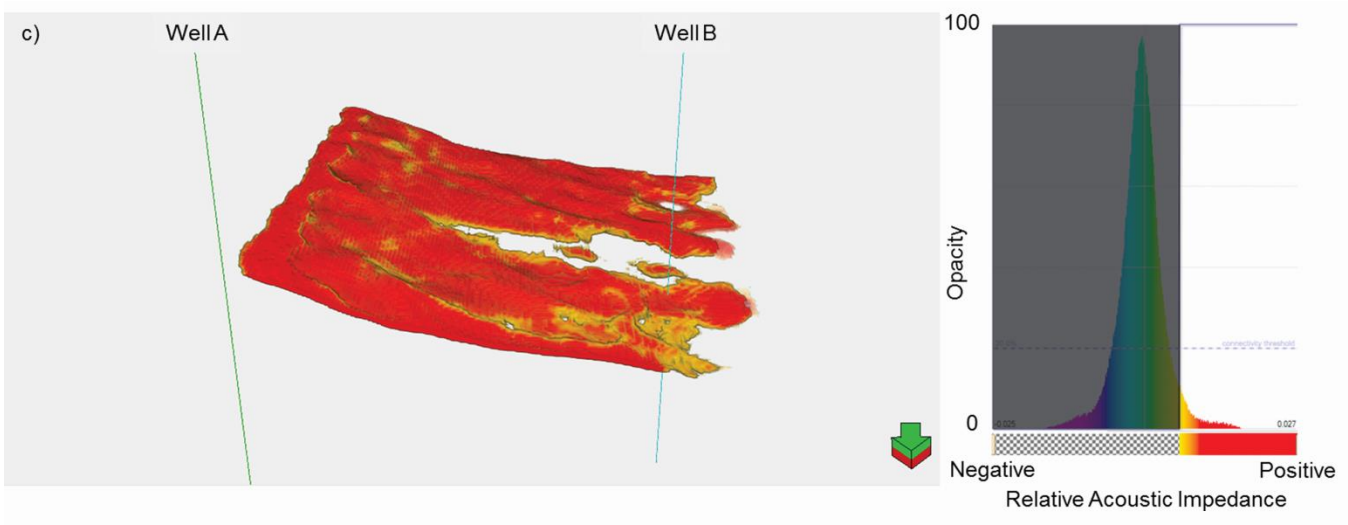

Figure 8.11: (a) RAI volume probe with all voxels in the probe plotted opaque. We will use opacity on the histogram to isolate the response of the top (magenta) and base (red) of the prograding sequence shown in Figure 10. Note that the clinoform interval has a distinctive response being delimited by the highest and the lowest values of RAI. (b) Setting the low amplitude voxels opaque isolates the top boundary of the clinoform interval. (c) Setting the high amplitude voxels opaque isolates the bottom boundary of the clinoform interval. We use these two geobodies as input for out seismic interpretation.

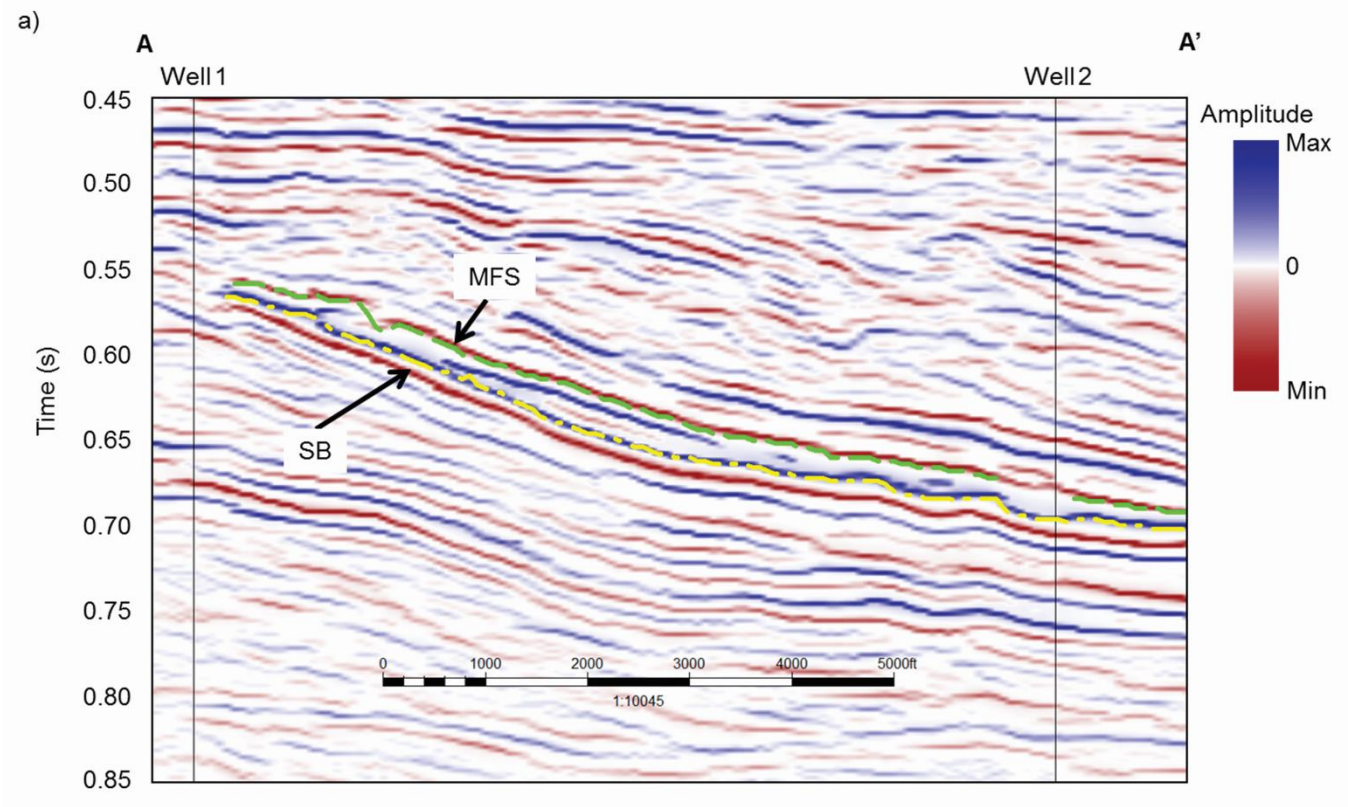
a)
A
A'
Well 1
Well 2
0.45
0.50
0.55
0.60
0.65
0.70
0.75
0.80
0.85
Time (s)
MFS
SB
Amplitude
Max
0
Min
0
1000
2000
3000
4000
5000ft
1:10045

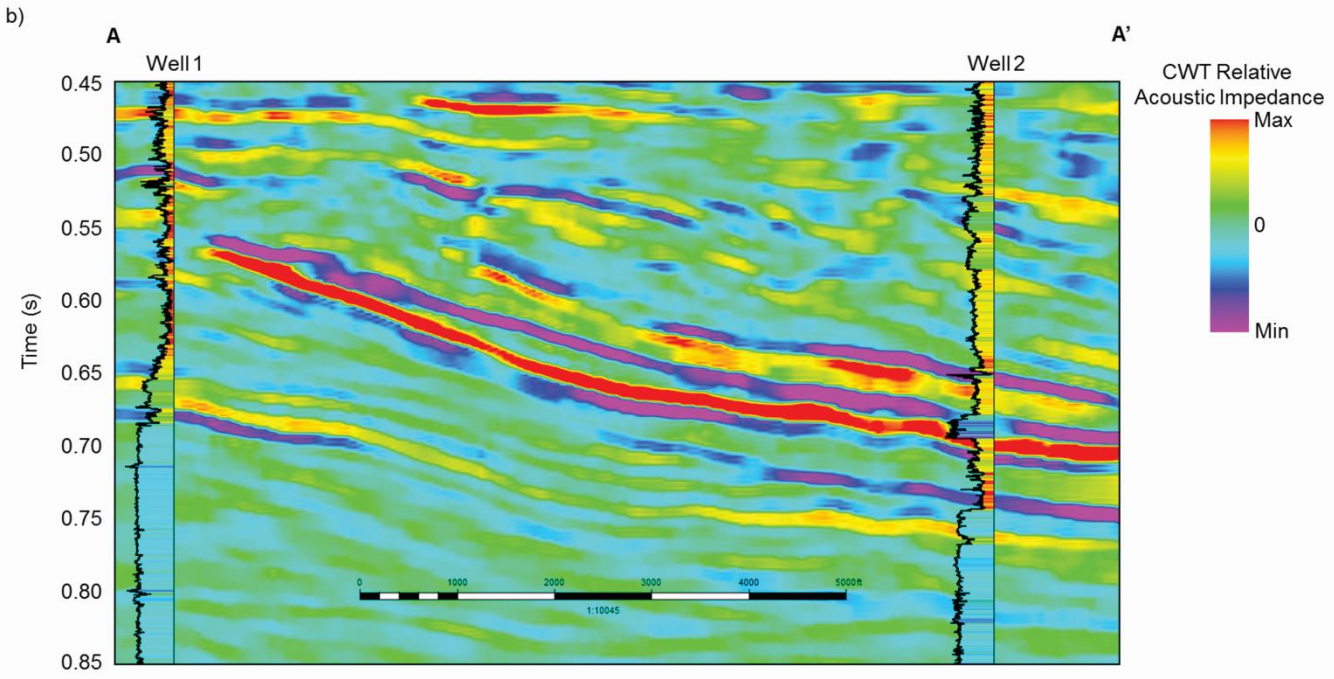

Figure 8.12: (a) Using the geobody extraction shown in Figures 11b and c, we convert the top and bottom of the prograding sequence to the green and yellow seismic horizons. We interpret the green horizon as a flooding surface (FS) and the yellow horizon as a sequence boundary (SB). This interpretation is corroborated by the results found in Figures 10 and 11. (b) Comparison of the relative acoustic impedance volume with the acoustic impedance (AI) log from wells 1 and 2. Acoustic impedance log decreases to the right. At the zone of interest AI log and shows an excellent correlation with the RAI attribute, demonstrating that the relative acoustic impedance algorithm is reliable, and can be used in frontier zones where wells are not present to delineate zones of interest.

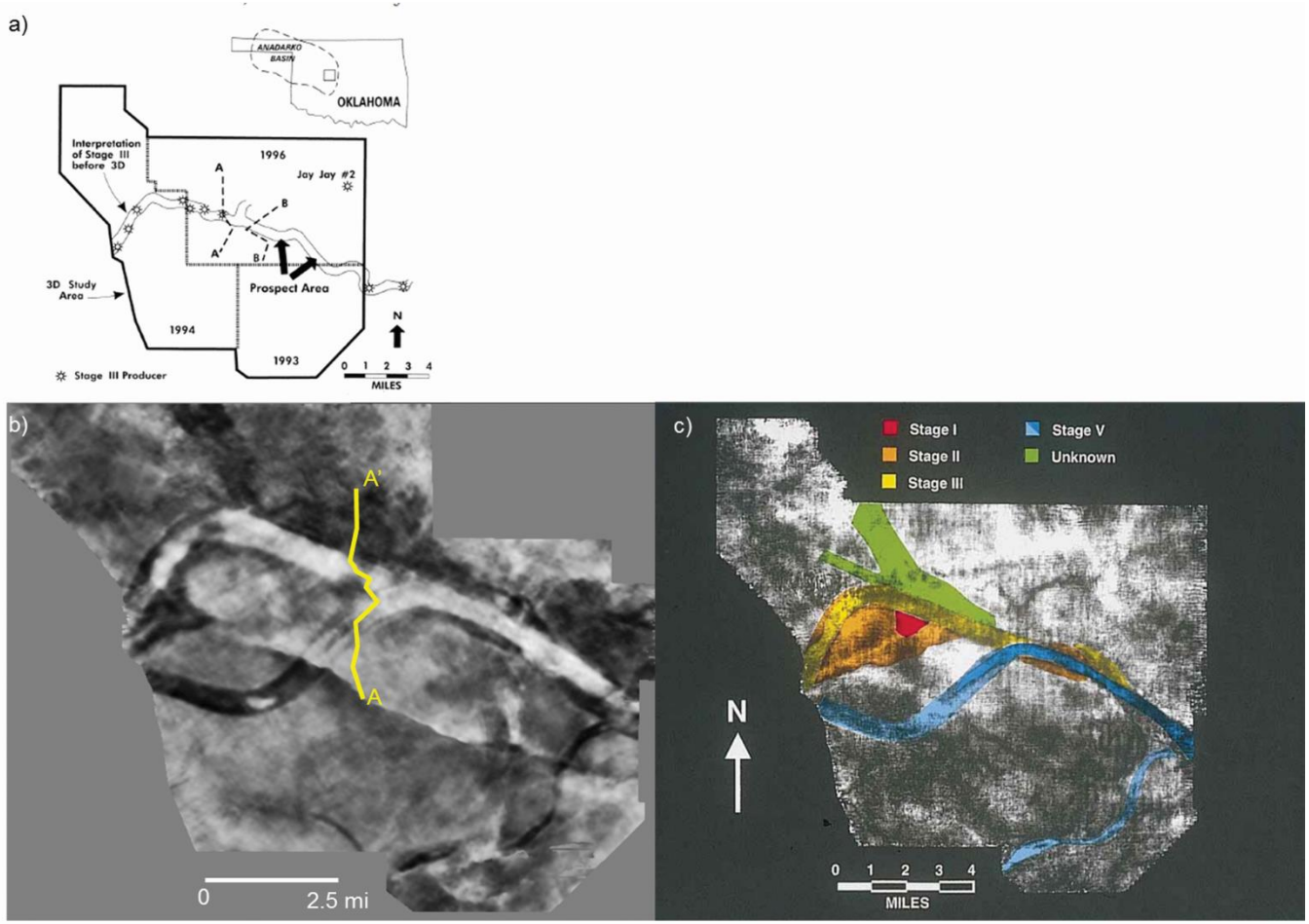

Figure 8.13: (a) Location of the Watonga dataset in the Anadarko Basin, OK (after Peyton et al., 1998). (b) Representative horizon through seismic amplitude at the top Pink Lime indicating the location of composite line AA'. (c) Red Fork incised valley stages I trough V (after Peyton et al., 1998).

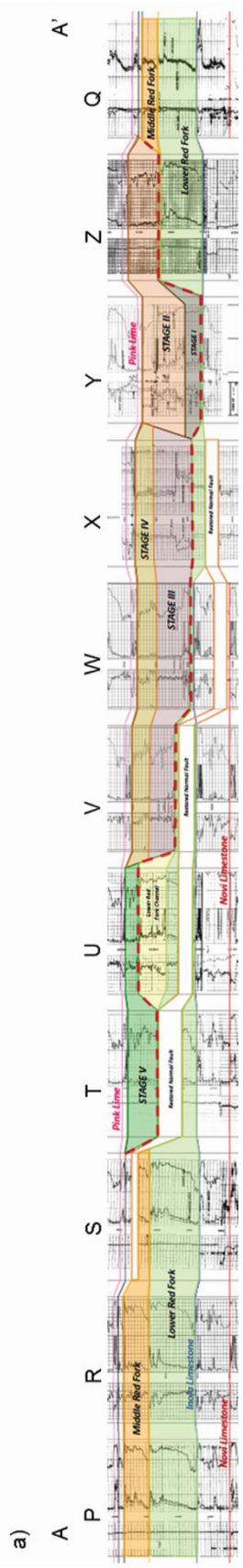
a)
A
P
R
S
T
U
V
W
X
Y
Z
Q
A'
Middle Red Fork
Lower Red Fork
Novi Limestone
Pink Lime
STAGE V
STAGE IV
STAGE III
STAGE II
STAGE I
Restored Normal Fault

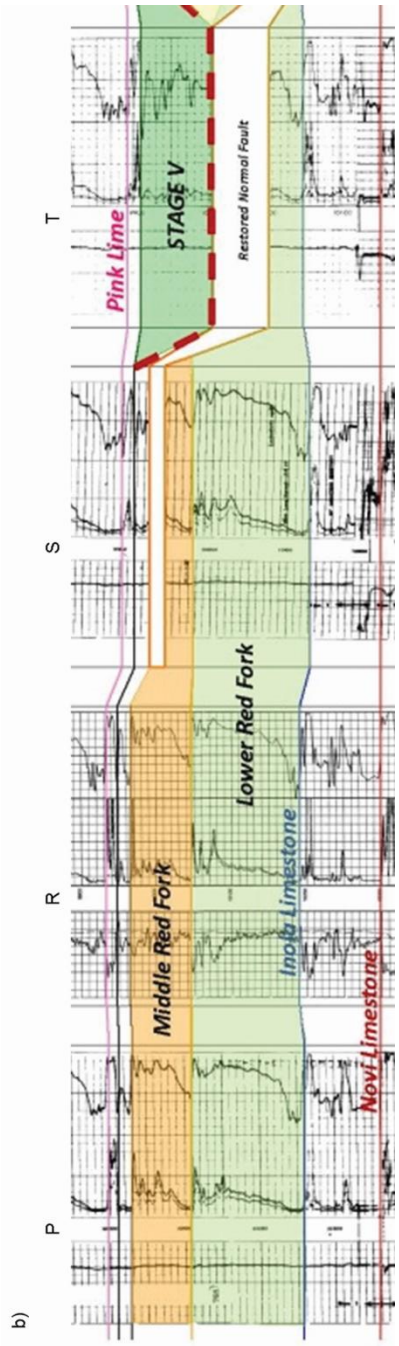
b)
P
R
S
T
Pink Lime
STAGE V
Restored Normal Fault
Middle Red Fork
Lower Red Fork
Inola Limestone
Novi Limestone

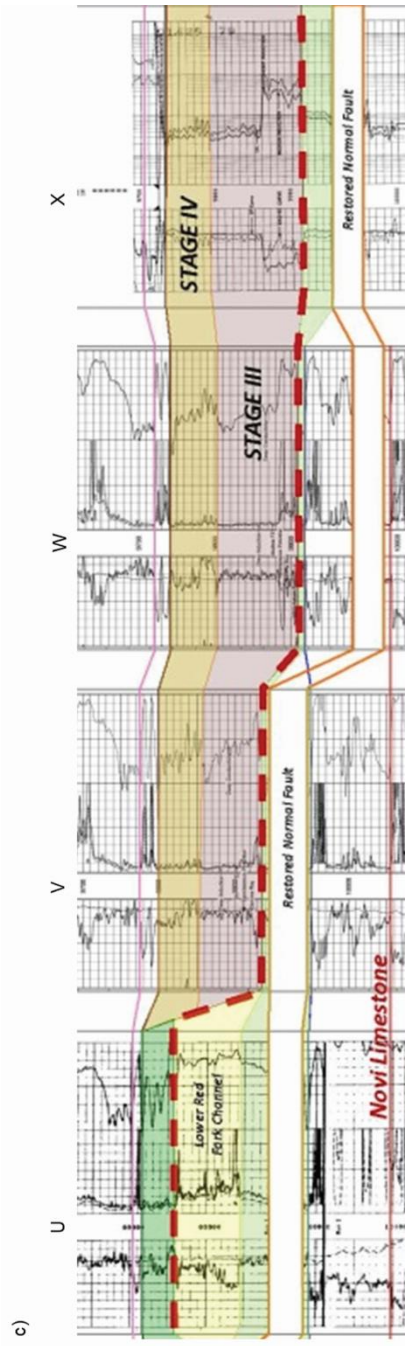
c)
U
V
W
X
STAGE IV
STAGE III
Restored Normal Fault
Restored Normal Fault
Lower Red Fork Channel
Novi Limestone

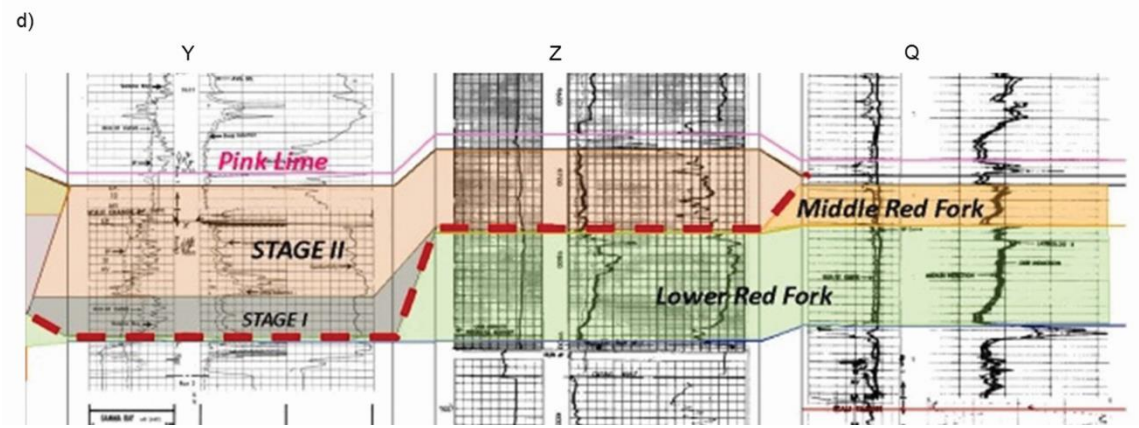

Figure 8.14: (a) Stratigraphic well log cross section A-A'. Based on the well log data and the interpreted well tops we define 5 incision stages on the Red Fork formation. This interpretation is similar to those of Peyton et al. 1998. (b)-(d) Zoomed portions of A-A' cross-section. Data and cross-section interpretation courtesy of Mark Falk and Al Warner, Chesapeake Energy Corporation.

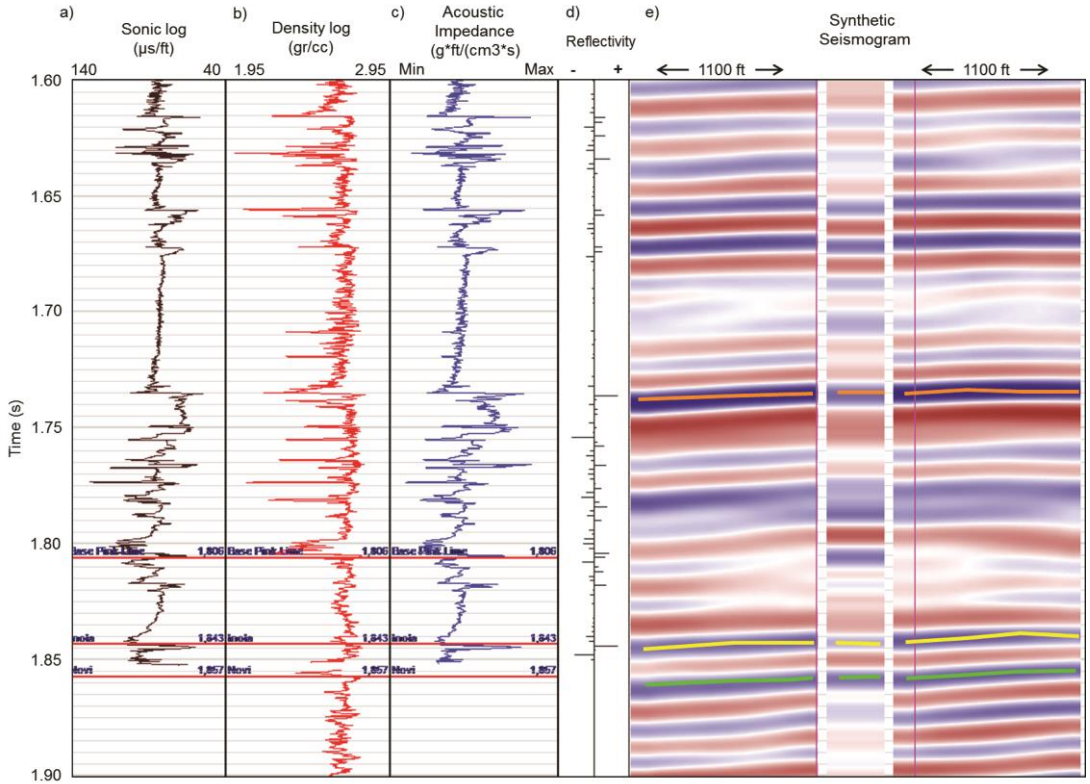

Figure 8.15: Well R synthetic seismogram using the seismic amplitude data. The correlation was done using a 250 ms window centered at 1800 ms. The correlation coefficient is 70%. Orange marker corresponds to the Oswego Limestone. Yellow marker corresponds to the Inola Limestone and green marker in the synthetic window corresponds to the top of the Novi Limestone.

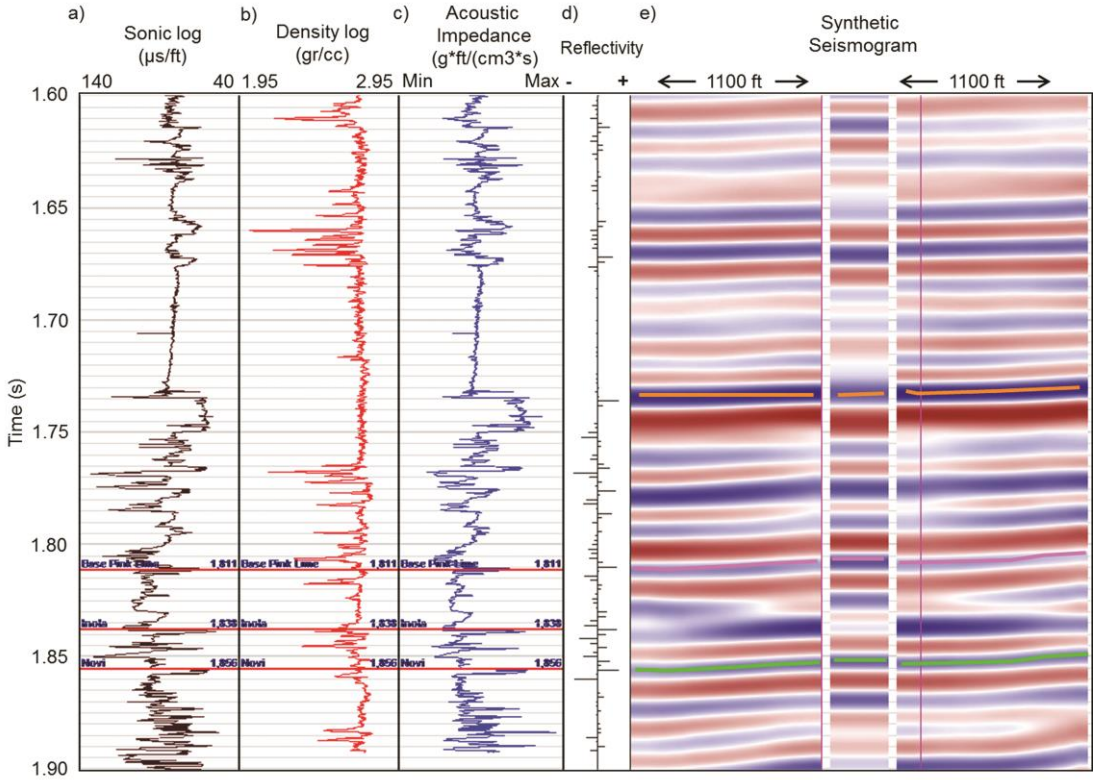

Figure 8.16: Well S synthetic seismogram using the seismic amplitude data. The correlation was done using a 300 ms window centered at 1800 ms. The correlation coefficient is 70%. Orange marker corresponds to the Oswego Limestone. Pink marker corresponds to the base of the Pink Lime and green marker in the synthetic window corresponds to the top of the Novi Limestone.

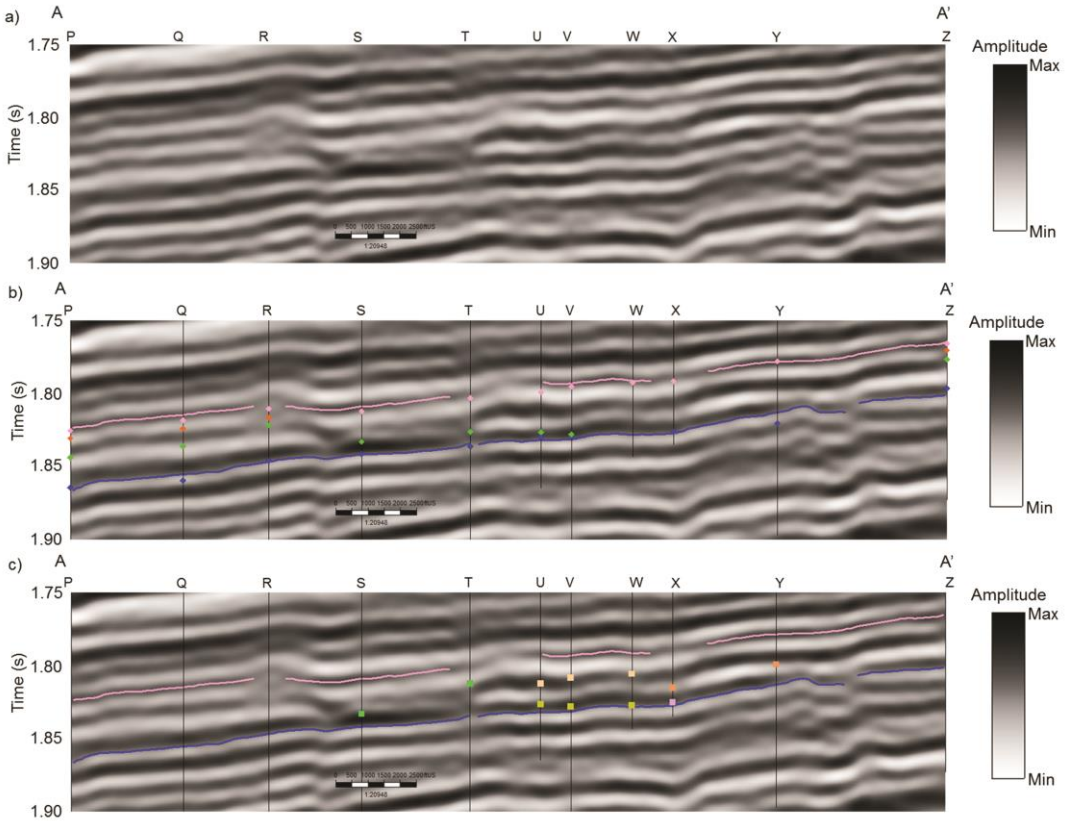

Figure 8.17: Vertical section AA' through (a) seismic amplitude data, (b) seismic amplitude data with Pink Lime (pink horizon) and Inola Limestone (blue horizon) interpreted on the seismic amplitude data using the guidance from the well-top data, and (c) interpreted seismic amplitude data with incision stages well-tops overlaid. (a) We are able to identify incision stage V between well S and U but stages I trough IV are "invisible" on the seismic amplitude data. (b) We interpreted the Pink lime and Inola limestone (pink and blue horizons respectively) and posted the interpreted tops for the same surfaces in each well to corroborate our interpretation. (c) By posting the interpreted incision stages surfaces from the well data we corroborate that stages I through IV of incision are "invisible on seismic vertical sections.

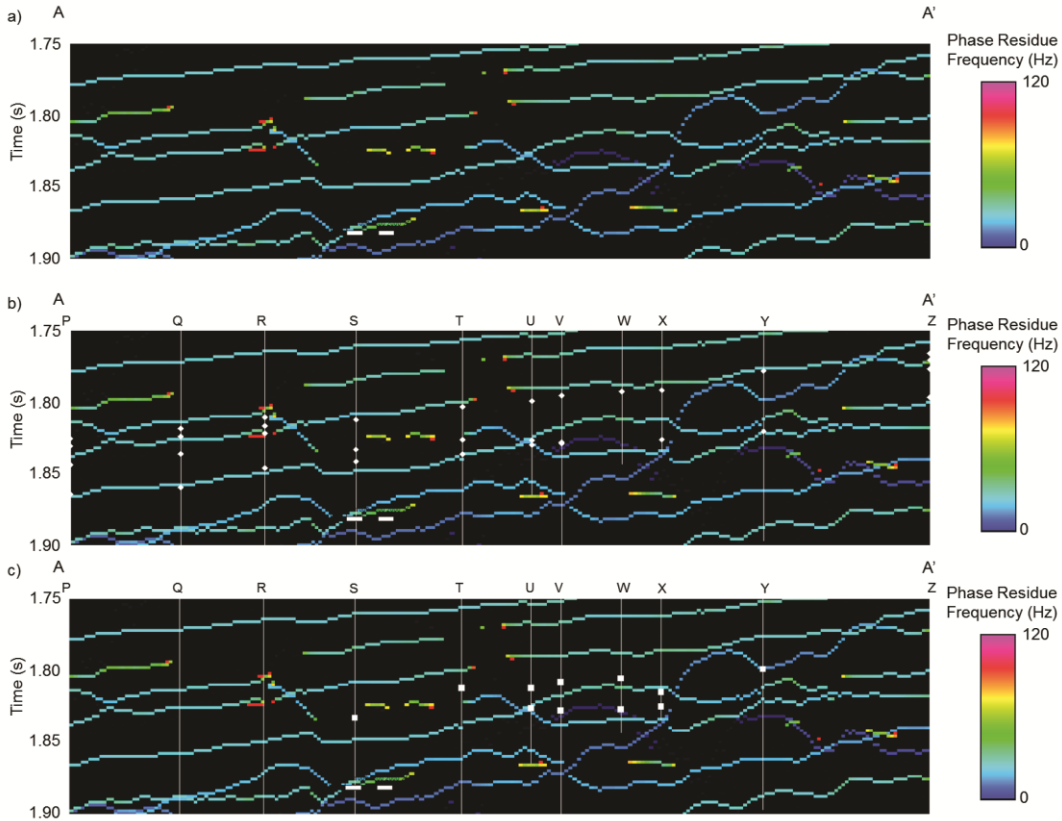

Figure 8.18: Vertical section AA' through (a) phase residues attribute, (b) phase residues with regional Red Fork the well-top data posted, and (c) phase residues with incision stages well-tops posted. (a) On the phase residues attribute we identify anomalies that resemble channel like features. (b-c) We corroborate that some of the anomalies seen in (a) match the interpreted regional Red Fork (diamond shapes) as well as the incision stages (square shapes) from the well logs.

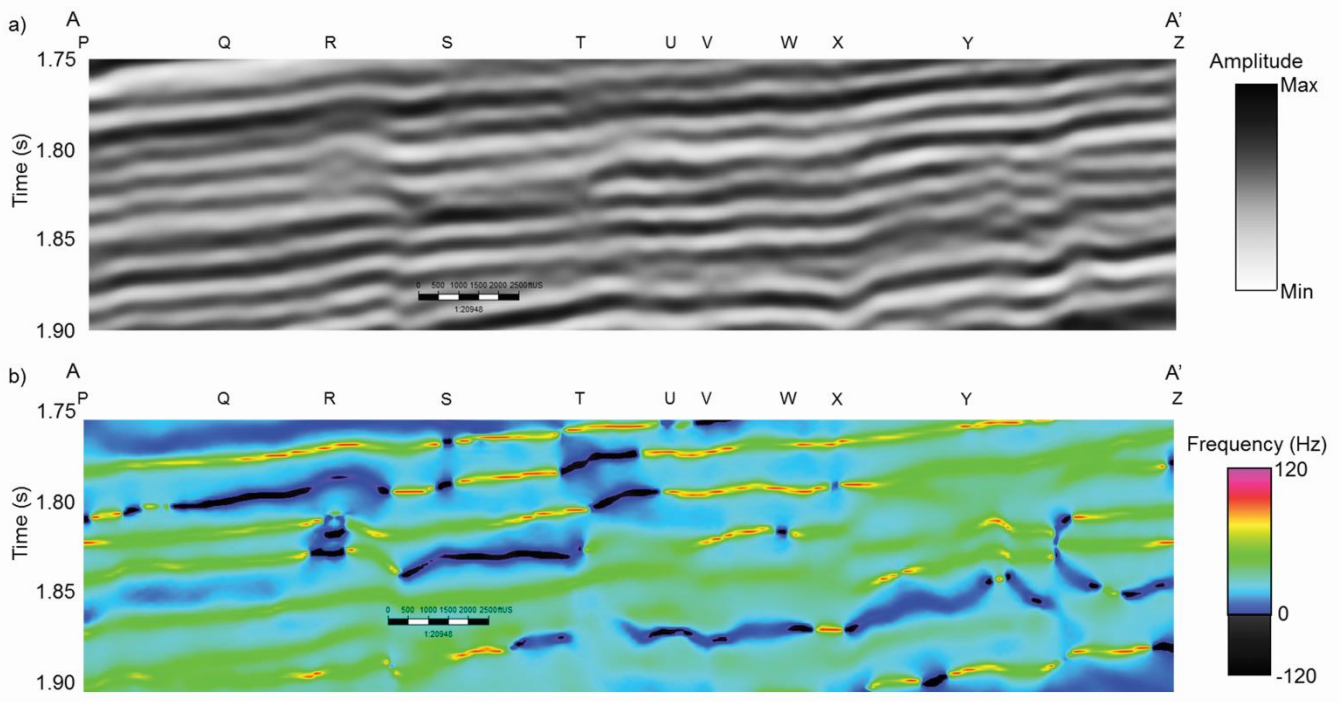
a)
A
A'
P
Q
R
S
T
U
V
W
X
Y
Z
1.75
1.80
1.85
1.90
Time (s)
Amplitude
Max
Min
b)
Frequency (Hz)
120
0
-120

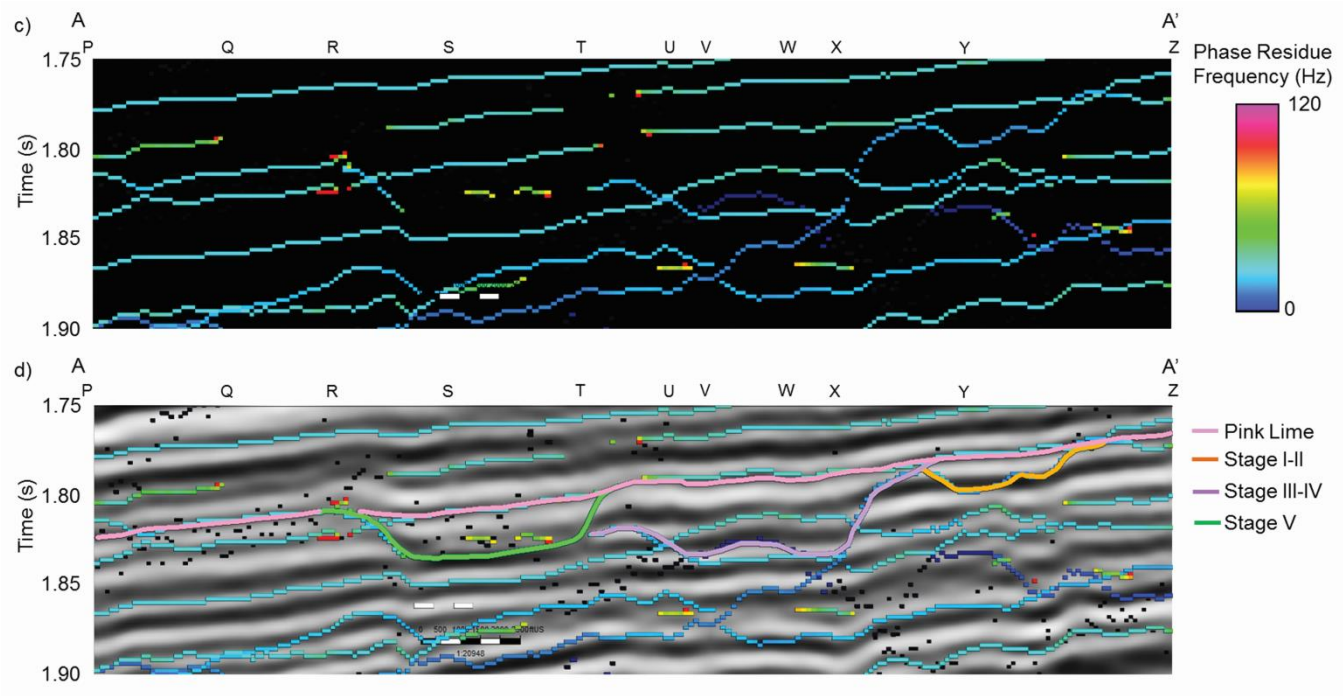

Figure 8.19: Vertical section AA' through (a) seismic amplitude data, (b) instantaneous frequency, (c) phase residues, and (d) seismic amplitude correndered with phase residues. (b) we are able to identify the anomaly generated by Stage V in the instantaneous frequency. (c) We interpreted the anomalies that matched the incision stages as well as the Pink Lime and the Inola Limestone. We generated surfaces from the five interpreted horizons to create a geological model.

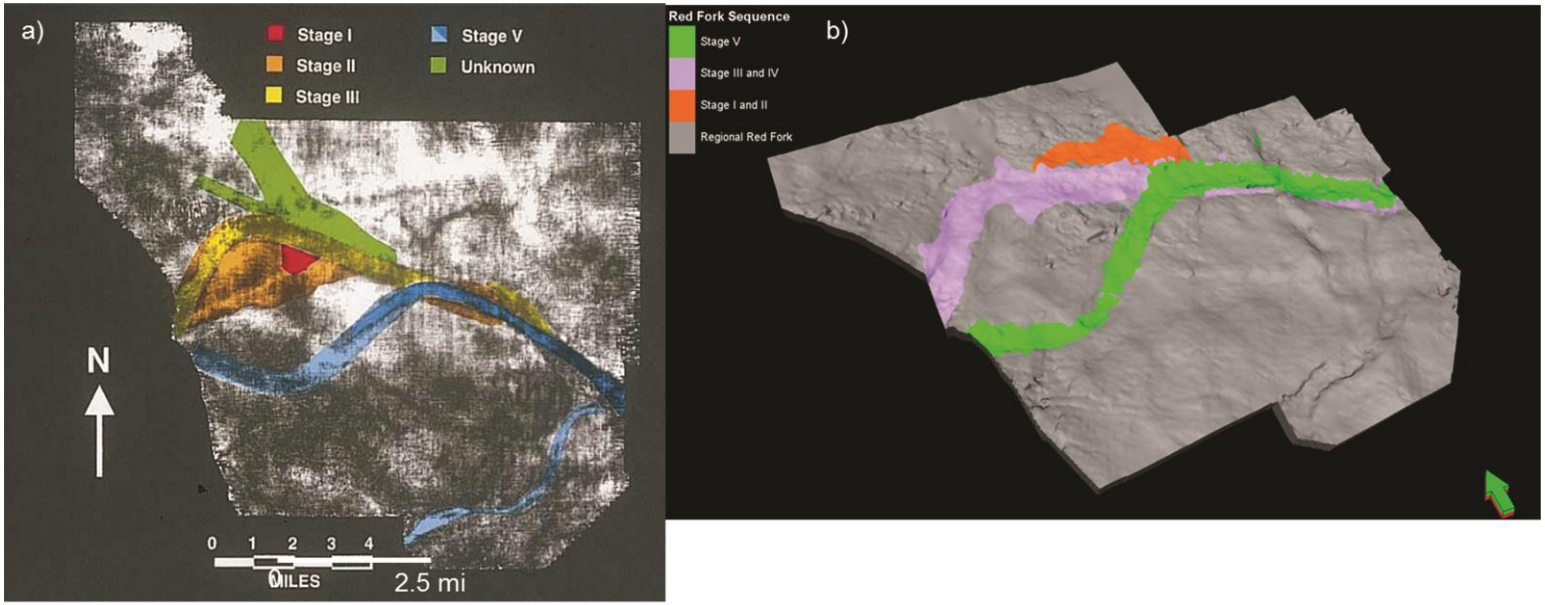

Figure 8.20: (a) Red Fork incised valley stages I through V interpretation from Peyton et al. 1998. (b) Resulting 3D geological model from well, seismic amplitude and phase residues data integrated seismic interpretation. (b) We obtained a 3D model that matches Peyton et al. 1998 original interpretation on spectral magnitude phantom horizon. Green arrow is pointing north.

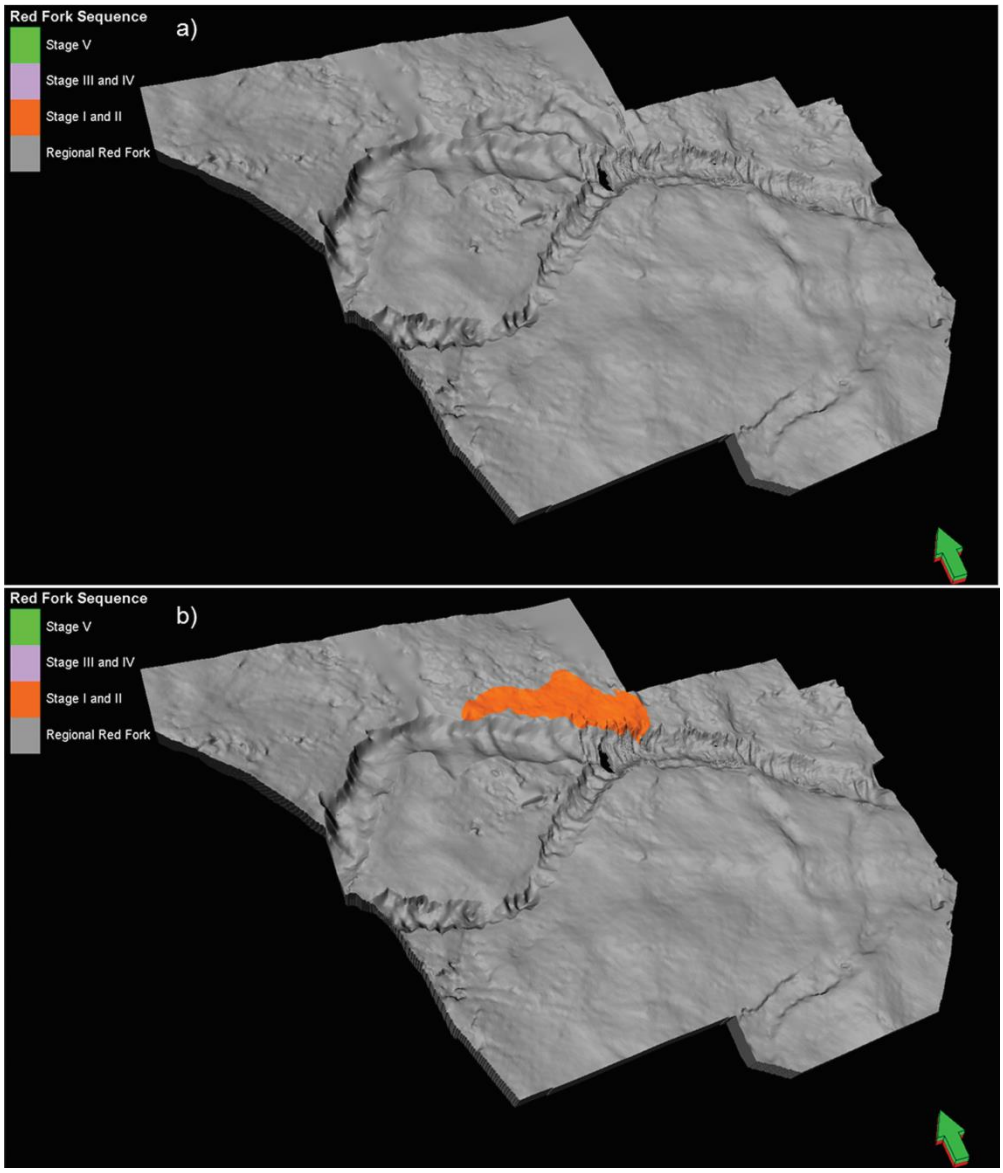
Red Fork Sequence
Stage V
Stage III and IV
Stage I and II
Regional Red Fork
a)
Red Fork Sequence
Stage V
Stage III and IV
Stage I and II
Regional Red Fork
b)

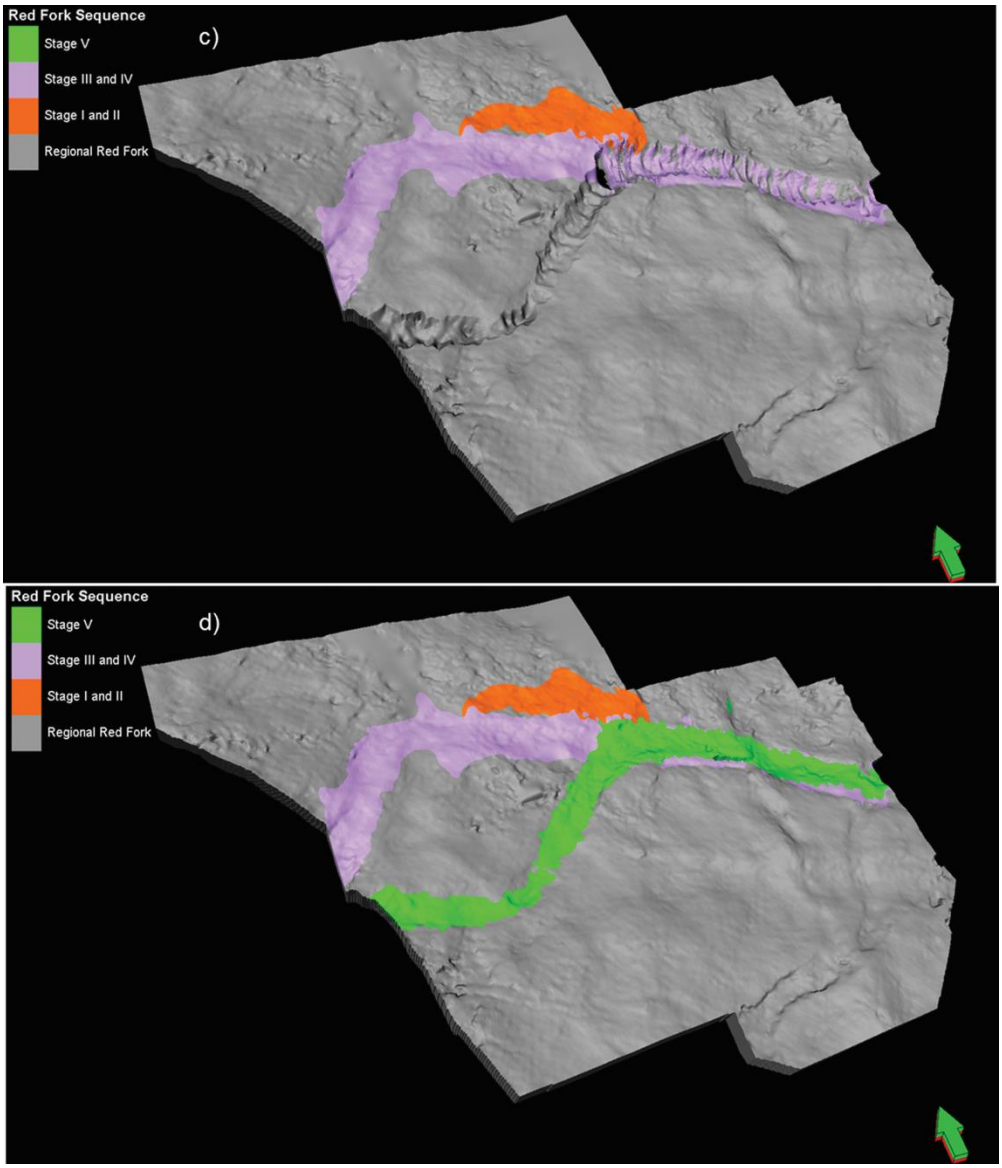

Figure 8.21: 3D view of (a) regional Red Fork, (b) incision stages I and II, (c) incision stage III and IV and (d) incision stage V obtained from the integrated seismic interpretation. Separating each stage from the regional Red Fork facilitates geologic modeling each stage to estimate reservoir properties consistent with the depositional environment.

REFERENCES

Barber, R, 2010, Challenges in mapping seismically invisible Red Fork channels: The Shale Shaker, 61, 147-162.

Berteussen, K.A., and B. Ursin, 1983, Approximate computation of the acoustic impedance from seismic data: Geophysics, **48**, 1351-1358.

Bone, D. J., 1991, Fourier fringe analysis: the two-dimensional phase unwrapping problem: Applied Optics, **30**, no. 25, 3627–3632.

Castagna, J., S. Sun and R. Siegfried, 2003, Instantaneous spectral analysis: Detection of low-frequency shadows associated with hydrocarbons: The Leading Edge, **22**, 120-127.

Cohen, L., 1993, Instantaneous "Anything": Proc. IEEE ICASSP-93, **4**, 105-108.

Devi, K.R.S., and H. Schwab, 2009, High-resolution seismic signals from band-limited data using scaling laws of wavelet transforms: Geophysics, **74**, WA143-WA152.

Ghiglia, D., and M. D. Pritt, 1998, Two-dimensional phase unwrapping: Theory, algorithms, and software: Wiley-Interscience.

Grossmann, A., and J. Morlet, 1984, Decomposition of Hardy functions into square integrable wavelets of constant shape: SIAM Journal on Mathematical Analysis, **15**, 723-736.

Herrmann, F., and C. Stark, 2000, A scale attribute for texture in well and seismic data: 70th Annual International Meeting, SEG, Expanded Abstracts, 2063-2066.

Liner, C, C. F. Lin, A. Gersztenkorn and J. Smythe, 2004, SPICE: A new general seismic attribute, 74th Annual International Meeting, SEG, Expanded Abstracts: 433-436.

Mallat, S., and S. Zhong, 1992, Characterization of Signals from Multiscale Edges: IEEE Transactions on Pattern Analysis and Machine Intelligence, **14**, 710–732.

Matos, M. C., O. Davogustto, K. Zhang, and K. J. Marfurt, 2011, Detecting stratigraphic discontinuities using time-frequency seismic phase residues: Geophysics, **76**, P1–P10.

Matos, M. C., and K. J. Marfurt, 2011, Inverse continuous wavelet transform "Deconvolution": 81st Annual International Meeting, SEG, Expanded Abstracts, 1861–1865.

Partyka, G., J. Gridley, and J. Lopez, 1999, Interpretational applications of spectral decomposition in reservoir characterization: The Leading Edge, **18**, 353–360.

Peacock, K.L., 1979, An optimum filter design for discrete integration: Geophysics, **44**, 722–729.

Pennell, S. and S. Melzer, 2003, Oxy Permian's Cogdell Unit CO_2 flood responds rapidly to CO_2 injection, World OIL Online, web, 05 March 2012.

Peyton L, R. Bottjer, G. Partyka, 1998, Interpretation of incised valleys using new 3-D seismic techniques: A case study using spectral decomposition and coherency: The Leading Edge, **17**, 1294-1298.

Smythe, J. A. Gertsztenkorn, B. Radovich C. F Li, C. Liner, Gulf of Mexico shelf framework interpretation using a bed-form attribute from spectral imaging: The Leading Edge, 23, 1208-1217.

Suarez, Y., K. J. Marfurt, and M. Falk, 2008, Seismic attribute-assisted interpretation of channel geometries and infill lithology: A case study of Anadarko basin Red

Fork channels: 78th Annual International Meeting, SEG, Expanded Abstracts, 963–967

Taner, M. T., F. Koehler, and R. E. Sheriff, 1979, Complex seismic trace analysis: Geophysics, 44, 1041–1063.

Taner, M. T., 2000, Attributes revisited: http://www.rocksolidimages.com/pdf/attrib_revisited.htm, 20 March 2013

Tu, C.L., and W.L. Hwang, 2005, Analysis of singularities from modulus maxima of complex wavelets: IEEE Transactions on Information Theory, **51**, 1049-1062.

Zeng, H. L., 2010, Geologic significance of anomalous instantaneous frequency: Geophysics, **75**, 23-30

9. Conclusions

In this dissertation, I have applied several geophysical techniques in order to understand and characterize the Horseshoe Atoll reservoir within the Diamond M field. I have estimated reservoir properties at three scales: core, well log, and surface seismic. The most important measurements from the core-scale study for subsequent data integration are porosity, density and acoustic and shear velocities (V_p and V_s). At the well-log scale the most important measurements are the porosity log, density log, and compressional and shear sonic logs. At the seismic scale, P-wave and S-wave impedance inversion provide the large scale rock property measurements, while reflector boundaries and shapes placed the reservoir components within a depositional and structural context.

At the core scale I found that velocities (V_p and V_s) are strongly dependent on porosity with Biot–Gassmann modeling providing an understanding of the pore scale connectivity. The reservoir rock is consistent with Biot-Gassmann model as long as the porosity is greater than 8%. Porosity, permeability and velocity (V_p and V_s) measurements as a function of pressure indicate that cracks represent a small percentage of the total porosity in the samples and do not contribute significantly to permeability.

At the log scale I found a similar 8% porosity sensitivity threshold. This 8% threshold indicates porosity estimates using elastic properties will have a significant amount of uncertainty. Thus, this threshold should be taken into account when predicting porosity of “tight” limestones using surface seismic impedance inversion. The reservoir displays high porosity zones alternating with “tight” zones. These variations correlate to episodes of exposure and drowning of the Horseshoe Atoll during

late Pennsylvanian to early Permian time. Fast and slow dipole sonic logs coupled with porosity measurements on core indicate that the anisotropy in the Horsehsoe Atoll is primarily due to horizontal stress.

At the seismic, scale I found that careful processing provides high fidelity images with P-wavelengths at the reservoir target ranging from 60 to 300 ft and S-wave resolution ranging from 75 to 400 ft. Although it took considerably more processing effort, the bandwidth of the S1 and S2 seismic images was 60% percent greater than the initial transverse shear wave image. The pre-stack Alford rotation technique of a high fold 2C by 2C survey successfully aligns the fast and slow shear modes to the inferred anisotropy direction in the area. The resulting anisotropy is aligned with the regional stress map and with the anisotropy measured by the dipole sonic log data. The uniform anisotropy suggests that fractures contribute a relatively minor amount with the fracture strike estimation from the log data comparable to the error in the measurements at the log scale.

In addition to improving the resolution of the S-wave data, I also improved resolution of the P-wave data, by applying a matching pursuit non-stretch NMO technique to increase the frequency content and stabilize the seismic wavelet behavior with offset. Since S-wave impedance and density inversion are heavily dependent on the farther offsets, increasing the bandwidth at mid and far offsets increased the bandwidth of the S-impedance and density estimates, resulting in a better match to the log data.

Finally I integrated the results from three different scales to perform a detailed evaluation of the Horseshoe Atoll reservoir to better understand which properties drive

production. I found that porosity is the main property that affects the behavior of the reservoir response to acoustic waves at core, log and seismic scale. Thus combining the inversion results with the log data, I was able to identify high porosity zones within the reservoir. I correlated the inversion derived attributes to the production data and proposed new drilling locations based on my analysis.

10.Recommendations

I envision five possible routes that the data I have generated can be used for further studies and understanding of the reservoir at the Diamond M field. This work can also be extended to the San Andres and Wolfcamp shale sections in the same field where the operator has growing interest presently.

1. Using the well data, a detailed sequence stratigraphy framework can be developed that will improve the definition of the porosity zones that I have defined in this work.
2. Using the sequence stratigraphy framework, I suggest a study to build a reservoir model at the well scale that can be taken into a reservoir simulator program to evaluate the production and understand the effects of upscaling on the reservoir.
3. Using the completion data, I suggest a study to evaluate the impact of completion techniques on production. Then, these results can be employed to develop a strategy for completions and frac jobs in the reservoir to enhance production.
4. Using the prestack P-wave data I suggest an azimuthal AVO study to identify lithology changes and understand the porosity distribution in the reservoir with more detail.
5. Using the prestack S-wave data I propose an extension to my developed Alford rotation technique that includes layer stripping.

Appendix A: Diamond M prestack compressional data processing

Given my objective of pre-stack inversion and anisotropy analysis, I needed to reproduce the Diamond M P-wave dataset. The data were acquired over the Diamond M Field in Scurry County, TX by Dawson Geophysical in 2005. The first step was to import the data onto Landmark ProMAX 3D software and extract the shot and receiver lines and locations from the trace headers. This geometric information was then written into the database files augmenting the CDP information with the SPS (Shell Processing Support) files containing geographical coordinates for the shot and receiver locations (Figure A1). The nominal fold of the data is 470 (Figure A2) I calculate the elevation statics using an elevation of 2300 ft. and a replacement velocity of 9000 ft./s. Next, I construct the parameter gates where defining the deconvolution, filtering and trace balancing gates on shot, receiver and cdp domains. Using these parameter tables I ran the trace statistics and mute, where I automatically eliminate "bad" traces using three specific trace attributes: spikeness, pre-firstbreak frequency and dominant frequency. Spikeness is calculated by dividing the maximum value of the trace energy by the average trace energy (ProMAX User Manual). Pre-firstbreak frequency is calculated as the inverse of the mean time measured in samples between zero crossings in the pre-first-break window. The dominant frequency is calculated in a similar way but within the deconvolution gate.

Next I address the reverberating refractions in the data. I accomplished this in two steps. First, I create a cross-spread geometry for the dataset and then I adaptively subtract the modeled ground roll from the data on the cross-spread domain. I characterize the ground roll using an f-k_x-k_y a velocity filter of 9000 ft./s. (Figures A3

and A4). I then pass the data through a flow that consists of a gated surface consistent deconvolution, time-variant spectral whitening and surface consistent amplitude balancing. The gated surface consistent deconvolution is done in three steps. First step is to calculate the spectra for all the traces I common shot, receiver, cdp, offset and cross-spread domains. The second decomposes the gated spectral windows into spectral components using seven iterations of Gauss-Seidel inversion. The third step uses all the components to design a predictive deconvolution operator using a 120 ms operator length, 40 ms prediction distance and 0.1 % pre-whitening. I then proceed to spectrally balance the data using 5-10-96-120 Hz operator. Surface consistent amplitudes balancing are applied calculated based on complex trace amplitude envelope for the common shot, receiver, CDP domains (Figure A5). To QC my progress, I stack the pre-processed data and generate a brute stack. I will compare any stack I make to this brute stack to understand how processes affect the original data and estimate how much improvement I have done with the processing flows. I proceed then to pick the first breaks using a seeded neural network algorithm. I check the receiver and shot geometry by estimating the position of the shot and receiver locations from the first break picks and comparing them to the true coordinates and elevations (Figure A6). Next I calculate the refraction statics using my first breaks picks, apply the refraction statics and stack the data (Figure A7). I proceeded then to iteratively pick velocities using 80x80, 40x40, 20x20 and 10x10 super-gather grids. In between each velocity picking pass I apply a structure oriented filter to the gathers and calculate residual statics. Figure A8 shows the result for this step by comparing the 10x10 velocity analysis panel for the raw data versus the processed data. Finally I stack the data using the residual statics solution and

compare to the brute stack (Figure A9). At this point I take the data to migration, no further processing needed.

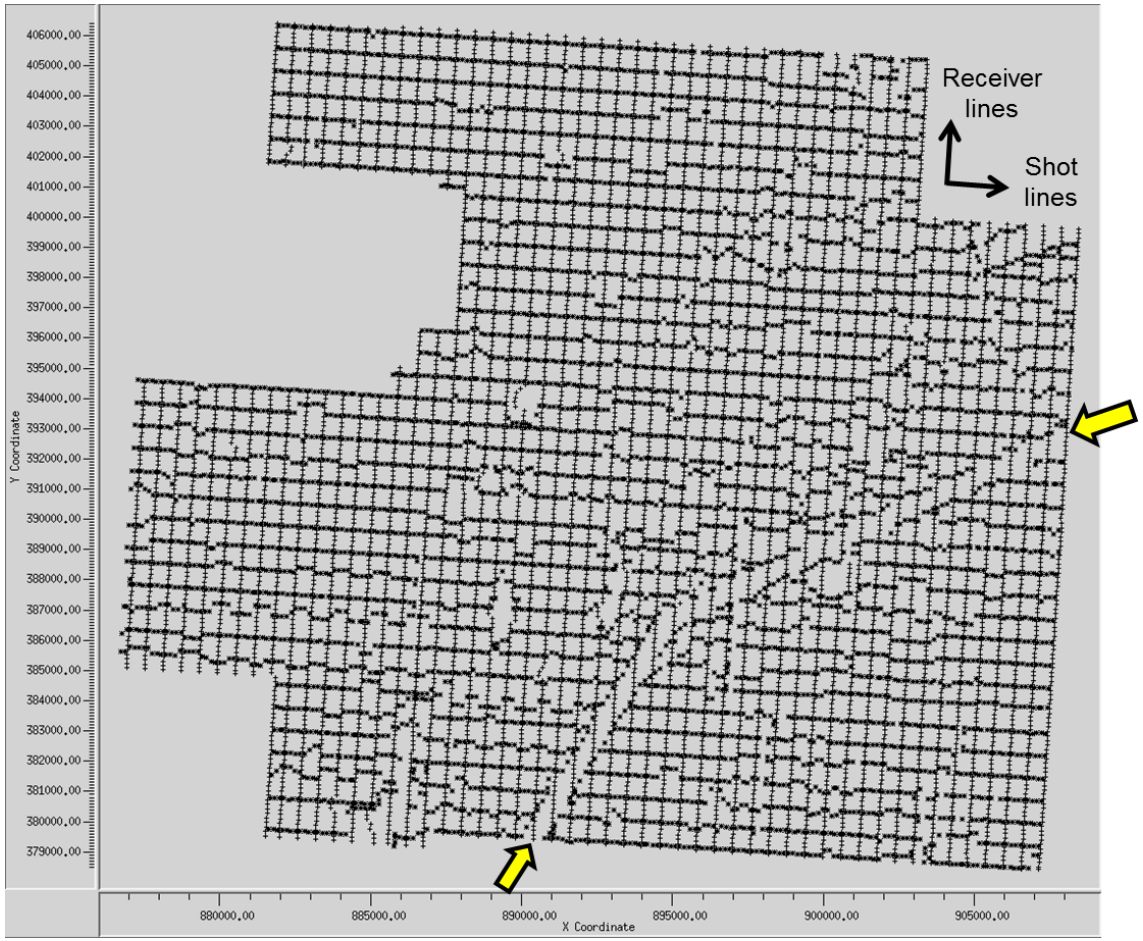

Figure A1: source (*) and receiver (+) base map. A highway is indicated by the block arrows.

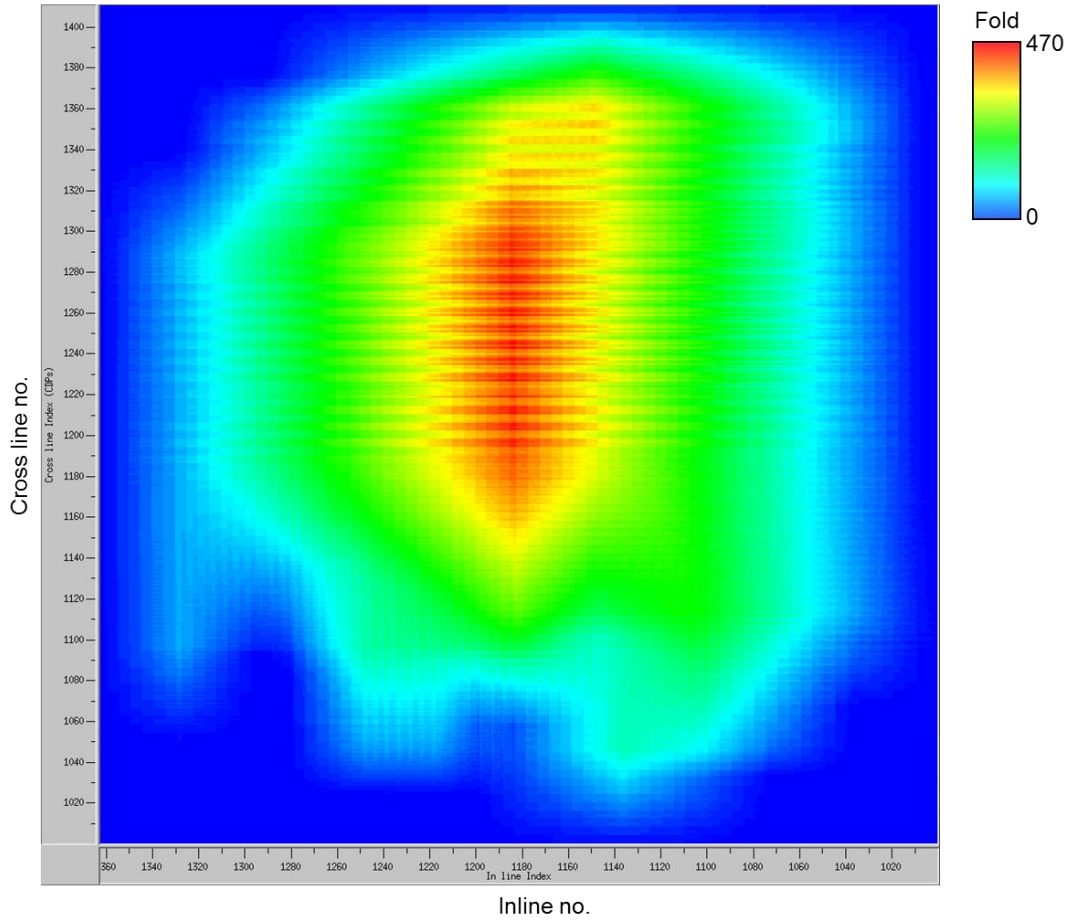

Figure A2: CDP fold map of the P-wave survey

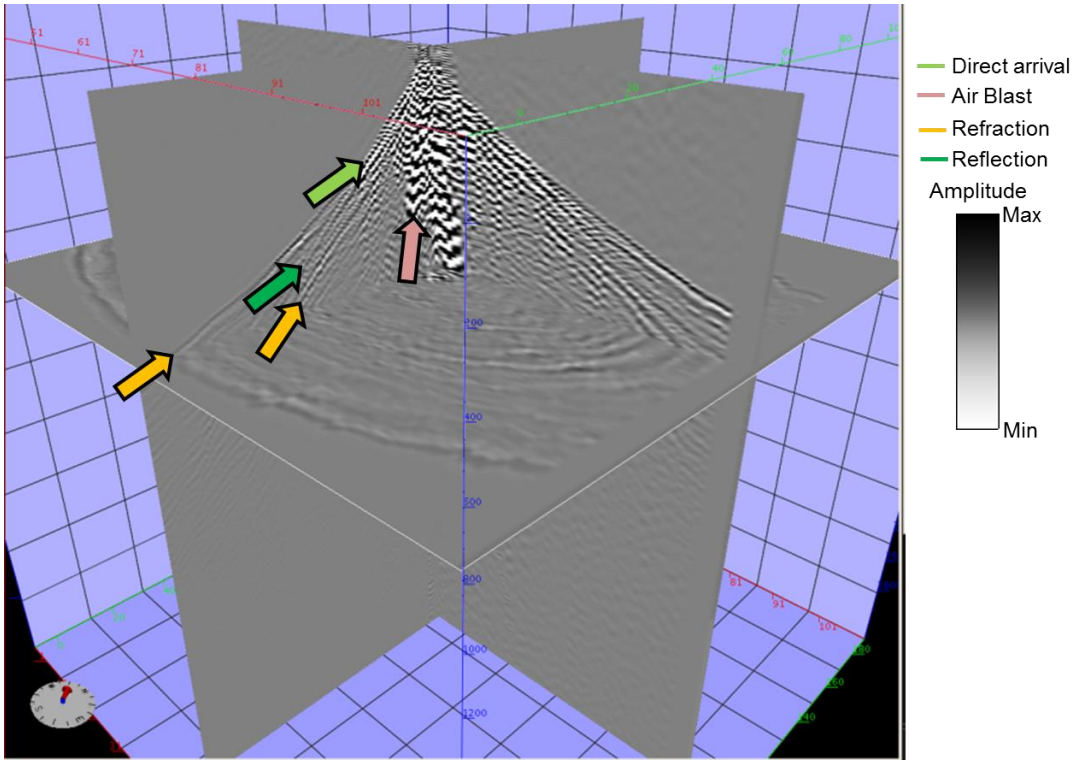

Figure A3: 3D view of a cross-spread gather from the P-wave data. I have identified several events observed in the data.

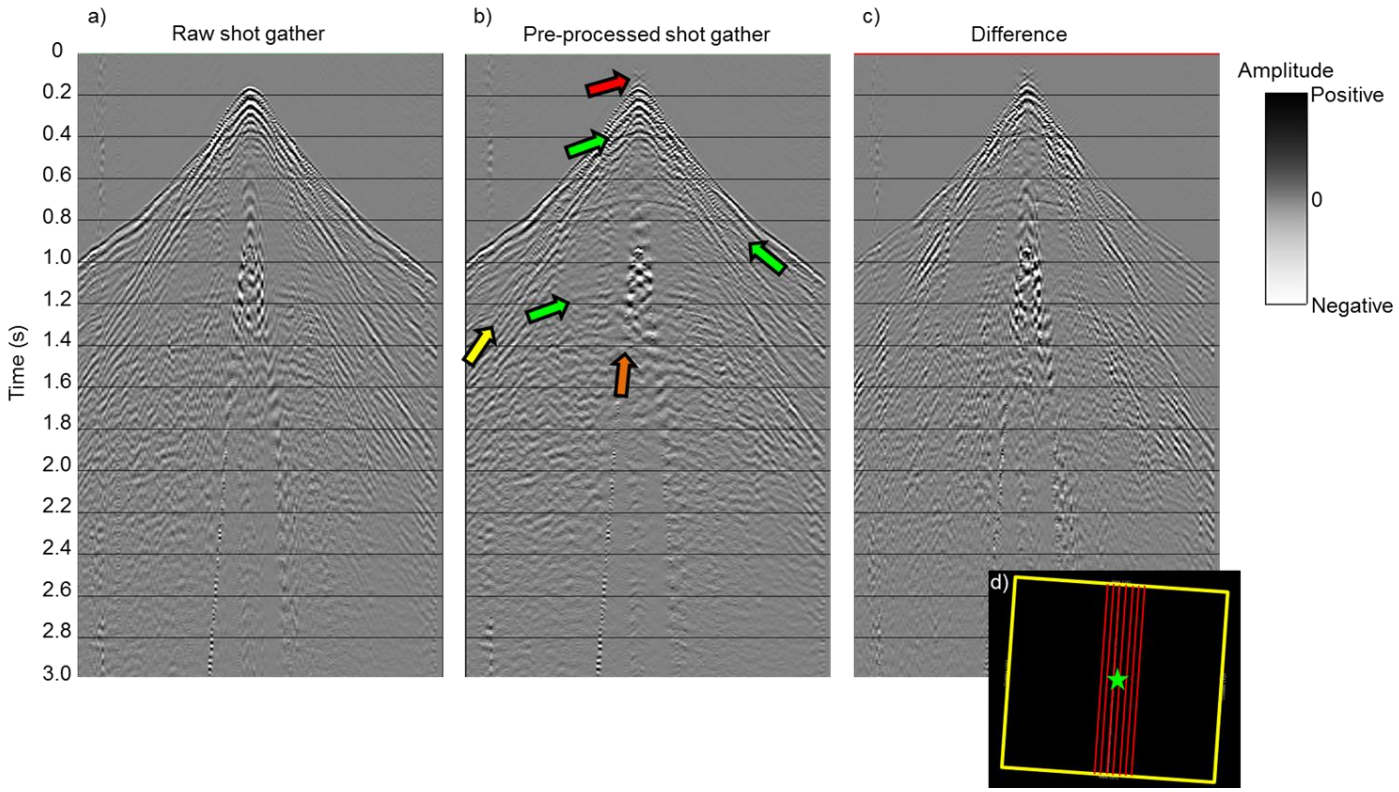

Figure A4:(a) original data, (b) FKK filtered data, (c) difference between (a) and (b) and (d) map indicating the shot location (green star) and live receiver lines (red lines). (a) green arrows indicate features that have been enhanced by the filtering process, yellow arrows indicate features that have marginally improved with the filtering, orange arrow indicates 12 Hz noise present in the data, and red arrows indicate features that have been introduced by the filtering process.

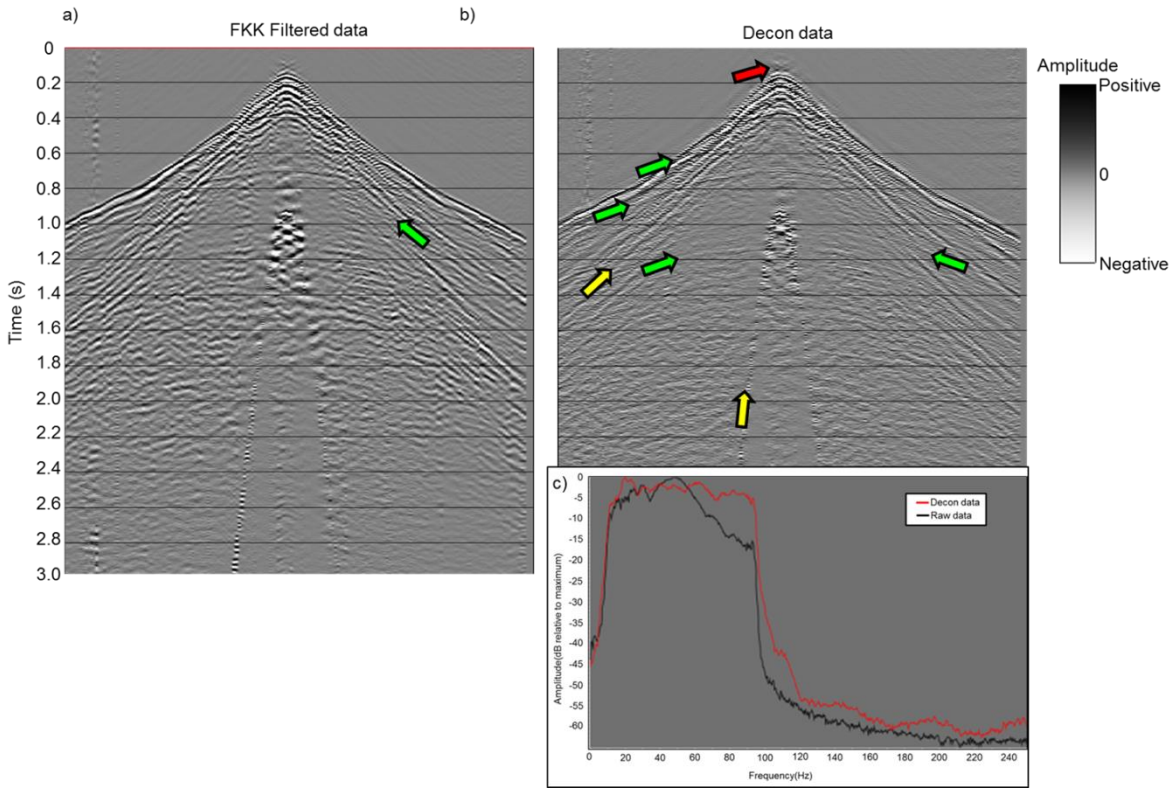

Figure A5: Data (a) before and (b) after deconvolution. The input data corresponds to Figure A4. (c) Power spectra for (a) and (b). (a) green arrows indicate features that have been enhanced by the filtering process, yellow arrows indicate features that have marginally improved with the filtering and red arrows indicate features that have been introduced by the filtering process. Note in (c) that the deconvolved data has a "flat" spectrum achieved by the gated surface consistent deconvolution coupled with the spectral whitening.

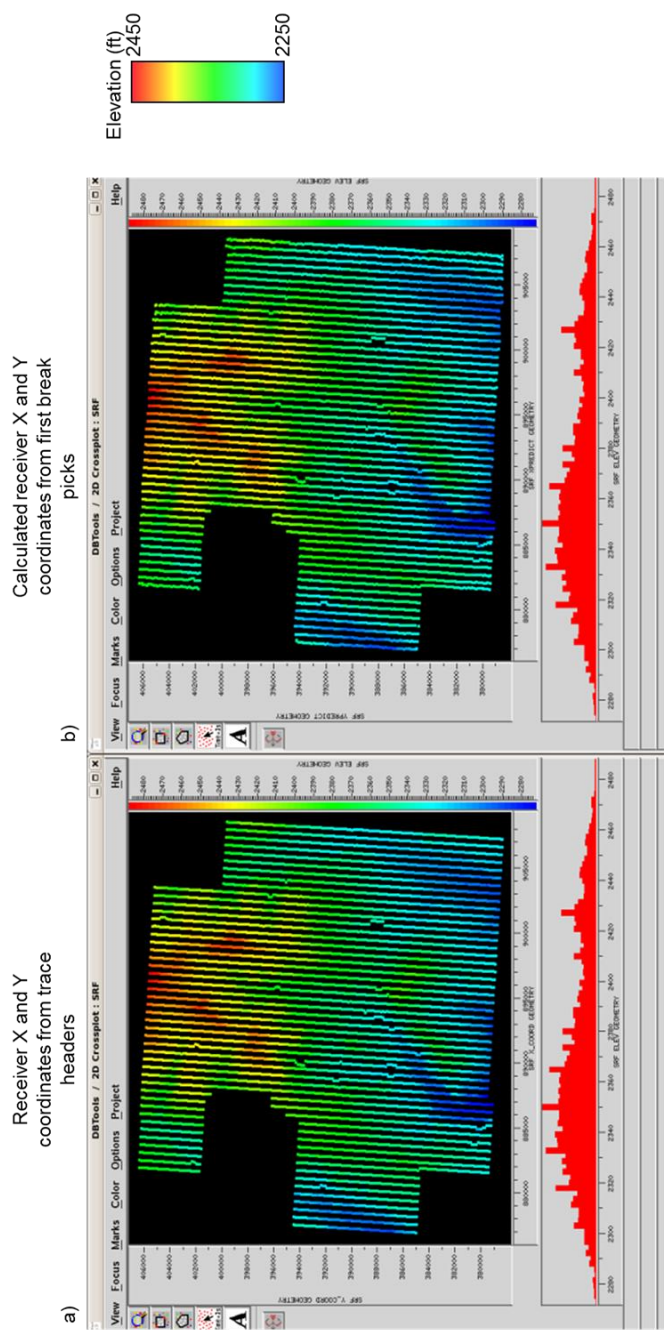
Elevation (ft)
2450
2250
a)
Receiver X and Y coordinates from trace headers
b)
Calculated receiver X and Y coordinates from first break picks

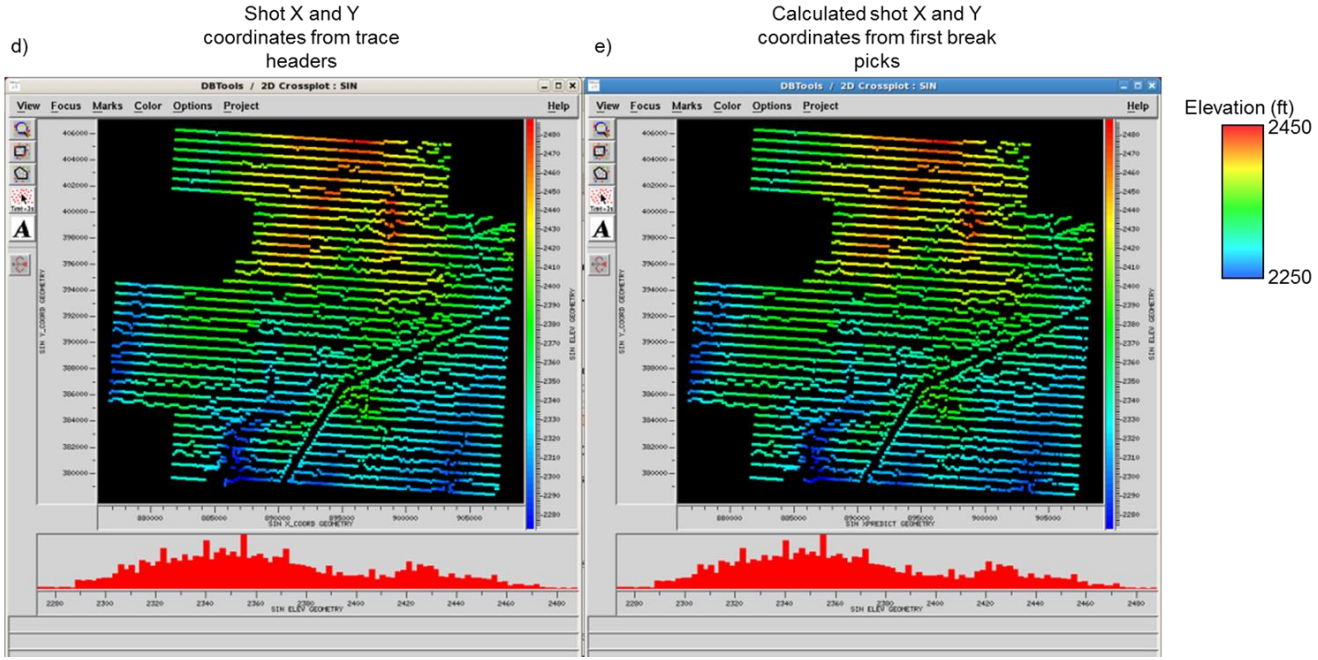

Figure A6: (a) Surveyed and (b) calculated from first breaks receiver positions for the Diamond M survey. Note that these two figures are almost identical, indicating a good solution from the calculated positions of the receiver locations (d) Surveyed and (e) calculated from first breaks shot positions for the Diamond M survey. Note that these two figures are almost identical indicating a good solution from the calculated positions of the shot locations

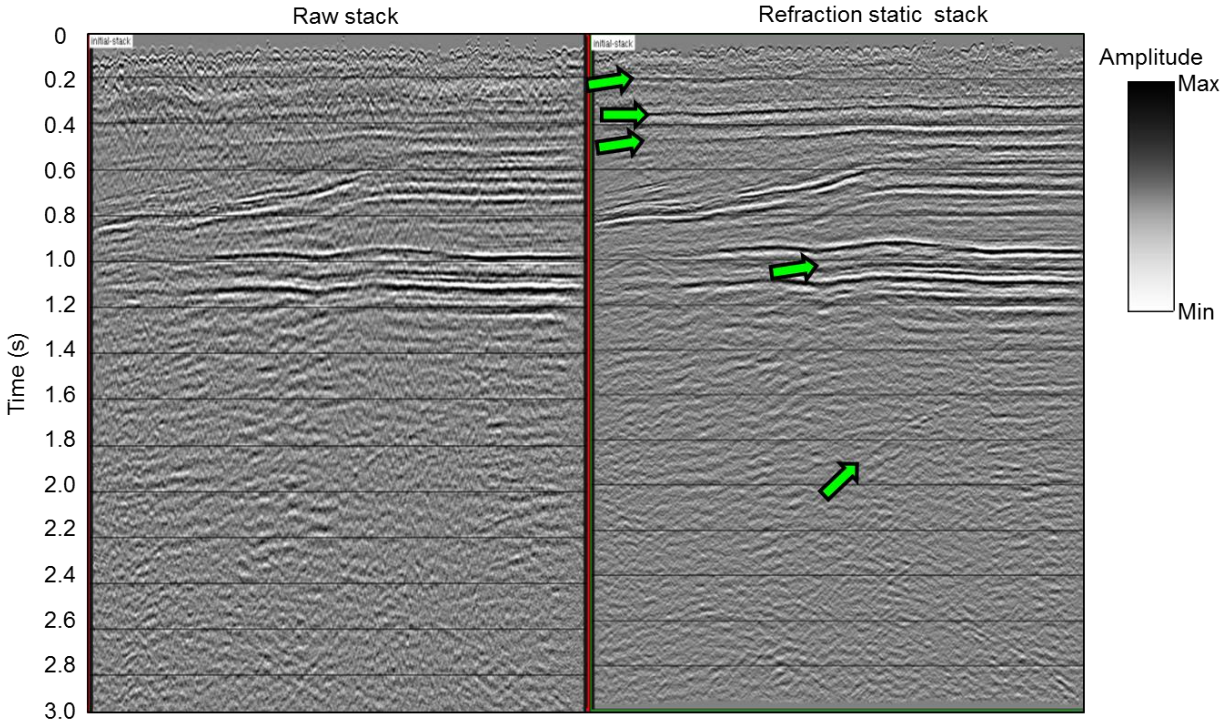

Figure A7: Vertical slice through stacked seismic amplitude data (a) before and (b) after refraction statics. (c) power spectra for (a) and (b). (b) Green arrows indicate reflectors with improved continuity after the refraction statics process.

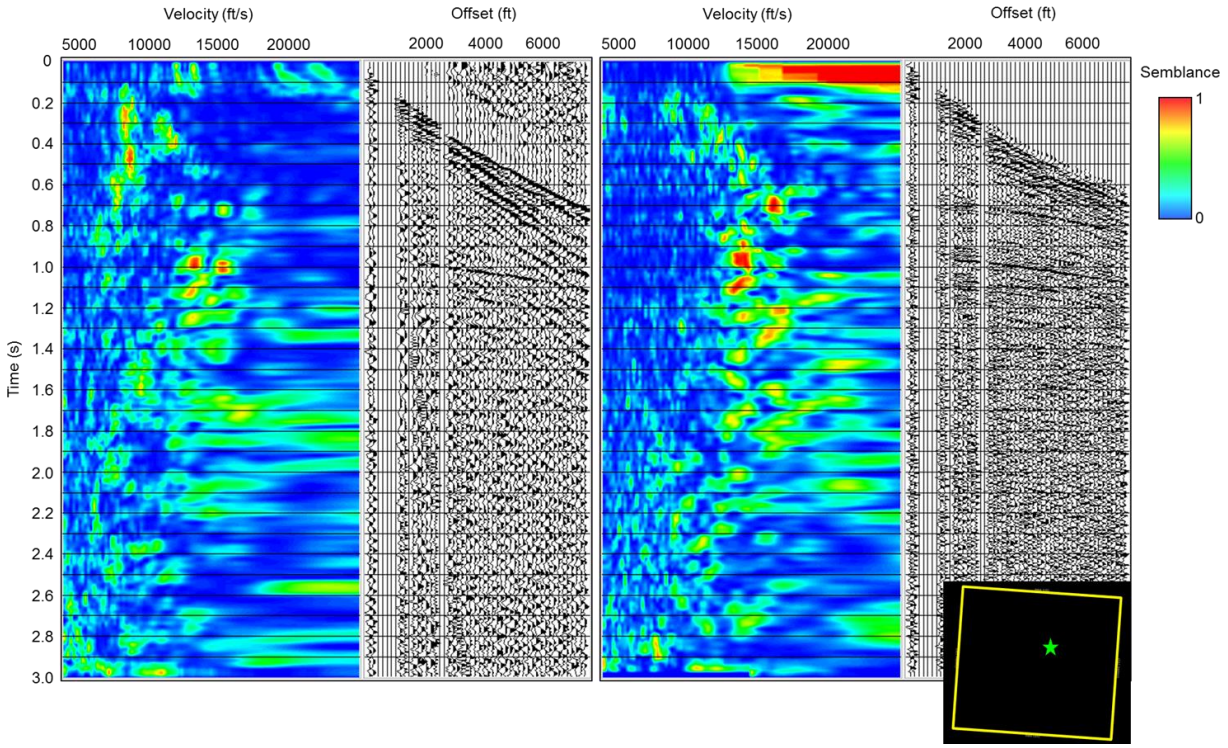

Figure A8: Velocity analysis of a representative gather (a) before and (b) after processing sequence. (c) Supergather location. (b) Note the improvement in the semblance panel for the shallow events and the increase of the frequency content after the processing sequence.

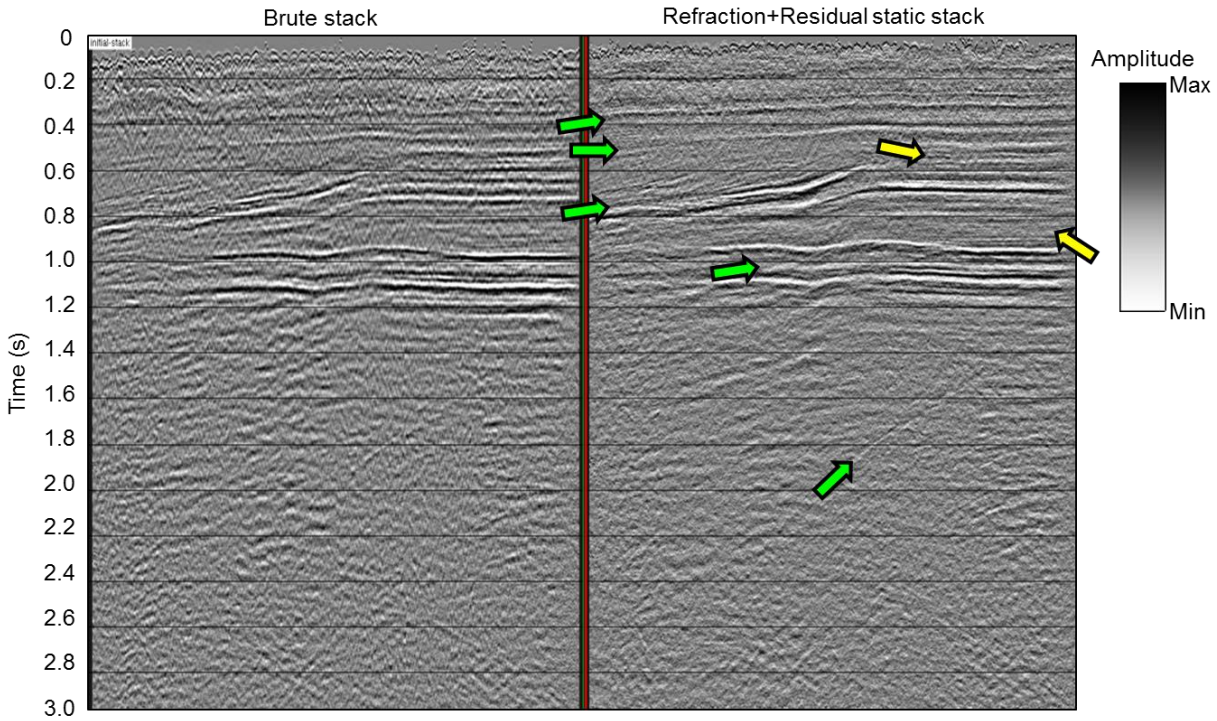

Figure A9: Vertical slice through stacked seismic amplitude data (a) before and (b) after refraction and residual statics. (c) power spectra for (a) and (b). (b) green arrows indicate reflectors with improved continuity after the refraction statics process. Yellow arrows indicate reflectors whose continuity has diminished by the residuals statics process but have been sharpened.

Appendix B: Programs Rotate 2C by 2C and Alford azimuth map

As part of my research, I wrote two programs in FORTRAN90 using the AASPI I/O modules. I created the interactive Graphical User Interfaces (GUIs), the shell scripts, LSF scripts and documentation for both programs so that OU students, OU staff, and AASPI consortium sponsors find the programs easy to use. Below I have included the documentation for both programs related to my research.

PROGRAM ROTATE 2C BY 2C

Computation flow chart

Program **Rotate 2C by 2C** computes the radial – transverse or Alford rotated data from field shear components. The input to program will be the four field components with no rotation applied. The radial - transverse data is calculated using the source – receiver azimuth calculated from the source and receiver locations on the headers. The Alford rotated data can be calculated in using a user specified single rotation angle or a user specified set of azimuths. Alford (1986) recognized the necessity of align multicomponent multisource data into the principal axes of anisotropy in order to properly image fractured reservoirs and facilitate the interpretation of shear seismic data recorded on an azimuthally anisotropic medium. His method consisted of pre- and post-multiplication of the recorded data by the Bond rotation matrix (Auld, 1973) given by:

$$\begin{bmatrix} D_{11} & D_{12} \\ D_{21} & D_{22} \end{bmatrix} = \begin{bmatrix} \cos\theta & \sin\theta \\ -\sin\theta & \cos\theta \end{bmatrix} \begin{bmatrix} d_{yy} & d_{yx} \\ d_{xy} & d_{xx} \end{bmatrix} \begin{bmatrix} \cos\theta & -\sin\theta \\ \sin\theta & \cos\theta \end{bmatrix} \qquad (1)$$

where D_{yy}, D_{yx}, D_{xy}, and D_{xx} are the data recorded in field coordinates, D_{11}, D_{12}, D_{21} and D_{22} are the data rotated to be aligned with the principal axis of anisotropy and θ is the

azimuth of the principal axis of anisotropy. The value of θ is output as a single sample seismic volume and is used as input to generate an average principal axis of anisotropy in program **alford_azim_map**.

In a similar way the radial – transverse rotated data can be calculated by:

$$\begin{bmatrix} D_{rr} & D_{rt} \\ D_{tt} & D_{tr} \end{bmatrix} = \begin{bmatrix} \cos\psi & \sin\psi \\ -\sin\psi & \cos\psi \end{bmatrix} \begin{bmatrix} d_{yy} & d_{yx} \\ d_{xy} & d_{xx} \end{bmatrix} \begin{bmatrix} \cos\psi & -\sin\psi \\ \sin\psi & \cos\psi \end{bmatrix} \qquad (1)$$

where D_{yy}, D_{yx}, D_{xy}, and D_{xx} are the data recorded in field coordinates, D_{rr}, D_{rt}, D_{tr} and D_{tt} are the data rotated to be aligned with the source-receiver azimuth direction and Ψ is the source receiver azimuth. Below is the flow chart showing the workflow for the prestack shear wave rotation:

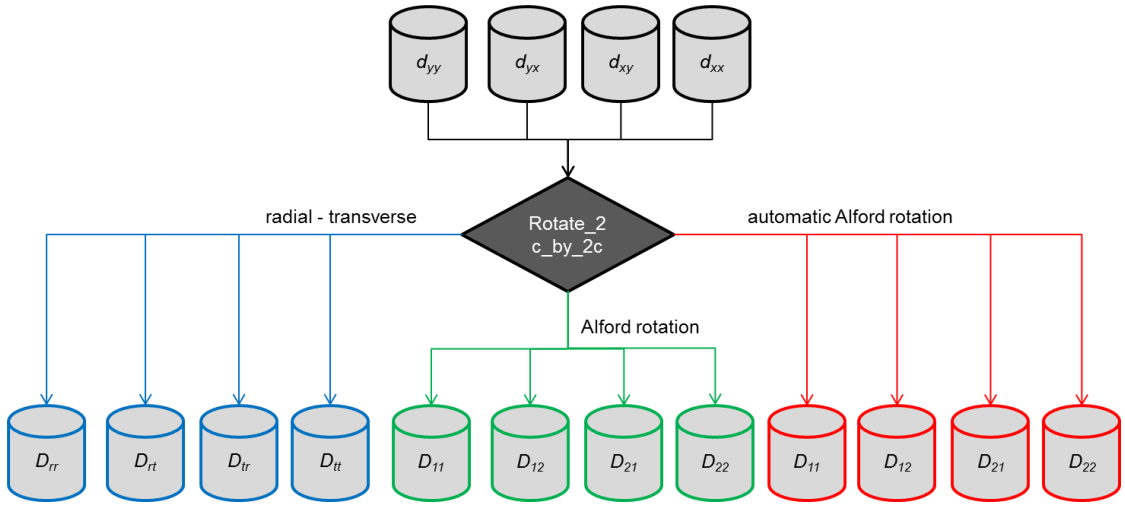

Running Rotate_2C_by_2C

Program **rotate_2C_by_2C** is launched from the prestack utilities within the main **aaspi_util_prestack** GUI

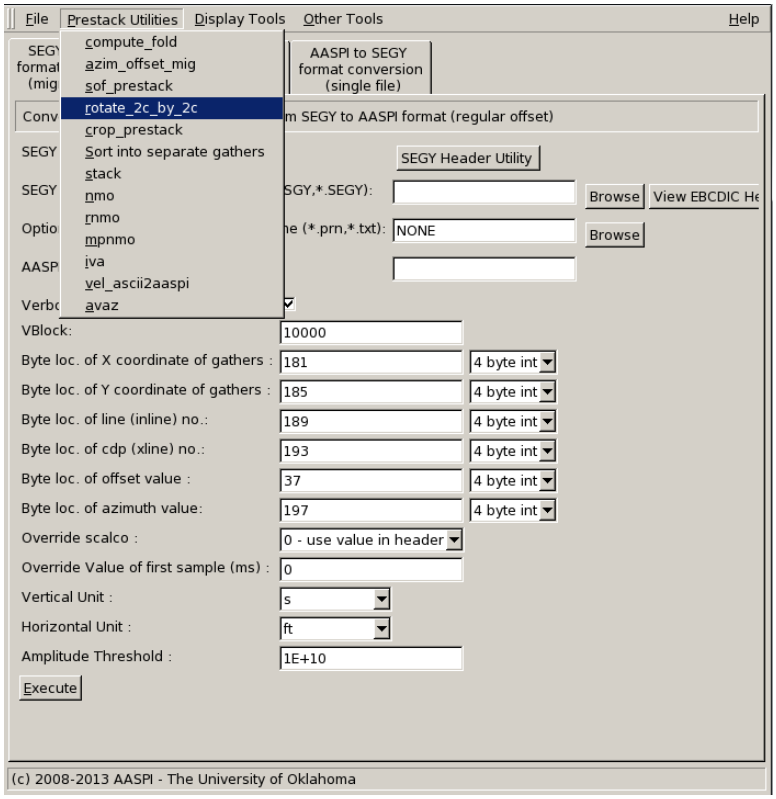

Use the browser in the first 4 lines (1 through 4) to select the input seismic data. The north and east component convention is relative to the survey acquisition layout. If performing all types of rotation select the respective boxes (7 through 9). Specify the single Alford rotation angle (5) and the number of azimuths for the automatic Alford rotation (6). Once the paramaters In the '*Extended*' tab the MPI options for the program can be specified.

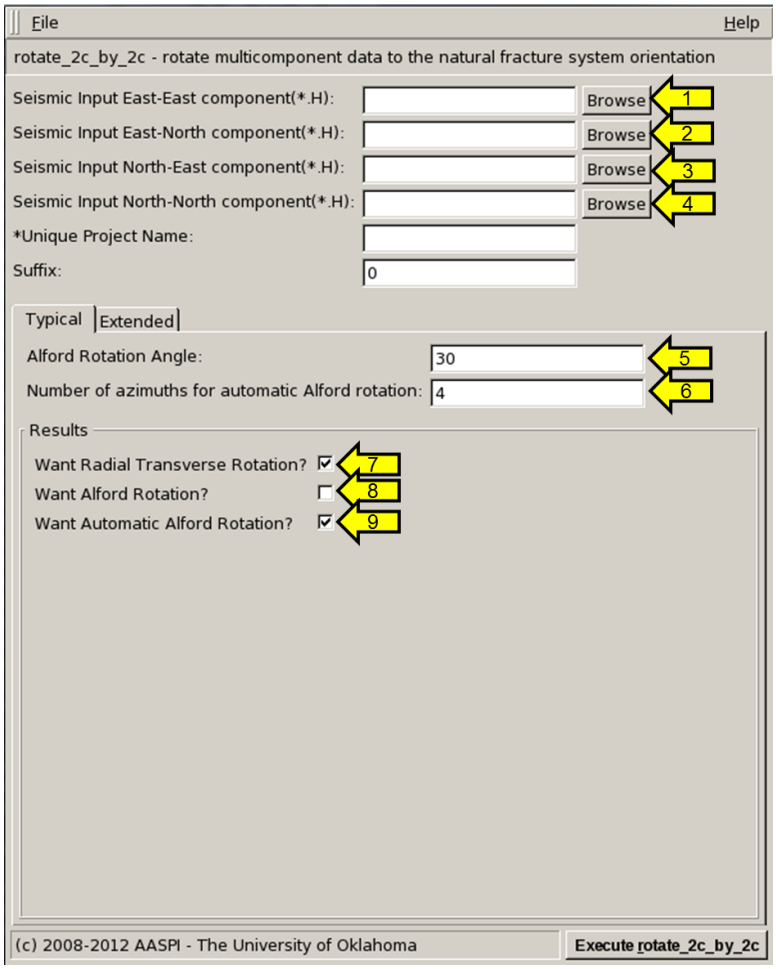

As in all AASPI codes, program progress is echoed to the xterm from which aaspi_util was launched. The end of the print-out looks like this:

```
 Checking block          34 from index           4 has           0
 this_process=           0 Sent term to           1
 this_process=           0 Sent term to           2
 this_process=           0 Sent term to           3
 this_process=           0 At barrier
 this_process=           3 Block=           0
 this_process=           3 At barrier
Closing file: /home/oswaldo/Data/Diamond_m/S_data/d_11_test_0.H
Closing file: /home/oswaldo/Data/Diamond_m/S_data/d_12_test_0.H
Closing file: /home/oswaldo/Data/Diamond_m/S_data/d_21_test_0.H
Closing file: /home/oswaldo/Data/Diamond_m/S_data/d_22_test_0.H
Closing file: /home/oswaldo/Data/Diamond_m/S_data/d_rr_test_0.H
Closing file: /home/oswaldo/Data/Diamond_m/S_data/d_rt_test_0.H
Closing file: /home/oswaldo/Data/Diamond_m/S_data/d_tr_test_0.H
Closing file: /home/oswaldo/Data/Diamond_m/S_data/d_tt_test_0.H
Closing file: /home/oswaldo/Data/Diamond_m/S_data/da_11_test_0.H
Closing file: /home/oswaldo/Data/Diamond_m/S_data/da_12_test_0.H
Closing file: /home/oswaldo/Data/Diamond_m/S_data/da_21_test_0.H
Closing file: /home/oswaldo/Data/Diamond_m/S_data/da_22_test_0.H
Closing file: /home/oswaldo/Data/Diamond_m/S_data/da_angle_test_0.H
Closing file: /home/oswaldo/Data/Diamond_m/S_data/xx.H
Closing file: /home/oswaldo/Data/Diamond_m/S_data/xy.H
Closing file: /home/oswaldo/Data/Diamond_m/S_data/yx.H
Closing file: /home/oswaldo/Data/Diamond_m/S_data/yy.H
```

If you type ‘ls –ltr’ in the above xterm, you find the most recent files to be:

```
-rw-rw-r--  1 oswaldo oswaldo  433 Jul 29 16:43 rotate_2c_by_2c.parms
-rw-rw-r--  1 oswaldo oswaldo   36 Jul 29 16:43 live_processor_list
-rw-rw-r--  1 oswaldo oswaldo  16K Jul 29 16:43 aaspi_rotate_2c_by_2c.out
-rw-rw-r--  1 oswaldo oswaldo 3.8K Jul 29 16:43 d_tt_test_0.H@@
-rw-rw-r--  1 oswaldo oswaldo 3.7K Jul 29 16:43 d_tt_test_0.H
-rw-rw-r--  1 oswaldo oswaldo 3.8K Jul 29 16:43 d_tr_test_0.H@@
-rw-rw-r--  1 oswaldo oswaldo 3.7K Jul 29 16:43 d_tr_test_0.H
-rw-rw-r--  1 oswaldo oswaldo 3.8K Jul 29 16:43 d_rt_test_0.H@@
-rw-rw-r--  1 oswaldo oswaldo 3.7K Jul 29 16:43 d_rt_test_0.H
-rw-rw-r--  1 oswaldo oswaldo 3.8K Jul 29 16:43 d_rr_test_0.H@@
-rw-rw-r--  1 oswaldo oswaldo 3.7K Jul 29 16:43 d_rr_test_0.H
-rw-rw-r--  1 oswaldo oswaldo 2.1K Jul 29 16:43 da_angle_test_0.H@@
-rw-rw-r--  1 oswaldo oswaldo 3.7K Jul 29 16:43 da_angle_test_0.H
-rw-rw-r--  1 oswaldo oswaldo 2.1K Jul 29 16:43 da_22_test_0.H@@
-rw-rw-r--  1 oswaldo oswaldo 3.7K Jul 29 16:43 da_22_test_0.H
-rw-rw-r--  1 oswaldo oswaldo 2.1K Jul 29 16:43 da_21_test_0.H@@
-rw-rw-r--  1 oswaldo oswaldo 3.7K Jul 29 16:43 da_21_test_0.H
-rw-rw-r--  1 oswaldo oswaldo 2.1K Jul 29 16:43 da_12_test_0.H@@
-rw-rw-r--  1 oswaldo oswaldo 3.7K Jul 29 16:43 da_12_test_0.H
-rw-rw-r--  1 oswaldo oswaldo 2.1K Jul 29 16:43 da_11_test_0.H@@
-rw-rw-r--  1 oswaldo oswaldo 3.7K Jul 29 16:43 da_11_test_0.H
-rw-rw-r--  1 oswaldo oswaldo 3.8K Jul 29 16:43 d_22_test_0.H@@
-rw-rw-r--  1 oswaldo oswaldo 3.7K Jul 29 16:43 d_22_test_0.H
-rw-rw-r--  1 oswaldo oswaldo 3.7K Jul 29 16:43 d_21_test_0.H@@
-rw-rw-r--  1 oswaldo oswaldo 3.7K Jul 29 16:43 d_21_test_0.H
-rw-rw-r--  1 oswaldo oswaldo 3.7K Jul 29 16:43 d_12_test_0.H@@
-rw-rw-r--  1 oswaldo oswaldo 3.7K Jul 29 16:43 d_12_test_0.H
-rw-rw-r--  1 oswaldo oswaldo 3.8K Jul 29 16:43 d_11_test_0.H@@
-rw-rw-r--  1 oswaldo oswaldo 3.7K Jul 29 16:43 d_11_test_0.H
-rw-rw-r--  1 oswaldo oswaldo  20K Jul 29 16:43 rotate_2c_by_2c_test_0.out
[oswaldo@dellpi S_data]$
```

These are the 13 possible output files of program rotate_2c_by_2c. The program was run in this instance asking for all the types of rotated data. A detailed description of the automatic Alford rotation is described in Chapter 5.

PROGRAM ALFORD AZIMUTH MAP

Computation flow chart

Performing the Alford rotation using program **rotate_2C_by_2C** will generate a file that contains the estimated principal axis of anisotropy direction for each group of traces from the prestack rotated shear data. This fracture azimuth file along with the velocity field of the data can be used to create an estimated average anisotropy direction for each CDP location using program **alford_azim_map**. Below is .the flow chart showing the workflow for the prestack principal axis of anisotropy estimation:

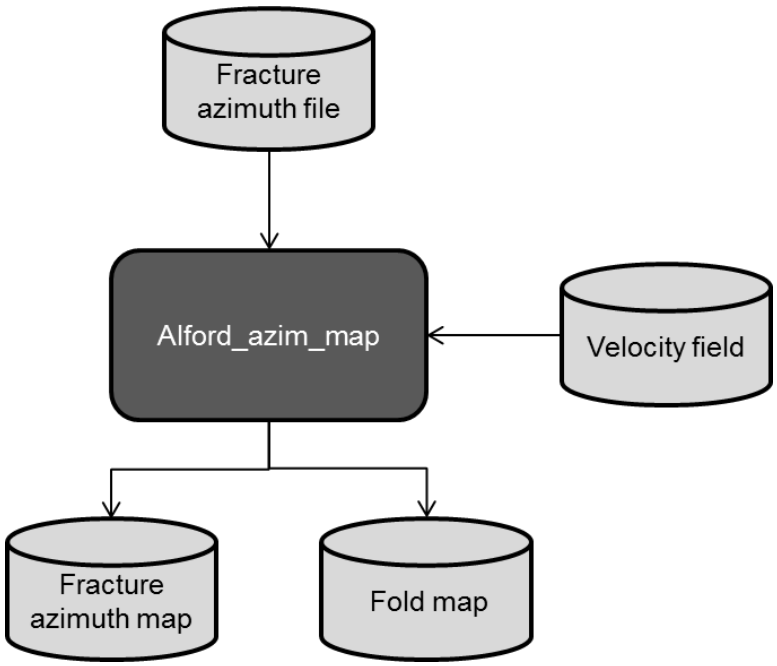

Running alford_azimuth_map

Currently the program can only be launched from the command line by typing *aaspi_alford_azim_map_pf*. Use the browser to select the fracture azimuth file from

program **rotate_2C_by_2C** (1) and the velocity filename (2). In the '*Extended*' tab the parameters for computing the map can be modified selecting the inline (3 and 4), crossline (5 and 6) and offset (7 and 8) range to be used in the map computation.

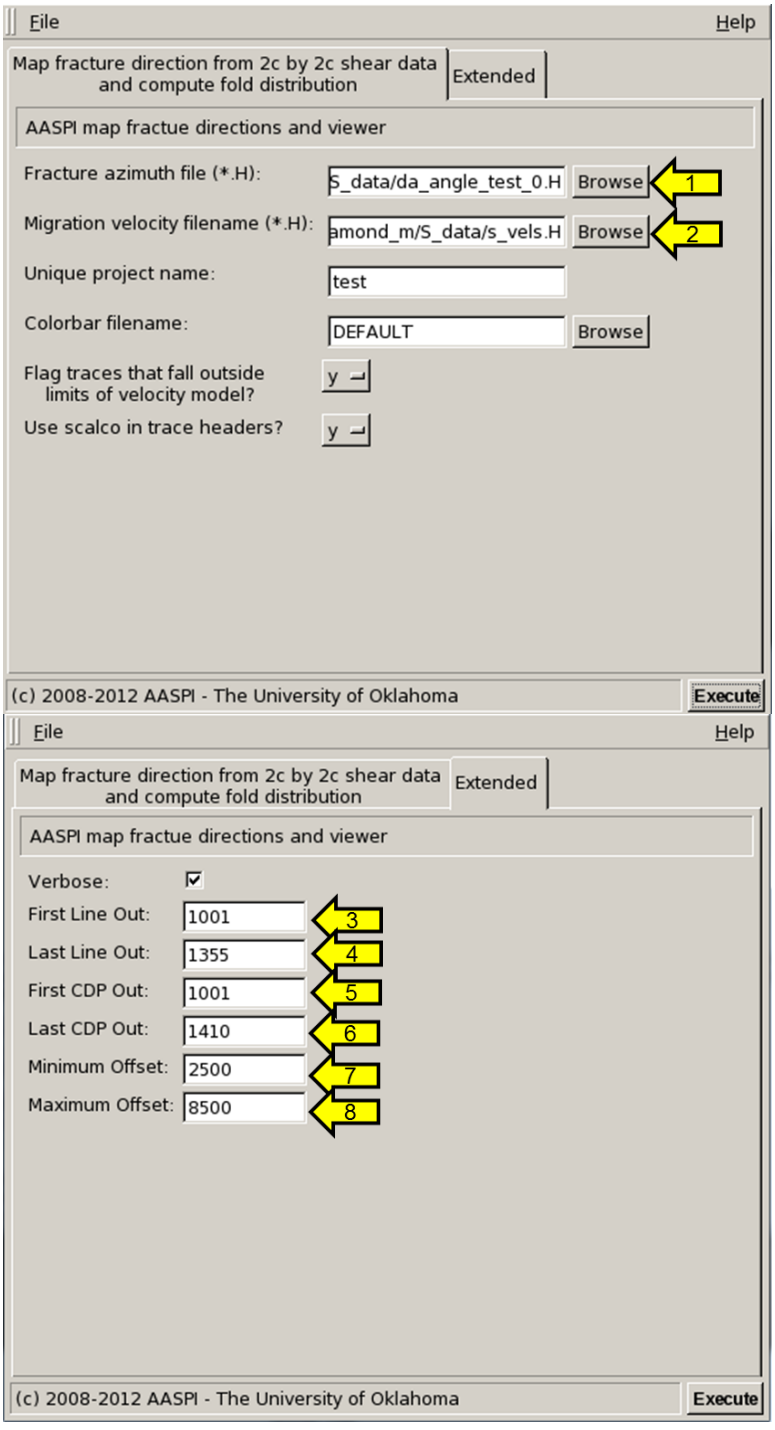

Once the program has finished computing the estimated average fracture directions two windows will pop-up displaying the fold map for the data and the estimated fracture azimuth map